LASER-INDUCED SUB-MILLISECOND STRUCTURAL FORMATION KINETICS IN BLOCK COPOLYMERS

A Dissertation

Presented to the Faculty of the Graduate School

of Cornell University

in Partial Fulfillment of the Requirements for the Degree of

Doctor of Philosophy

by

Alan G. Jacobs

January 2017

LASER-INDUCED SUB-MILLISECOND STRUCTURAL FORMATION KINETICS IN BLOCK COPOLYMERS

Alan G. Jacobs, Ph.D.

Cornell University 2017

Block copolymer (BCP) self-assembly has found broad use in applications ranging from nanocomposites to nanolithography by exploiting the precise control of nanoscale order possible over macroscopic length scales. One application garnering significant attention for commercialization uses this nanoscale order to augment current photolithography patterning to achieve sub-20 nm features through directed self assembly (DSA). Extending current lithography to these smaller length scales is critical to enable cost-effective next-generation semiconductor devices, furthering technological progress and maintaining the pace of Moore's law.

As with many of these applications, DSA utilizes BCPs starting from deeply metastable states. Detail of the initial phase segregation process, structure formation, and refinement are critical to device function, efficacy, and yield. However, understanding of this initial phase segregation from deeply metastable states, especially the temporal evolution, is currently lacking. This ignorance stems in part from both a difficulty in experimentally measuring the short time structural response of polymers, and on the computational difficulty in modeling large enough systems at high fidelity over molecular timescales. Furthermore, for DSA, the anneal must achieve a near perfectly aligned equilibrium structure. The timescale required, and thus the cost, to reach the fully aligned state is dependent upon kinetic pathways, especially past any potential trapped

defect states.

Laser spike annealing (LSA) can achieve high temperatures for short durations allowing investigation of potential process windows in the microsecond to millisecond time scales. In this work, a CO_2 gas laser (120 W, λ=10.6 μm) and a solid state diode laser (250 W, λ=980 nm), were used to achieve peak temperatures up to ~1000 °C on time scales from 50 μs to 10 ms. Additionally, high throughput experiments of the lateral gradient LSA (lgLSA) method were used to fully explore these time and temperature regimes. This has enabled exploration of a previously inaccessible temperature regime and the determination of kinetic parameters that potentially offers access to new processing regimes and resulting structures.

For these short duration anneals, it is shown that the thermal stability of typical organic materials is extended by over 450 °C compared to hot plate limits. This stability was quantified using Arrhenius kinetics with activation enthalpies ranging between 0.6 and 1.2 eV. The activation energies appear to scale with the primary (backbone) bond formation energy and inversely with the bond polarity.

This extended thermal stability was exploited to probe the self-assembly kinetics of cylinder forming poly(styrene-*block*-methyl methacrylate) (PS-*b*-PMMA, 54 kg/mol, f_{PS}=0.67) by annealing at temperatures up to 550 °C for timescales from 250 μs to 10 ms with heating and cooling rates in excess of 10^6 K/s. Segregation kinetics were quantified by X-ray scattering (μ-GISAXS) and electron microscopy (SEM), resulting in kinetic phase maps that describe the phase segregation behavior. The onset of phase segregation and of disordering were found to be kinetically suppressed for times below 1 ms, exceeding the expected transition temperatures by 70 °C at 250 μs. This is shown to be

consistent with the diffusion behavior on these timescales.

These BCP segregation kinetics control the ordering and templating required for DSA lithography. High temperature LSA near the order-disorder transformation temperature (T_{ODT}) was explored as a means to reduce the segregation driving force, increase polymer mobility, and ultimately reduce defectivity by allowing polymer alignment to the directing template with higher fidelity. Hot plate and/or LSA alone result in films with high defectivity. However, an LSA anneal first to establish the initial segregation, followed by a conventional hot plate anneal, can reduce the defectivity by >80 %. This is believed to this reflect nanoscale 3-d ordering in the BCP and interactions with the directing template during the very short LSA near the ODT.

This demonstrated defectivity reduction only highlights the need for better understanding of BCP phase segregation kinetics from deeply metastable states, which ultimately will advance our ability to rationally design processing for improved efficacy. While PS-*b*-PMMA is an important model system, significant opportunities lie in exploring other systems with varying chemistries and glass transition temperatures, especially for highly incompatible systems where disordering is not typically observed thermally. Beyond studying polymer behavior, short duration annealing, and kinetic suppression of structural motifs, presents opportunities for spatially resolved chemistry and other novel applications.

BIOGRAPHICAL SKETCH

Alan G. Jacobs is originally from Bismarck, North Dakota where he grew up on a hobby farm (40 acres) helping to raise llamas. He decided to pursue a Chemical Engineering degree from the University of Minnesota as he liked Physics and Chemistry but wanted to work on actual products, which supposedly meant engineering. After having experienced some of the realities of the curriculum, Alan decided that he was more interested in Materials Science but kept taking extra Physics courses and labs. At the end of four years, he had attained a Bachelors of Materials Science and Engineering, Summa Cum Laude, a Bachelors of Science in Physics with Engineering Emphasis, with distinction, and a minor in Astronomy.

While in undergrad, two major events happened. First, he met his soon-to-be lifetime partner in crime and married in 2011. Second, his eyes were opened to research under the direction of Professor Eray Aydil working on PbSe quantum dot solar cells. This was soon followed by research on light extraction films for OLEDs at 3M and the PhD program at Cornell University working on polymer self-assembly kinetics. He has decided to pursue a career in materials research and is joining the Naval Research Lab upon graduation.

To Stephanie, love of my life, ever present accomplice, partner, and best friend.

To my family, who got me where I am – I am forever grateful.

To my collaborators, for boundless inspiration.

To Greg, my father, ever caring, curious, and wide eyed;

To Heidi, my sister, infinitely loving, kind, and generous:

We will always remember you.

ACKNOWLEDGEMENTS

This document and my education could not have been possible without the contributions of so many – I cannot appropriately express my gratitude in mere words. What follows only touches on these contributions and I thank everyone along the way.

Perhaps the most important people in my research career has been my advisors. Especially Michael Thompson who has been ever patient and incredibly brilliant. I have learned so much and hope to one day emulate your simultaneous competence, patience, and joy. My minor committee members, Ulrich Wiesner, Christopher Ober, and Clifford Pollock, were all chosen for practical research purposes but have dedicated so much more. Thank you.

At Cornell, my research could not have been possible in a technical sense without the countless hours and conversations from the Thompson, Ober, and Wiesner group members and collaborators everywhere. I must first and foremost thank Byungki Jung for all his mentoring and work on LSA. I was mentored by so many and thank in particular Kwan Tan and Rachel Dorin for all that pesky chemistry stuff that I was so ignorant of. Bob Bell has been my laboratory partner in crime since Day 1: a perfect sounding board and intellectual complement for me, David Lynch has been so indispensable for lab and CNF work, and Victoria Sorg challenged myself and LSA with interesting new substrates and materials systems while always brightening the room and balancing David's antics.

My work has benefited greatly from the efforts of the CNF, CCMR, and CHESS and I must thank all current and past contributors to these excellent centers. In particular, I wanted to thank Chris Alpha, Garry Bordonaro, Rob Ilic, Aaron Windsor, and Sam Wright of the CNF along with John Grazul, Steve

Kriske, Don Werder, and Phil Carubia of the CCMR for their continual technical excellence and assistance in whatever project or scheme I had thought up at the time. CHESS has particularly been important to my research progress as it enabled me to acquire the plethora of data that my dissertation is based upon. I must especially thank Detlef Smilgies and Ruipeng Li for giving me tremendous help in running my X-ray experiments and teaching me the ropes of GISAXS and other techniques.

Without collaborators, I would be stuck in a black hole of my own ignorance. In particular, Katherine Barteau, Sarah Hesse, Joerg Wanner, and Brandon Wenning have been so helpful for synthesis of materials and expanding my knowledge of polymers. I also want to acknowledge all the discussions, help, and advice from Peter Beaucage, Clemens Liedel, Katherine Camera, Alicia Cintora, Qi Zhang, Spencer Robbins, Roselynn Codero, and Jing Jiang (JJ).

Industrial colleagues and collaborators have greatly impacted both the direction and opportunities I have had and I wanted to thank my colleagues at EMD Performance Materials (previously AZ Electronic Materials), Intel, and Tel for their support, samples, and discussions.

All the Thompson group members have been my surrogate family and colleagues and I will miss the discussions, ideas, and fantastic enrichment you have brought to my work and life. For that, I especially thank Kathryn Roach, Chen-Yang Chung, Bin Zhu, Michael Willemann, and Megan Hill.

As the dedication hints at, my family has always been supportive and I can only begin to thank them. Stephanie has always been my rock through this exciting adventure. Words can't even begin to express my gratitude. Thank you all.

CONTENTS

LIST OF TABLES

LIST OF FIGURES

CHAPTER 1

INTRODUCTION

1.1 Block Copolymers

In recent decades, improvements in synthetic methods have empowered chemists of create and refine a broad range of new block copolymer (BCP) systems, combining dissimilar chemistries within a single system. Such systems consist of a controlled molecular weight of polymer A covalently bonded to a separate polymer B, and potentially as many blocks as desired. While linear block copolymers are most common, other structures are possible including stars or repeated block chains (e.g. ABABA, ABCBA, ABCABC, etc). These systems enable otherwise inaccessible chemical moieties and phase behavior, leading potentially to boundless new applications. The sheer number and diversity of possibilities ensures discovery within the BCP arena to continue for the foreseeable future. Already many important practical and research applications have emerged.

The vast majority of currently implemented applications for block copolymers are based on the ability of the polymer to retain properties from individual blocks and incorporate these properties into a bulk material better suited to its application. Though the synthesis of linear diblock copolymers occurred as early as the 1930's, significant synthetic diversity did not develop until the 1960's with the early work on styrene-isoprene based ABA triblock copolymers and other subsequent architectures. This synthetic ability, with the potential for mass production, opened up a new arena of organic materials which could incorporate the rubber elasticity of isoprene with the hardness of styrene leading to improved longevity and wear resistance compared to pure isoprene com-

pounds and improved fracture resistance compared to polystyrene[1].

Industrially important materials in common use today include styrene-butadiene rubbers (SBRs) and high impact polystyrene (HIPS). Synthetic SBRs and their derivatives are responsible for significant improvements in traction, lifetime, and efficiency of automobile tires and shoe outsoles. Similarly, HIPS is commonly used for consumer products, particularly children's toys for its high fracture toughness and stiffness at ambient and moderately elevated temperatures. While both of these materials are used as bulk materials, other block copolymers have found significant use as compatibilizing agents in polymer blends for many consumer and industrial products. Without such compatabilizers, many polymer blends potentially phase segregate with significant physical weakness along phase boundaries or macroscopically anisotropic properties.

1.1.1 Potential Applications with Nanoscale Self-Assembly

These industrially important applications exploit the ability of block copolymers to bridge dissimilar chemistries and rely primarily on "averaging" the properties of the monomers in a "scalar" type manner[1]. However, BCPs can also phase segregate into ordered structures on the nanoscale. Exploiting both the nanoscale effects of materials and the potential perfection of self-assembly processes affords significant opportunities for future applications in "high value" markets such as microelectronics, catalysis, filtration, and drug delivery. Figure 1.1 depicts these different regimes of block copolymer applications.

The use of BCPs can be separated into two general regimes, one based on the bulk behavior as a compatibilizer or to mix dissimilar block properties, and the second based on the nanoscale structure that can develop within the BCP.

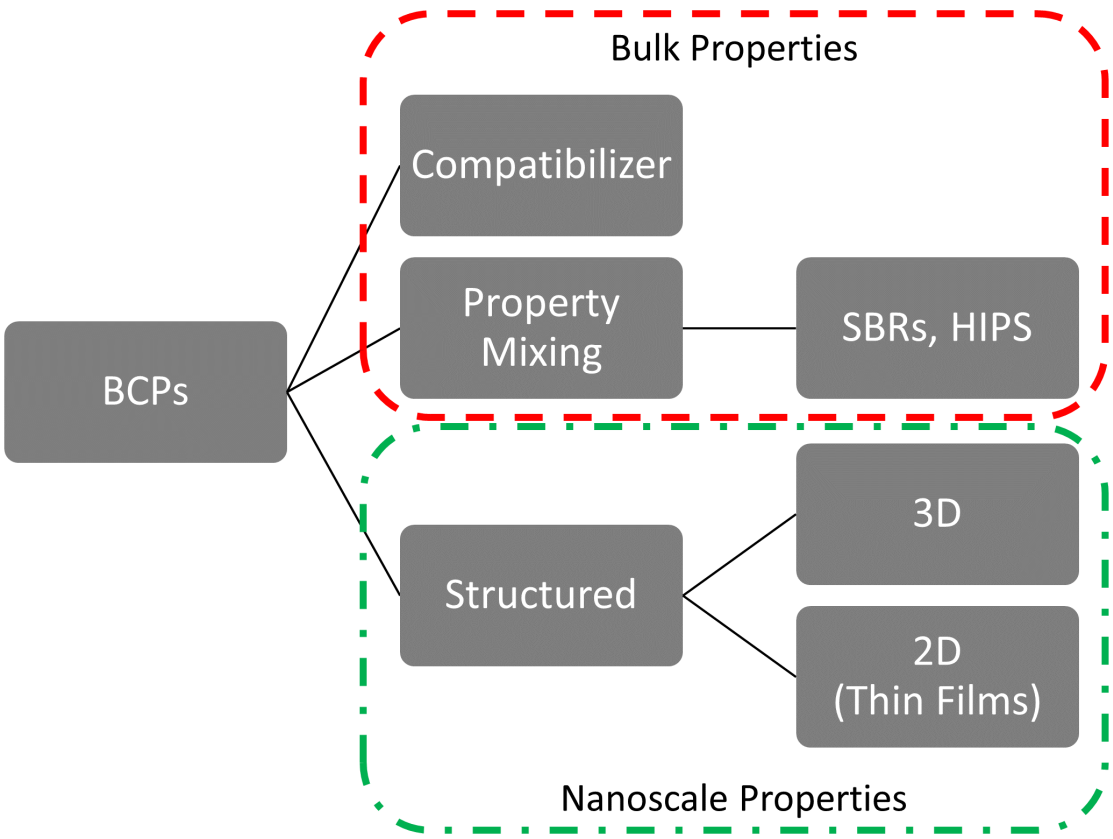

Figure 1.1: Representation of block copolymer applications stemming from the polymer bulk properties or nanoscale structural control.

This regime can be further subdivided into applications where all product dimensions are much larger than the nanoscale ordering dimension utilizing the full 3-d structure, or for thin films where the thickness is comparable to the BCP order dimension leading to pseudo 2-d structures.

The inherently 3-d phase segregation and self assembly process can produce a myriad of structures. Figure 1.2 schematically shows the equilibrium structures for a diblock copolymer composed of varying fractions of generic A (red) and B (blue) blocks. Depending on the relative size of the A and B blocks, the system will phase segregate into various structures.

For low relative volumes of A, the material forms spheres of A in a matrix of B. As the volume fraction of A is increased, hexagonally packed cylinders are formed followed by a complex gyroid phase. At near equal volume fractions A and B, a lamellar system is formed with the pattern symmetric whether A or B rich. The boundary for these phases depends on the interaction between A and B as defined by the χN parameter described later in Chapter 2. In practice, these and other structures have been observed for 2 component systems and an even richer phase space is available for ABC linear or miktoarm star terpolymers. These complex structures can be utilized in their full 3-d form with applications from filtration to catalysis and beyond or in 2-d via thin films.

The reduction of the bulk structures to thin films allowing the 3-d structure to mimic 2-d patterns has received significant industrial attention. One important area currently being explored is use of BCPs to supplement conventional photolithography patterning for semiconductor manufacturing. Critical dimensions for devices today are <20 nm, which is far smaller than the wavelength of light currently used to create patterns (193 nm) but on the scale of BCP phase segregation (5-50 nm). BCP based lithography today competes with advanced pattering technologies including extreme-UV (EUV) lithography using 13.5 nm light.

The unique size scale of block copolymer phase segregation and a chemically defined uniform repeat size are of particular interest. Since the size scale is preprogrammed into the material chemistry, a bottom-up self assembly process could potentially greatly increase throughput relative to the top-down image formation of traditional lithography. This has garnered industrial interest in augmenting traditional lithography via directed self-assembly (DSA) where an initial, fast, low-resolution pattern directs the natural polymer self-assembly to

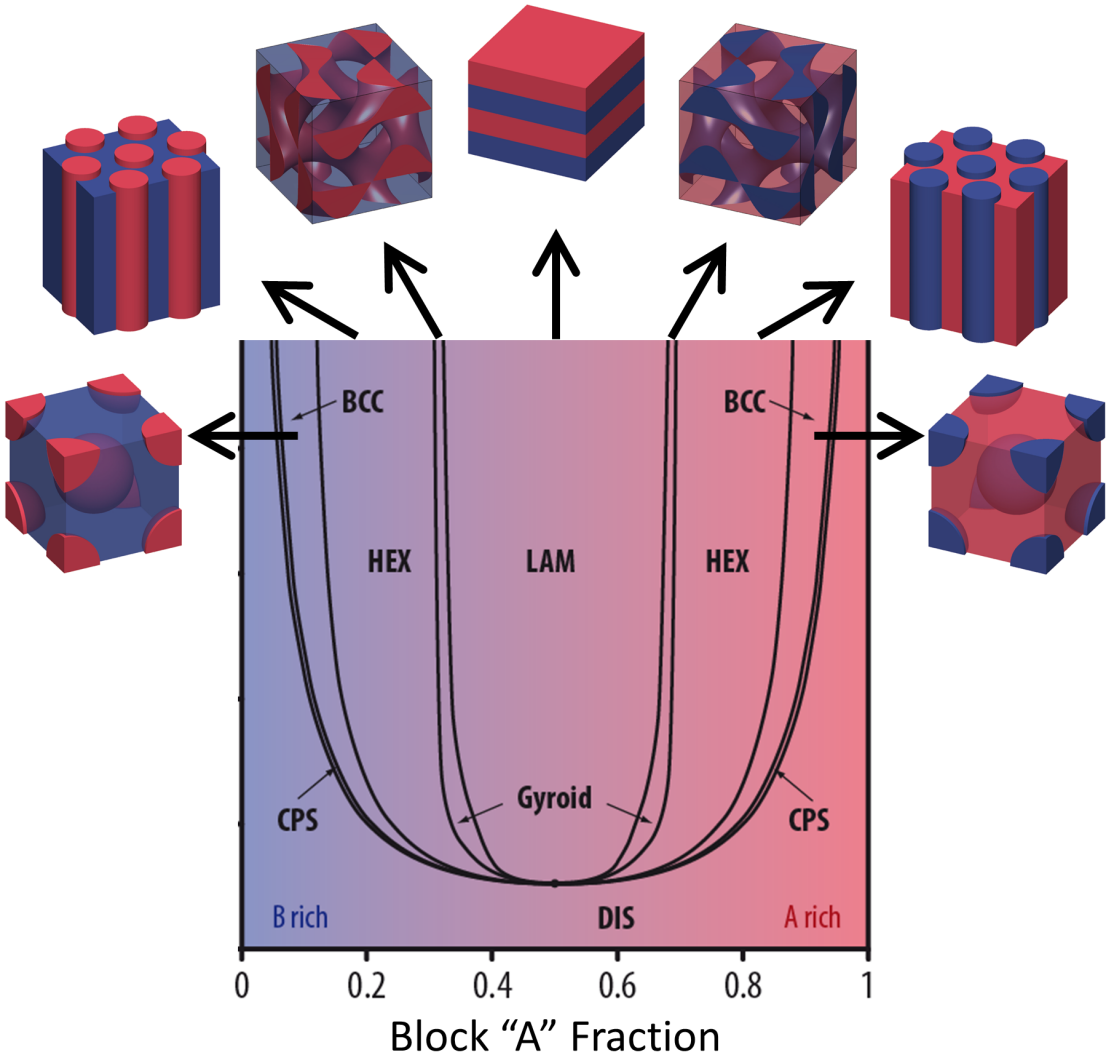

Figure 1.2: Diblock copolymer phase diagram showing expected equilibrium phases as function of the block volume fraction. Reproduced with permissions from Cochran *et al.*[2], copyright Macromolecules 2006.

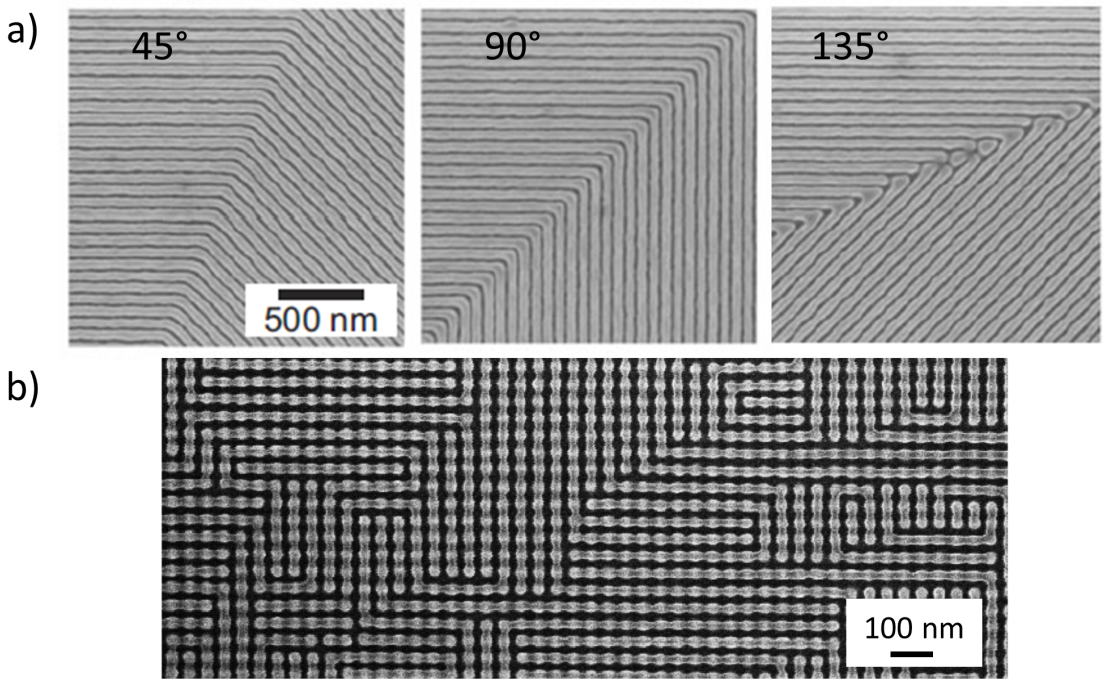

Figure 1.3: Example technologically relevant structures derived from directed self-assembly (a) exhibiting subset of possible angled junctions, reproduced and modified with permissions from Stoykovich *et al.*[3], copyright Science 2005, and (b) example device oriented structures reproduced and modified with permissions from Chang *et al.*[4], copyright Nature Communications 2014.

provide high resolution, dense, large area features at low cost. Figure 1.3 shows just a couple technologically important examples of DSA.

Common to all these potential applications is the development of desired microstructures with low defect density. Defects vary by application, but in DSA, common defects for lamellar forming polymers include dislocation or disclinations where individual lamella exhibit breaks or junctions. The very same unique ability for these polymers to phase segregate due to mutual repulsions leads to challenges in producing such desired structures as the mutually insoluble regions can significantly hinder polymer motion to remove defects. In order

to achieve the desired structures, annealing has been explored extensively using thermal processing, solvent annealing, and a combination called solvo-thermal annealing. Due to the inherent tendency of organic materials to degrade thermally, traditional thermal annealing techniques are constrained to temperatures below about 300 °C. Solvent annealing has been extensively utilized to further increase the polymer mobility by swelling the material with the incorporation of solvent, however, significant structural perturbations can occur via preferential solvent interaction between the polymer blocks and quenching from the solvated state typically yields modified metastable structures.

From a practical standpoint, industrial applications significantly benefit from inexpensive rapid processing with high yield. This, in part, caused the exploration of solvents to decrease material annealing duration. However, process times remain long and the simplicity of purely thermal annealing reduces cost and the need to work with potentially hazardous materials. This raises the question whether modifying the kinetic constraints can enable rapid cost effective annealing.

Toward that end, many have explored annealing in proximity to the solvated or thermal regime where the polymer blocks become miscible, thus reducing barriers toward defect reduction and with increased polymer mobility. For solvent annealing, the polymer must be significantly swelled to reach this limit and upon solvent removal, the material is significantly modified upon shrinking. In the case of thermal annealing, temperatures remain constrained by thermal decomposition which precludes use with large or strongly interacting polymers.

To circumvent these limitations and maintain simplicity, one can thermally anneal organic materials on millisecond and shorter timescales to high temperatures, while maintaining stability for the short anneal duration. In order to

achieve such high temperatures for short durations, non-traditional annealing techniques, such as laser spike annealing (LSA), are needed. Laser spike annealing uses a high power continuous wave (CW) laser to heat thin film materials by absorption within a substrate, typically silicon. As the laser passes the sample area, heat is then quenched into the substrate allowing heating and cooling rates to beyond 10^7 K/s. This allows access to previously untenable (high temperature) regimes where polymers can exhibit vastly enhanced mobility and mixing, but would thermally degrade on long timescales.

Due to the unexplored nature of this new processing regime, it is imperative to understand the kinetic behavior of these polymers to enable use of short duration, high temperature annealing. In addition, studies of the high T behavior may lead to fundamental understanding of the annealing process in all regimes, including traditional anneals for minute to hour timescales. Thus, this dissertation explores the structural formation kinetics in block copolymers in the previously unexplored millisecond and sub-millisecond regime.

1.2 Thesis Outline

This work culminates in the use of short duration heating for the targeted investigation of the segregation kinetics of deeply metastable block copolymers and its application to directed self-assembly defectivity. The necessary background and motivation for this work is included in Chapter 2. Chapter 3 is dedicated to giving the reader an understanding of the unique annealing methods and considerations critical for making determinations of process kinetics beyond a cursory analysis.

In order to study these organic systems in deeply metastable states, the material must remain stable at extended temperatures. Chapter 4 presents data

under short duration heating for multiple organic and inorganic systems with so called "rules of thumb" developed to determine the relative stability of systems and their extended thermal stability for short duration heating.

The kinetic segregation determination of poly(styrene - *block* - methyl methacrylate) is explored in Chapter 5 yielding kinetically limited behavior with causal links to diffusion and various kinetic models discussed. Considerations for other systems and the initial exploratory work into the poly(isoprene - *block* - styrene) system is presented in Chapter 6. Beyond experimental observations, basic numerical finite elements analysis using current segregation theory is included in Chapter 7.

Finally, the utilization of lessons learned for the application of directed self-assembly defect annealing and suppression is presented in Chapter 8 yielding significant improvements. Conclusions and proposed future directions are included in Chapter 9.

CHAPTER 2

MOTIVATION AND BACKGROUND

2.1 Motivation

In the ever evolving world, modern devices and subsequent quality of life is inherently tied to technological efficiency and computational power. The recent primary driver of this progress has been the silicon revolution ushering in the information age. Critical to the diverse and ubiquitous use of computers is the ability to create repeatable and precise patterns on increasingly smaller length scales. The process of microlithography or nanolithography defines the limitations of what we can create these patterns within device manufacturing. Several methods of microlithography have been developed to address the diverse requirements of semiconductor manufacturing and to enable the prophecy of progress dictating the pace of technological improvements expected of the information age. To enable this progress, new patterning technologies are needed to address resolution and throughput requirements.

2.1.1 Lithography Overview

Moore's Law

In 1965, the progress of integrated circuits, and the capabilities and devices they enabled, was revolutionizing modern life with devices fabricated at length scales of human hair at tens of microns. Gordon E. Moore, then a director of research at Fairchild Semiconductor, published a forward looking summary noting that the device density per integrated chip was exponentially growing in time and predicted this trend would continue for the near future with device

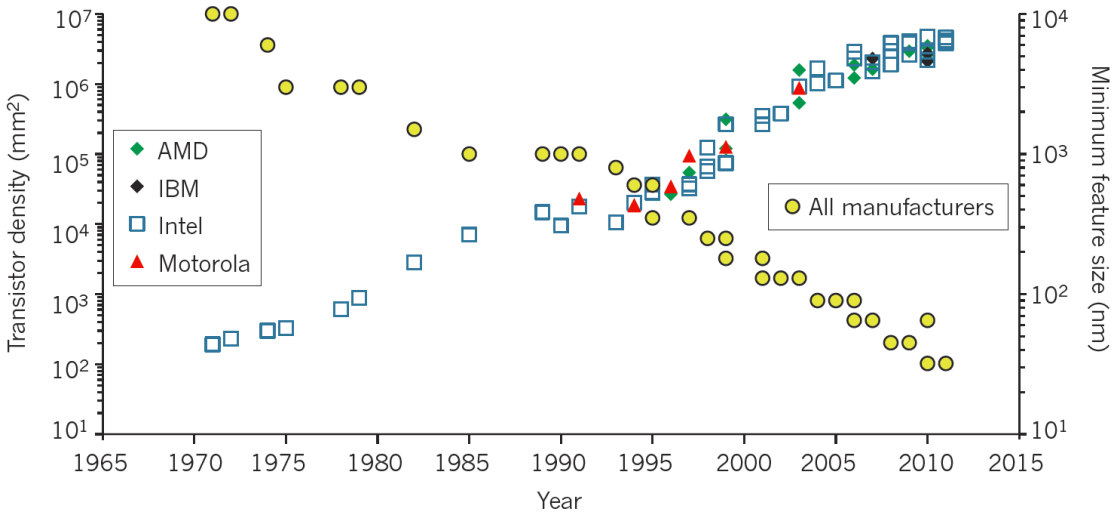

Figure 2.1: Graphical depiction of "Moore's Law" where transistor density follows exponential trend in time enabled by reduced feature sizes. Reproduced with permission from Ferain *et al.*[7], copyright Nature 2011.

density doubling every ~18 months[5–7].

This observation, turned proclamation, has directed the goals for the international technology roadmap for semiconductors (ITRS) to increase transistor density with smaller devices reaping benefits in device speed, power consumption, and cost per transistor. For a remarkable duration, industry has sustained this pace, as shown in Figure 2.1, where transistor density (left axis) increased roughly exponentially in time enabled by the decrease in feature sizes (right axis).

Patterning at higher resolutions is key to continuation along Moore's law. Conventional lithography, and its limitations, are briefly reviewed here before introducing and discussing the evolving field of directed self-assembly (DSA) of block copolymers (BCPs), a potential augmentation to current conventional lithography for improved resolution and throughput.

Lithography

Lithography is the generic term for the creation of patterns and has accompanied technological revolutions throughout history. In the semiconductor field, lithography describes any of several methods for creation of micron to nanometer scale patterns, primarily by photons (photolithography) or electrons via electron beam (e-beam) lithography. Fundamentally, photolithography is relatively fast as it exposes large areas simultaneously, but the potential resolution is limited by the wavelength of light used. E-beam lithography has much higher resolution stemming from short electron wavelengths and beam focusing, down to a few nm, but remains an extremely slow process as it exposes a very small area at once. Industry combats these contrasting abilities by utilizing photolithography for high volume manufacturing and e-beam lithography for lab-scale testing and low volume, high resolution, production processes, such as production of photolithography masks.

Patterning Process

Both photolithography and e-beam lithography follow similar image formation processes, shown schematically in Figure 2.2. The process uses a specially formulated, energy sensitive material, typically made from polymers and known as a resist. This resist is spin coated on the substrate and exposed to light or electrons to perform some chemistry during a subsequent step. In the case of photolithography (shown), a mask is utilized to define the pattern of light on the resist while for e-beam lithography, the electron beam is directed to expose desired areas.

The resist material generically comes in two categories, positive and negative tone. For positive tone resists, the exposed area becomes more soluble

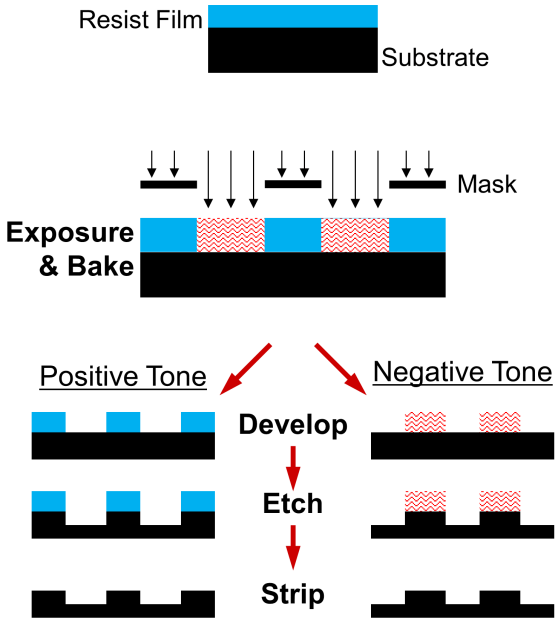

Figure 2.2: Schematic representation of typical photolithography process for positive and negative tone resists.

in a development solution, typically a weak base, exposing the substrate to be etched or deposited upon before removal in a stripping solution. The resist material is called "positive" in this case as the resulting substrate modification is a direct duplication of the initial exposure area. For negative tone resists, the exposed area becomes less soluble in the development solution resulting in the "negative" image of the initially exposed area on the substrate.

In order to improve processing throughput for photolithography, current photoresists utilize chemical amplification in order to produce multiple chemical modification events per incident photon. In these resists, the key chemical processes occur in a post exposure bake (PEB) commonly involving the modification or cleavage of polymer side groups for both positive and negative tone resists. Figure 2.3 schematically shows one potential side change cleavage chemical amplification schema. In this process, incident photons are absorbed by a

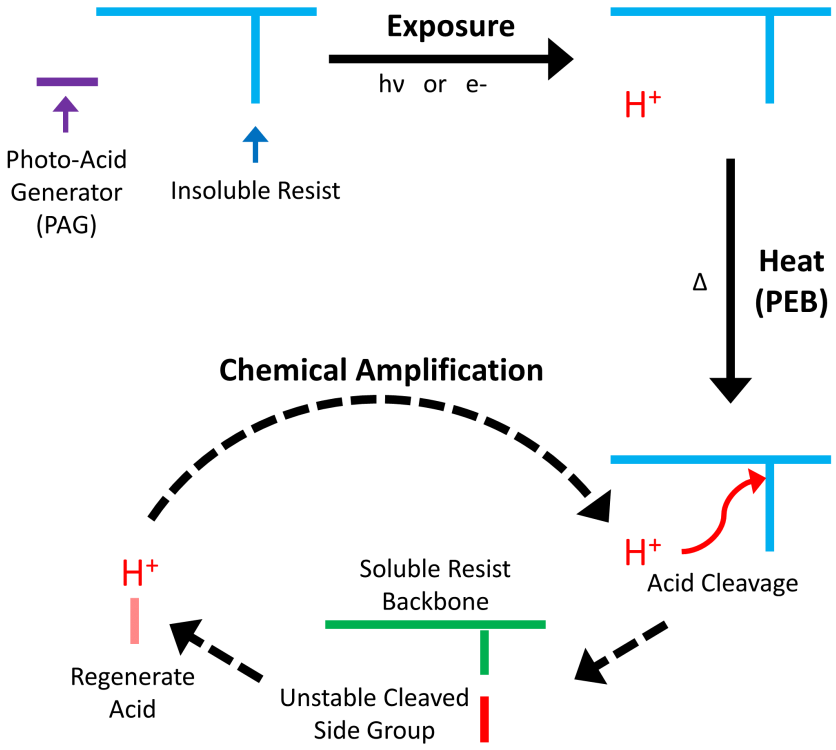

Figure 2.3: Schematic representation of a chemically amplified photoresist deprotection process for a generic positive tone resist.

photo-acid generator which releases a proton or other acid. During the PEB, this acid attacks the polymer side group, cleaving off an unstable byproduct. This cleaved byproduct stabilizes with the generation of another acid allowing for further cleavage events to occur. The modified resist subsequently exhibits a solubility change in the development solution.

2.1.2 Photolithography Limitations

From a practical standpoint, the most important aspects of photolithography for production are the minimum resolvable feature size, throughput, and image imperfections like placement error and roughness. Table 2.1 summarizes the published ITRS lithography guidelines[8] for current and future technology

nodes as of 2015. Notably, resolution for the current production node is near 20 nm with control of the critical dimensions (CDs) and roughness (to 3 standard deviations) near 2.4 nm. State of the art production photolithography tools expose 300 mm diameter wafers at rates exceeding 275 wafers per hour (~13 seconds per wafer) at 30 mJ/cm^2 exposure dose[9]. Following the ITRS guidelines, these resolutions and control limits are also aggressively scaled with minimum feature sizes shrinking by 3x within 7 years. Though the guidelines are aggressively scaled, it should be noted that actual solutions needed to achieve the 7 nm node and beyond are significantly lacking.

Table 2.1: Select ITRS lithography technology requirements.

Production Year	2015	2017	2019	2021	2024
Logic "node" [nm]	21	18	12	10	6
Critical dimension (CD) control 3σ [nm]	2.4	1.8	1.2	1.0	0.6
Line edge roughness (LER) 3σ [nm]	2.4	1.8	1.4	1.0	0.9
Overlay control 3σ [nm]	5.2	3.6	2.4	2.0	1.2

To develop effective solutions for the near term nodes, the current lithography resolution must be improved. Within the realm of photolithography, the minimum feature size is dictated by diffraction limits and quantified by the Rayleigh criterion. This provides the minimum resolved feature size and the effective depth of focus (DOF) given by:

$$Resolution = k_1 \frac{\lambda}{n \sin\theta} = k_1 \frac{\lambda}{\mathrm{NA}} \tag{2.1}$$

and

$$\mathrm{DOF} = k_2 \frac{\lambda}{n \sin^2\theta} = k_2 \frac{n\lambda}{\mathrm{NA}^2} \tag{2.2}$$

where NA = n sinθ is the numerical aperture, n is the index of refraction of the imaging medium (typically air or water), θ is the half angle subtended by the first optical element, and k_1 and k_2 are Rayleigh coefficients and dependent upon the resist material and image formation technique. In modern steppers, k_1 can be as low as 0.25[10]. To further increase resolution, one can primarily decrease the wavelength of light or, to a lesser extent, increase the tool numerical aperture.

In practice, the former was done by decreasing the UV exposure wavelength from mercury lamp wavelengths of 435 nm down to "deep UV" KrF excimer laser light at 248 nm to 193 nm light from ArF excimer lasers. This however becomes difficult to continue as the typical fused silica optical components (and most materials) absorb significantly at wavelengths below 193 nm. To decrease the operational wavelength further, reflective optics in a vacuum environment are required as well as a suitable high intensity source.

The latter method of increasing the numerical aperture has also been used by modifying the optical stack and, furthermore, by moving to an immersion system where the sample exposure occurs under a high index fluid[11]. Today, this has culminated in the use of 193-*immersion* tools which expose samples under high purity water yielding a numerical aperture of ~1.35[10]. Given a Rayleigh k_1 coefficient of 0.25-0.3, this yields a resolution limit of ~35-45 nm, though with commensurate reduction in the depth of focus requiring precise alignment and planarization.

In addition to the process resolution, strict precision of feature size replication and edge roughness is also paramount. Within a single chip, variations in the CD cause variations in device performance and reduce yield. Two major drivers of roughness and CD uniformity are exposure dose dependent noise

from stochastic effects and finite size effects of the resist material. Table 2.2 lists the target exposure sensitivities for several photolithography techniques at varying wavelengths. As the wavelength decreases, photons are typically more difficult (costly) to produce motivating an increase in sensitivity to use less photons. The energy per photon also increases with decreasing wavelength meaning that significantly fewer photons of light are utilized causing relative variations in exposure dose to drastically increase.

Table 2.2: ITRS requirements for resist material sensitivity.

Lithography Technology	Exposure Dose	photons/nm^2
248 nm photolithography	20-50 mJ/cm^2	250-630
193 nm photolithography	20-50 mJ/cm^2	190-490
EUV (13.5 nm) lithography	10-20 mJ/cm^2	6.8-13.6

Additionally, photoresist polymer molecules are of several nm in extent and no longer excessively small compared to the targeted feature sizes. If an entire chain of polymer is removed, it can cause intrinsic roughness to features, irrespective to the exposure conditions. This has prompted research into small molecule and nanoparticle based resists.

2.1.3 Current and Future Lithography Solutions

193-*immersion* (193-*i*) Lithography

The current workhorse lithography system responsible for high volume manufacturing is 193-*immersion* lithography (193-*i*). Current tools achieve an impressive throughput at >275 wafers per hour at critical dimensions of ~40 nm (~80 nm full pitch). Though high resolution relative to the 193 nm wavelength

light is achieved, it is insufficient for modern devices. For fabrication of smaller features, clever tricks must be used to increase the feature density, such as double, quadruple, or octuple patterning, which has been demonstrated to sub-10 nm features[12]. However, each additional process step reduces throughput and increases costs. In order to improve throughput and simplify processing, several potential solutions are being pursued. Among them, EUV lithography and directed self assembly (DSA) lithography have shown significant promise.

Extreme Ultraviolet (EUV) Lithography

An extension to current photolithography processes called extreme ultraviolet lithography uses 13.5 nm light. Due to the significantly higher photon energy, all materials absorb EUV photons to some extent requiring use of all vacuum processing and multilayer reflective optics. Additionally, masks are currently made from alternating molybdenum and silicon films 3-4 nm thick. The source of EUV photons is a tin plasma which introduces optics to particulate contamination, primary mirror sputtering damage, and photon production is incredibly inefficient, requiring ~1 MW to produce 200 W of photons adding significant heat loads to many components. In addition to the optics, mask, and source challenges, resist materials must also contend with the generation of multiple excited electrons per absorbed photon, significant shot noise effects, and modified photon absorption cross section compared to the UV requiring further innovation[13, 14].

While some of these challenges are new, the processing is analogous to current methods and compatible with current mask and device layouts. With the recent demonstration of ~200 W sources with >75% uptime[15], a major hurdle for implementation has been overcome. This has allowed a demonstrated

throughput of 1300 wafers per day (>50 per hour) at 20 mJ/cm^2 dose with the potential for ~100 wafers per hour[16] suggesting EUV may find a niche role for the most stringent layers with more general geometries. Though impressive, challenges achieving these resist sensitivities and the true cost of implementation remains a question.

Directed Self Assembly (DSA) Lithography

Even with recent photolithography advancements, there is still a large push toward alternative techniques, especially toward directed self assembly. This is particularly the case in order to address multiple drawbacks to current high resolution solutions. Critical dimensions are evolving significantly beyond the resolution limits as 193-*i*, which is already patterning beyond its nominal limit via clever tricks, and EUV remains to be proven economical and developed in time for features that do not require double patterning with EUV, further diminishing the already poor throughput and economics. Edge roughness from patterning is also a challenge which could be intrinsically improved upon by using a non-stochastic process while the requisite CD uniformity could benefit from a molecular determinant of size. Additionally, for EUV, as the wavelength is decreased by over an order of magnitude, the depth of focus also shrinks resulting in potentially untenable requirements for resist film thickness, surface alignment, and substrate curvature.

Block copolymer self-assembly, discussed in detail in the next section, has garnered significant interest in augmenting current 193-*i* patterning. Figure 2.4 schematically shows the chemoepitaxial "LiNe" flow where a substrate is patterned at a large pitch to direct the subsequent polymer self-assembly, typically increasing the initial patterning pitch. This process, called directed self-

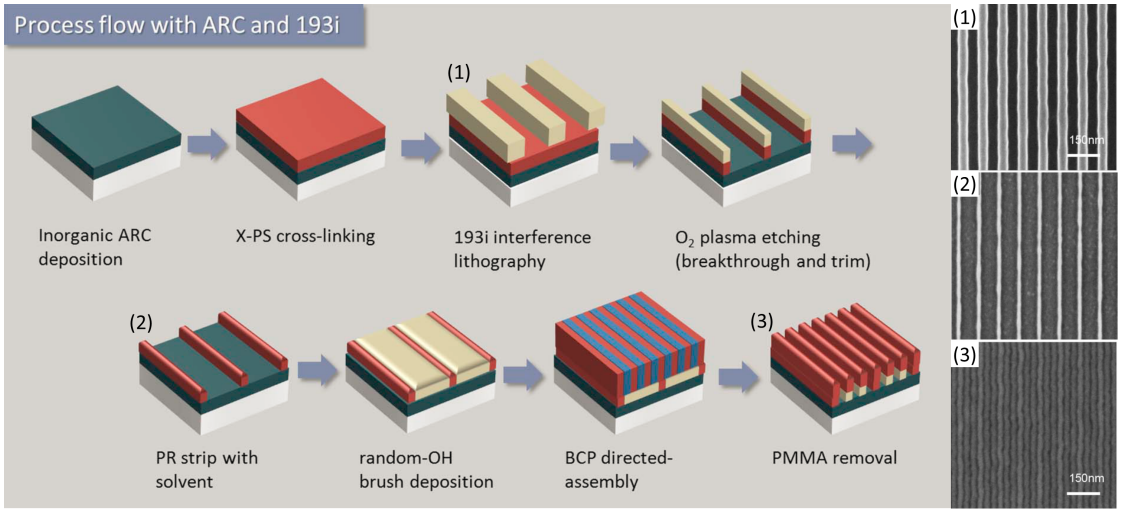

Figure 2.4: Schematic representation of directed self-assembly "LiNe" flow, modified with permissions from Liu *et al.*[17], copyright JVSTB 2010.

assembly (DSA), starts by patterning resist on top of a chemoepitaxial directing layer, in this case, a cross linked polystyrene (PS) mat for the poly(styrene-*block*-methyl methacrylate) (PS-*b*-PMMA) BCP. The pattern is transfered to the PS mat using an oxygen plasma etch.

The oxygen plasma etch also trims the large initial features to be commensurate in width to the BCP structure by a lateral etch. After attaining the preferred width, the photoresist is removed and a random copolymer brush is grafted to the exposed anti-reflective coating (ARC) layer. This random copolymer acts to produce a net neutral interaction and promotes a vertical morphology. In general, the interfacial interactions between the block copolymer and the substrate or the free surface are critical to obtaining the desired morphology.

The block copolymer is then coated and annealed, providing the self-assembly which is directed into parallel lines in this example. After annealing, the BCP is etched to remove one of the blocks yielding the dense pattern. In the

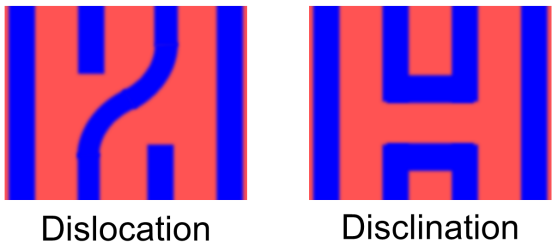

Figure 2.5: Schematic representation of intrinsic directed self-assembly defects.

case shown by Liu *et al.*, the initial 193-*i* pattern is subdivided by a factor of 3. In general, the initial patterning can be some integer multiple of the BCP periodicity to yield significant resolution enhancement with low defects for proper engineering of interfaces and the directing pattern geometry. In addition to directing patterns chemically, DSA can also use physical features as a directing pattern as in graphoepitaxy. This dense pattern is then selectively removed via a cut mask step, though it should be noted that this is already commonly used and not necessarily an additional process step.

Naturally, this technique adds some processing steps, however, the added steps are primarily organic film deposition (spin coating) and annealing which requires no significant expense in new equipment. The material dictates the feature size and only a hot plate or oven is necessary for annealing. Throughput is primarily dictated by the anneal duration, typically of order minutes, and can be increased by parallelizing the relatively inexpensive annealing method. In contrast to EUV lithography, effectively an extension of traditional photolithography, a significant learning curve must be overcome to work with this different patterning scheme and materials set, especially with respect to feature roughness and pattern defects.

As the DSA guiding pattern is determined by the initial 193-*i* lithography,

any placement errors or low spatial frequency deviations are imparted on the BCP pattern and are correlated across multiple nearby features. In addition to this new correlation aspect, new defects are possible. The block copolymer segregation process can have intrinsic defects from imperfect self-assembly or alignment. In the case of the line/space (L/S) patterns, these look like dislocations or disclinations, shown schematically in Figure 2.5. Though computational studies suggest that the defect formation energy is high and the equilibrium thermal defect concentration for monodisperse polymers should be effectively zero[18], other materials aspects like polydispersity, homopolymer inclusion, purity, and oxidation significantly affect these intrinsic defects and removal kinetics. To combat these intrinsic defects in a cost and time effective manner, additional understanding of the annealing process is necessary. Specifically, the kinetic constraints and drivers for defect annealing, as well as knowledge of the phase segregation process, are absolutely critical to develop methods to reduce defects to appropriate levels.

2.2 Block Copolymers (BCPs)

Directed self-assembly is based on the behavior of specially formulated block copolymers. In contrast to random or alternating copolymers with adjacent monomers of differing chemistries, block copolymers (BCPs) consist of homopolymer chains (blocks) covalently bonded at specific points to form a longer polymer chain with multiple blocks. Figure 2.6 schematically depicts the simplest examples where different colors denote different monomer chains. In practice, the simplest block copolymer has only two blocks, generically A and B, while more complex materials may include additional blocks (ABCD, ABABA, etc.), a star morphology (ABC bonded near a single atom), and combinations

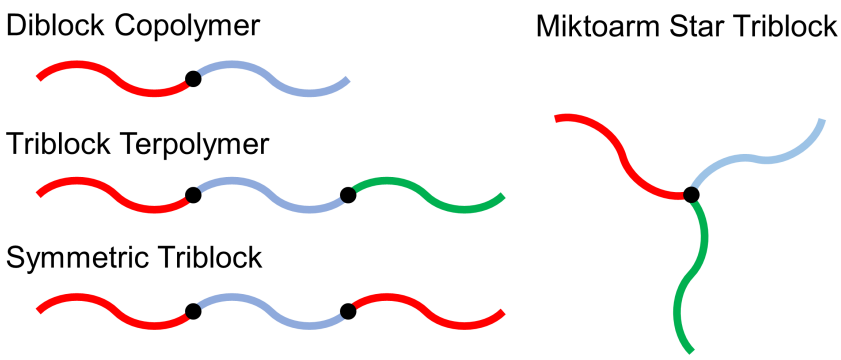

Figure 2.6: Cartoon of the most basic block copolymer types including linear diblock and linear and star triblock systems where color denotes species.

therein. In all cases, the blocks may be different lengths with their relative size and arrangement largely determining the final microstructure.

As noted in the introduction, utilizing multiple blocks can exploit the beneficial properties of several polymers such as the rubber elasticity of polyisoprene and the abrasion resistance of polystyrene. But more powerfully, BCPs allow for properties to be spatially controlled by phase segregation. The inherently complex interactions of BCPs yields a rich field of possible structures which can be further diversified by kinetic effects[19–21]. This has led to an increasingly diverse set of applications including DSA lithography[22], bit patterned media[23], filters[24], and optoelectronic devices[25]. All of these require advanced understanding of the phase segregation behavior.

2.2.1 Segregation

Base Theory and Corrections

Very few polymers will spontaneously mix as a binary blend of homopolymers. By covalently bonding the dissimilar polymer chemistries in a BCP, prox-

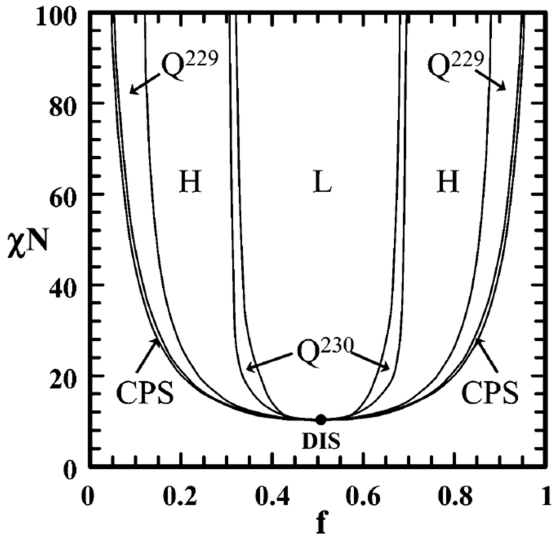

Figure 2.7: Calculated diblock copolymer phase diagram showing expected equilibrium phases as function of the block volume fraction and interaction strength χN. The phases present include close packed spheres (CPS), body centered cubic spheres (BCC), hexagonally packed cylinders (HEX), gyroid, lamellar (LAM), and disordered (DIS). Reproduced with permission from Cochran *et al.*[2], copyright Macromolecules 2006.

imal contact between the chemistries is ensured. However, covalently bonding the blocks together does not intrinsically modify these interactions and block copolymers typically phase segregate locally, but are unable to do so on a macro scale. This yields phase segregation at the length scale of the polymers themselves, typically of order 5-50 nm. Figure 2.7 shows the calculated phase diagram for a generalized diblock copolymer system where the block copolymer composition, in volume fraction of A, is shown on the abscissa and the total interaction strength between the blocks, characterized as product χN, is on the ordinate.

For BCPs, the interaction strength is regulated by the monomer-monomer incompatibility, as characterized by the Flory-Huggins interaction parameter (χ),

and the number of monomer units in the chain (degree of polymerization, N). In theory, the Flory-Huggins interaction parameter is linked to the excess free energy of mixing for a polymer-polymer or polymer-solvent system and characterizes the enthalpic interactions with a 1/T temperature dependence expected of χ. In practice, the simplifying assumptions behind the model are violated and measured χ parameters are normally fit to $\chi = \chi_{enthalpic} + \chi_{entropic} = A/T + B$ to give the excess free energy of mixing. These deviations stem from the presence of excess free volume, monomer structure, chain flexibility, and end effects. While multiple models have been developed to address these shortcomings[26–29], empirical measurements are typically used to express the system behavior when available.

This phase behavior is dominated by the total interaction strength and the relative size of the polymer blocks. For sufficiently short chains or weakly interacting monomers, the product χN is low and the material mixes into a disordered phase (χN<10.5 for symmetric polymers). To understand why short polymer chains tend to mix, one can take the limit of a polymer (oligimer) consisting of short (a few mers) chain of A bonded to an equally short chain of B. This molecule must pay an enormous entropic penalty to segregate A from B to form sheets/lamellae, thus promoting mixing. At the opposite limit, long polymers, or ones with a very strong interaction, are said to be in the strong segregation limit at large χN (typically χN>50). Within the weak segregation limit (~10.5< χN<50), polymer fluctuations play a key role in determining phase behavior.

The equilibrium phase behavior of BCPs has been extensively studied both theoretically[20, 30–36] and experimentally[37–40]. Early mean field theory[30] was successful in developing both the strong segregation limit and the order-

ing boundaries for infinite chains (of fixed χN) for diblock copolymers yielding the often quoted critical value of χN=10.495≈10.5 for a symmetric composition (f_A=0.5). This value is only valid for symmetric BCPs and any asymmetry in block sizes increases the interaction required for segregation, as demonstrated by the increasing χN envelope for the disordered phase in Figure 2.7. As an example, for asymmetric polymers with f_A=0.7 (cylinder forming), the infinite molecular weight critical value is χN=14.6[31].

Subsequent theoretical work has shown the importance of fluctuation effects[31], quickly confirmed by experimental evidence[37, 41], and significant effects from finite chain lengths[20, 32–36]. In particular, finite chain effects further increases the χN required for segregation. The same cylinder forming polymer with f_A=0.7 at a reasonable degree of polymerization of 10^4 requires χN≈17. For DSA, the chains are relatively short (N of 10^3) requiring χN≈21 at the same volume fraction. Although this example is a bit extreme, even symmetric polymers with an N of 10^3 require χN≈13.3, far greater than the often quoted value of 10.5. This dependence upon polymer size and asymmetry is sometimes neglected in the literature leading to confusion.

These corrections apply both in bulk and thin films. However, the incorporation of nearby surfaces for thin films also significantly modifies the phase behavior and kinetics. Substrate and air interfaces tend to promote segregation due to preferential interactions of one block to the surface. This surface interaction penetrates several 100 nm[42] and can modify the order–disorder transition temperature (T_{ODT})[43], structure periodicity[44], and structure orientation[45].

As stated previously, χ is fit to the empirical form $\chi = A/T + B$, leading to a temperature dependence on the ordinate axis of Figure 2.7. As temperature increases, χ generally decreases, and one moves downward on the phase diagram,

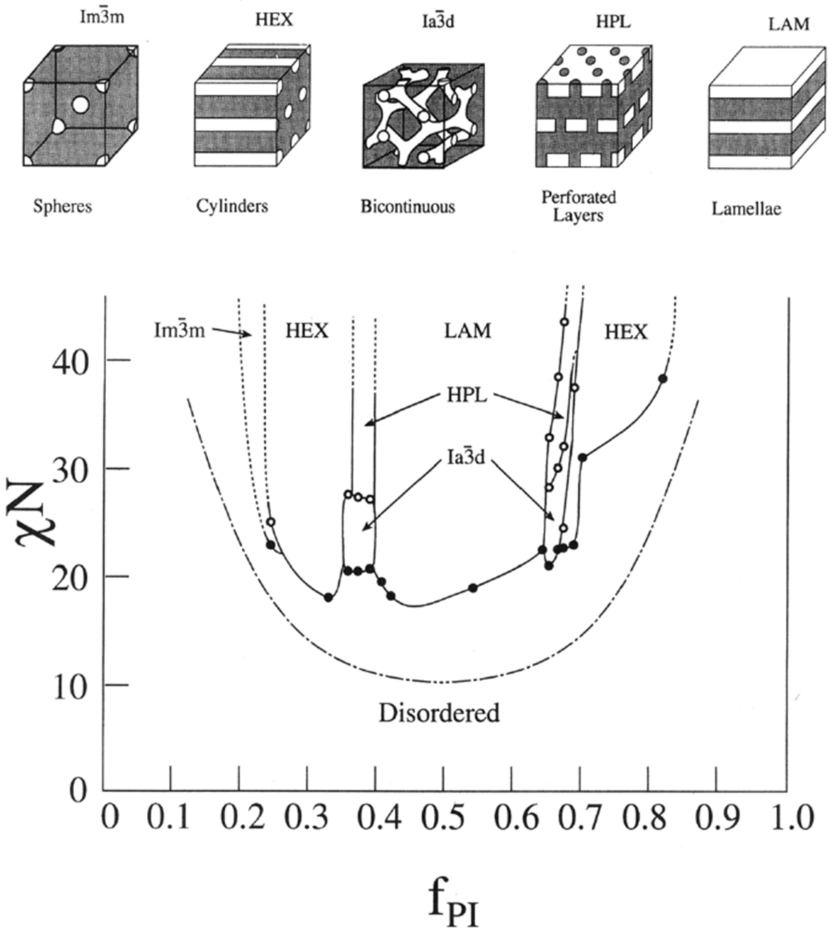

Figure 2.8: Measured phase diagram for PS-PI with order–order transitions (open circles), order–disorder transitions (closed circles), and calculated infinite chain disordering envelope theory[30]. Solid lines to guide the eye. Reproduced with permission from Khandpur *et al.*[46], copyright Macromolecules 1995.

promoting mixing. This proves useful as it allows the structure to be readily modified by temperature as well as composition, with order–disorder transitions (ODTs) or an order–order transitions (OOTs) occurring at critical temperatures.

In contrast to the symmetric simplicity of the calculated phase diagram (Figure 2.7), observed phase behavior deviates significantly for many systems. Figure 2.8 shows the measured phase diagram for the well studied PI-*b*-PS system.

As expected, the observed boundaries are higher in χN than the mean field estimate due to finite chain lengths. In addition, the diagram shows significant asymmetry, especially apparent for the hexagonally packed cylinder phase. The asymmetry stems from significant asymmetry in the relative polymer stiffness of the two blocks, as reflected by their glass transition temperatures (T_g) of ~-70 and 100 °C respectively. Another deviation is the formation of the additional phase of hexagonally perforated lamellae which has been shown to have very similar formation energies to gyroids and can be stabilized as the transition between lamellae and cylinders[47].

Phase Segregation Kinetics

This equilibrium behavior does not necessarily reflect common BCP use as not all applications drive the material to full equilibrium. In some systems, the kinetic pathway determines the final metastable state and subsequent properties. Theory suggests that BCP phase segregation during quench from the disordered structure occurs by spinodal decomposition for symmetric diblock copolymers, but via a nucleation and growth mechanism for sufficiently asymmetric BCPs[48–52]. While computational approaches have successfully modeled kinetic pathways between ordered states in simplistic systems, such studies, by necessity, require coarse graining of the molecular structure (beading) or minimal spatial and temporal simulation scales[53–60].

Thermodynamics establishes the critical order-disorder transition temperature (T_{ODT}) where χN reaches its critical value. However, the undercooling (quench depth below T_{ODT}) and the system mobility determine the kinetics of the transition. Previous kinetic studies[61–63] have followed the ordering kinetics in pure polymer systems for shallow quench depths on the order of ~10 °C.

These studies observed nucleation and growth kinetics for both asymmetric and symmetric BCPs. Other studies have examined the ODT[64–69] or the OOT[70–73] kinetics in solvent/polymer systems at comparable quench depths while inducing the phase transformation by controlling temperature[65–73] or changing the solvent volume fraction[64], and similarly found nucleation and growth kinetics.

Direct measurements of the segregation process, however, are difficult at quench depths beyond ~10 °C[61–63] due to the fast kinetics and short timescales involved. Even *in-situ* measurements are relegated to seconds timescales meaning the earliest stages of segregation are difficult to capture and little work has been reported in such deeply metastable regimes. However, one might expect that spinodal decomposition and nucleation behavior would behave in accordance with conventional metallurgical theories and increasing quench depth should reduce the nucleation barrier.

Measurement Methods

Measurement of the BCP segregation can be done via scattering (X-ray, neutron, electron, etc.), imaging (SEM/AFM/TEM), rheology, or thermal methods. Each method probes different material volumes and characteristics yielding differing appropriate use. Scattering experiments, typically the most powerful but somewhat laborious, can yield quantitative structural information on large volumes and can also provide some surface information at small angles of incidence. Imaging is often faster and more easily interpreted for surface structures, but is often qualitative and difficult to quantify. Rheological and thermal methods are easily performed, however, they require blocks to have different T_gs to discern ordering behavior.

Scattering methods generally rely on some form of density contrast in a periodic structure. For X-ray and electron methods, scattering occurs from changes in electron density. For crystals, this is the periodic arrangement of atomic orbitals acting as pseudo point charges. Neutrons similarly scatter from nuclei with significant contrast variations between elements or isotopes. For phase segregated block copolymers, scattering is due to variations in density within the material phases averaged over many monomers. This can stem from different species or densities between blocks (all carbon in polystyrene but oxygen included in methyl methacrylate) or, for neutron scattering, by selective tagging of one block with deuterium rather than hydrogen. In addition, if scattering is done *ex-situ*, compounds such as RuO_4 and OsO_4[74] can be selectively incorporated by their preferential reaction to some polymers to increase contrast and scattering.

Small angle X-ray and neutron scattering have both been extensively used to probe BCP segregation. Small angle scattering is necessary to access information on the large (relative to particle wavelength) structures of the polymers. In addition to observing structural information, scattering significantly changes across the ODT. Figure 2.9 schematically shows the scattering intensity and bulk structural spacing behavior of BCPs under equilibrium heating in the region near T_{ODT}. As the BCP blocks mix, the scattering intensity discontinuously decreases across the ODT by ~2 orders of magnitude to a residual intensity arising from concentration fluctuations of a similar length-scale. This coincides with a discontinuous broadening of the scattering signal[41, 75] due to variations of the concentration fluctuation periodicity. Consequently, several groups have used this scattering intensity as an estimate of a segregation order parameter[61–65], here defined as Γ.

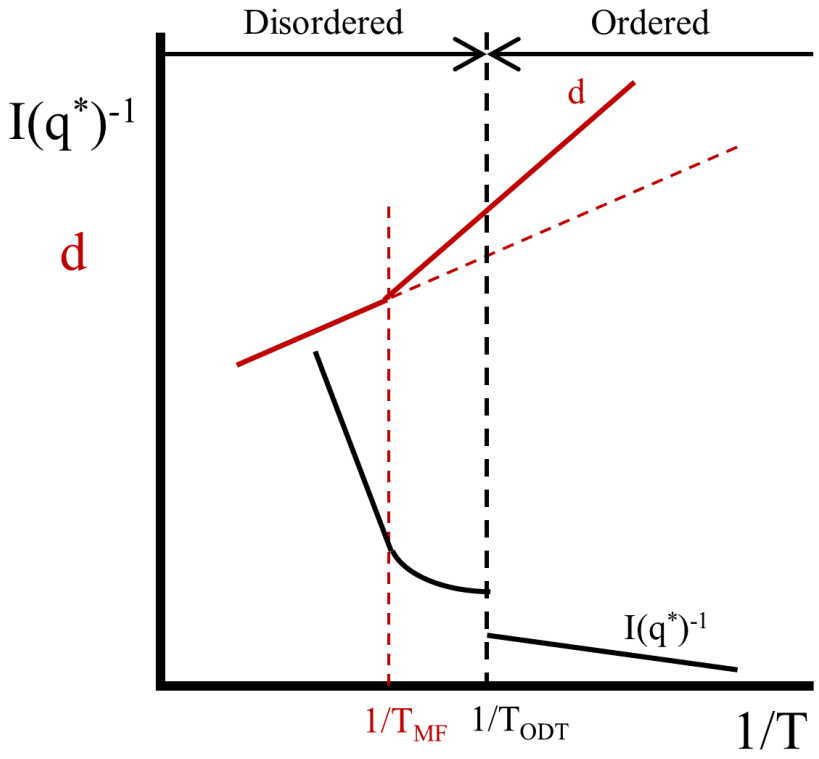

Figure 2.9: Schematic equilibrium BCP inverse scattering intensity (I^{-1}) and bulk spacing (d) versus inverse temperature in the region of the ODT. Adapted from Sakamoto *et al.*[76].

Depending on composition and driving forces, phase segregation can potentially occur by either (i) a nucleation and growth mechanism or (ii) a spinodal decomposition. For a nucleation and growth mechanism, where disordered volumes contribute little scattering intensity while ordered volumes fully scatter, Γ would be roughly linear in scattering intensity (commonly used in literature but rarely explicitly stated). For spinodal decomposition, or mechanisms where segregation varies more locally, a more complex relationship is required as the scattering intensity scales with the square of the density contrast ($\Delta\rho$)[77] with perturbations for interface roughness and segregation size distribution.

Rheological methods rely on measuring the bulk low frequency BCP melt

viscosity. For BCPs, the aggregate melt viscosity is dominated by the low T_g block when mixed but by the high T_g block when segregated. This behavior stems from the segregation precluding free motion of the low T_g block as it is effectively held in place by the high T_g block. Upon mixing, the low T_g block acts as a plasticizer and reduces the overall viscosity.

Thermal methods rely on measuring the bulk enthalpy of mixing at the ODT. This is analogous to measuring the enthalpy of melting of crystals and, similar to rheological methods, shows significantly enhanced signal when blocks exhibit significantly different T_gs when the low T_g block acts as a platicizer.

In order to measure the initial stages of phase segregation, and especially for deeply metastable states quenched far above or below the ODT, rapid *in-situ* measurements are ideal along with rapid heating and cooling. The macroscopic volume of material used for rheological and thermal methods make them somewhat poor candidates for such *in-situ* measurements. While rheological methods can be modified with relatively low volumes and fast heating elements to perform measurements on seconds timescales, the requirement of measuring the low frequency viscosity precludes measurements on any shorter timescales.

In contrast, scattering experiments can both measure both bulk and thin film samples. Thin films allows for rapid heating and cooling with minimal temperature lag from thermal transport. In principle, scattering experiments can be done at arbitrarily fast timescales given enough flux and a fast enough detector. However, in practice, neutron sources suffer from low fluxes which precluding their use for sub-second measurements. Third generation synchrotron X-ray sources, and more recently, X-ray free electron lasers (XFELs), have significant flux ($>10^{16}$ photons/s at ~10 keV) capable of probing the structure even when there is weak scattering due to the low electron density contrast between

blocks. In the near future, X-ray scattering at these sources may be limited by the measurement technologies rather than flux. Current fast imaging detectors operate at up to 500 Hz. However, measurements at this rate would require a flux that would cause significant damage to the polymers. In addition, at high flux, direct heating of the system by the X-ray beam must also be managed.

For these reasons, phase segregation measurements in this work primarily relied on *ex-situ* X-ray scattering intensity as a quantitative metric with AFM and SEM used to provide a real space picture of the resultant morphologies and to verify the segregation behavior. These *ex-situ* measurements are be coupled with rapid heating and cooling from anneals described in Chapter 3 to probe the time dependent morphology evolution.

2.2.2 BCP Annealing Methods and Restrictions

For practical applications, the proper morphology with low defect density must be achieved. In BCPs, this often occurs via specific annealing steps to attain the useful morphology. Typically, anneals utilize temperature, solvents, or a combination of both to increase the polymer mobility and allow the system to relax toward the equilibrium configuration. The benefits and limitations of these methods are briefly explored here.

Thermal Annealing

Thermal annealing of BCPs without solvent yields the relatively simple phase behavior enumerated previously and allows for defect removal following a typical diffusion limited process. In an industrial setting, thermal annealing is typically preferred due to its simplicity and to avoid potentially costly mitigation of hazardous materials. Even with elevated temperatures, polymer diffusion

is typically sluggish, especially for high molecular weight polymers, and thus typical thermal anneal durations may be from the minutes to days timescales. Efforts to significantly increase the annealing temperature, and thus reduce annealing times, are limited by thermal degradation limits.

As with all organic systems, BCPs exhibit decomposition via a myriad of pathways when exposed to high temperatures including oxidation, pyrolosis, and depolymerization. Though the details of decomposition varies between polymers, very few tolerate temperatures higher than ~300 °C in the minutes timescales. But, as with all processes, decomposition exhibits a kinetic component, and hence, this decomposition limit is anneal duration dependent.

Solvent Annealing

In the case of very large polymers, the kinetics are so sluggish that thermal annealing fails to improve mobility before the onset of damage. In order to further increase the polymer mobility, solvents are used instead. Solvent incorporation swells the polymer and provides more volume for the chain reptation, and thereby facilitate much higher chain mobility. Similar to increasing temperature, as more solvent is introduced, the system will, at some point, tend to favor mixing of the segregated blocks. This behavior stems from the reduced polymer-polymer interaction after swelling and, at large swelling ratios (or solvation), leads to a solvent induced ODT.

In addition to modifying the interaction between polymer blocks, preferential solvent interactions with the polymer blocks can add a third component, which allows for even greater morphology diversity including micelles and other structures. For good (theta) solvents for both blocks, each block is equally swelled until eventually solvated. In the case of preferential interactions, the

phase behavior can be significantly modified. For small swelling ratios, one block swells more, effectively changing the volume fraction of that species allowing "lateral motion" across the phase diagram[78]. Interestingly, this can also be done with the incorporation of homopolymers, which similarly shifts morphologies and modifies the relative spacing of lamellae, etc. With increasing solvent incorporation, further modification of the segregated structure occurs potentially yielding micelles, exfoliated sheets, or multiphase systems.

Most practical applications do not retain solvents in their final use, and thus solvent removal is a critical step. Solvent removal changes the size scale and potentially the equilibrium phase, requiring additional polymer motion. This often leaves the system in a non-equilibrium state, sometimes with strained structures, a completely different structure from equilibrium, or spatially nonuniform and/or directionally dependent structures[79–81]. While this can be very useful, as the case with filtration applications[24], it can be deleterious in other applications.

Solvent incorporation can also be combined with thermal annealing as solvothermal annealing. This further improves polymer mobility but increases complexity due to modifying both the polymer-polymer interactions and temperature. In practice, solvothermal annealing also requires special gas handling equipment and inert atmospheres to control the annealing ambient[82].

2.2.3 BCPs for DSA

Overview

Polymers utilized for directed self-assembly have traditionally been lamellar or cylinder forming morphologies. For example, line/space patterns are created from standing (out-of-plane) lamellae or from cylinders lying down (in-plane).

Other features, such as contact hole patterns, typically use standing cylinders. Through film morphologies, like standing lamellae or cylinders, are preferred for the greatest thickness contrast between patterned areas allowing greater etch depth for a constant etch contrast[17, 22, 83, 84].

The primary considerations for choosing polymer chemistries for DSA include the size of features resolvable, etch contrast between the blocks for processability, and the ability to attain through-film morphologies. The absolute feature size of the segregation scales primarily as the radius of gyration, or as $N^{1/2}$, and weakly as the segregation strength, $(\chi N)^{1/6}$. Smaller polymers produce smaller features but, as the polymer size shrinks, mixing becomes preferred. The smallest accessible feature size is determined by the Flory-Huggins interaction parameter. Highly incompatible, or high χ systems, enable the smallest features as it is possible for shorter chain polymers to achieve the critical χN for segregation.

In order to be useful for microelectronics patterning, the two blocks must have the ability to be preferentially removed by some chemical (wet) or plasma (dry) etch process without modifying the pattern. Wet etches can be very effective with large etch contrasts but also have surface tension from the typically aqueous environment, causing pattern collapse at small feature sizes, and can cause pattern delamination with poor adhesion. For these reasons, dry etches are preferred. Organic systems are universally attacked by oxygen reactive ion etches (RIEs) and fully organic systems show minimal etch contrast. To increase contrast, groups have incorporated inorganic atoms to these systems such as silicon or iron[4, 82, 83, 85, 86], or have infiltrated one of the blocks with organometallic compounds such as trimethyl aluminum[87].

Through film morphologies are preferred to enable better etch properties.

Film thickness can promote a standing morphology when the material is coated to an incommensurate film thickness to make the in plane morphology least favorable. For example, a lamellar forming polymer with a repeat spacing of L_0 coated to an average thickness of 1.5 L_0 must either form islands of 2.0 L_0 and 1.0 L_0 or have a standing morphology where the segregation repeat spacing is not constrained by the surface. In practice, complex 3-d contortions to the system morphology can occur to minimize the overall system energy, but using incommensurate film thicknesses is an important driver for standing morphologies.

In addition to modifying the film thickness, the anneal conditions can also be used to promote standing morphologies. In general, the surface energy of each block is different causing preferential segregation of one block to one or both interfaces. Typically, these surface energies exhibit different rates of change as a function of temperature and solvent incorporation. Anneals can be targeted to temperatures or solvent atmospheres where the surface energies are roughly equalized. While fairly easy to accomplish for a single interface, this can be difficult or impossible to simultaneously attain for both the substrate-polymer and polymer-air surfaces.

In lieu of modifying anneal conditions, the interface chemistry can be modified to provide a more neutral interaction. This often takes the form of a random copolymer grafted onto the substrate below the BCP and/or a top-coat for the air interface[88]. Though it may seem that a purely random copolymer at each surface should readily fix this issue by providing an intermediate interaction between the blocks, these random copolymers can be difficult to produce and the interface chemistry leading to standing morphologies has proven complex and difficult to readily engineer.

Although through film morphologies are preferred, the preferential segre-

gation of one block to one or both surfaces proves problematic for multiple systems. At the expense of the etch characteristics, in-plane morphologies are sometimes used. By carefully choosing the film thickness, the in-plane morphology can be encouraged and used for patterning. In this case, a single layer of in-plane cylinders or spheres can be used for line/space or contact hole patterns respectively. However, this not only exacerbates the already poor etch contrast, but also can require more complex etch processes from needing to remove a surface layer of the alternate chemistry[88–90]. More often, the annealing environment, interface properties, and film thickness are modified to obtain the through-film behavior.

Select DSA Chemistries

Much of the initial DSA work focused on the poly(styrene-*block*-methyl methacrylate) (PS-*b*-PMMA) system[3, 17, 18, 55, 58, 84, 86, 91–99]. This system is readily fabricated with low polydispersity and high purity, has moderately high T_g blocks (~100 °C) to retain pattern fidelity after annealing or etch, and has very similar surface energies (PMMA has a slight preference to wet the air and substrate interfaces) enabling though-film morphologies. Despite these benefits, PS-*b*-PMMA is considered a "low χ" system with a room temperature χ ~0.03-0.06[43, 100–103] and only enables lamellar features down to a ~12 nm half-pitch and has only marginally acceptable etch contrast. Even with the relatively similar surface energies, neutral layers are still required at the substrate interface to promote a standing morphology.

Subsequent work has focused on developing several moderate or high χ systems which would enable smaller features. However, these systems typically suffer from greater disparities in block surface energies. Commonly studied

systems include poly(styrene-*block*-4-vinyl pyridine) (PS-*b*-P4VP), poly(styrene-*block*-2-vinyl pyridine) (PS-*b*-P2VP), poly(isoprene-*block*-styrene) (PI-*b*-PS), and poly(styrene-*block*-dimethylsiloxane) (PS-*b*-PDMS). Of these, PS-*b*-P4VP and PS-*b*-P2VP have higher χ than PS-*b*-PMMA, and maintain high T_g in both blocks, but are used as in-plate assembly due to the difficulty in obtaining out-of-plane morphologies[104]. Alternatively, PI-*b*-PS and PS-*b*-PDMS contain a low T_g block potentially enabling faster annealing kinetics. In addition to the smaller features theoretically possible with higher χ, PS-*b*-PDMS contain silicon in the PDMS block which significantly increases the etch contrast.

DSA polymers are typically deposited via spin coating which rapidly removes solvent. For BCPs with moderately high T_g blocks, this rapid solvent quench results in deposited polymer films that are a random mixture of chains. From this deeply metastable state, the polymer is heated for segregation, alignment, and defect annealing at relatively slow rates compared to diffusive motion. This initial phase segregation step from the deeply metastable state is not well understood and potentially critical to defining defects and their annealing pathways.

2.3 Kinetics Background

Kinetic transformations of materials, chemical reaction rates, and diffusion have been studied extensively in inorganic, organic, and polymer systems. While many of the characteristics of kinetics in polymers are similar to those for small molecules, there are significant differences associated with the constrained dynamics of polymer motion. The basics of these kinetics are outlined below for the reader.

2.3.1 Reaction and Diffusion Kinetics Models

Chemical reactions and diffusion in many simple systems often follow Arrhenius kinetics. A notable exception is polymer diffusion, which is complex owing to entanglements, interspecies interactions, and free volume effects. One important temperature dependent empirical form which describes many polymers is the Williams-Landel-Ferry (WLF) model. This model significantly deviates from Arrhenius kinetics and is typically valid in the melt and within ~100-200 °C of the glass transition temperature. However, at temperatures far above T_g, small molecule diffusivity in polymers was found to transition from the WLF behavior to an Arrhenius behavior more typical of unconstrained kinetics[105]. Though not surprising for diffusivity in a low viscosity liquid state, transitions in diffusion behavior provide additional complexity when working in extended temperature regimes.

Arrhenius

Arrhenius kinetics describe a thermally activated process which must overcome an energetic barrier via thermal fluctuations. The classic models of diffusion by atomic hopping, or of simple chemical reactions overcoming a singular large energetic barrier, are examples of processes which follow Arrhenius rates. This thermal activation process yields an exponentially growing rate in temperature given by:

$$R = R_0 \, exp\left(-\frac{\mathrm{E_A}}{k_b T}\right) \tag{2.3}$$

where R is the rate, R_0 is a pre-exponential factor (fit parameter), E_A is the energetic barrier or activation energy, and k_b is Boltzmann's constant. Experimental rate data is often plotted on a so called Arrhenius plot as the log of the rate versus the inverse absolute temperature. The plot slope readily yields the ac-

tivation energy. In the case of multiple simultaneous/competing independent Arrhenius processes, those with the higher activation energy dominate at high temperatures, while low activation energies dominate at lower temperatures. Mathematically, this stems from the larger changes in rate with temperature for the higher activation energy process, which provides a larger response to changes in temperature relative to a lower activation energy process.

Williams-Landel-Ferry (WLF)

In contrast to the model based Arrhenius kinetics, WLF diffusion (and viscosity) fits the observed behavior of vitrifying materials to the form:

$$D = D_{T_{ref}}\, exp\left(\frac{C_{1,ref}(T - T_{ref})}{C_{2,ref} + (T - T_{ref})}\right) \tag{2.4}$$

where $D_{T_{ref}}$ is the diffusivity at a reference temperature T_{ref}, and $C_{1,ref}$ and $C_{2,ref}$ are fit parameters. Often T_{ref} is tied to T_g (with constants denoted C_{1g} and C_{2g}), but this is not always the case. C_1 is typically of order 10 (unitless) and C_2 is of order 50 K.

This WLF behavior is somewhat analogous to Arrhenius diffusion where the diffusion drops to zero as T approaches T_{ref} - C_2 (rather than at zero absolute temperature). Figure 2.10 compares the rate behavior of an Arrhenius (solid line) and a WLF (dashed line) process on an Arrhenius plot. The Arrhenius process is linear with the slope dictated by E_A while the WLF process is only linear at high temperature (low inverse temperature) and goes to zero at T_{ref} - C_2.

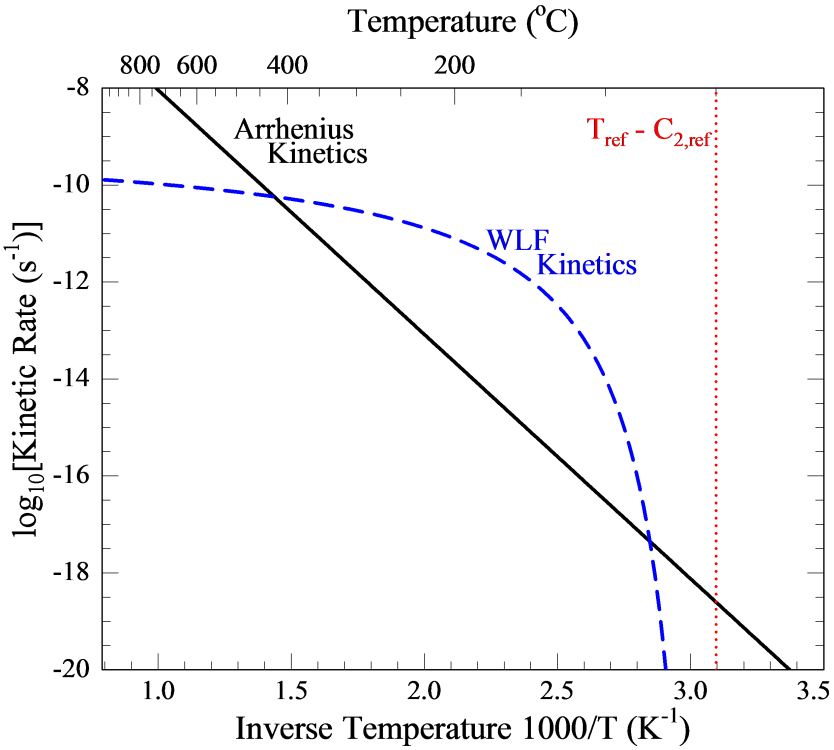

Figure 2.10: Example kinetic rates following Arrhenius (solid) and WLF (dashed) functional forms plotted on log - inverse temperature axes.

2.3.2 Phase Transformation Development Models

Diffusion mediated phase transformations follow either a nucleation and growth or spinodal decomposition behavior depending on the metastable material's free energy landscape. In general, materials follow a nucleation and growth mechanism when it is thermodynamically favorable to form a new phase but there is an energetic barrier for the formation of this new phase; most often this is an energetic penalty for the formation of a interface between the old and new phases, and is classically described with a surface energy term. In contrast, spinodal decomposition occurs when compositional fluctuations intrinsically lower the overall system free energy; fluctuations hence can immediately

grow being limited only by the diffusive motion.

In all materials, thermal fluctuations cause transient perturbations to the average structure or local composition. In the case of nucleation, these perturbations act as nascent nuclei which must stochastically overcome the energetic barrier before the nucleus will be stable and the incorporation of additional material to the nucleus will lower the overall system free energy allowing growth. The balance between the surface energy penalty and volumetric energy density gain from the transformation yield the critical nucleus size $r*$ and the energetic barrier, $\Delta G_{hom}*$, for homogeneous nucleation as:

$$r* = \left(\frac{2\gamma_{AB}T_{trans}}{\Delta H}\right)\frac{1}{\Delta T} \tag{2.5}$$

and

$$\Delta G_{hom}* = \left(\frac{16\pi\gamma_{AB}^3 T_{trans}^2}{3(\Delta H)^2}\right)\left(\frac{1}{\Delta T}\right)^2 = \frac{E_A T_{trans}^2}{(\Delta T)^2} \tag{2.6}$$

where γ_{AB} is the surface energy between the A and B phases, T_{trans} is the transformation temperature, ΔH is the enthalpy of formation of the stable phase, ΔT is the undercooling or superheating past the transition temperature, and E_A is the nucleation activation energy. The surface energy between the two materials is effectively invariant near the transition temperature so, as the material is supercooled, the initial phase is increasingly metastable and the free energy gain for transformed volume increases, in turn reducing the critical nucleus size and energetic barrier by ΔT and $(\Delta T)^2$ respectively.

Since the perturbations that form these nascent nuclei are thermally generated, the reduction of the energetic barrier increases the nucleation rate exponentially and increases and can be described by the modified Arrhenius rate of:

$$\dot{N} = \dot{N}_0\, exp\left(-\frac{E_{A1}}{k_b T}\right)\, exp\left(-\frac{E_{A2}T_X^2}{k_b T(\Delta T)^2}\right) \tag{2.7}$$

where terms relating to the nucleus geometry (heterogeneous or homogeneous) are combined in the pre-exponential term $\dot{N}_0$, surface energy and volumetric free energy are combined in E_{A2}, attempt frequency (typically diffusion mediated) is contained within E_{A1}, and the change in the energetic barrier with temperature is captured by the factor $T_X^2(\Delta T)^{-2}$ where T_X is the transformation temperature and ΔT is the quench depth. As the material becomes more metastable with distance from the transition temperature, this barrier decreases and eventually the transformation becomes diffusion limited.

In order to capture the time dependent nature of these models, Kolmogorov, Johnson and Mehl[106], and Avrami[107–109] described these processes in a generalized form tracking the phase transformation in time at a constant temperature. These equations, now known as KJMA or Avrami equations (Avrami published expansive work with derivation and description), follow the general form:

$$\Gamma = 1 - exp\,(-\beta t^n) \tag{2.8}$$

where Γ is volume transformed, t is time, β is the combined nucleation and growth rate defined below, and n is the "Avrami exponent" which can be tied to the nucleation rate and growth dimensionality. This combined nucleation and growth factor β is defined as:

$$\beta = \dot{N}\dot{G}^d \tag{2.9}$$

where $\dot{N}$ is the nucleation rate and $\dot{G}$ is the one dimensional growth rate, and d is the dimensionality of growth (e.g. 3 for 3-d growth, etc.). This generalized form was adopted to account for the various material growth regimes of spherical (3-d), plate like sheets (2-d), or needles/rods (1-d). Additionally, nucleation can be treated in several cases, most commonly as constant nucleation or as an instantaneous burst followed by no nucleation. Phenomenologically these

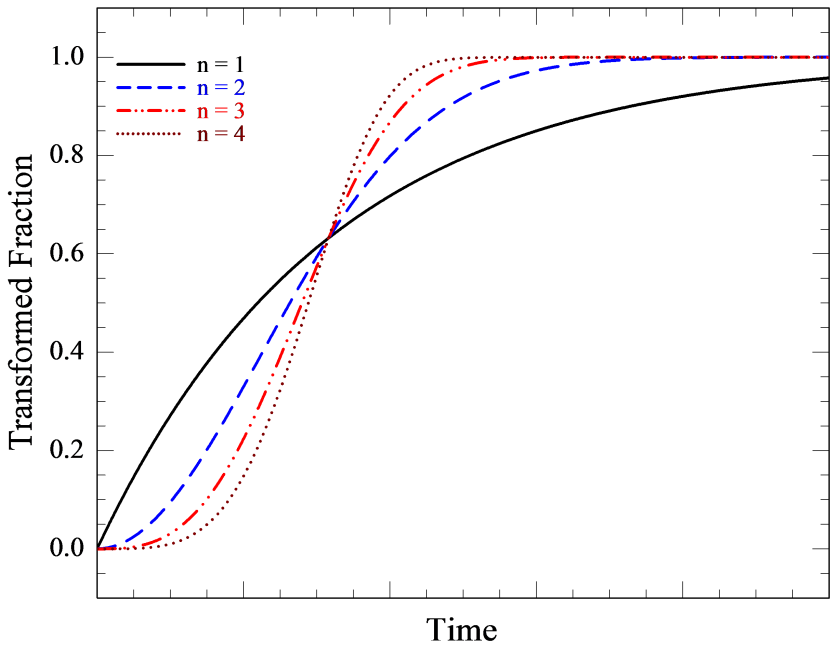

Figure 2.11: Temporal volumetric transformation fraction of KJMA nucleation and growth model for Avrami exponents 1 (solid, black), 2 (dashed, blue), 3 (dot dashed, red), and 4 (dotted, magenta).

result from a single or two step annealing process where the latter includes a nucleation step at large ΔT to define nuclei and growth at a small ΔT where there is effectively no nucleation. In the latter case, $\beta = \dot{G}^d$ and the Avrami exponent is $n = d$. In the opposite limiting case of constant nucleation, the Avrami exponent is $n = d + 1$. In principle, the one dimensional growth rate is also a thermally activated process is related to the diffusion of species to the interface as necessary.

Figure 2.11 shows the transformation fraction as a function of time for the commonly interpreted Avrami exponents. As the Avrami exponent increases, the transformation rate after initiation increases, ultimately asymptotically approaching the fully transformed state. This simple and general form allows for significant flexibility and accurately describes the initial transformation kinetics

of many systems. Though more complex models are sometimes required to accurately describe the end effects (such as of grain impingement and nucleation retardation) and complex systems with multiple growth mechanisms[110–114], significant insight can be gained using this simple model. While instructive, in the case of non-isothermal conditions, the KJMA expressions may or may not be valid as the growth dimensionality and especially nucleation behavior can vary significantly with temperature. It nonetheless is a valid starting point for kinetic analysis.

2.4 Summary of Dissertation Terms

To be absolutely precise, the following phrases are defined for clarity and to avoid confusion with occasionally interchangeable phrases in the literature.

Phase segregation, **segregation**, or **ordering**: The process by which a mixed phase of A and B blocks or polymers move to localized regions with an average monomer makeup preferential to individual blocks. The inverse process may be referred to as **phase mixing**, **mixing**, or **desegregation**.

Alignment: The process by which individual phase segregated domains align to a directing template or other feature in DSA. This is distinct from phase segregation and can only occur after at least partial phase segregation. It is possible for incompletely segregated domains to align but some segregation must occur before alignment. This term is commonly used interchangeably with the term "ordering" in the literature. For the purposes of this text, these two terms are not synonyms. A well ordered (phase segregated) film does not necessarily exhibit well aligned and defect free DSA patterning.

Order-Disorder Transition: A thermodynamic discontinuity (transition) between an ordered and a disordered equilibrium state. This acronym is used irrespective of direction (i.e. ODT = DOT) and thermodynamically occurs at a specific temperature (T_{ODT}) for polymers without solvent incorporation. Disordering/mixing can also be induced by swelling or solvation. Since no solvent incorporation is presented in this work, the T_{ODT} is treated as a singular value defined by the properties of the BCP. In older literature, T_{ODT} is also called the microphase segregation temperature or MST.

Gamma (Γ): A measure of the degree of block copolymer segregation where Γ=1 is considered "full" segregation while Γ=0 is a completely random mixed solution.

CHAPTER 3

EXPERIMENTAL METHODS

3.1 Overview

In order to access the millisecond phase segregation behavior in deeply metastable block copolymers (BCPs), rapid annealing methods are required. Furthermore, to fully understand the dynamic behavior, the full time-temperature profile of both hot plate and rapid annealing methods must be considered along with how these dynamics are probed by the available metrology techniques.

Conventional annealing methods using a hot plate or an oven are explored here within the context of current of block copolymer segregation theory, and as a precursor for annealing far from equilibrium materials. Millisecond timescale anneals were achieved using a focused, high power, continuous wave (CW) laser as a heat source, enabling heating and cooling rates of up to ~10^7 K/s. Significant attention has been paid to both the metrology and broader applicability of this particular technique.

3.2 Hot Plate and Oven Considerations

In most work, hot plate or oven anneals are approximated as ideal isothermal anneals and are reported with a single time and temperature. However, to understand kinetics of systems far from the equilibrium, the full temporal history of the sample is important, including the initial heating and particularly the final cooling transients. In contrast to the assumed isothermal approximation for furnace type anneals, the slow ($\sim 10^{-1} - 10^2$ K/s) heating and cooling rates can

induce significant modification of structures during these transients.

As an example, PS-*b*-PMMA, a common DSA BCP with a T_g of ~100-110 °C, is typically processed by a traditional hot plate anneal on minutes timescales at 250 °C. The polymer becomes mobile above T_g and can phase segregate and adjust its structure during even a fast (~1.5 s) heating to the desired temperature. Previous work[61–63] has shown that, for moderate temperatures, phase segregation occurs on the seconds timescale implying initial phase segregation occurs during heating rather than at final target temperature. This stands in contrast with the idea of an "isothermal" anneal where all phase development occurs at the target temperature. This heating transient effectively creates a two step anneal, with segregation occurring during the temperature ramp followed by refinement and alignment during the isothermal window.

Hot plate anneals for this work were performed on a custom vacuum chucked thermal gradient hot plate. Samples were annealed in normal lab ambient or nitrogen rich environments (estimated P_{N_2} >95%). After anneals, samples were quenched on a stainless steel surface for rapid cooling. Heating and cooling rates were estimated to be near 10^2 K/s for 250 °C anneals. Additional anneals were performed for 12-24 hours in a vacuum-oven chamber and allowed to cool under vacuum for an extended period of time to near T_g. The measured temperature implies the initial and terminal vacuum-oven cooling rates were on the order of 10^{-1} and 10^{-2} K/s respectively.

3.2.1 Specific Considerations for DSA

In general, organics are thermally unstable at high temperatures and can degrade via multiple mechanisms, both with and without the presence of oxygen. For conventional hot plates, this limits the annealing temperature range

to below ~275 °C for PS-*b*-PMMA; typical anneals for DSA are consequently 1 – 5 minutes at 250 °C.

Industry measures the efficacy of a DSA anneal almost solely on the basis of the resultant defectivity. By this metric, DSA polymers are susceptable to multiple environmental factors beyond degradation. Recent work transferring lab-scale studies to the semiconductor cleanroom equipment and environment exhibited a surprise drop in defectivity, eventually linked to the elimination of particulates which may cause intrinsic DSA defects. Subsequent work also indicated that oxygen and humidity also increase defectivity, though the direct cause has not been publicly reported [private communication, Feb. 2015]. Current reported annealing techniques specify anneals in a clean, inert, and dry atmosphere for 1–2 minutes.

3.3 Laser Spike Annealing (LSA)

Laser induced millisecond annealing, in the form of laser spike annealing (LSA), was originally developed to address issues of dopant activation and diffusion in shallow semiconductor junctions[115, 116]. Laser spike annealing consists of scanning a tightly focused, continuous wave (CW) laser on an absorbing substrate. Figure 3.1 schematically shows the sample geometry under LSA where the laser is scanned in the y- direction generating a thermally affected line of material after the laser scan. The anneal duration is quantified by the laser dwell time (τ_{dwell}), defined as the laser full width at half maximum (FWHM) in the scan direction divided by the scan velocity. The maximum anneal temperature is determined by the incident laser power and the dwell time.

Laser energy absorbed in the substrate results in a temperature rise with heat conducted to surface films. As the laser passes, this absorbed energy is

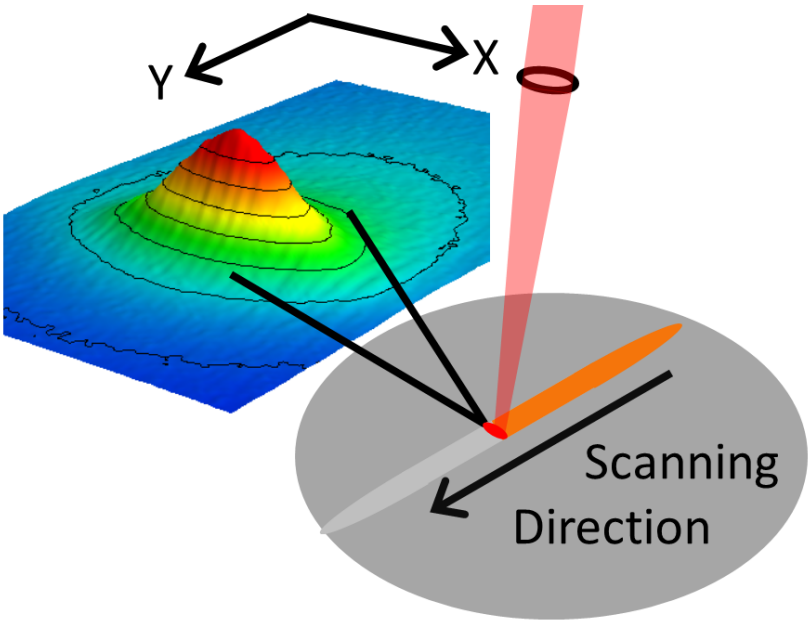

Figure 3.1: Schematic representation laser spike annealing process and measured thermal profile. Laser is scanned in the y- direction with a 2-d thermal profile depicted in the upper left.

quenched into the bulk substrate. This rapid heating and thermal quench allows for precisely controlled, consistent, short duration anneals with heating durations down to ~10 μs at temperatures limited by the laser power and materials constraints (e.g. substrate melt). For silicon substrates and moderately focused ~100 W infrared lasers, dwell times of 100 μs to 100 ms at temperatures up to the melt of silicon at 1414 °C are readily accessible.

What follows is an introduction to LSA spatial and temporal temperature profiles and a high throughput experimental technique using LSA, developed by Bell *et al.*[117]. The compatibility requirements of substrates and films for experiments under LSA, along with temperature calibration and measurements, are discussed in Appendix A.

3.3.1 LSA at Cornell

In 2008, Intel donated two Ultratech LSA alpha demo tools equipped with 120 W, 10.6 μm CO_2 gas lasers, associated optics, and scanning stages capable of annealing 300 mm wafers at up to 400 mm/s scanning rates. These systems were modified extensively and expanded to include a 250 W, 980 nm fiber coupled solid state diode laser, and *in-situ* bright-field and dark-field cameras. The ability to anneal under controlled atmospheres (solvent, reactive, inert), or at elevated substrate temperatures was added. While the system has primarily been used to anneal silicon substrates at anneal durations from ~100 μs to 10 ms at temperatures up to ~1400 °C, a multitude of substrates have been utilized including InP, Al_2O_3/Sapphire, GaN, SiC, and metal foils with thin films ranging over polymers, nanoparticles, polymer-nanoparticle composites, porous oxides, oxide blends, metallic glasses, transparent semiconductors and others.

3.3.2 LSA Characteristics

Temporal and spatial thermal profiles were measured using platinum thin film thermistors. Absolute temperatures were calibrated to the melt of gold and silicon. These techniques and their associated errors are described in detail in Appendix A.

Temporal Temperature Behavior

Laser spike annealing obtained its name from the "spike" like nature of the sample time-temperature profiles. Figure 3.2 shows measured thermal profiles for a 10 ms and a 250 μs dwell anneal to 500 °C. Note that the total duration shown is only a tenth of one second. These profiles show that the sample rapidly heats to the peak temperature, remains near the peak temperature for roughly the dwell

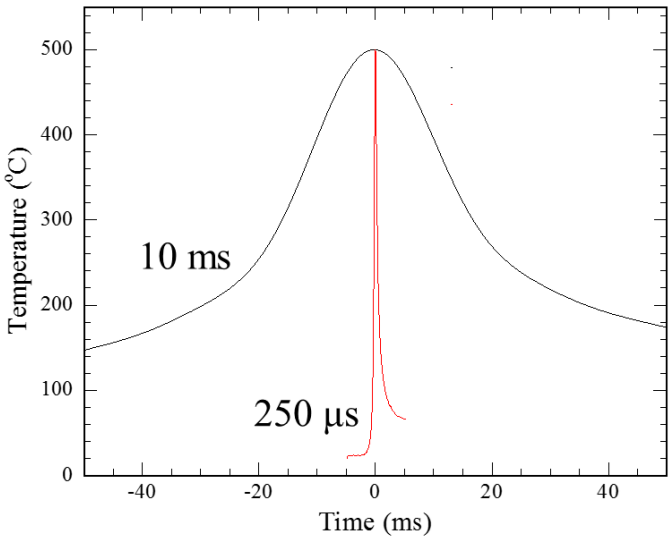

Figure 3.2: Measured sample time-temperature LSA profiles for 10 ms (black) and 250 μs (red) anneals to a peak temperature of 500 °C. Time zero delineates passage of the laser center over the probe position.

time, and rapidly cools back towards ambient. The heating and cooling rates are dwell dependent but the temporal profile shows that the anneal remains within ≈5% of the peak temperature for 1 dwell time.

The details of the temporal profiles are slightly dependent on the dwell time and peak temperature attained, even when normalized for both. Figure 3.3 compares a 10 ms dwell anneal to 1000 °C with a 250 μs dwell anneal to 1000 °C. The 10 ms LSA is nearly symmetric in time, while the 250 μs LSA is significantly asymmetric with a substantially faster heating rate than quench rate.

This asymmetry in both temporal profiles (very slight for the 10 ms LSA) stems from the dynamics of the heating process. In the long time limiting case (dwell $\rightarrow \infty$), the laser appears stationary and heats material by thermal conduction creating a Gaussian-like spatial profile in temperature. For LSA on shorter times, the laser scans across the substrate with "cold" material passing into the

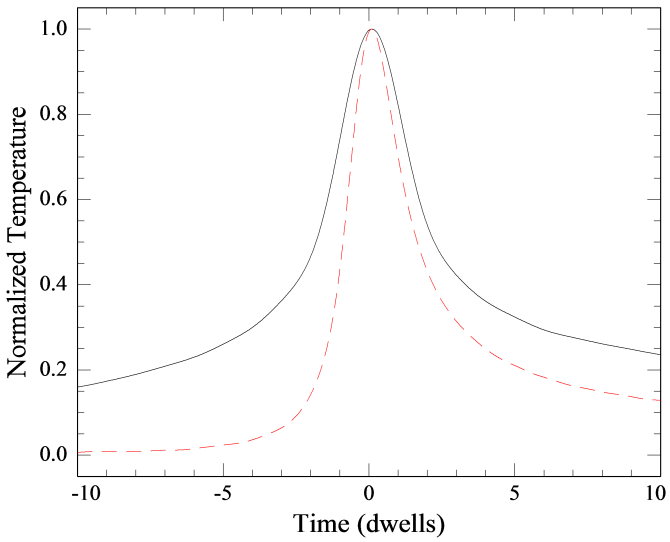

Figure 3.3: Measured sample time-temperature LSA profiles for 10 ms (solid black) and 250 μs (dashed red) anneals to a peak temperature of 1000 °C normalized by the peak temperature and dwell time. Time zero delineates passage of the laser directly over the sample area.

laser light. As the laser scan velocity increases (decreasing dwell), this cold material is not pre-heated by thermal conduction before the laser directly heats the material. This causes the leading edge (negative time) to remain closer to ambient temperature until reaching the laser. This also explains the higher quench rate for the short anneals as the thermal gradient has not been reduced by thermal conduction.

Figure 3.4 shows 250 μs LSA anneals to 1000 and 300 °C (solid black, dashed red respectively), normalized in peak temperature and as a function of the normalized time (dwell). While very similar, the higher peak temperature anneal quenches more rapidly towards ambient primarily due to the greater thermal gradient as well as the temperature dependence of the heat capacity and thermal conductivity.

As a rough estimate, the peak quench and heating rates can be estimated

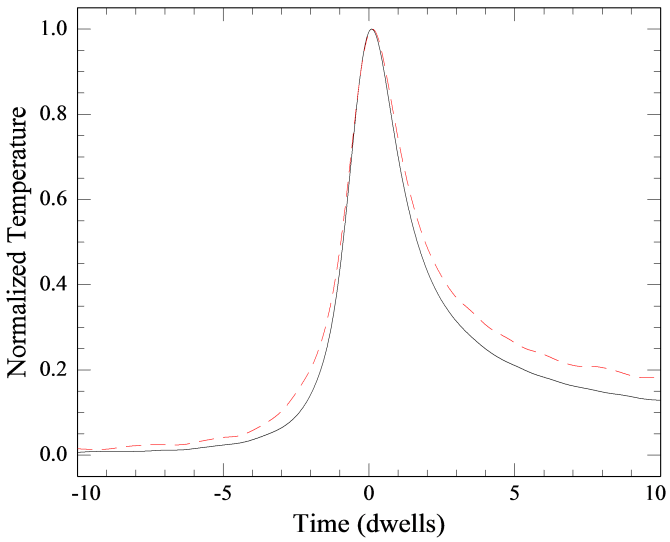

Figure 3.4: Measured sample time-temperature LSA profiles for 250 μs anneals to peak temperatures of 1000 °C (solid black) and 300 °C (dashed red), normalized by the peak temperature and dwell time. Time zero delineates passage of the laser directly over the sample area. Changes in the normalized profile reflect temperature dependent thermal properties.

as approximately $T_{peak}/2\tau$. However there are some significant differences in the tail behavior depending on the dwell. For example, Figure 3.3 shows the significantly longer cooling tail of the 10 ms LSA. A short anneal effectively quenches into an infinitely thick substrate as the room temperature thermal diffusion length in silicon for a 250 μs anneal is ~140 μm, substantially less than the typical substrate thickness of 350-500 μm. For the long 10 ms anneal, the thermal diffusion distance is ~900 μm and the substrate is thermally thin with the thermal diffusion field perturbed by the substrate – chuck interface. This interface is an additional thermal resistance decreasing the long-time quench. The long time quench tail behavior can also be exacerbated for small samples where the lateral heat transport is influenced by edge effects.

In practice, the long tail behavior is often ignored as Arrhenius kinetics make

most materials primarily sensitive to the peak temperature rather than the long, low temperature tail. However, there are cases where this tail cannot be ignored and the quench to ambient is important. In organic systems, for example, additional diffusive motion may occur due to Williams-Landel-Ferry (WLF) dynamics and damage in polymers may accumulate from a long, moderate temperature, soak.

Validity of Dwell Time as Anneal Duration

For thin films, LSA is essentially isothermal within the top few microns of the surface. Even for organic systems with poor thermal conductivity, a 100 nm thick film thermally equilibrates within 10 μs ($\sqrt{Dt}$ ~300 nm for D=10^{-4} cm^2/s). For dwells >250 μs, common film thicknesses are thermally thin and experiences essentially a uniform (in depth) thermal profile.

Due to the inherently transient nature of LSA, the specific anneal temperature and time must be precisely characterized. Multiple choices (peak temperature, average temperature, half-maximum temperature, etc.) are potential representative values with no single value immediately identifiable as most appropriate to represent the dynamic sample environment, especially after the quench to room temperature.

Thermally activated kinetic processes are inherently most sensitive to the highest temperatures reached during anneals. For Arrhenius kinetics, integration of the LSA time-temperature history using Equation (3.1) yields an equivalent isothermal ($\frac{dT}{dt} \rightarrow \infty$ heating and quench) anneal at the peak temperature:

$$t_{\text{eff}} = \int e^{-\frac{E_A}{k_b}\left(\frac{1}{T(t)}-\frac{1}{T_{peak}}\right)} dt \tag{3.1}$$

For "typical" E_A values of ~100 kJ/mol (1 eV), this effective isothermal time varies from 0.7 to 1.3 τ while integrating the LSA temporal temperature profiles

from –25 τ to +25 τ. Greater integration ranges increase the equivalent anneal duration as samples at room temperature (long before or after the anneal) contribute nonzero to the sample kinetics. The integration range of ±25 τ includes the long time tail behavior to within approximately a tenth of the peak temperature of the 10 ms LSA and complete tail behavior of shorter dwells.

Though not all processes exhibit Arrhenius behavior, the broad applicability of Arrhenius kinetics indicates the dwell time and peak temperatures are a reasonable metric for the annealing conditions. For increased thermal activation energies, the effective isothermal anneal duration shortens to slightly less than the dwell time, while for decreased thermal activation energies, the effective anneal duration increases. Table 3.1 summarizes the calculated values for important dwell times and peak temperatures of 300 and 1000 °C.

Table 3.1: Equivalent isothermal anneal duration (in dwell times) for measured LSA time-temperature profiles and Arrhenius kinetics. Long dwell LSA (>5 ms) results may be skewed due to the long tail from small thermistor size and thermally thin transport to a plastic package during measurements.

E_A (eV)	0.5	1	2	5	0.5	1	2	5
T_{peak} (°C)	300	300	300	300	1000	1000	1000	1000
150 μs LSA	1.15	0.73	0.50	0.31	1.29	0.86	0.59	0.37
250 μs LSA	1.22	0.77	0.53	0.33	1.24	0.83	0.58	0.36
500 μs LSA	1.32	0.83	0.57	0.35	1.31	0.88	0.61	0.38
1 ms LSA	1.42	0.87	0.59	0.37	1.36	0.90	0.63	0.39
2 ms LSA	1.43	0.88	0.60	0.37	1.44	0.95	0.65	0.41
5 ms LSA	1.59	0.93	0.63	0.39	1.48	0.95	0.66	0.41
10 ms LSA	2.29	1.32	0.90	0.56	2.02	1.32	0.92	0.58

For the specific case of polymer phase segregation, the disordering behavior

should be most sensitive to the highest temperature achieved rather than some average temperature. Time spent above T_{ODT} will initially disorder the material, while quenching just below T_{ODT} with partially ordered/disordered films will asymptotically approach the ordered state again. This will favor quenched morphologies in between the fully ordered and fully disordered states. For these reasons, the maximum LSA temperature is reported for polymer ordering behavior. It is also important to note that the dominance of Arrhenius over WLF diffusion kinetics at high temperatures has been previously shown in some systems[105].

Spatial Temperature Behavior

Each laser scan used to anneal material also exhibits a temperature profile that varies spatially in the x- direction of Figure 3.1. The general shape of this temperature profile can be engineered by the choice of the incident beam shape. Of the many possible temperature profiles, LSA often uses "top-hat" (square wave) and Gaussian temperature profiles. At Cornell, the 980 nm semiconductor diode laser has been focused to a "top-hat" profile and the 10.6 μm CO_2 gas laser has been focused to a Gaussian profile. In general, these profiles are laser agnostic and dependent upon the incident beam intensity shape. For spatial profiles, we distinguish between the maximum temperature attained at the center of a specific anneal (at one dwell and power) as T_{max}, while the maximum temperature of a local position, not necessarily at the beam center, is referred to as T_{peak}.

In the case of a top-hat profile, significant modifications to the spatial beam temperature profile occur from thermal spreading of the absorbed laser intensity. Figure 3.5 shows the measured beam intensity for the 980 nm diode laser currently in use exhibiting a ~300 μm Gaussian FWHM in the scan direction

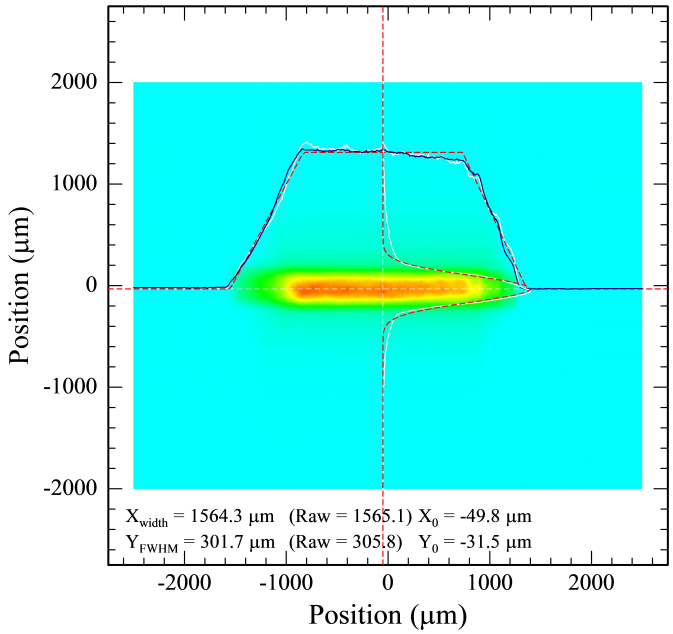

Figure 3.5: Measured 980 nm semiconductor diode laser "top-hat" intensity profile. Dashed curves give integrated profiles in the scan direction (y) and laterally (x).

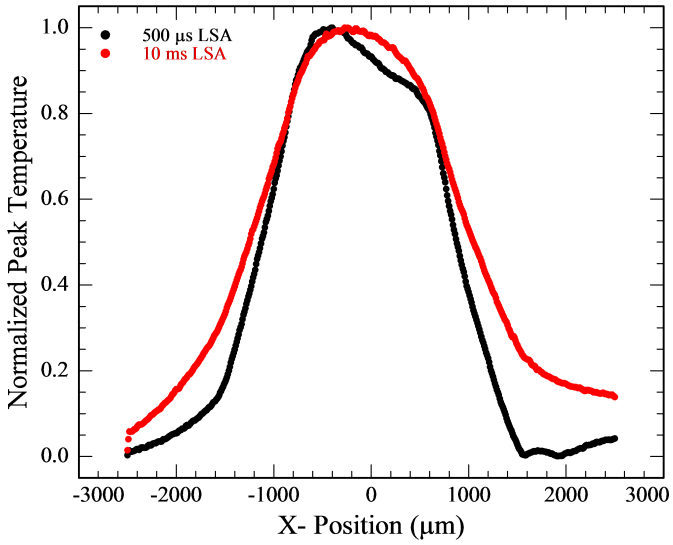

Figure 3.6: Measured lateral temperature profiles for 500 μs (black) and 10 ms (red) LSA anneals for the 980 nm semiconductor diode laser "top-hat" intensity profile. T_{max} for each profile was 250 and 400 °C respectively.

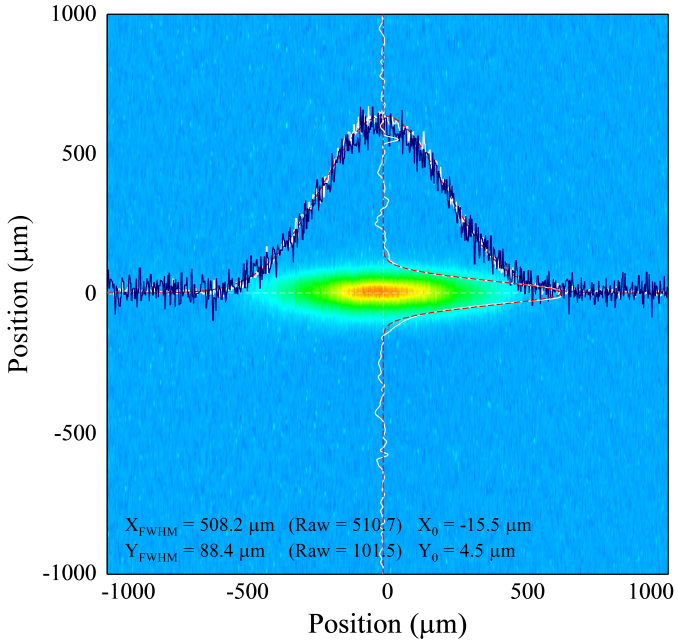

Figure 3.7: Measured 10.6 μm CO_2 gas laser Gaussian-like intensity profile. Dashed curves give integrated profiles in the scan direction (y) and laterally (x).

and a near square wave profile in the x- direction with a flat (slightly sloped) distance of ~1.6 mm. For short anneal durations, this intensity profile is closely replicated in the measured peak temperature as a function of lateral (x) position, as shown by the 500 μs LSA temperature profile in Figure 3.6 (black). At long dwells, thermal transport smears the temperature profiles producing a more Gaussian-like lateral profile, as seen by the 10 ms temperature profile in Figure 3.6 (red).

In contrast, the lateral Gaussian intensity profile of the CO_2 laser is largely maintained (Figure 3.7) throughout all dwells, but widens at long dwell times due to thermal conduction. Figure 3.8 shows the thermal broadening between a 250 μs and a 5 ms dwell time for the Gaussian intensity profile. This spreading also exhibits longer spatial tails. However, this may be biased due to the

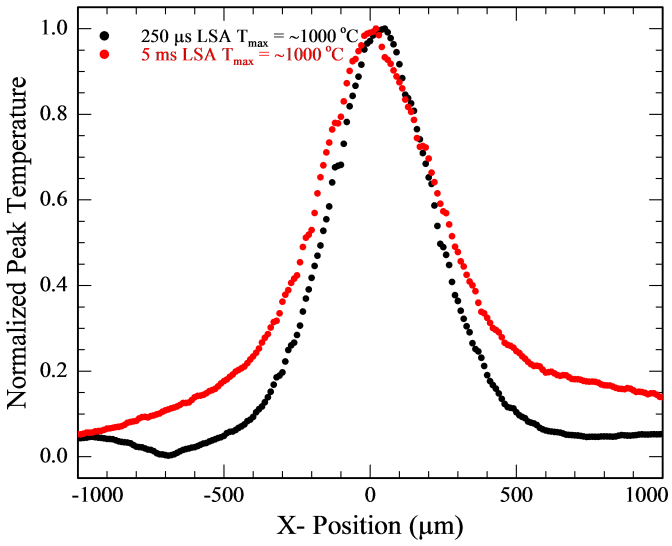

Figure 3.8: Measured lateral temperature profiles for 250 μs (black) and 5 ms (red) LSA anneals for the 10.6 μm CO_2 gas laser Gaussian-like intensity profile to a maximum temperature of ~1000 °C.

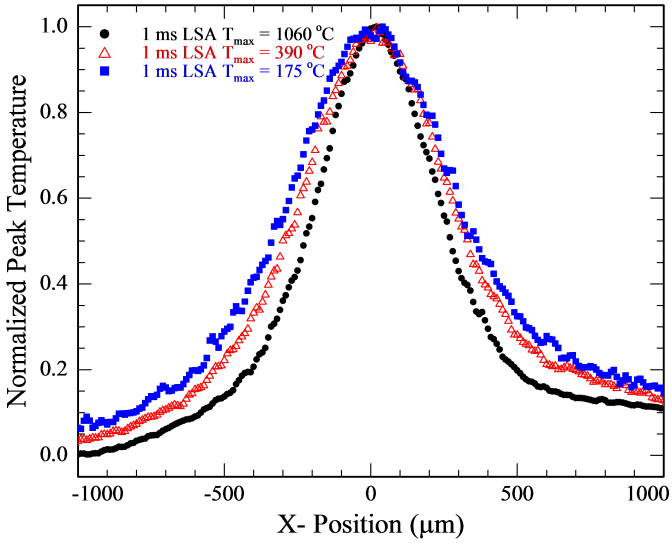

Figure 3.9: Measured lateral temperature profiles for 1 ms LSA anneals for the 10.6 μm CO_2 gas laser Gaussian-like intensity profile to peak temperatures of ~1060 (black circles), 390 (red open triangles), and 175 °C (blue squares). The higher thermal conductivity of silicon at low temperatures results in increased broadening for a lower T_{max}.

measurement technique, as discussed in Section A.3 of Appendix A.

In addition to the general thermal broadening at longer dwell times, the spatial temperature profile also varies slightly with peak temperature within a single dwell. Figure 3.9 shows measured temperature profiles for a 1 ms LSA at different peak temperatures. At high temperature (black), the profile is significantly narrowed compared to low temperature (blue). This reflects the reduced thermal conductivity of the substrate at higher temperatures caused by phonon-phonon and phonon-electron scattering. High temperature anneals, with decreased thermal diffusivity near the beam center, creates a bottleneck which concentrates the heat further[118]. Experimentally this effect is evident with the narrowing of the temperature profile FWHM.

3.3.3 Annealing Techniques

Area Anneals

For practical applications, it is usually necessary to create uniform anneals over large areas. In this case, a spatial temperature gradient over a single scan is deleterious to processing large areas. This is typically countered in two ways: optimization of a "top-hat" temperature profile which is carefully stitched together at the edges, or rastering the LSA scans with significant overlap.

Carefully stitching together individual scans is time efficient but may lead to non-uniformity at the stitch point while overlapping scans can significantly increase the number of scans and total process time. However, the latter process can be used with effectively any beam profile and will yield uniform anneals if the distance between overlapping scans (track spacing) is small relative to the thermal gradient. For Gaussian profiles, using a FWHM/5 track spacing exhibits a peak temperature perturbation of <4% over the entire area.

To reduce the peak temperature variations, the track spacing can simply be decreased. For example, a track spacing of FWHM/10 reduces temperature variations to <1%, but requires twice the time to process. Additionally, as the track spacing decreases, the effective total anneal duration increases as the overlapping spatial temperature profiles anneal the same area multiple times. Experimentally, the track spacing must be carefully noted as an anneal at the same dwell and peak temperature but with different track spacings can show different behavior due to the increased total anneal duration with decreased track spacing.

Single Scan Anneals

Though many applications require uniform anneals, the inherent lateral temperature gradients can be useful and provide a high-throughput testing technique when properly implemented. For a single LSA scan, areas of the sample reach temperatures from ambient (no anneal) to the maximum temperature (T_{max}) at the thermal profile center. Using spatially resolved metrology techniques, one can systematically probe sample properties continuously for all temperatures up to T_{peak} at a single anneal duration within a single LSA scan. This technique, called lateral-gradient laser spike annealing (lgLSA)[117], was developed to provide high throughput characterization of materials and is broadly compatible with many metrology techniques.

This annealing method can also be incorporated with other high throughput techniques, such as composition gradients, to provide even higher throughput, with data acquisition and analysis the experimental limiting step. In addition to high throughput, experimental uncertainties are often reduced as sample-to-sample variability can be largely removed since all temperatures are probed

within a single sample (or a relatively small sample area) and in a self-aligned manner where data taken across the full spatial temperature profile must yield symmetric behavior on either side of T_{max}.

3.4 BCP Metrology Operational Details

3.4.1 Scanning Electron Microscopy (SEM)

Secondary electron scanning electron microscope images were obtained on a Tescan Mira3 FESEM at 5 keV acceleration potential and 5 mm working distance. To enhance imaging contrast on PS-*b*-PMMA, the PMMA block was preferentially etched (~40 nm) in an oxygen plasma (Oxford 80/2, 50 W, 60 mTorr, 50 sccm O_2, 15 s for ~40 nm etch, 4 s for ~15 nm etch). Sample charging was mitigated with a thin Au-Pd coating (3 s, ~10 Torr).

3.4.2 Atomic Force Microscopy (AFM)

Atomic force microscopy images were obtained in tapping mode on both pristine BCP surfaces and after oxygen plasma etching. Phase contrast on pristine segregated polymer surfaces yielded visible structure but with poor contrast due to the similar T_g of PS and PMMA. Height and phase contrast after etching exhibited better imaging qualities and qualitatively matched observed structures on pristine surfaces. All AFM images presented in this document were taken after etch.

3.4.3 X-ray Scattering (GISAXS / μ-GISAXS)

Microbeam Grazing Incidence Small Angle X-ray Scattering (μ-GISAXS) studies were performed using 10.6 keV photons from the Cornell High Energy Synchrotron Source (CHESS). In order to probe materials spatially, the nominally 0.5 mm wide X-ray beam was focused to a ~20 μm wide (FWHM) micro-beam via capillary X-ray optics[119, 120] (Chapter 5) or knife edges (Chapter 6). At this X-ray energy, the critical angles of silicon and PS-*b*-PMMA films are ~0.2 and 0.13 degrees respectively and samples were measured at ~0.15 degrees to enhance interaction with the polymer structure.

Due to the similar electron density between the blocks, PS-*b*-PMMA exhibits only weak scattering, and etching or staining is often used to enhance the scattering intensity[121]. However, to ensure no structural modifications or swelling from the infiltration of etching or staining compounds, PS-*b*-PMMA films were initially measured as annealed (Chapter 5). Subsequent studies confirmed minimal or no changes in structure for *ex-situ* studies with staining compounds. Some preliminary data with and without staining compounds is presented in Chapter 6.

While the incident X-ray beam for μ-GISAX was reduced to an approximately 20 μm wide top hat profile, the glancing incidence angle of 0.15 ° geometrically spreads the beam to ~8 mm in the beam direction. This spreading means data is acquired across an area approximately 20 μm wide by 8 mm long necessitating precise rotational alignment of the μ-GISAXS beam relative to the LSA scan lines. Alignment was achieved using an *in-situ* microscope camera and sample alignment burn marks.

To enable this alignment, LSA was performed at high temperatures (~1200 °C) for short dwells (typically 250 or 150 μs) to burn off sample material

in narrow lines at both ends of the sample and near the middle, but off center. This enabled consistent loading of the sample and precise alignment with the X-ray beam. To identify the exact alignment of the X-ray beam, virgin sample area was exposed to X-rays for an extended period of time (~10-60 minutes) to cause visible material changes. This X-ray modified line was noted using dry-erase marks on the microscope monitor and verified using a fluorescent plate and burn paper. Before data acquisition, LSA burn marks were then aligned to the dry-erase marks on the microscope monitor by the rotational stepper stage; alignment precision was estimated to be approximately ±0.2 °.

Due to the similar uncertainty in alignment of the dry-erase marks, the alignment error estimate was increased to ±0.4 °error (±0.2 °random error plus ±0.2 °systematic error). To account for data acquired by other users who may not be as precise or have a different interpretation of rotational alignment, and to account for experimenter fatigue, the total alignment error between the LSA and μ-GISAXS acquisition areas was estimated as ±0.5 °and used for all relevant error calculations.

This misalignment error causes an LSA temperature uncertainty due to smearing of the Gaussian-like lateral temperature profile, where multiple adjacent LSA peak temperatures are simultaneously measured. This error is greatest in areas of greatest lateral spatial temperature gradients, occurring on the shortest dwell times and highest peak temperatures. For reference, a 0.5 ° misalignment would add a maximum temperature uncertainty of ~15 °C for the greatest spatial temperature gradient used in Chapter 5 (T_{max}=550 °C, τ_{dwell}=250 μs). This misalignment error was included in temperature error estimates along with maximum temperature and position uncertainty.

CHAPTER 4

THERMAL STABILITY OF ORGANIC, CONJUGATED, AND INORGANIC HYBRID POLYMERS UNDER LASER-INDUCED SUB-MILLISECOND HEATING

4.1 Introduction

Organic systems typically exhibit a limited thermal stability, indeed organics and polymers generally considered to be among the least thermally stable materials class[122, 123]; degradation generally occurs at temperatures of 200-400 °C. However, as with most chemical reactions, degradation generally follows Arrhenius behaviors, often though with multiple activation enthalpies when examined over large temperature ranges reflecting multiple mechanistic pathways.

As organic and polymeric systems are of increasing interest for research at extended temperature ranges, understanding of the thermal stability and kinetic behavior of these systems is of increasing importance. Thermal decomposition is normally studied using methods such as thermogravimetric analysis (TGA), differential scanning calorimetry (DSC), Fourier transform infrared spectrometry (FTIR), and mass spectrometry (MS). Reported decomposition activation enthalpies of 50-200 kJ/mol have been observed for systems ranging from aliphaic to conjugated structures[124–129]. In general, such organic systems begin to decompose at 200-400 °C. Even the most stable polymeric systems, such as certain polyimides, completely decompose by 700 °C during typical hot plate or furnace heating[130, 131].

The thermal stability of organic materials can be extended by incorporate polymer layers into silicate nanocomposites[132, 133], optimizing intermolec-

ular bonds[134], and stabilizing structures by using metal-organic frameworks (MOFs)[135, 136]. However, most of these methods require extensive structural modification of the materials. Similarly, it is well known that material properties and reaction kinetics depend strongly on heating conditions, including ramp and quench rates. As an example, the glass transition in organic systems can shift by 80 °C as the quench rate is increased from 10^{-1} K/s to $\sim 2x10^{3}$ K/s[137]. Similarly, decomposition reaction kinetics should permit polymeric materials to withstand considerably higher temperatures as long as the time is kept sufficiently short.

On short timescales, the thermal stability of polymers is poorly known. Using laser annealing methods, a few polymeric systems have been shown to be stable to nearly 1000 °C in the millisecond to microsecond regime[105, 138–140], and over 1400 °C in the nanosecond regime[141, 142]. In this work, the role short duration annealing on decomposition kinetics is systematically studied for various linear, aliphatic, conjugated, and inorganic (silicon based) structures. This study demonstrates the universality of stability at short times and establishes trends of thermal stability enhancement for use in the rational design of polymeric systems. Results may enable future applications such as high temperature tolerant flexible electronics substrates, or seed studies of fundamental chemical reaction kinetics in this previously inaccessible regime[138, 140].

4.2 Experimental

Laser-induced sub-millisecond heating, in the form of laser spike annealing (LSA), was initially developed to address issues of dopant activation and diffusion for shallow semiconductor junctions[115, 116]. While conventional heating methods (furnaces and hot plates) operate in the seconds time-frame with heat-

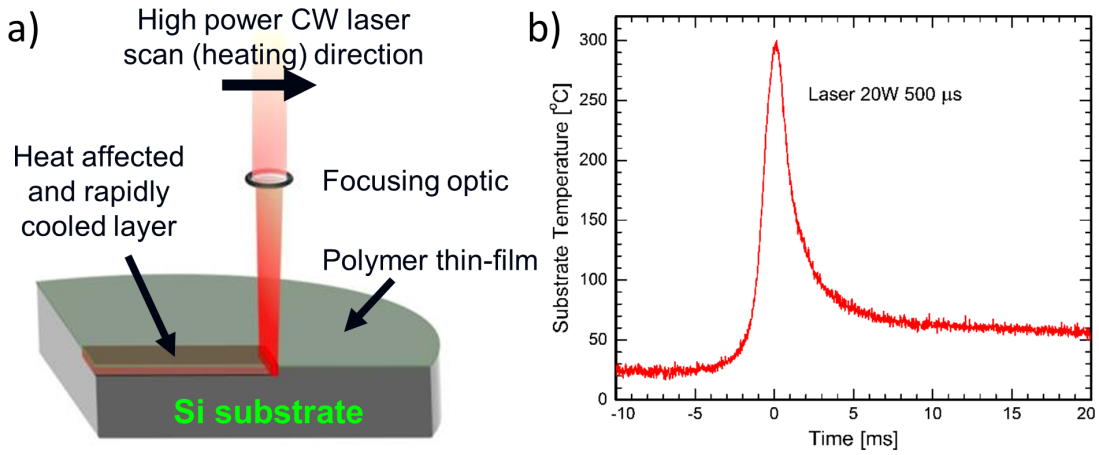

Figure 4.1: (a) Schematic representation of laser spike annealing geometry and (b) time-temperature profile for a nominal 500 μs LSA at 300 °C.

ing rates up to ~10^3 K/s, LSA operates with anneal durations from microseconds to milliseconds at heating and cooling ramp rates of 10^4-10^7 K/s. These extreme rates are achieved by scanning a line focused (~600 μm by 90 μm on the lab scale) continuous wave CO_2 laser (λ = 10.6 μm) across thin film samples with the rapid thermal quench enabled by heat conduction into the substrate. Figure 4.1a schematically shows this LSA geometry where power from a CO_2 laser is absorbed in the substrate, conducted to the thin polymeric film, and cooled by conduction into the substrate after the laser has passed.

The anneal duration of LSA is described in terms of the characteristic laser dwell time (τ), defined by the beam intensity full width at half maximum (FWHM) in the scan direction divided by the laser scan velocity, with typical dwell times ranging from 50 μs to 10 ms. For this characteristic dwell time, a surface polymer film's temperature will remains within 5% of the peak temperature for ~1τ, followed by rapid quench to within 10% of room temperature at ~10τ. Figure 4.1b shows measured time-temperature profiles for a 500 μs dwell

LSA to a peak temperature of 300 °C with maximum heating and quench rates of 3x10^5 K/s. In this work, absolute temperatures were calibrated to silicon and gold melt with temporal and spatial profiles determined using thin film platinum thermistors[118]. Temperature uncertainties are estimated to be ±1% of the peak temperature. For additional detail, see Chapter 3.

Due to the intrinsically transient nature of LSA, the anneal duration must be carefully evaluated for proper comparison to isothermal anneals. During LSA, an effective annealing time at the peak temperature (T_{peak}) can be defined assuming an Arrhenius kinetic behavior, as shown in Equation (A.3).

$$t_{\text{eff}} = \int e^{-\frac{E_A}{k_b}\left(\frac{1}{T(t)}-\frac{1}{T_{peak}}\right)}dt \tag{4.1}$$

where E_A is the activation enthalpy and k_b is Boltzmann's constant. For "typical" E_A values of 60-100 kJ/mol (0.6-1 eV), this effective isothermal time varies from 0.7 to 1.3 τ for integrated LSA temporal temperature profiles from –25τ to +25τ. Consequently, the dwell τ, can be used as a reasonable estimate of the equivalent isothermal heating time.

This novel heating approach can be widely applied to thin polymer films due to their typical transparency at the CO_2 wavelength[143]. Though polymers are typically poor thermal conductors (D~10^{-3}-10^{-4} cm^2/s), the characteristic thermal diffusion distance $(Dt)^{1/2}$ for even a 50 μs LSA is greater than 700 nm. Consequently, even a ~100 nm thick polymer film is essentially isothermal throughout its thickness.

In this work, we utilize LSA to measure the decomposition kinetics of a variety of polymeric materials, including simple organic chains, organic-inorganic (silicone) hybrids, and conjugated polymers as summarized in Table 4.1 and includes several technologically important polymer systems.The polymers were categorized into three broad groups: vinyl, hybrid, and conjugated polymers. In

this context, vinyl signifies an alkane backbone, hybrids include silicon or oxygen containing backbones, and conjugated polymers include backbone double bonds.

Table 4.1: Summary of investigated materials, abbreviations, and categories.

Polymer	Abbreviation	Category
Polystyrene	PS	Vinyl
Poly(4-hydroxystyrene)	PHOST	Vinyl
Poly(4-vinylpyridine)	P4VP	Vinyl
Poly(styrene)-*b*-poly(methyl methacrylate) 6:25	PS-*b*-PMMA	Vinyl
Poly(2-methyl-2-adamantyl methacrylate-co-γ-butyrolactone-2-yl methacrylate)	P(MAdMA-*co*-GBLMA)	Vinyl
Poly(styrene)-*b*-poly(ethylene oxide)	PS-*b*-PEO	Hybrid
Poly(4-t-butyl styrene)-*b*-poly(ethylene oxide)	PtbS-*b*-PEO	Hybrid
Poly(styrene)-*b*-poly(dimethylsiloxane) 16:13	PS-*b*-PDMS 16:13	Hybrid
Poly(styrene)-*b*-poly(dimethylsiloxane) 4:1	PS-*b*-PDMS 4:1	Hybrid
Poly(3,4-ethylene dioxythiophene): poly(styrene sulfonate)	PEDOT:PSS	Conjugated
Poly(2-methoxy-5-(2-ethyl hexyloxy)-1,4-phenylene vinylene)	MEH-PPV	Conjugated

The effect of electron donating groups and substituent effects were explored by comparing PHOST, P4VP, and PS. The role of the backbone or other structural based effects was investigated using styrene and methacrylate based block copolymers. Finally, two conjugated polymers were investigated due to their increasingly widespread use in model systems for organic LEDs and electronic devices. All polymers were studied in ambient air with changes in the ambient almost certain to modify these results. This would be especially true for inert

environments which would expose alternative degradation mechanisms.

All polymers were dissolved in appropriate solvents at 3 wt% concentrations. These solutions were spin coated on to heavily doped (0.01-0.02 Ω-cm, p-type) silicon substrates with a target thickness of ~100 nm followed by a bake on a vacuum-chuck hot plate for 90 s to evaporate any remaining solvent (see Section 4.5). For traditional hot plate thermal decomposition studies, films were heated to temperatures from 50-600 °C for 15-60 s in ambient air. In the millisecond and microsecond regime, films were heated by LSA to peak temperatures from 200-1000 °C for 50-1000 μs, also in ambient air. To quantify the thermal stability, film thickness was measured using ellipsometry, profilometry, and spectral reflectance techniques. Thermal stability of the bulk polymers on long time scales was also confirmed using thermogravimetric analysis (TGA) in flowing N_2 gas. Additional characterization was performed using Fourier transform infrared (FTIR) spectroscopy to identify characteristic decomposition byproducts.

TGA is commonly used to determine the decomposition threshold of bulk organic polymers and small molecules by measuring mass changes as a function of temperature during a slow ramp at 0.002-0.2 K/s (corresponding to rates of ~0.1-10 °C/min)[124–126, 144]. While mass can be readily tracked during TGA, comparable measurements during laser-induced heating at high ramp rates (10^4-10^7 K/s) are difficult. However, since the density of polymers are approximately constant and near unity[123], the mass change can be correlated to the normalized thickness change in these films. This equivalence, confirmed experimentally, the results below, enables characterization of decomposition behavior as a function of the heating duration across a significantly larger range of durations and temperatures with ramp rates up to 10^7 K/s.

4.3 Results and Discussion

To characterize and compare the decomposition behavior of these polymers between seconds and sub-millisecond heating, thickness loss from 100 nm films on Si substrates were measured as a function of hot plate time and temperature or LSA dwell and peak temperature. Data from PHOST are shown in Figure 4.2a as an example. In addition to the hot plate and LSA results, the mass loss from TGA is also shown (right axis). Under TGA, slight mass losses are observed (<10%) as temperatures approach 300 °C, which has been previously attributed to the loss of the least thermally stable hydroxyl components[127, 145, 146]. At ~340 °C, the mass rapidly decreases as the polymer decomposes with complete decomposition by ~420 °C. The behavior after a 60 second hot plate anneal is essentially identical to this TGA result in both the temperature threshold and the detailed curve shape. For the purposes of this investigation, the decomposition temperature is defined at the 20% thickness (or mass) loss threshold. For PHOST, this yields a decomposition temperature (T_d) of ~350 °C for both the 60 s hot plate anneal and the 5 °C/min TGA.

As expected, reducing the hot plate heating time to 15 s enhances the thermal stability with T_d increasing by ~50 °C. Shifting to LSA heating, the decomposition threshold increases dramatically while the shape remains essentially identical for all heating durations. With the heating duration reduced to 50 μs, the thermal stability of PHOST is extended to ~810 °C. This is an increase of ~460 °C as the heating time is reduced by six orders of magnitude.

Although the material loss curves are similar, the decomposition mechanism could well change with heating duration. To confirm that the decomposition mechanism and byproducts are equivalent, FTIR spectra were taken after a 500 μs LSA and a 60 s hot plate anneal. Figure 4.2b compares spectra in the fin-

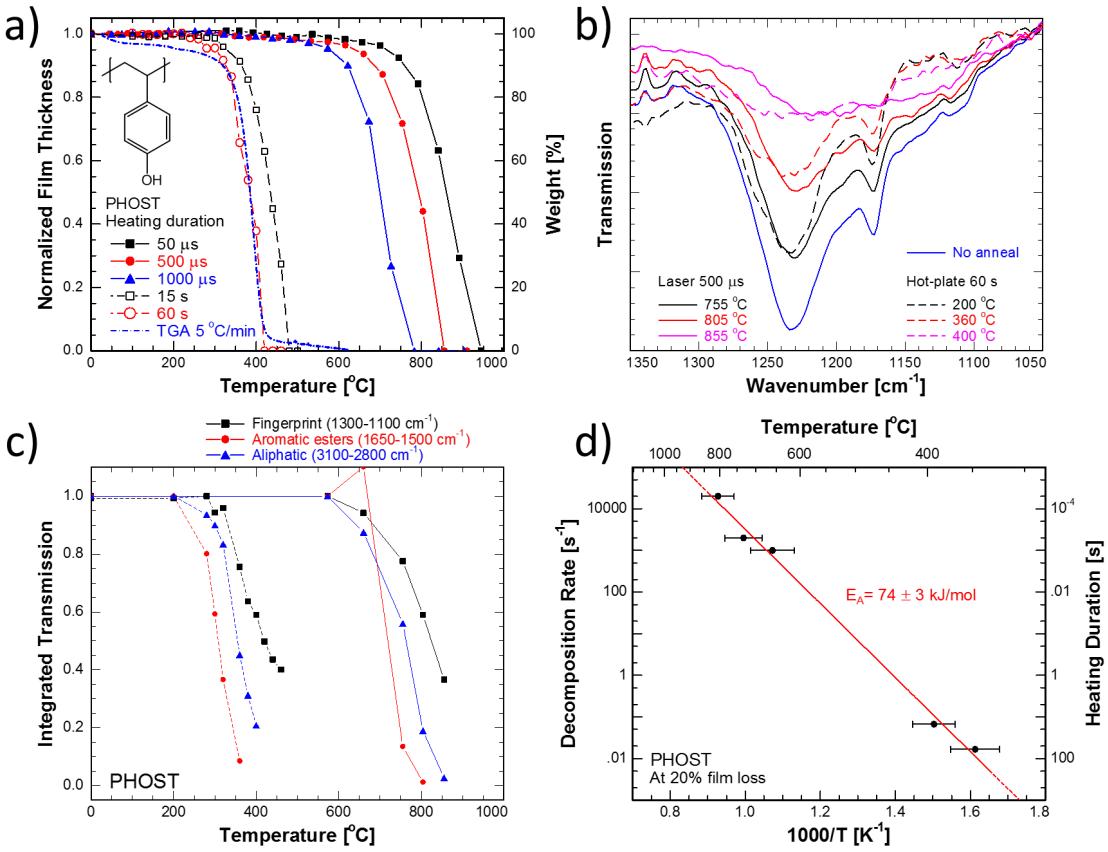

Figure 4.2: Decomposition behavior of PHOST under varying time anneals. (a) Normalized thickness (left axis) and TGA mass (right axis) of ~100 nm film and bulk samples, respectively, for various heating times, (b) FTIR absorption spectra from before annealing (blue), at $T<T_d$ (black), ~50% decomposition (red), and >90% decomposition (maroon) for LSA (solid) and hot plate (dashed) anneals, (c) integrated FTIR signal for 50 μs LSA and 60 s hot plate anneals in fingerprint, aromatic, and aliphatic regions, and (d) Arrhenius plot of 20% decomposition threshold exhibiting linear behavior.

gerprint region before annealing, after annealing at a temperature significantly below T_d, at a temperature corresponding to ~50% material loss, and after full decomposition for both LSA and hot plate. The overall decomposition behavior appears similar though the detailed pathways differ slightly with timescales. Signals from 1170-1270 cm^{-1} (in the fingerprint regime) after annealing at $T<T_d$, at ~50% decomposition, and at full decomposition is effectively replicated in both time regimes indicating the same structural changes. However, in the 1100-1170 cm^{-1} band, the FTIR signal is reduced even for low temperature hot plate anneals (100-200 °C, dashed lines) while it remains significant under 500 μs LSA heating to the highest temperatures. We believe that this region corresponds to adsorbates that must be desorbed rather than decomposed due to the rapid loss at even the lowest hot plate anneal, but retention to high temperatures under LSA. Outside the band from 1100-1170 cm^{-1}, the FTIR spectra show remarkable similarity between LSA and hot plate heating.

If the decomposition mechanism is independent of heating times, the FTIR signal should exhibit a similar progression with temperature. This was verified by integrating the FTIR signal intensity as a function of temperature for three characteristic regions, as shown for PHOST in Figure 4.2c. For hot plate anneals, peaks in the aromatic region are lost first as the decomposition occurs, followed by loss of signal from the aliphatic and lastly the fingerprint regions. The sequence is identical for LSA, but is shifted to much higher temperatures. This supports the hypothesis that the decomposition mechanism remains the same in both time regimes.

Given equivalent decomposition pathways, it is reasonable to expect that the rates can be directly compared and modeled by an Arrhenius behavior with a single activation enthalpy. Figure 4.2d plots the 20% decomposition thresh-

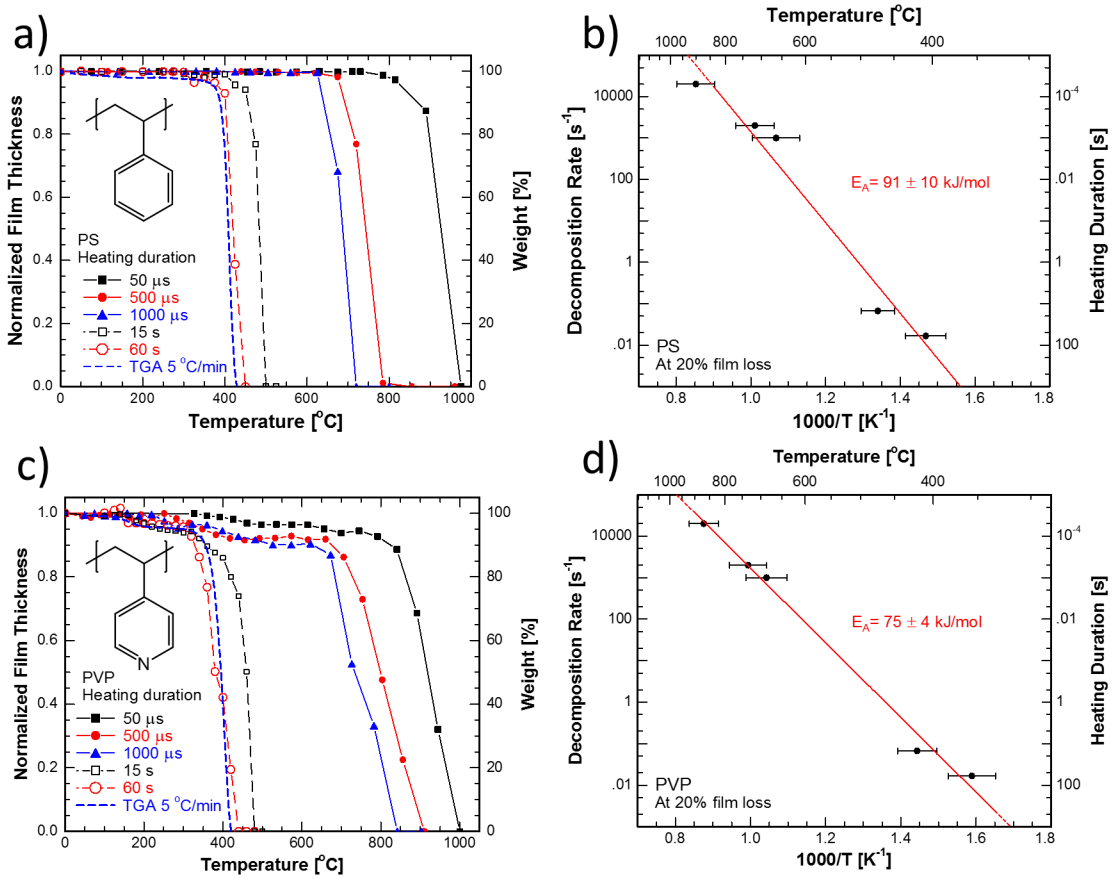

Figure 4.3: Decomposition behavior of PS and P4VP: (a) PS and (c) P4VP normalized thickness (left axis) or TGA mass (right axis) of ~100 nm film and bulk samples respectively, (b) PS and (d) P4VP Arrhenius plot of 20% decomposition threshold exhibiting linear behavior.

old temperature for PHOST in an Arrhenius form; the decomposition rate was taken as proportional to the inverse anneal duration. Over the ~6 orders in magnitude of heating duration, the data are consistent with a single decomposition activation energy of 74±3 kJ/mol. This is comparable to earlier measurements of various polymer decomposition activation energies in the range of ~50-200 kJ/mol[126, 129].

PS has a very similar structure to PHOST, but lacks the hydroxyl side groups.

Figure 4.3a shows hot plate and LSA decomposition data for PS exhibiting a more rapid decrease in thickness at similar decomposition temperatures. This sharp decomposition transition, in contrast to the more gradual change in PHOST, may stem from the uniform bonding environment in the backbone and phenyl side groups. This uniformity may mean that once decomposition begins, it rapidly proceeds throughout the entire molecule. In contrast, PHOST contains the electron donating hydroxyl group potentially reduced stability by providing a chemical reaction site or providing stabilization of intermediate structures during decomposition by forming resonant structures. Additionally, it can undergo hydrogen bonding providing modification of the reaction kinetics. Either effect would allow for a more gradual decomposition process as a function of temperature and reduce the decomposition activation energy. Indeed, PS exhibited a decomposition activation energy of 91±10 kJ/mol (Figure 4.3b) whereas E_a=74±3 kJ/mol for PHOST highlighting the effect of individual functional groups on decomposition. A third related polymer, P4VP, has a similar electron donating nitrogen substituted in the phenyl ring, and exhibits a decomposition activation energy of E_a=75±4 kJ/mol, nearly identical to PHOST. Table 4.2 summarizes the activation energies observed for all of the materials examined in this work.

Most polymers exhibited a single stage decomposition. However, the methacrylate based P(MAdMA-*co*-GBLMA) polymer's decomposition occurred in two stages at significantly different temperatures (Figure 4.4a). From FTIR and NMR measurements, the cleavage of both side group esters occurs first followed by backbone decomposition at high temperature[105, 138]. This gives two activation energies, E_a=64±4 kJ/mol for ester cleavage and E_a=110±10 kJ/mol for backbone decomposition (Figure 4.4b). The carbonaceous

Table 4.2: Summary of decomposition temperatures and activation energies of studied systems, detailed data in Section 4.5. ∗P(MAdMA-*co*-GBLMA) data exhibits atypical behavior discussed below.

Polymer	$T_d^{60\,s}$ (°C)	$T_d^{50\,\mu s}$ (°C)	E_a (kJ/mol)	Category
PS	408	900	91±10	Organic
PHOST	347	805	74±3	Organic
P4VP	356	869	75±4	Organic
P(MAdMA-*co*-GBLMA)				Organic
(ester cleavage)	235	665∗	64±4	
(backbone loss)	403	822∗	110±11	
PS-*b*-PMMA	338	722	79±4	Organic
PS-*b*-PEO	368	901	70±1	Organic
PtbS-*b*-PEO	327	862	66±2	Organic
PS-*b*-PDMS 16:13	428	851	107±19	Hybrid
PS-*b*-PDMS 4:1	418	847	103±15	Hybrid
PEDOT:PSS	371	791	86±9	Conjugated
MEH-PPV	343	855	71±4	Conjugated

backbone cleavage has a relatively high activation energy consistent with PS decomposition while the ester cleavage yields a statistically significant low activation energy. This decreased activation energy correlates with the the addition of electron withdrawing methacrylate group and potential stabilization due to resonance on the methacrylate group.

Thermal decomposition within these systems is endothermic. Mechanistically, decomposition occurs by ionic or radical pathways[127] which then propagate, furthering decomposition along the polymer chain, or decay into more stable species. This suggests that in the decomposition reaction scheme, the forward reaction (decomposition) should be dominated by the $\Delta G_{formation}$ of the

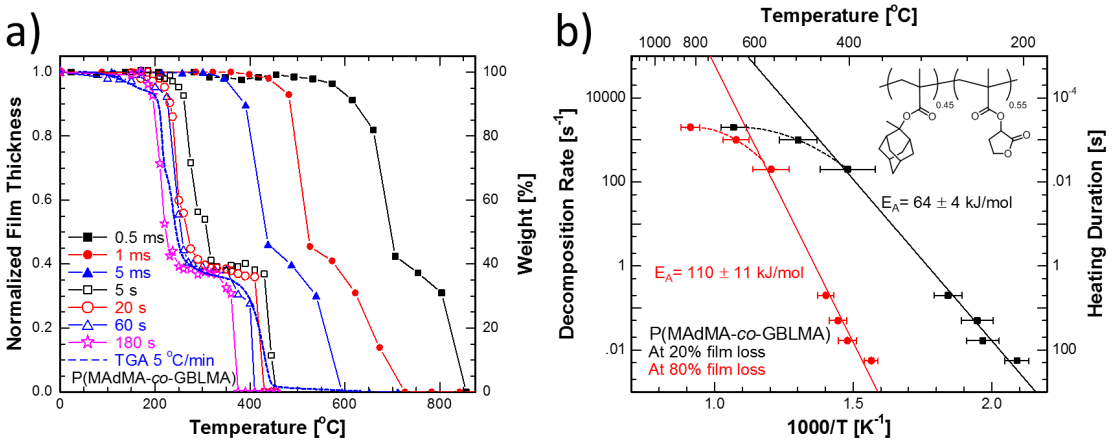

Figure 4.4: Decomposition behavior of P(MAdMA-*co*-GBLMA): (a) normalized thickness of 100 nm films (left-axis) normalized TGA mass of bulk polymer (right axis), and (b) Arrhenius plot of methacrylate cleavage (black) and backbone cleavage (red) exhibiting two distinct slopes and E_a values, short time deviations shown with dashed line to guide the eye.

subsequent broken bonds with perturbations due to the decomposition byproduct stability, resonance structures, and particular pathways.

Notably, Figure 4.4b exhibits a roll off in decomposition rate at high temperatures shown by the nonlinear trend at high temperatures. This behavior can stem from several sources, particularly a change in mechanism or a decomposition initiation time. In the former case, the highest rate is expected to dominate thus a change in mechanism should exhibit an increased slope and higher rates, contrary to the observed trend. While the availability of an additional trap state at high temperatures could potentially explain the drop in decomposition rate, it seems more likely that this may represent an initiation time for decomposition in this system, though the direct identification of the cause will likely require significantly more investigation.

Ester cleavage before backbone decomposition is well documented[147, 148]. The low activation energy of ester cleavage relative to backbone decom-

position can be explained in terms of the relative bond stability. The increased substitution of electron donating or withdrawing groups (EDGs, or EWGs) has likely inductively increased that particular bond reactivity as well as stability of decomposition byproducts allowing easier cleavage. Between the extremes of P(MAdMA-*co*-GBLMA) ester cleavage and PS decomposition with uniform bonding, PS-*b*-PMMA (with ~20% PS) was found to exhibit an intermediate activation energy with a more monotonic decomposition. Due to the incorporation of PMMA, one might expect a similar two-step process. However, only a slight indication of a two step process was evident at ~40% mass loss compared to the expected ~20%. Though comparison of block copolymer decomposition to homopolymers or random copolymers is not necessarily as elegant, we expect intermediate behavior between the block homopolymers for block chemistries which are not too dissimilar. For very disparate chemistries, or if the bonding group between blocks is significantly weaker, a two stage decomposition could occur, however, we this was not commonly observed, and no other polymer tested showed as distinct of a two step decomposition like P(MAdMA-*co*-GBLMA).

Further evidence of inductive electron influence on decomposition can be seen comparing PS-*b*-PMMA to PS-*b*-PEO where E_a decreases from 79±4 kJ/mol to 70±1 kJ/mol. Structurally, the backbone changed from purely carbon with electron withdrawing side groups to an electron donating $(C–O)_n$ backbone potentially stabilizing cleavage of backbone units rather than only side group cleavage. Other substitution effects are also present, as exhibited by the comparison of PS-*b*-PEO and PtbS-*b*-PEO, showing activation energies of 70±1 and 66±2 kJ/mol respectively. The presence of the tert-butyl group in Ptbs-*b*-PEO could stabilize decomposition byproducts by hyperconjugation of radical

byproducts[**Grassley1987**] possibly causing the lower E_a.

Increasing the bond formation enthalpy can be achieved by moving to a siloxane backbone as in PDMS. For comparison, two PS-*b*-PDMS systems were tested with increasing PDMS fraction. From the pure PS polymer, moving to 20% PDMS increases E_a from 91±10 kJ/mol to 103±15 kJ/mol. Futher increasing siloxane content to 45%, PS-*b*-PDMS 16:13 has an E_a=107±19 kJ/mol. The increased bond energy of Si–O bonds over C–C or C–O bonds (~450 kJ/mol vs ~350 kJ/mol) increases the energetic barrier to cleavage and decomposition however comparing PS-*b*-PDMS to PS is not completely equivalent as Si–O bond is much more polar than C–C bonds and even C–O bonds.

The more proper comparison is between PS-*b*-PEO to PS-*b*-PDMS 4:1, for which E_a increased from 70±1 to 103±15 kJ/mol from the inclusion of the higher energy Si-O vs C-O bond. This more accurate comparison shows the significant impact of bond formation energy in determining the decomposition behavior of these polymers. Though not as elegant a comparison, the lower activation energy of PEDOT:PSS relative to PS also follows this trend potentially due to the lower enthalpy, and non-polar, C-S bonds in the PEDOT:PSS backbone, however, a direct comparison is problematic due to multiple differences between these materials.

The conjugated polymers investigated here, PEDOT:PSS and MEH-PPV, yielded very similar decomposition activation energies compared to the simple aliphatic systems tested. This is striking as polymers with high bond formation enthalpy backbone bonds were correlated with a higher decomposition activation energy and an increased activation energy might be expected due to the increased formation enthalpy of the carbon-carbon double bond. The decomposition of MEH-PPV, with an all- carbon backbone, yielded E_a =71±4 kJ/mol

while PEDOT:PSS, (PEDOT has sulfur on backbone, PSS is all carbon) decomposed with E_a =86±9 kJ/mol. Though it is difficult to discern a trend with these disparate polymers, it is striking that the decomposition activation energy is so similar to the other classes measured.Though no truly analogous system was measured to compare conjugation alone, it does not seem that conjugation alone greatly increases E_a. This relative lack of change with conjugation may stem from the ability to first break the pi- or sigma- bonds individually rather than through a single step cleavage as is required for Si–O bonds in PDMS.

Although this discussion has focused on the decomposition rate activation energy, the absolute decomposition rate is also determined by the Arrhenius rate prefactor. It is expected that this prefactor can be strongly affected by backbone mobility and contamination of samples with radical initiators, salts, or acids/bases by potentially initiating decomposition. Selective addition of these species could ultimately discern these effects; however, the trends based on the polymer chemistry should remain intact while the absolute decomposition temperatures may shift. The focus on activation energy reduces the sensitivity of these measurements to any contamination issues.

In sum, these results yield three key trends or "rules of thumb" that help predict the general behavior of polymer thermal decomposition. First, as expected, the bond formation enthalpy appears to have the strongest impact. Second, incorporation of electron withdrawing or donating groups or groups enabling hyperconjugation decreases the decomposition activation energy, likely by stabilizing ionic and radical decomposition byproducts. Third, conjugation does not dramatically increase the decomposition activation energy in and of itself.

4.4 Conclusions

The thermal decomposition of simple organic, hybrid Si containing, and conjugated polymers was investigated using laser-induced sub-millisecond heating. Decomposition behavior of selected polymers was studied by correlating the weight loss obtained from TGA with the film thickness loss of a 100 nm film. At elevated temperatures, similar losses in both mass and film thickness were observed and FTIR suggests comparable decomposition of chemical components within the polymer. Heating durations reduced by six orders of magnitude from the conventional seconds time frame enhanced the stability of all examined polymer systems considerably, exceeding 900 °C for some systems, enabling kinetic studies of thin-film polymers at high temperatures for sub-millisecond time frames. Decomposition activation energies were obtained for all investigated systems in the range of ~60-110 kJ/mol.

The greatest determinant of the decomposition activation energy was found to be the bond formation enthalpy with perturbations due to placement of electronegative atoms and hyperconjugating side groups stabilizing decomposition products. Pure carbonaceous polymers and backbones were found to have decomposition activation energies near 95 kJ/mol while the inclusion of electron withdrawing and hyperconjugating species decreased the decomposition activation energy by ~30%. Incorporation of backbone dimethylsiloxanes was found to increase the decomposition activation energy by ~50% from 70 kJ/mol to ~105 kJ/mol for the comparison of PS-*b*-PEO and PS-*b*-PDMS. For conjugated polymers, backbone conjugation alone did not greatly enhance the activation energy, however, additional studies are necessary for these complex systems. The unique ability of LSA to probe short durations has demonstrated extended polymer thermal stability by over 500 °C and enabled precise measurement of

decomposition behavior.

4.5 Supporting Information

Figures 4.6 through 4.15 show detailed data for the other six polymers examined but not discussed in detail in the discussion section. Figure 4.6 shows comparisons between film thickness loss and TGA results, Figure 4.7 shows thickness curves for hot plate and laser annealed films, Figure 4.8 shows the measured decomposition activation energies, Figures 4.9-4.14 show the detailed FTIR scans, and Figure 4.15 shows the integrated FTIR signals. FTIR data from PS, PVP, P(MAdMA-*co*-GBLMA), PS-*b*-PEO, and PtbS-*b*-PEO were not taken during this investigation however it is likely the spectra would show similar behavior to the 7 materials that has FTIR acquired.

Table 4.3: Summary of utilized solvents, drying temperatures, and current applications for of the each investigated material systems.

Chemical	Solvent	Solvent Removal	Applications
PS	PGMEA	130 °C	Consumer, Feedstock
PHOST	PGMEA	130 °C	Photolithography[149]
P4VP	Methanol	60 °C	Consumer, Feedstock
P(MAdMA-*co*-GBLMA)	PGMEA	130 °C	Photolithography[105, 138]
PS-*b*-PMMA	THF	60 °C	Directed Self Assembly[3, 85, 150]
PS-*b*-PEO	THF	60 °C	Catalysts, Filters, Bio[150]
PtbS-*b*-PEO	THF	60 °C	Catalysts, Filters, Bio[150]
PS-*b*-PDMS 16:13	Toluene	100 °C	Directed Self Assembly[3, 85, 150]
PS-*b*-PDMS 4:1	Toluene	100 °C	Directed Self Assembly[3, 85, 150]
PEDOT:PSS	DI Water	90 °C	OLED Acceptor Material[151, 152]
MEH-PPV	DI Water	90 °C	OLED Donor Material[151, 152]

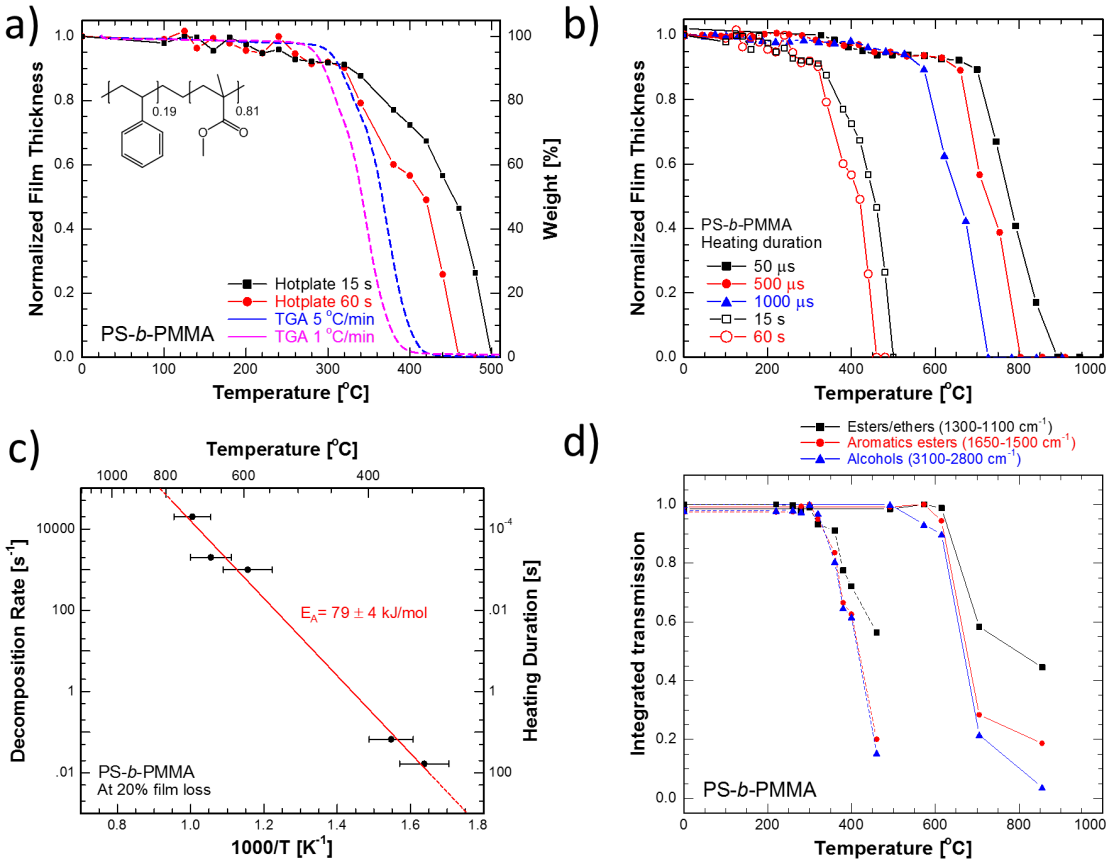

Figure 4.5: Decomposition behavior of PS-*b*-PMMA: (a) normalized thickness (left axis) and mass loss during TGA (right axis), (b) normalized thickness loss across tested heating durations, (c) Arrhenius plot determining decomposition activation energy, and (d) integrated FTIR signal evolution for hot plate and 500 μ s LSA anneal.

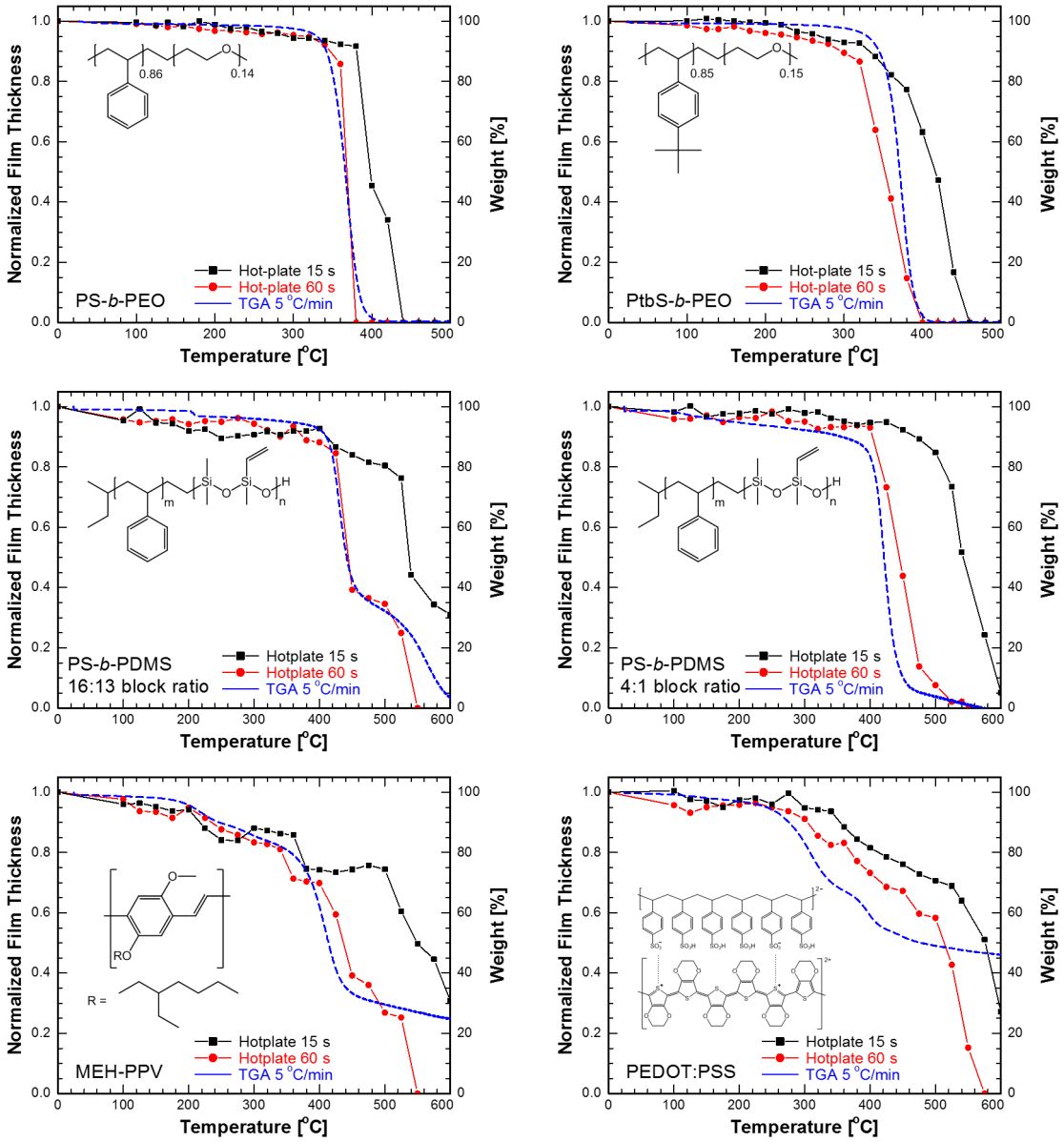

Figure 4.6: Comparison between thin film thickness loss after hot plate anneals (left axis) and TGA mass loss data (right axis) for remaining six polymer systems validating thickness measurement technique.

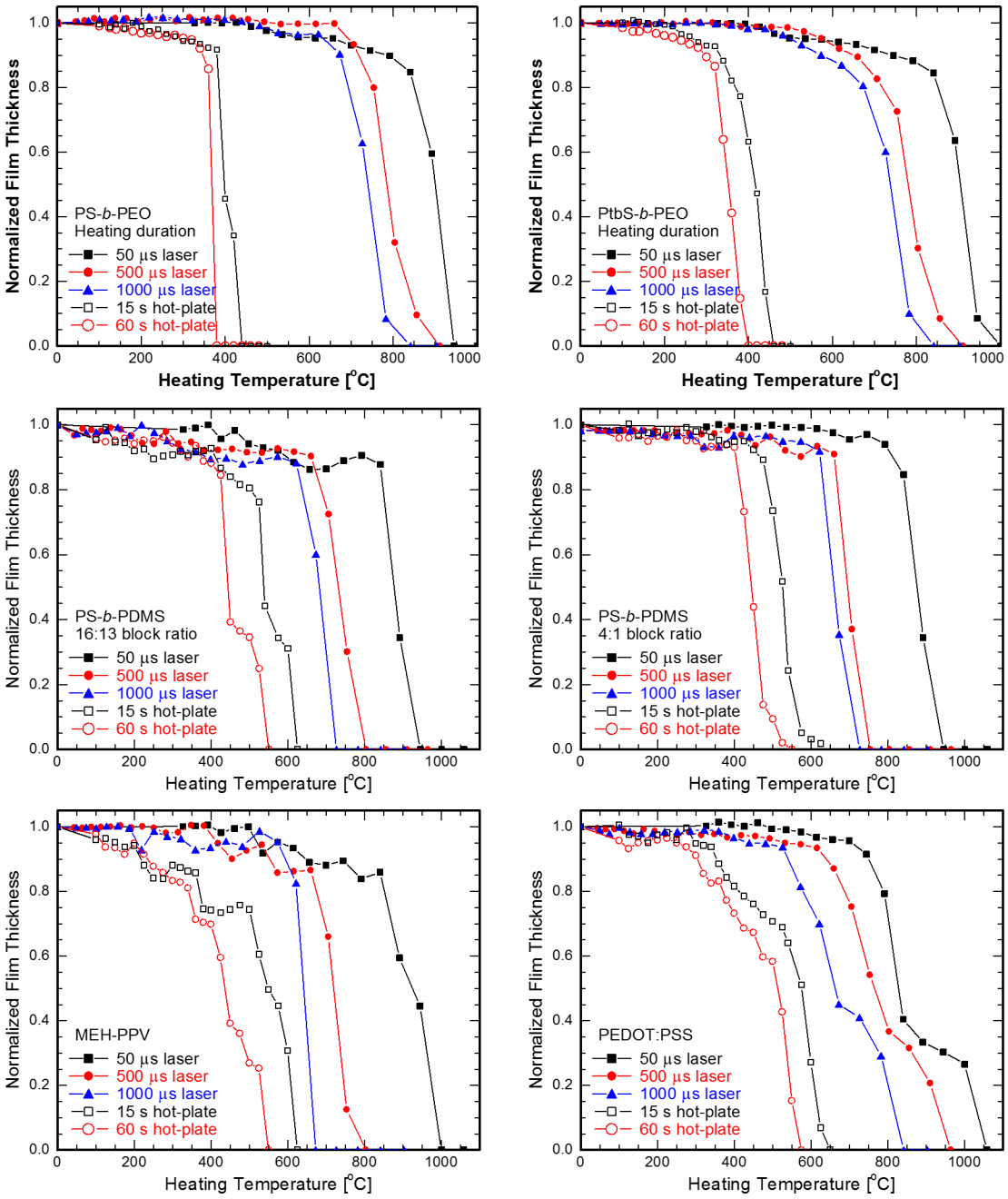

Figure 4.7: Thin film thickness loss after annealing by hot plate and laser. Decomposition temperature used to determine activation energy was defined at the 20% loss point.

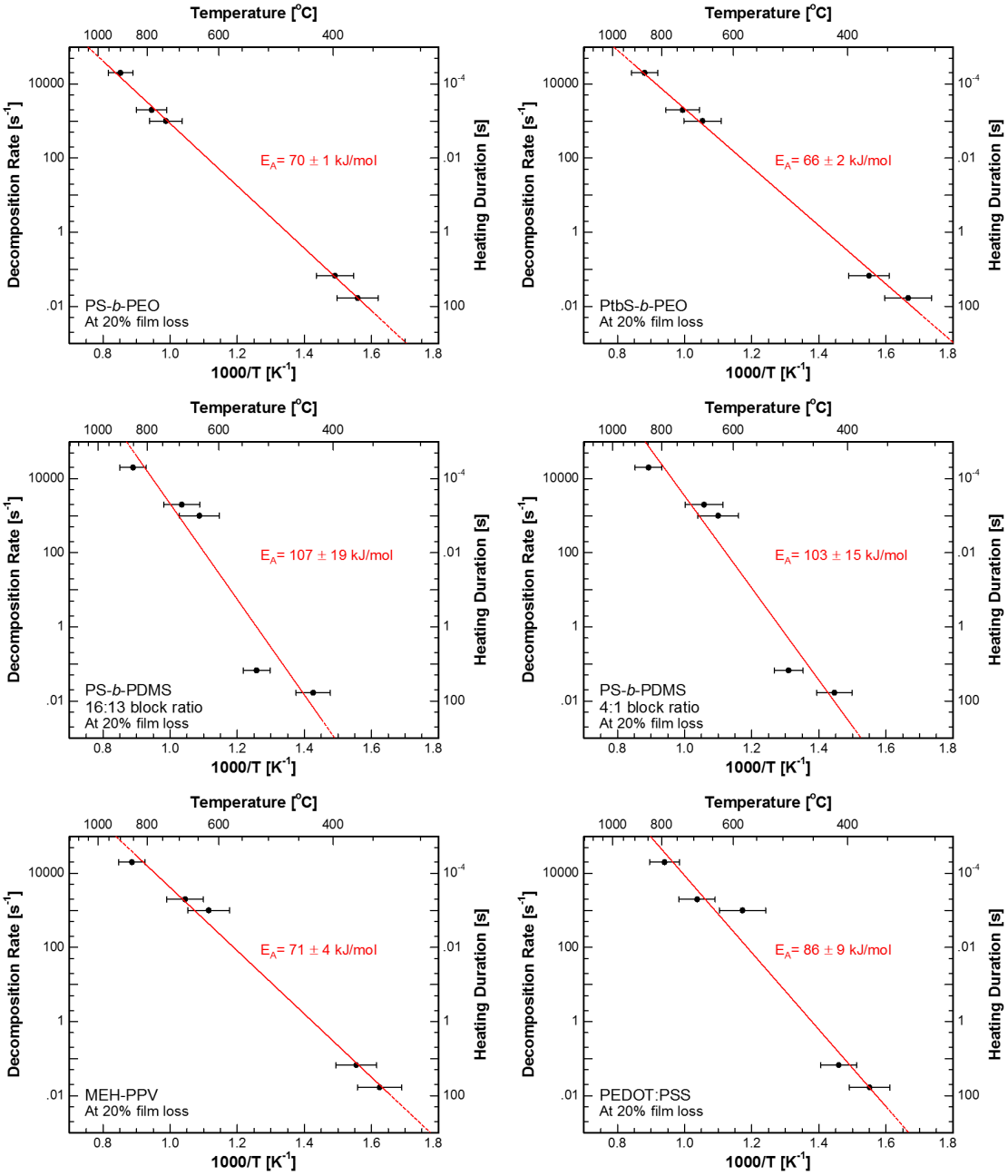

Figure 4.8: Arrhenius plots of decomposition rates and identified temperatures for remaining six polymer systems exhibiting linear behavior in all cases.

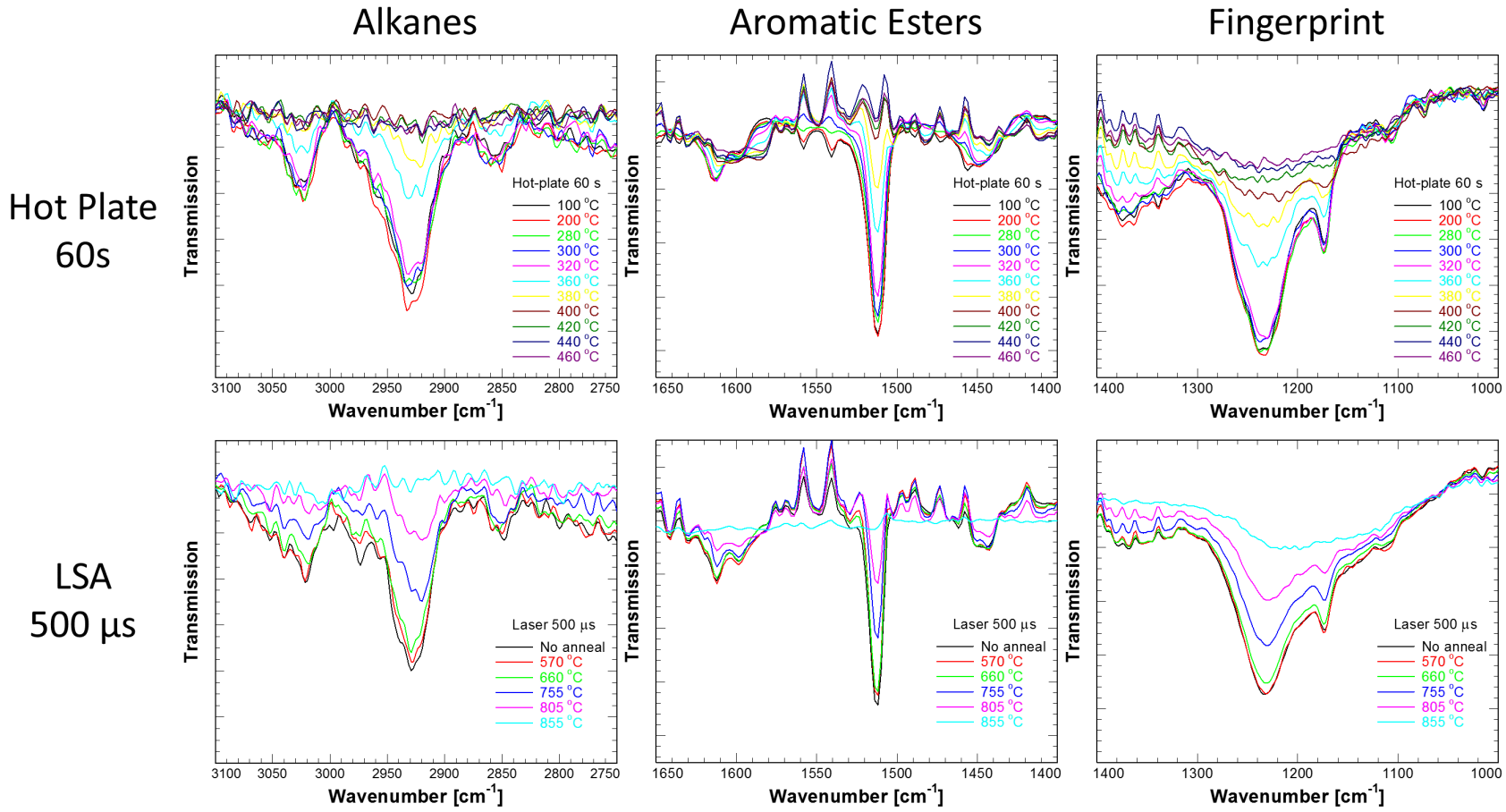

Figure 4.9: Detailed FTIR spectra for PHOST.

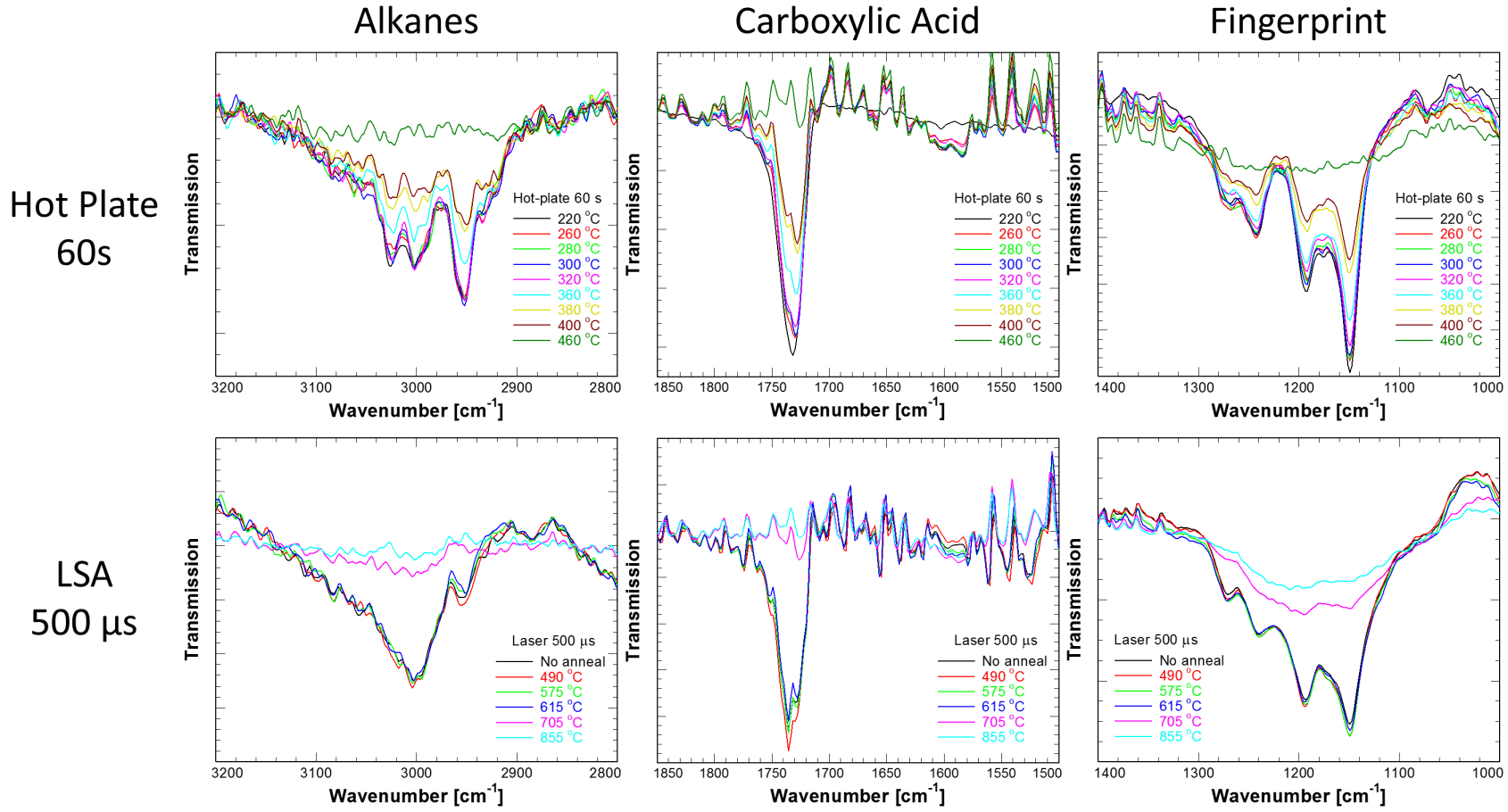

Figure 4.10: Detailed FTIR spectra for PS-*b*-PMMA.

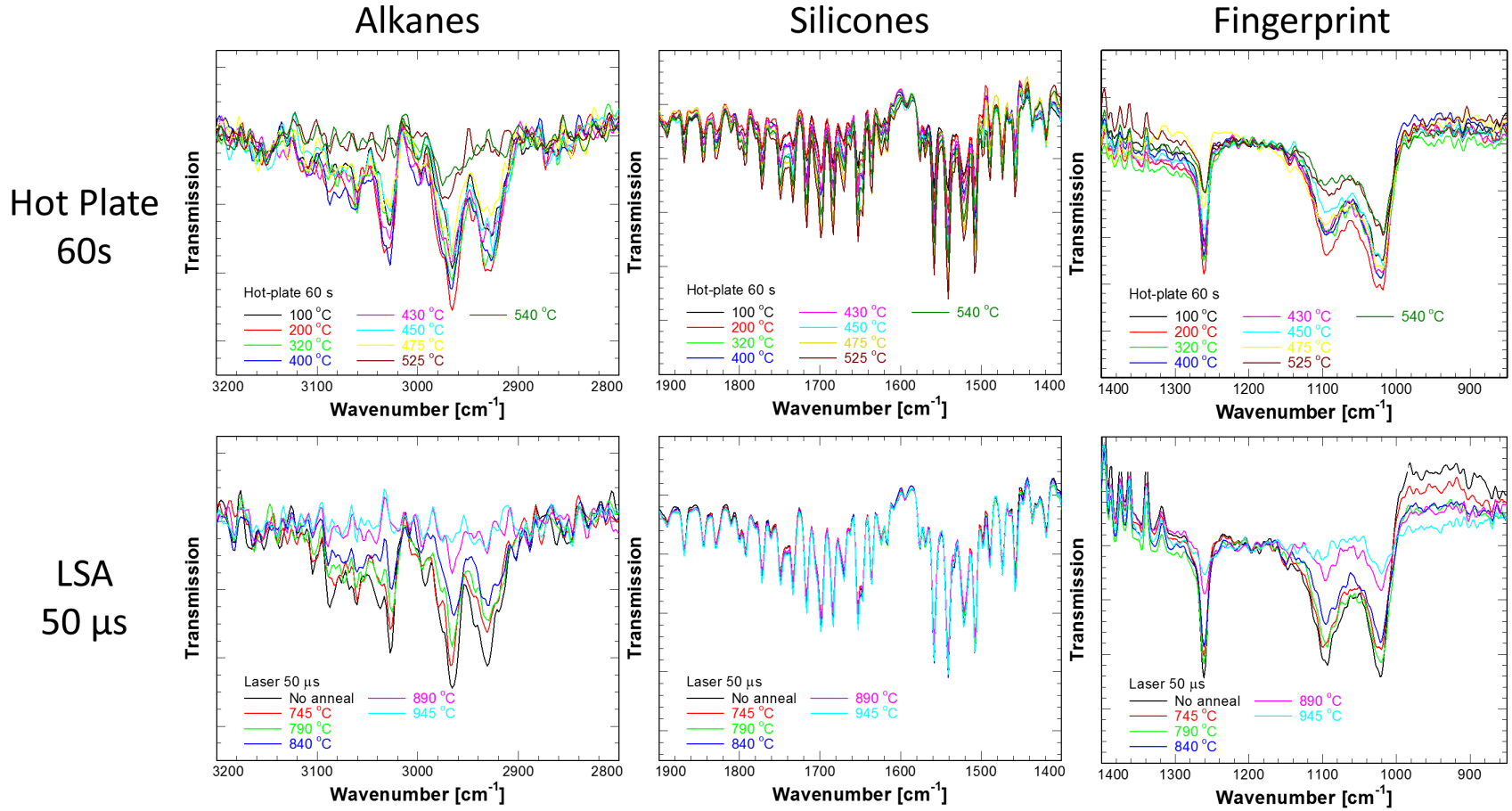

Figure 4.11: Detailed FTIR spectra for 16:13 PS-*b*-PDMS.

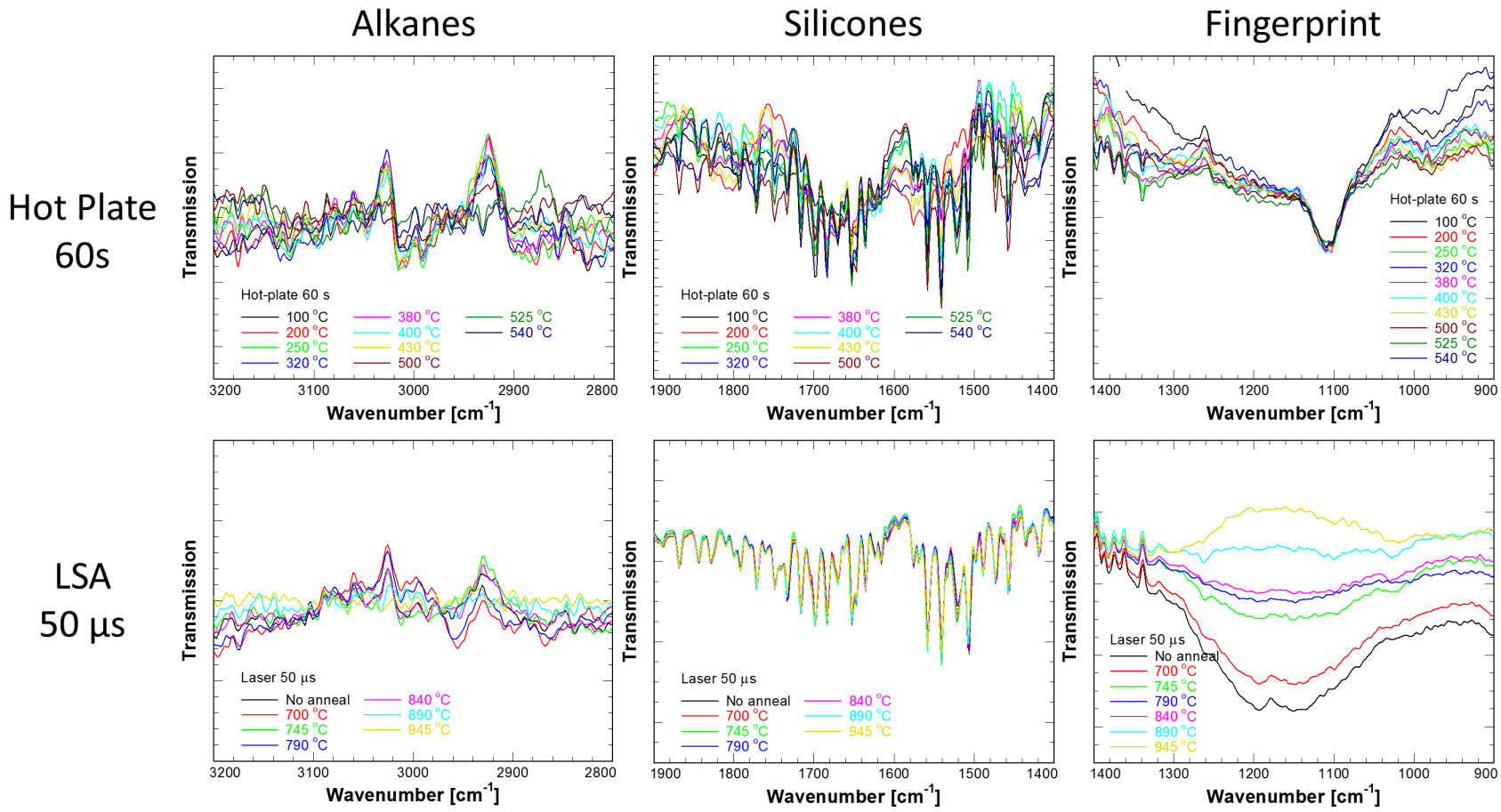

Figure 4.12: Detailed FTIR spectra for 4:1 PS-*b*-PDMS. The difference in behavior in the fingerprint region (900-1400 cm^{-1}) under LSA is likely an artifact from atmospheric contamination and background normalization.

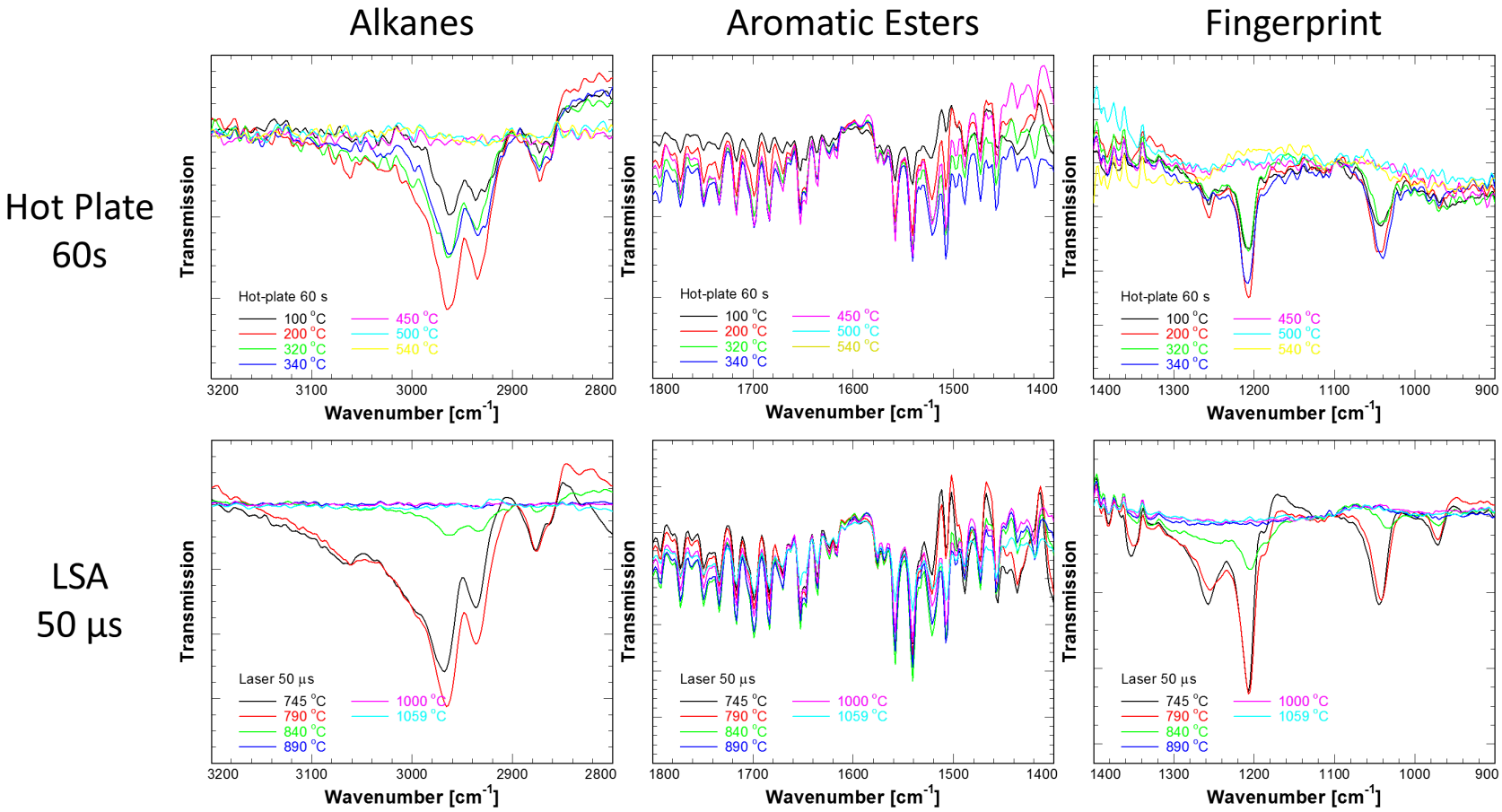

Figure 4.13: Detailed FTIR spectra for MEH-PPV.

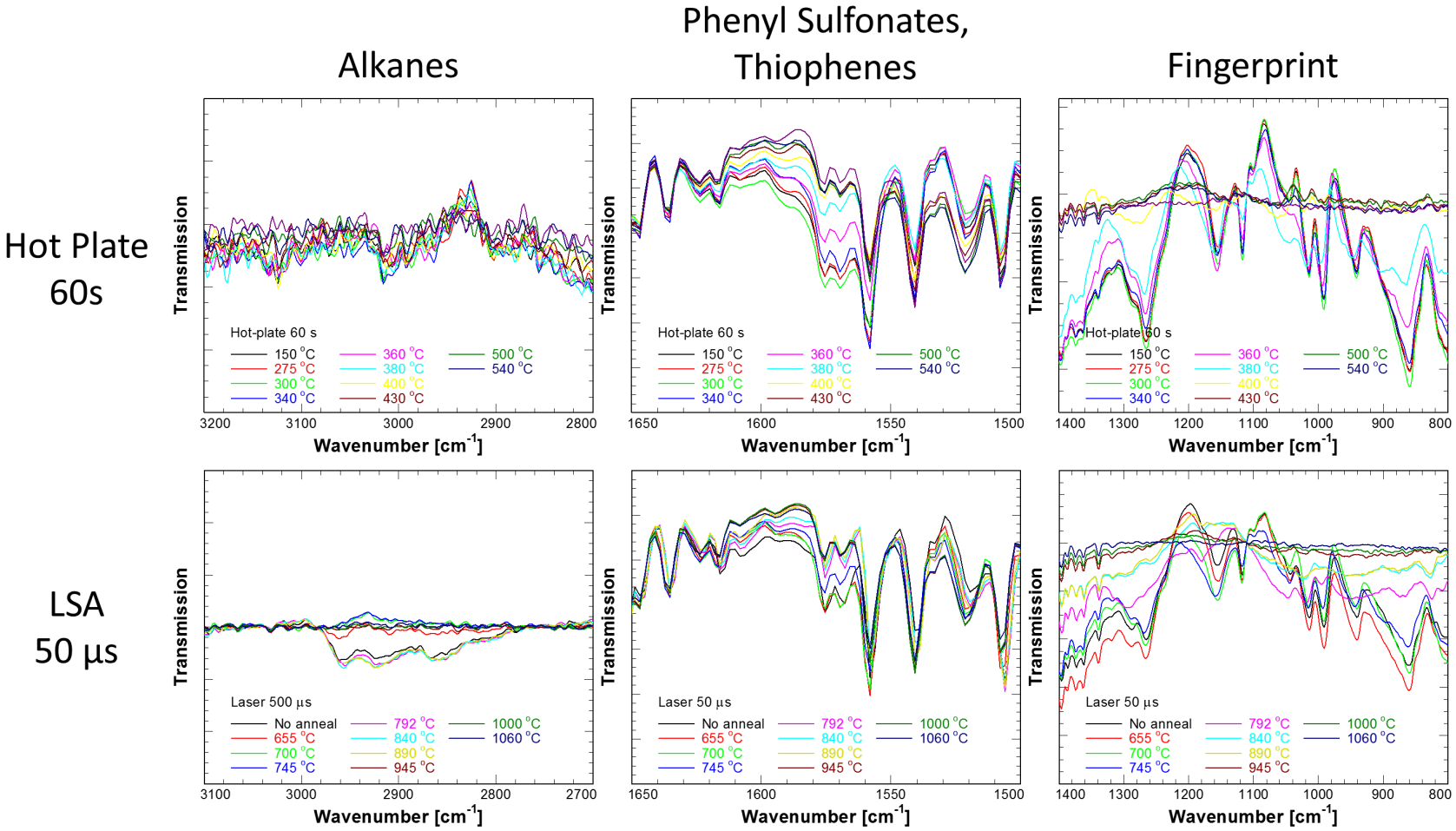

Figure 4.14: Detailed FTIR spectra for PEDOT:PSS.

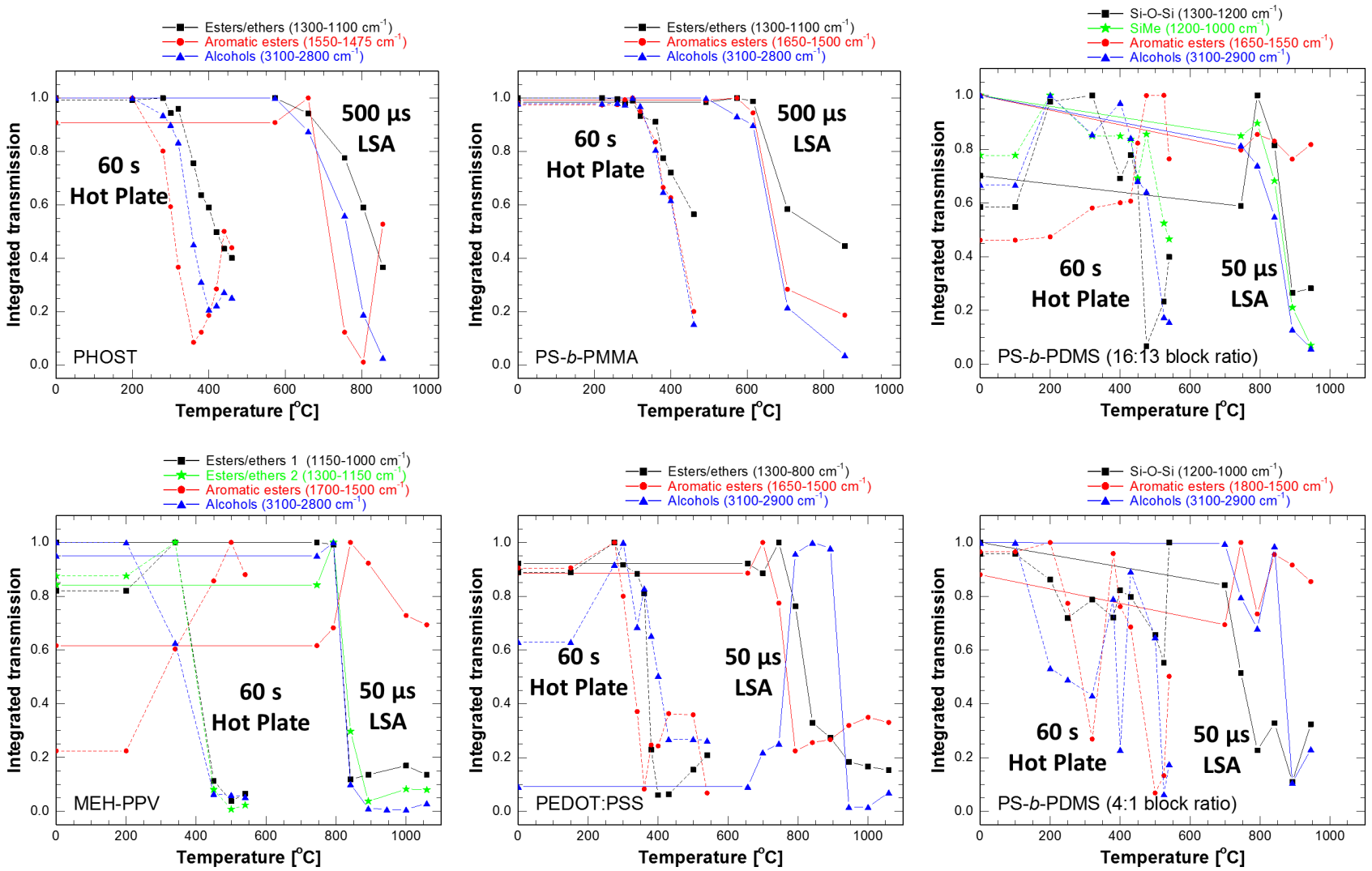

Figure 4.15: Summary of integrated FTIR signal data comparing 60 s hot plate and 500 or 50 μs LSA experiments.

CHAPTER 5

MILLISECOND BCP SEGREGATION KINETICS IN POLY(STYRENE)-*BLOCK*-POLY(METHYL METHACRYLATE) (PS-*B*-PMMA)

5.1 Introduction

[1] Typical anneal durations for BCP applications are on the minutes to hours timescale. However, several groups have studied morphological development induced by laser annealing on shorter times[82, 92, 95, 99, 139, 153–156]. These studies have demonstrated the ability to form phase segregated structures in the sub second regime and have investigated long range alignment of segregated domains to directing templates[139, 155]. In addition, alignment has been achieved in short timescales using large thermal gradients during solvothermal annealing[82], by thermal expansion induced shear stress[92, 95, 154, 157], and on much longer timescales via zone annealing[157–160]. However, the phase segregation kinetics remains largely unexplored.

Early stage phase segregation of block copolymers BCPs critically impacts the material's final structural properties, and understanding the kinetics of these processes is essential to intentional design of systems for practical applications. Understanding the BCP behavior in the deep quench regime is especially critical for many applications that begin in the metastable state. One such application is DSA lithography, where BCP films are spin-coated on substrates followed by annealing to phase segregate and ultimately align the BCP to a directing template. To probe these polymer dynamics in the condensed state, heating at rele-

[1]The majority of this Chapter was published as: "Kinetics of Block Copolymer Phase Segregation During Sub-millisecond Transient Thermal Annealing," A. G. Jacobs, C. Liedel, H. Peng, L. Wang, D. M. Smilgies, C. K. Ober, M. O. Thompson, *Macromolecules*, **2016**, v. 49, n. 17, 6424-6470. DOI 10.1021/acs.macromol.6b00698.

vant microsecond to millisecond timescales is necessary. Additionally, to enable *ex-situ* measurements for the greatest metrology flexibility, the samples must rapidly quench to the vitrified state to lock in the high temperature structure for observation.

In this work, the structural response of BCPs after short duration heating at extreme undercoolings is measured. In the millisecond and sub-millisecond time frame, the enhanced thermal stability of polymers enables tracking segregation dynamics and kinetics even in high molecular weight or high χ systems that typically decompose before reaching T_{ODT}. Laser spike annealing (LSA), originally developed to address dopant activation and diffusion in shallow junctions[115, 116], heats and cools thin films on millisecond timescales with heating and quench rates up to 10^7 K/s. LSA, utilizing a scanned continuous wave laser as the heat source, is typically characterized by a dwell time, defined in the experimental section, in the range of 50 μs to 50 ms. On these short timescales, polymers tolerate temperatures far in excess of their normal thermal decomposition limit[105, 138, 139, 155, 156, 161]; for example, in poly(styrene-*b*-methyl methacrylate) (PS-*b*-PMMA), annealing temperatures up to 1000 °C are feasible with a 250 μs dwell.

The sample temperature during LSA is inherently dynamic; Figure 5.1 schematically shows the expected kinetic behavior. With a peak anneal temperature above T_{ODT} (Figure 5.1a), times spent above T_g but below T_{ODT} will induce phase segregation (ordering regime) while times above T_{ODT} will disorder. Figure 5.1b schematically depicts the time dependence of an order parameter for films starting from the fully ordered (Γ = 1) and fully disordered (Γ=0) states. From the ordered state, disordering occurs rapidly once T exceeds T_{ODT}, with partial order redeveloping during cooling from T_{ODT} to T_g (solid curve Fig-

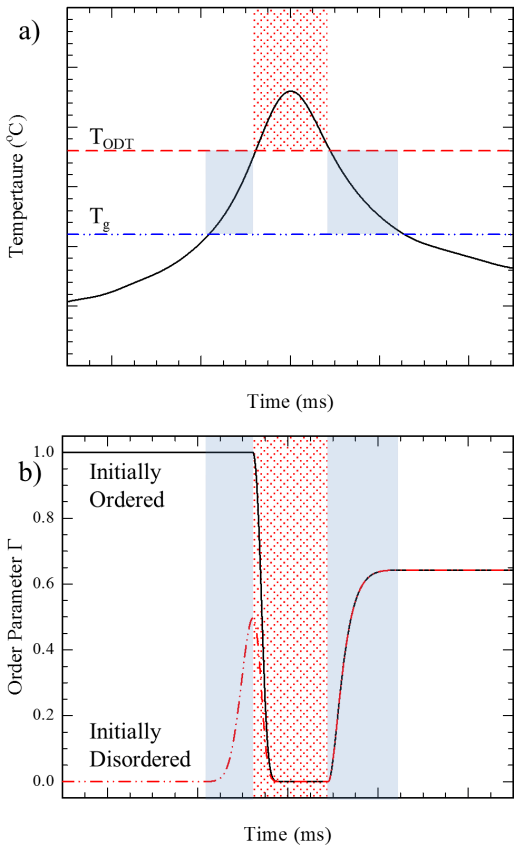

Figure 5.1: Schematic representation of kinetics during an LSA anneal. (a) Temperature profile with the ordering (T_g<T<T_{ODT}) and disordering (T>T_{ODT}) regimes highlighted. (b) Schematic ordering as a function of time from an initially ordered (solid line) or disordered (dashed line) state for this annealing condition.

ure 5.1b). From a disordered state, ordering occurs during heating to T_{ODT}, and then follows similar behavior once above T_{ODT} (dashed curve).

Figure 5.1b specifically depicts the case where there is sufficient time at T>T_{ODT} for the BCP to fully disorder leading to a final state that is independent of the initial state. This end state is thus dependent only on the quench to room temperature and, in particular, should be independent of additional time spent above T_{ODT}. The final state order will depend primarily on the quench rate, polymer mobility, and any kinetic limitations due to nucleation of ordered

domains[37, 48, 107, 108, 162–164]. In this work, the kinetics of both the disordering and phase segregation within these regimes is quantified as a function of the heating duration and quench rate (dwell) and the peak temperature.

5.2 Experimental

5.2.1 Materials

Cylinder forming PS-*b*-PMMA (M_N = 37-*b*-16.8 kg/mol, T_g=101-*b*-122 °C respectively) was obtained from Polymer Source, Inc. (P2784-SMMA) and used as received. From literature, T_{ODT} was estimated to be in the range 100-200 °C[43, 100–103]. However, the estimated T_{ODT} is extremely sensitive to BCP molecular weight and volume fraction uncertainties, and increases with diminishing film thickness[43]. A neutral layer was specifically not utilized to ensure consistency of polymer-substrate interaction independent of grafting efficiency, and to eliminate the possibility of an unexpected high temperature interactions. A cylinder forming block ratio was chosen in order to show features regardless of BCP phase orientation on the bare silicon substrates (silicon preferentially wets the PMMA block).

5.2.2 Sample Preparation

Polymers were dissolved in toluene at a 2 wt% concentration, filtered to 0.1 microns, and spin-coated to a thickness of 94±2 nm on highly doped bare silicon (native oxide) wafers. This particular film thickness was chosen for ease of fabrication, X-ray scattering intensity, and LSA design parameters. As-spun films were confirmed to exhibit minimal initial segregation by both GISAXS and

SEM. To study the disordering behavior, some as-spun samples were annealed at 180 °C in a vacuum oven for 12 hours to develop well-ordered and fully segregated structures prior to millisecond heating. Disordered (as-spun) and ordered (oven annealed) samples were laser annealed at peak temperatures up to 550 °C for dwell times from 250 μs to 10 ms in air. Films remained thermally stable under all conditions as measured by film thickness loss.

5.2.3 Laser Spike Annealing

Millisecond thermal anneals were achieved by scanning a line-focused continuous wave CO_2 laser (λ=10.6 μm, ~90 μm by 500 μm FWHM focus) as shown in Figure 5.2a. To ensure sufficient free carrier absorption at the CO_2 wavelength, silicon wafers were heavily doped (0.01-0.02 Ω-cm). Heating duration is characterized by a dwell time, defined as the laser full-width at half-maximum (FWHM) in the scan direction divided by the scan velocity. Although polymers are generally poor thermal conductors (diffusivity $D_T \sim 10^{-4}$ to 10^{-3} cm^2/s), the characteristic thermal diffusion distance $(Dt)^{1/2}$ for a 150 μs anneal is still greater than 1.2 μm resulting in essentially isothermal conditions throughout the ~100 nm thick films. Absolute temperatures as a function of time and position were determined using gold and silicon melt and platinum thin film thermistors[118, 156]. Though inherently transient in nature, samples remain at temperatures within 5% of the peak temperature for approximately one dwell time followed by an initial quench at ~10^4-10^6 K/s. Cooling from a peak temperature near 500 °C to below 100 °C requires approximately 10 τ_{dwell} dwell times for a 10 ms LSA and ~5 τ_{dwell} for a 250 μs LSA.

A lateral gradient LSA (lgLSA) technique was used to explore the segregation behavior as a function of the peak anneal temperature. Orthogonal to the

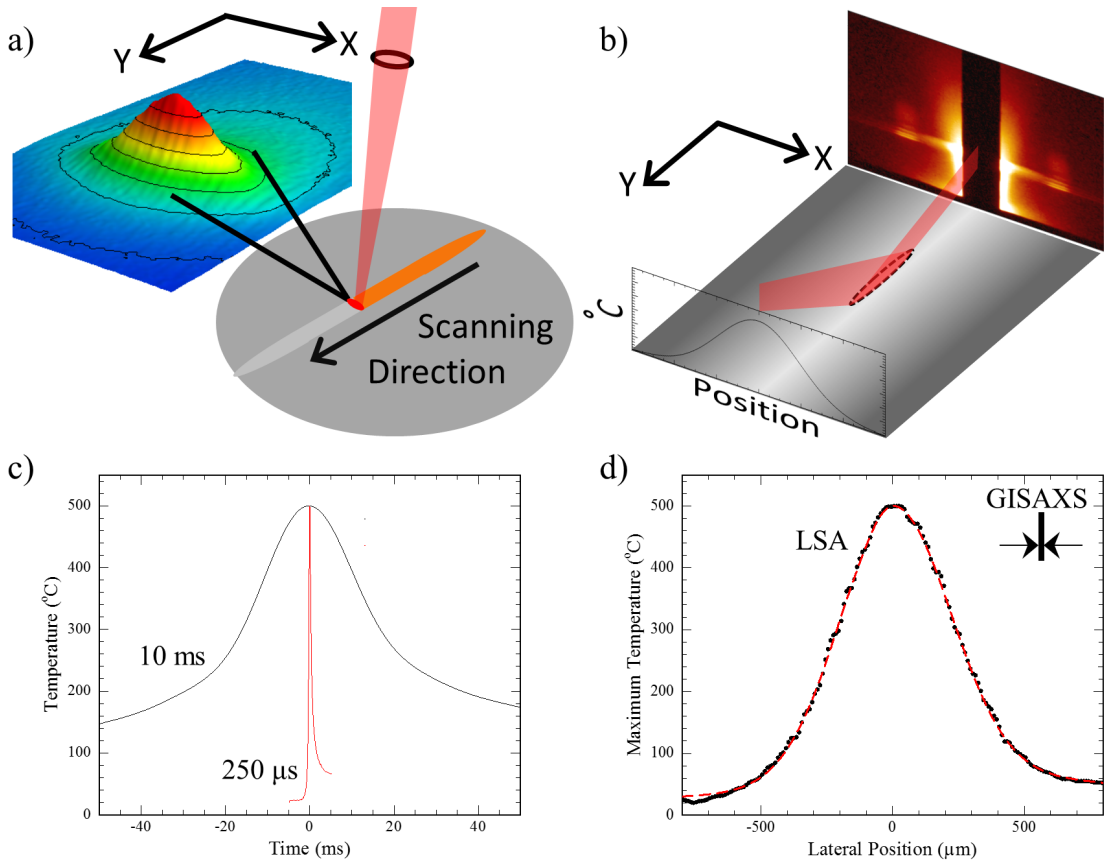

Figure 5.2: (a) Schematic of LSA geometry with a measured temperature profile in the heated zone. (b) Scale representation of GISAXS probe geometry on lgLSA area, GISAXS FWHM in x- is ~20 μm, in y- FWHM is ~8 mm. (c) Time-temperature profiles of long (10 ms) and short (250 μs) duration anneals to a peak temperature of 500 °C, and (d) 250 μs LSA spatial maximum temperature profile in the x- direction and approximate GISAXS probe width.

scan direction, the laser intensity varies approximately as a Gaussian with a 500 μm FWHM, resulting in peak annealing temperatures from ambient at the edges to a maximum at the center. Spatially resolved probes measured film properties across this orthogonal direction to develop the full temperature dependent behavior resulting in a robust, high throughput, internally referenced measurement[117]. Figure 5.2b schematically shows the μ-GISAXS measure-

ment geometry relative to the LSA spatial temperature profile. Example measured time-temperature profiles for 10 ms and 250 μs LSA anneals to a peak temperature of 500 °C are shown in Figure 5.2c. Figure 5.2d shows one measurement of the maximum temperature experienced as a function of lateral position across a 250 μs LSA with the relative μ-GISAXS beam size for comparison.

Laser scans were made over a minimum length of 20 mm to ensure adequate sample volume for GISAXS measurements. The initial and terminal transient LSA regions were cleaved off to ensure uniform annealing along the entire length of measurement volumes. In order to determine accurate temperatures, the center of the LSA scan must be precisely determined. Manual alignment was used to register the μ-GISAXS beam with the scan, with alignment typically better than 100 microns. Spatial temperature profiles were then laterally shifted to ensure overlay of the measured properties as a function of temperature from both sides of the spatial temperature profile. This provides a very sensitive internal alignment reference resulting in overall estimated temperature uncertainties of ±18 °C including both peak temperature and alignment errors.

5.3 Results and Discussion

To identify temperature regimes of interest, SEM was used to observe the expected cylindrical microstructure of an asymmetric PS-*b*-PMMA block copolymer as a function of the peak LSA temperature. Figure 5.3 shows film morphologies for initially ordered (oven annealed) samples after a 250 μs (top) and a 10 ms (bottom) lgLSA as a function of peak temperature. Reduced order was observed between 280-320 °C for the 250 μs dwell while the transition occurred between 220-240 °C for the longer 10 ms dwell. Only minimal order redevelops even at the highest temperatures for the 250 μs anneal while the 10 ms anneal de-

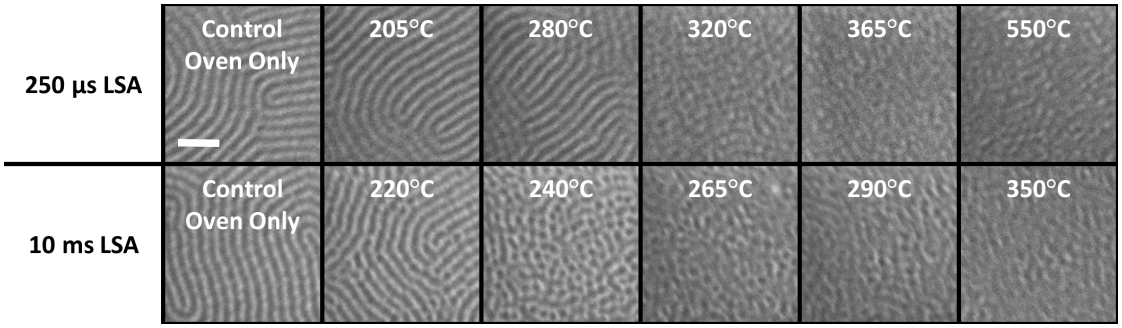

Figure 5.3: Morphology of initially ordered films as a function of the estimated peak LSA temperature. The 250 μs LSA (top row) exhibits morphology changes near 300 °C while the 10 ms LSA (bottom row) is modified near 230 °C. Scale bar 100 nm.

velops some phase segregation (difficult to discern in SEM images but readily apparent in later data) during quench from all temperatures up to damage.

Quantitative estimates of the order parameter were obtained from micro-grazing incidence small angle X-ray scattering (μ-GISAXS) experiments. PS-*b*-PMMA films developed a well-ordered structure with μ-GISAXS (Figure 5.4a) exhibiting a principle peak at a $q_{\parallel}$ of 0.23 nm^{-1} (27.3 nm bulk spacing, matching the 27.1 nm measured by SEM) extending vertically in $q_{\perp}$ due to the thin film dimension. While higher order peaks ($q_{\parallel}$ ~0.40 and above) were visible with an unfocused X-ray beam, they do not appear in these images due to short acquisition times and divergence of the capillary focused X-rays. Line cuts were taken and the signal was integrated in $q_{\perp}$ across the Yoneda-Vineyard[165, 166] band for further analysis (dashed box in Figure 5.4a). Figure 5.4b shows this integrated scattering as a function of $q_{\parallel}$ where the background was fit to Porod's law[167], $q_{\parallel}^{-4}$, functional form (blue line) and the remaining polymer signal was fit as a Gaussian peak.

For each position across the lgLSA scan, this peak scattering intensity was normalized by the background scattering intensity to account for incident beam

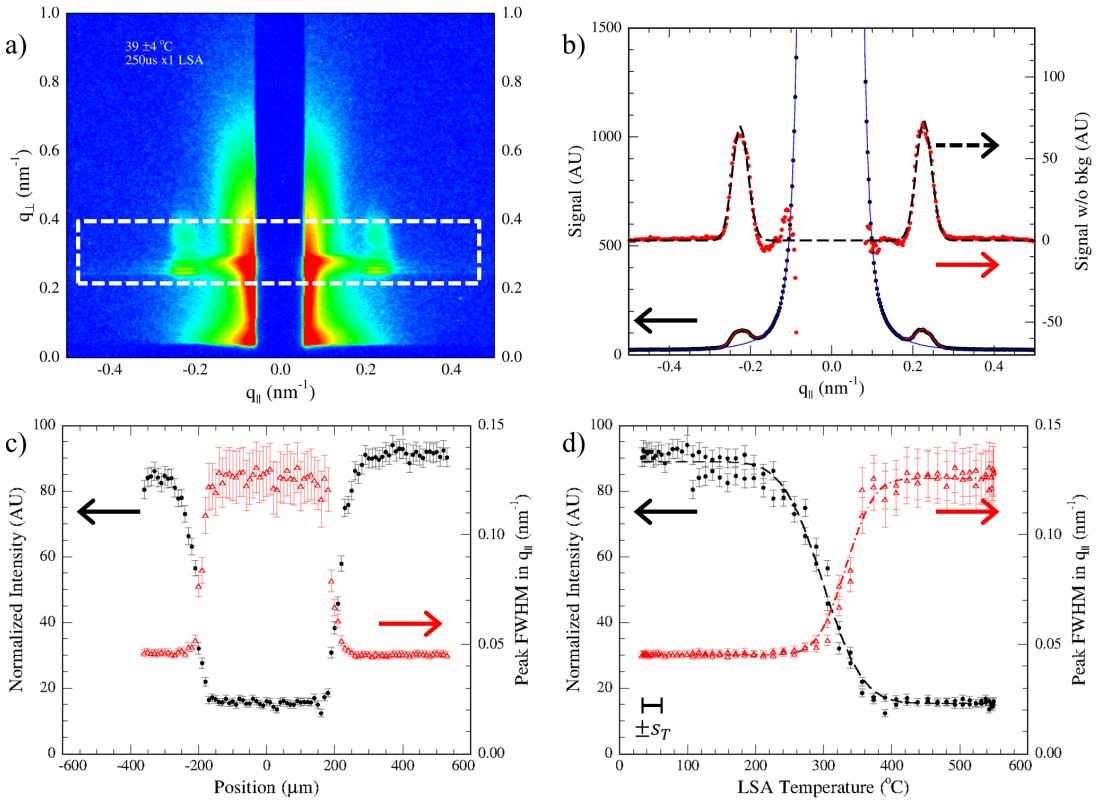

Figure 5.4: Example analysis of GISAXS data. (a) Raw data for a low temperature 250 μs LSA anneal of an initially ordered film. Dashed box indicates integration area in $q_\perp$. (b) Integrated signal values (black points), background fit (blue line), signal after background subtraction (red points), and Gaussian signal fit (dashed black line). (c) Spatial intensity and peak width as a function of the distance from the laser beam center across an lgLSA scan with T_{max} = 550 °C and (d) corresponding intensity and width as a function of anneal temperature. Uncertainties in temperature (maximum s_T = ±18 °C), intensity, and peak width are indicated.

intensity changes and small shifts in scattering geometry. As an example, Figure 5.4c shows the intensity as a function of position across a 250 μs lgLSA scan (orthogonal to the lgLSA scan direction) and as a function of peak temperature in Figure 5.4d. Under these conditions, the PS-*b*-PMMA film demonstrates a stark decrease in scattering intensity near 300 °C which is consistent with the onset of disordering.

The observed disordering at T>300 °C under 250 μs lgLSA occurs following a complex thermal history that is dependent on peak temperature, dwell and quench rate to T_g. While not directly comparable, it is instructive to consider similarities between these data and *in-situ* measurements obtained at near-equilibrium during slow ramp-rate heating. Figure 5.5a shows the conventional analysis for T_{ODT} based on the inverse scattering intensity as a function of *static* inverse temperature. With a ramp rate of 1 °C/minute (at least 10^5 times slower than any LSA anneals), these data approximate the steady-state "equilibrium," with the intersection of the low- and high-T regimes giving the equilibrium T_{ODT} of 179 °C.

Figure 5.5b plots data from the 250 μs lgLSA experiment, starting from a well ordered state, using the same protocol. As with the slow ramp data, low- and high-T regimes can be identified and one can reasonably define a *kinetically limited* disordering temperature at their intersection of 310 °C. Due to the complex thermal history, disordering actually occurs over a range of peak temperatures from ~240 °C to ~360 °C while this inverse q analysis identifies only a single effective disordering temperature. The simultaneous increase in the peak width (right axis Figure 5.5b) further suggests that this is a reasonable definition and metric for disordering behavior under LSA. The dramatic increase in this effective disordering temperature compared to T_{ODT} highlights kinetic contribu-

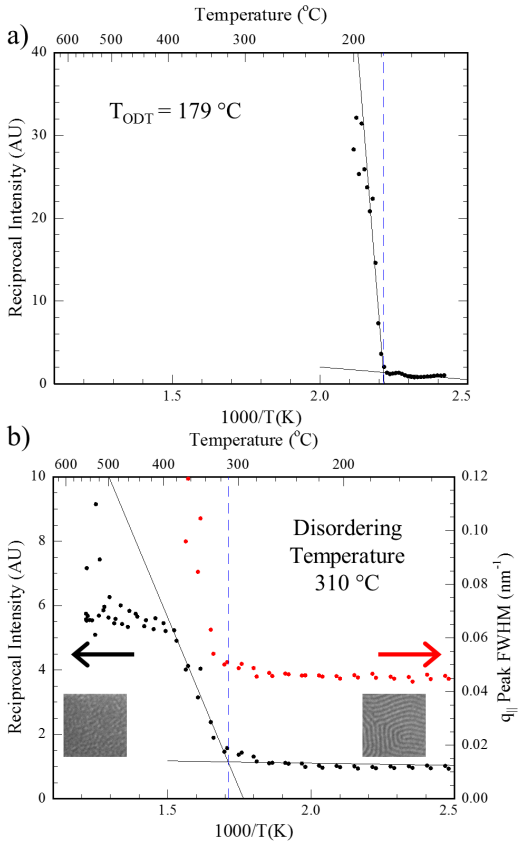

Figure 5.5: Inverse scattering intensity as a function of inverse temperature to estimate the disordering temperature. (a) *In situ* hot plate heating with an "equilibrium" T_{ODT} of ~179 °C. (b) 250 μs lgLSA indicating an effective kinetic disordering temperature of ~310 °C.

tions to the block copolymer dynamics, and is clearly higher than the true T_{ODT} due to the limited time for disordering during the short anneal duration and reordering that occurs during quench. In practice, the final residual order for LSA at this peak temperature is approximately midway between the low- and high-temperature limiting behaviors seen in Figure 5.4d. An alternative metric would be the onset of signal intensity loss, indicative of the onset of disordering, which occurs at slightly lower temperatures. Identified transition temperatures for both metrics at all dwells are included in Section 5.6.

The residual phase segregation after annealing far above this kinetic disordering temperature reflects the quench from T_{ODT} to T_g and is a strong function of the dwell time. Figure 5.6a shows the peak intensity as a function of the peak anneal temperature for 250 μs and 10 ms dwell anneals starting from both a disordered (as-spun) state, and from the phase segregated (oven annealed) state. From the disordered state, the degree of order developed after the quench increases with annealing temperature, saturating above some critical temperature. From the initially ordered state, the film begins to disorder above T_{ODT} but ultimately saturates at the same scattering intensity at high temperature. The equivalent final scattering intensity, regardless of starting state, is consistent with our model of history independent behavior for anneals at temperatures sufficiently high, and for appropriate durations, to erase any initial segregation (Figure 5.1b). In addition, repetitive scans over the same area yields the same level of this redeveloped order independent of the number of scans.

Figure 5.6b shows this redeveloped order after high T annealing as a function of the dwell time on a log scale showing a nearly linear correlation. After quench, this redeveloped order is ~20% of the fully ordered state for the 250 μs dwell and increases to ~50% for the 10 ms dwell. Extrapolation of these data suggests that full phase segregation would be developed for dwell times of 10 seconds, corresponding to a quench rate below 10 K/s, and full disorder would be retained for dwell times less than 10 μs (10^7 K/s).

From the disordered, as-spun state, the sample undergoes ordering both during heating and again during the quench (Figure 5.1). This would suggest that, for LSA anneals near T_{ODT}, the polymer would have approximately twice the ordering duration compared to samples annealed at very high temperatures. However, Figure 5.6a shows a monotonic increase in the ordering of

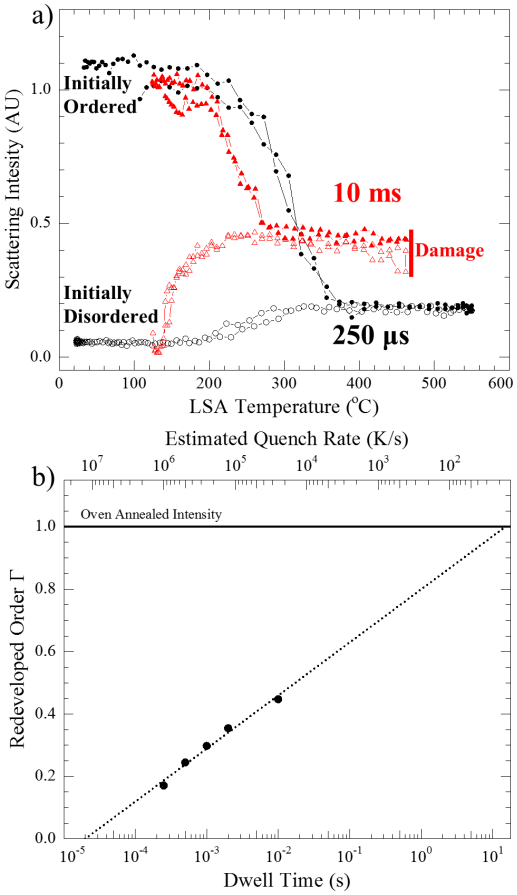

Figure 5.6: (a) Normalized intensity for short and long duration lgLSA on initially ordered and disordered films. (b) Redeveloped scattering intensity after quench as a function of dwell on a log scale.

as-spun films with no enhancement near T_{ODT}. The absence of this enhancement may suggest that ordering is significantly suppressed during the initial heating, especially on short timescales.

The origin of this behavior is unclear. At short times (250 μs), segregation may be limited by nucleation of domains within the as-spun film, which potentially lacks sub-critical nuclei due to the rapid quench from the solvated state during spinning. Significant segregation is then only established during quench from the high temperature disordered state with more nearly equilibrium com-

position fluctuations. Indeed, there is essentially no measurable redeveloped order at 250 μs, even for a peak temperature of 220 °C, far above T_g. At longer times (10 ms) however, growth of segregated domains from the initial configuration does occur starting near T_g (~110 °C) and continuing up to T_{ODT} (179 °C). Dwells between 250 μs and 10 ms exhibit behaviors between these two limiting cases.

The detailed kinetic behavior as a function of the peak annealing temperature and dwell time can be summarized in a "phase map," as shown in Figure 5.7. For an initially segregated film (Figure 5.7a), the initial order is retained for all temperatures below T_{ODT} and, at short dwells, to substantially higher temperatures ($T_{disorder}$ =T_{ODT}+70 °C for a 250 μs dwell), identified by the onset of scattering intensity reduction. At higher temperatures, the initial order is partially lost as disordering and ordering compete during the heat and quench phases (transitional order regime). Above a critical temperature, the resultant order is dependent solely on the quench rate as any initial order will be lost during heating.

This behavior is only minorly modified when annealing from an initially disordered state (Figure 5.7b). At a critical temperature above the glass transition, T_{order}, the final scattering intensity is observed to increase. This marks the lower boundary of the transitional order regime. In addition, as there is no order that must be destroyed before entering the quench rate determined regime, the upper bound occurs at a lower temperature. As noted earlier, there is evidence that the retention of the initial state may be divergent in temperature as the dwell approaches 10 μs. Equally, as the dwell moves into conventional hot plate regimes, the boundaries of the transitional order regimes asymptotically approaches T_g and T_{ODT}.

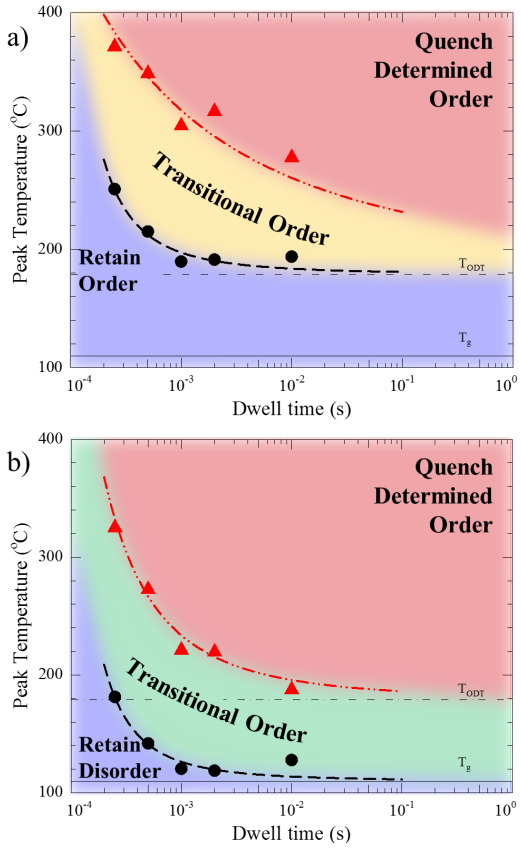

Figure 5.7: BCP phase map after lgLSA from (a) initially phase segregated material and (b) initially disordered, as-spun material. Dashed lines are guides to the eye only. All measured values and methodology are included in Section 5.6.

An intriguing characteristic of this phase map is the sharp increase in disordering temperature at short timescales, which must arise from some kinetic limit to the polymer motion. This limit may be related to polymer diffusivity or alternatively to an induction time. Conceptually, an induction time would represent the minimum heating period required to move to a new configuration. However, multiple anneals at 250 μs, below the observed disordering onset temperature (~250 °C), show a continuous shift in disordering behavior suggesting a diffusion related explanation.

The observed disordering temperature convolves polymer diffusivity, seg-

regation driving force, and experimental sensitivity. Since GISAXS is most sensitive to electron density contrast[77], disorder can only be observed once the polymer has mixed sufficiently. Local perturbations of interfaces would be difficult to observe by GISAXS, accounting for the cumulative effects of repeated anneals.

The diffusivity can be estimated from the time required to perturb the concentration of the center of a cylinder. Fickian diffusion for cylindrical geometry requires a thermal dose of $Dt/r^2 \approx 0.085$ to perturb the cylinder center concentration by 10% (an arbitrary sensitivity)[168]. The effective diffusivity required to modify the PMMA cylinders for a particular dwell time is then simply $D=0.085r^2/\tau_{dwell}$. For a cylinder to cylinder spacing of 27.3 nm, the approximate cylinder radius was estimated at 6.1 nm yielding a required diffusivity of $3.2\text{x}10^{-11}$ and $1.3\text{x}10^{-10}$ cm^2/s for 1 ms and 250 μs dwell times respectively.

From Figure 5.7a, these diffusivities correspond to peak temperatures near 200 °C and 250 °C respectively. As a comparison, the interdiffusivity of polystyrene at similar molecular weights[169] are $3\text{x}10^{-11}$ cm^2/s at ~200 °C and ~(2-4)x10^{-10} cm^2/s near ~250 °C. This agreement suggests that diffusion is indeed responsible for the observed kinetic suppression of disordering at short dwells. Though appropriate for a first order approximation, this estimation neglects the potentially significant effects from concentration/chemical potential dependent diffusivity.

From a practical standpoint, these phase maps are a valuable tool as they embody the full kinetics of BCP phase segregation in the deeply quenched, metastable, regime. This regime, previously inaccessible and essentially unexplored, can now be quantitatively described on sub-millisecond timescales and at temperatures far above both T_g and T_{ODT} providing a critical test of phase

segregation models, especially as molecular weights and interaction potentials (χ) are increased. In addition, as both ordering and disordering kinetics diverge at heating durations below one millisecond, it is also now possible to retain metastable order to significantly higher temperatures. This can accelerate kinetics for other chemical or structural alignment processes, such as directed self-assembly.

5.4 Conclusions

The ordering and disordering kinetics of cylinder forming PS-*b*-PMMA on sub-millisecond timescales (250 μs to 10 ms) at temperatures up to 550 °C was investigated using the lateral gradient laser spike annealing method coupled with micro-beam grazing incidence small angle X-ray scattering. The use of sub-millisecond heating allowed measurements in kinetically limited regimes and at temperatures far in excess of normal thermal decomposition limits. From initially phase segregated films, the onset of observed disordering is delayed by over 70 °C for short duration anneals due to limited polymer diffusion and begins at T_{ODT} for dwells greater than ~10 ms.

Annealing to temperatures sufficiently high, and for sufficient times, results in quenches from a fully disordered state leading to a history independent final structure. The final redeveloped phase segregation is then determined primarily by the time required to quench between T_{ODT} and T_g. This behavior was demonstrated starting from fully ordered and fully disordered films. Data suggests that this system will retain the initial state to extreme temperatures for quench rates exceeding 10^7 K/s (10 μs dwell), and will develop full phase segregation for quench rates below 10 K/s (10 s dwell). The full kinetic behavior can be represented in "phase maps" relating order development from initially

mixed or segregated states as functions of time and temperature. This allows for prediction of the final phase segregation across many orders of magnitude of anneal durations.

The unique characteristics of laser spike annealing grants access to previously inaccessible regimes in polymer characterization and processing. This broadly applicable technique can be used on a wide range of polymer systems with minimal concern for conventional thermal decomposition limits. For temperature sensitive high χ or high molecular weight systems, this opens up the potential to experimentally identify T_{ODT}, and to critically test segregation models across a broad range of time and temperature regimes. On sufficiently short times, LSA also enables a new regime of processing at temperatures far above T_g and T_{ODT} while retaining order in BCP systems. This demonstrates the potential for spatially templated chemistry at high temperatures in such ordered systems. Further exploration of this regime is certain to provide exciting opportunities for novel chemistries and hierarchical schema.

5.5 Acknowledgments

The authors wish to thank EMD Performance Materials (Merck KGaA) for supplying materials and discussions, Professor Ulrich Wiesner for useful discussions and equipment, Clemens Liedel for analytical assistance, and Ruipeng Li and Detlef-M Smilgies for experimental and analytical GISAXS support. AGJ acknowledges the Department of Defense (DoD) for financial support through the National Defense Science & Engineering Graduate Fellowship (NDSEG) Program.Work was performed in part at the Cornell NanoScale Facility (CNF), a member of the National Nanotechnology Coordinated Infrastructure, which is supported by the National Science Foundation (Grant ECCS-1542081), at the

Cornell Center for Materials Research (CCMR) shared facilities which are supported through the NSF MRSEC program (DMR-1120296), and at the Cornell High Energy Synchrotron Source (CHESS) supported through the NSF and NIH/NIGMS via award DMR-1332208.

5.6 Supporting Information

Phase Map Temperature Identification

Figure 5.8a shows scattering intensity as a function of the peak annealing temperature for the 250 μs LSA. The boundaries for the phase map were determined as the intersection of linear extrapolation within each temperature regime. Figure 5.8b shows the traditionally used reciprocal intensity method which identifies an effective kinetic disordering temperature, $T_{ODT,eff}$, between the onset of decreased signal intensity and the history independent temperature. Figures 5.9–5.12 show data for 500 μs to 10 ms respectively.

Similarly, Figure 5.13 shows the identification of T_{ODT} for hot plate anealing. Due to the slow heating rate (1 °C/min), these data exhibit a much steeper slope and hence a well define T_{ODT}. In contrast, LSA data show much more gradual changes in the final scattering intensity and the $T_{ODT,eff}$ extracted by this method becomes less precise. In lieu of the traditional inverse scattering intensity method, the first onset of GISAXS scattering intensity loss was taken as indication of the onset of disordering ($T_{disorder}$). The identified temperatures are summarized in Table 5.1 and were used to create the phase maps. Note that the uncertainty in the intersection temperature listed in Table 5.1 does not include the additional ±18 °C systematic temperature uncertainty for these LSA data. Figure 5.14 shows the phase maps from the identified temperatures in Table 5.1.

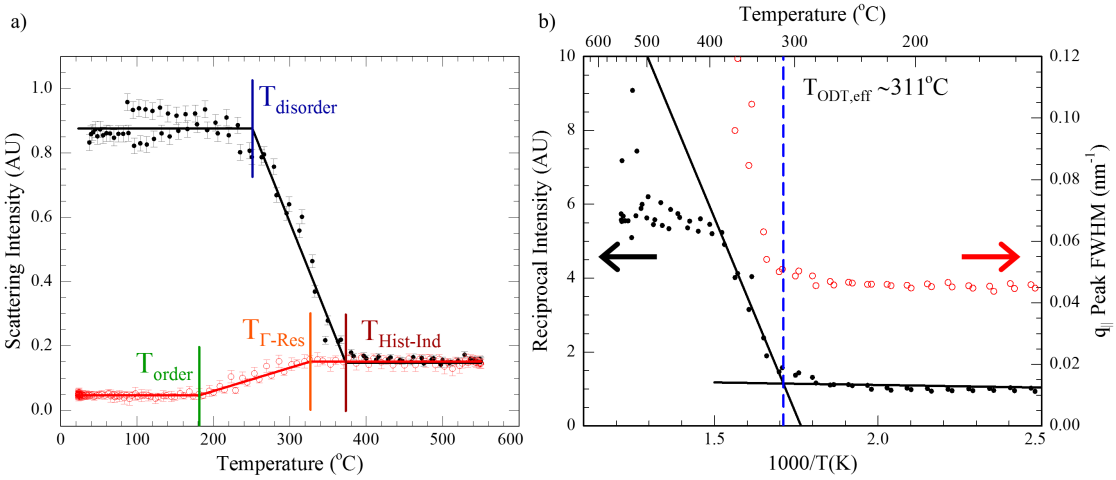

Figure 5.8: Identification of critical temperatures by linear extrapolation for the 250 μs LSA for (a) $T_{disorder}$, $T_{History-Independence}$, T_{order}, $T_{\Gamma_{residual}}$, and (b) $T_{ODT-effective}$.

Figure 5.14a includes the additional identified $T_{ODT,eff}$ which shows a different absolute disordering temperature but follows the same trend.

It should be noted that although all films remained stable for all conditions as measured by film thickness loss, distinct damage is apparent for 1 ms and longer anneals at the highest temperatures where GISAXS scattering intensity signal is lost. This degradation did not impact identification of transition temperatures as it occurred beyond the region of interest for all anneals.

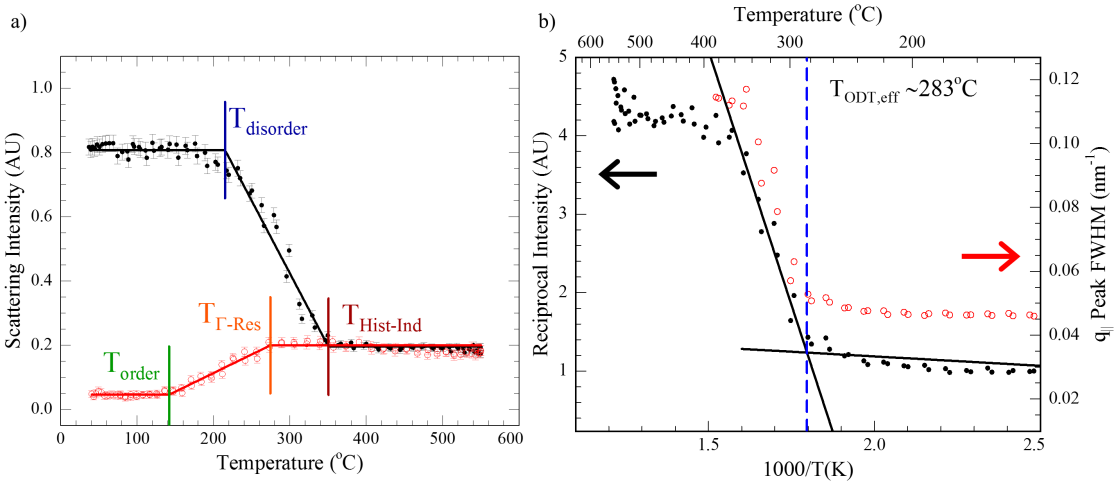

Figure 5.9: Identification of critical temperatures by linear extrapolation for the 500 μs LSA for (a) $T_{disorder}$, $T_{History-Independence}$, T_{order}, $T_{\Gamma_{residual}}$, and (b) $T_{ODT-effective}$.

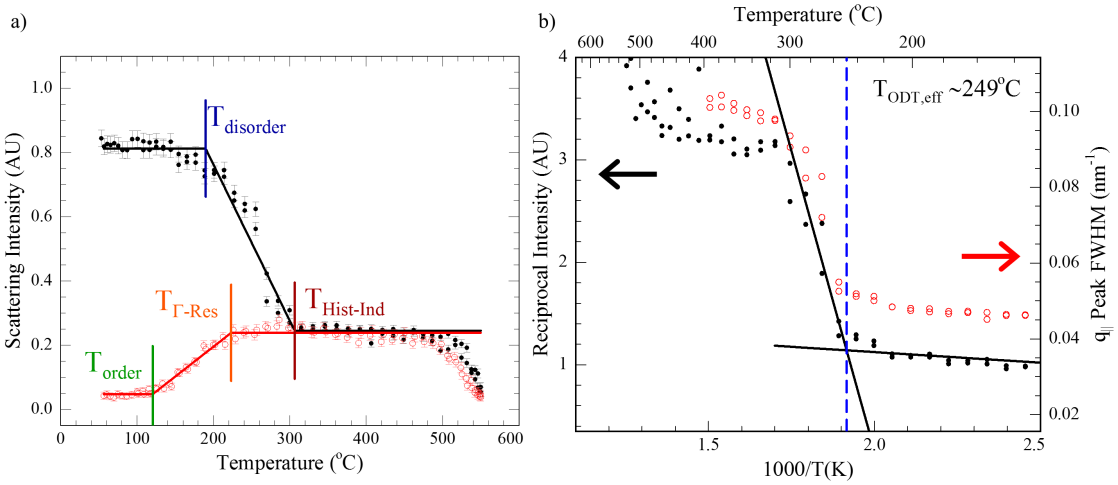

Figure 5.10: Identification of critical temperatures by linear extrapolation for the 1 ms LSA for (a) $T_{disorder}$, $T_{History-Independence}$, T_{order}, $T_{\Gamma_{residual}}$, and (b) $T_{ODT-effective}$.

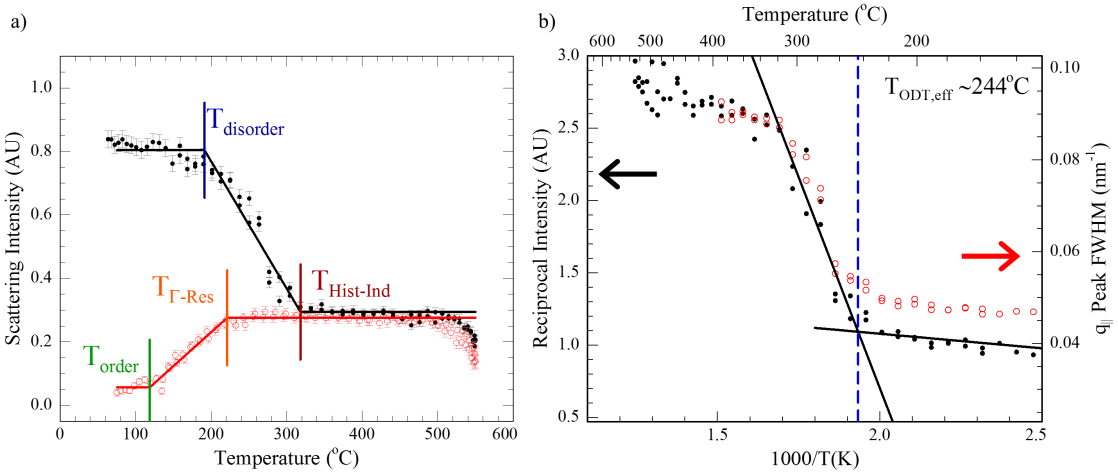

Figure 5.11: Identification of critical temperatures by linear extrapolation for the 2 ms LSA for (a) $T_{disorder}$, $T_{History-Independence}$, T_{order}, $T_{\Gamma_{residual}}$, and (b) $T_{ODT-effective}$.

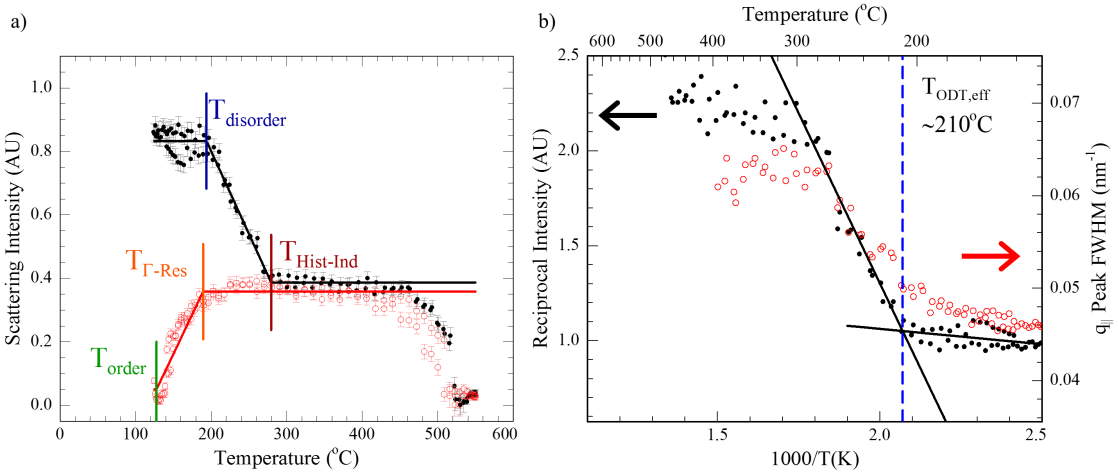

Figure 5.12: Identification of critical temperatures by linear extrapolation for the 10 ms LSA for (a) $T_{disorder}$, $T_{History-Independence}$, T_{order}, $T_{\Gamma_{residual}}$, and (b) $T_{ODT-effective}$.

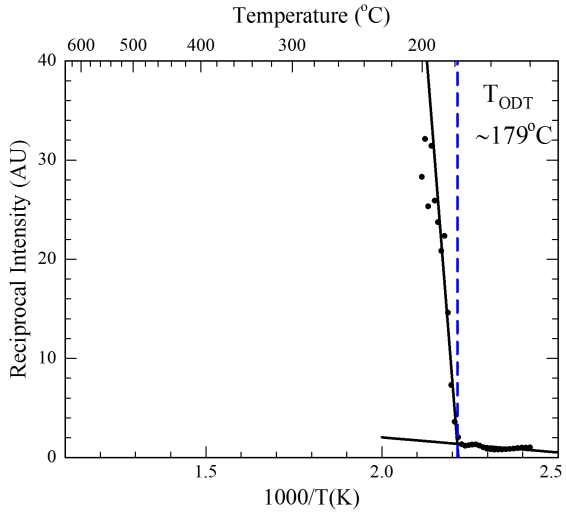

Figure 5.13: Identification of T_{ODT} for *in-situ* hot plate annealing.

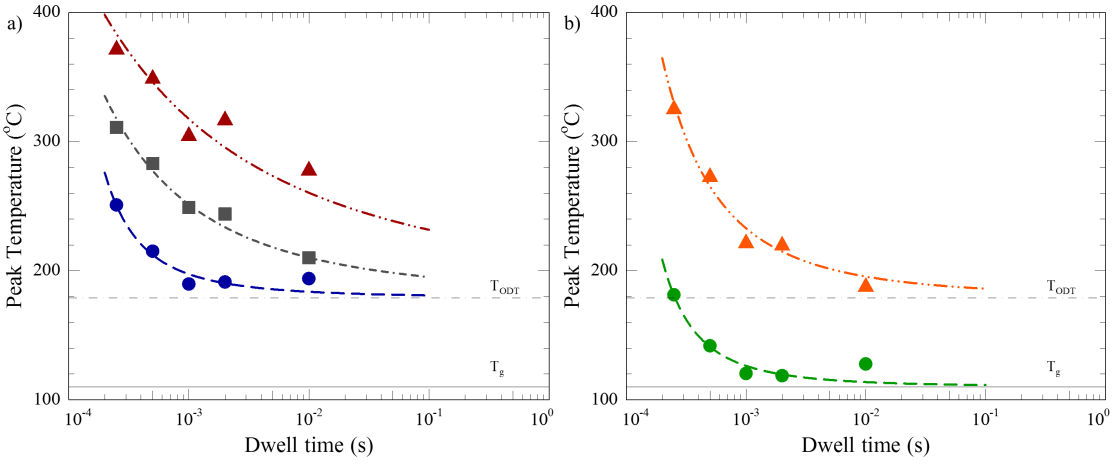

Figure 5.14: Phase map after lgLSA from (a) initially phase segregated material showing $T_{disorder}$ (dashed curve, blue circles), $T_{ODT,eff}$ (dash-dash-dot curve, grey squares) , and $T_{Hist-Ind}$ (dash-dot-dot curve, red triangles). (b) Phase map from intially disordered, as-spun material showing T_{order} (dashed curve, green circles) and $T_{\Gamma_{residual}}$ (dash-dot-dot curve, orange triangles). Lines to guide the eye only.

Table 5.1: Summary of critical temperatures identified for phase segregation and disordering.

Anneal Duration	$T_{disorder}$ ±2 °C	$T_{ODT,eff}$ ±5 °C	$T_{Hist-Ind}$ ±3 °C	T_{order} ±3 °C	$T_{\Gamma_{residual}}$ ±3 °C	$\Gamma_{residual}$
250 μs	251	311	373	181	326	0.171
500 μs	215	283	351	142	275	0.245
1 ms	189	249	306	120	223	0.298
2 ms	191	244	318	119	221	0.355
10 ms	194	210	279	<128	189	0.448
Hot Plate	T_{ODT}	179±2 °C	-	T_g	-	<0.025

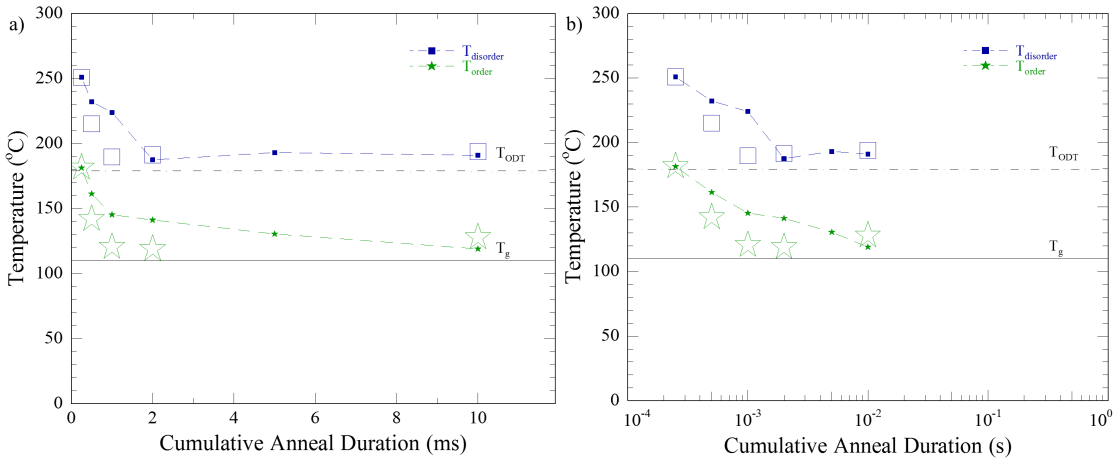

Figure 5.15: Time dependence of disordering and ordering onset temperatures for consecutive 250 μs anneals (closed symbols, line) compared to single LSA anneals of longer duration (open symbols) shown on (a) linear time scales and (b) log time scales.

CHAPTER 6

MILLISECOND BCP SEGREGATION KINETICS IN ADDITIONAL BCP SYSTEMS

6.1 Introduction

In order to fully understand the short time segregation behavior of block copolymers in general, several additional steps are necessary. First, the segregation kinetic behavior must be understood with regard to the polymer size. The polymer molecular weight, or degree of polymerization, strongly affects the segregation kinetics by determining the stable phase, the driving force ($\Delta\chi N$) for segregation, and the polymer mobility (diffusivity). Secondly, the kinetics will depend entirely on the monomer groups. Having blocks with different T_g's will impact the system mobility, which also then depends on the degree of segregation. Some proposed and initiated research is discussed in this chapter while early efforts to model this process using a finite elements approach is discussed in Chapter 7.

In order to expand this dissertation work to a more generalized systems, two paths are suggested and preliminary data are reported. First, segregation studies of PS-*b*-PMMA are extended to additional molecualr weights which allows deconvolution of diffusion and driving force components. Second, various chemistries, such as poly(isoprene)-*block*-poly(styrene) (PI-*b*-PS), which contain both high T_g and low T_g blocks provides insight into how T_g contrast affects the segregation and mixing kinetics. The PI-*b*-PS system, and several like it, are also of interest for DSA as they exhibit a higher χ compared to PS-*b*-PMMA. Finally, I will comment on several systems as they pertain to DSA investigations under LSA.

6.2 High Molecular Weight Poly(styrene)-*block*-poly(methyl methacrylate) (PS-*b*-PMMA)

[1] For preliminary studies of high molecular weight BCP phase segregation, cylinder forming PS-*b*-PMMA (M_n = 57-*b*-25 kg/mol) was obtained from Polymer Source, Inc. (P8269-SMMA) and used as received. In comparison, Chapter 5 utilized the much smaller 37-*b*-16.8 kg/mol polymer. As the bare silicon surface is preferentially wetted by the PMMA block, a cylinder forming morphology was chosen in order to show features regardless of BCP phase orientation. The polymer was dissolved in toluene to create a 2 wt% solution and spun coat to a target thickness of 100 nm on highly doped bare silicon (native oxide). No attempt was made to match the thickness to a multiple of the BCP periodicity; for these samples, we were interested only in identifying the phase segregation. As-spun samples were annealed at temperatures from 300-620 °C for dwell times from 250 μs to 10 ms utilizing the CO_2 laser. For comparison purposes, control samples were annealed in a vacuum oven at 180 °C for 24 hours.

SEM images were obtained both directly after annealing and after a short oxygen plasma etch to enhance contrast. Film morphologies were independent of the etch time indicating uniformity through the film thickness and subsequent images were generally taken after a 15 second oxygen plasma etch to preferentially remove the PMMA block.

[1] Portions of this section were published as: "Control of ps-b-pmma directed self-assembly registration by laser induced millisecond thermal annealing," A. G. Jacobs, B. Jung, C. K. Ober, and M. O. Thompson, *Proc. of SPIE*, **2014**, v. 9049, 90492b-1. DOI 10.1117/12.2046513.

6.2.1 Phase Segregation During LSA

Due to the higher polymer molecular weight, two effects were expected. First, T_{ODT} will increase due to the higher degree of polymerization coupled with the weak temperature dependence of χ reported in the literature[43, 100–103, 170–172]. For the phase maps after lgLSA shown in Figure 5.7, this should move all of the transition boundaries to higher temperatures. Secondly, polymer diffusivity is reduced at a given temperature due to the larger polymer size and resulting entanglements, potentially shifting identified phase boundaries to longer times or changing the curvature of these boundaries. Since the increase in T_{ODT} also increases the temperatures of interest (and diffusivity at temperature), the net effect could in principle shift boundaries to either shorter or longer times depending on the relative impact of each term.

For as-spun films annealed by LSA to peak temperatures of 300 to 550 °C with a 10 ms dwell, SEM images show significant structure development even at the lowest temperature of 300 °C with increasing structure for temperatures up to 420 °C (Figure 6.1). At the highest temperatures, the morphology becomes comparable to that of oven annealed samples. Above 450 °C, the morphology becomes invariant up to the damage threshold. This reflects a morphology that is only dependent on the quench rate and yields a rough identification of T_{ODT} for this molecular weight. This temperature, ~435±15 °C, is significantly higher than that observed in Chapter 5 for the lower molecular weight system of ~180-200 °C.

For LSA annealed as-spun films, the onset of this temperature independent morphology (~T_{ODT}) occurs at approximately the same temperature (to the precision under SEM of 50 °C) for all dwells. However, the "spot" size and "definition" of the segregated regions scales with the dwell, and hence inversely with

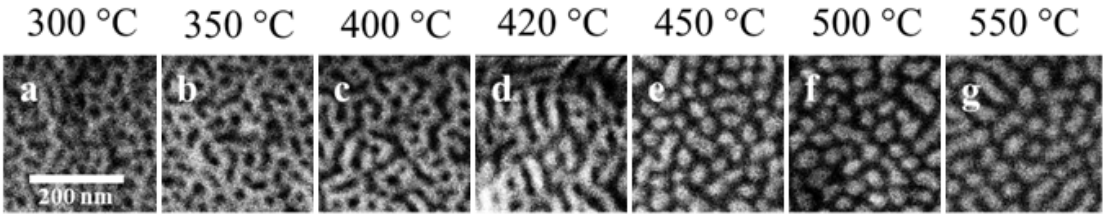

Figure 6.1: Cylinder forming PS-*b*-PMMA films laser annealed for 10 ms to peak temperatures of (a) 300 °C (b) 350 °C (c) 400 °C (d) 420 °C (e) 450 °C (f) 500 °C and (g) 550 °C.

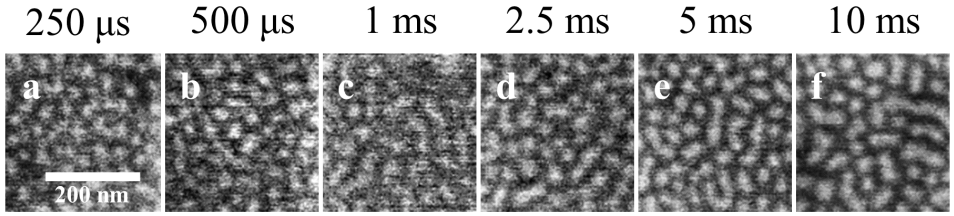

Figure 6.2: Isothermal segregation behavior of cylinder forming PS-*b*-PMMA as a function of dwell time at 520 °C for (a) 250 μs (b) 500 μs (c) 1 ms (d) 2.5 ms (e) 5 ms and (f) 10 ms.

the quench rate. This behavior, shown in Figure 6.2, is consistent with the observed GISAXS quench dependent order development[156] in lower molecular weight PS-*b*-PMMA (Chapter 5).

To initially explore the limits of phase segregation at this molecular weight, studies at a constant peak temperature of 420 °C (just below the identified T_{ODT}) were performed at dwell times from 250 μs to 10 ms (Figure 6.3 a-f). These data indicate that phase segregation requires approximately 2-5 milliseconds for development of the cylinder structures. Increasing the dwell further refined this segregation with a 10 ms LSA achieving patterns of equal connectivity and similar structure to oven annealed samples. This shows that the polymer diffusivity at 420 °C allows significant structure evolution and is not severely limited by

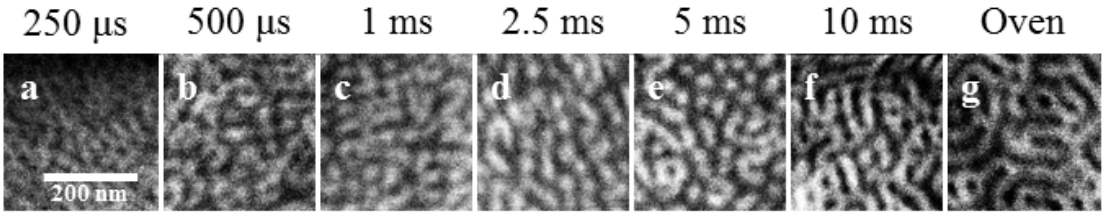

Figure 6.3: Isothermal segregation behavior of cylinder forming PS-*b*-PMMA as a function of dwell time at 420 °C for (a) 250 μs (b) 500 μs (c) 1 ms (d) 2.5 ms (e) 5 ms and (f) 10 ms. (g) Reference oven annealed substrate for 24 hours at 180 °C in vacuum.

entanglements. Even at this molecular weight, 10 ms appears to be sufficient to fully order and segregate a limiting morphology comparable to the long term oven anneals.

Estimation of the expected T_{ODT} from literature values is challenging. There are no direct experimental determinations for T_{ODT} at these molecular weights, nor has χ been measured at the 400 °C temperatures observed in this work. Applying typical corrections for finite chain lengths and fluctuation effects[30, 31, 41], the cylinder morphology (for N~800) would be expected to disorder at $\chi N \leq 21$, or $\chi \leq 0.0263$. Literature values for χ vary widely with some measurements suggesting that χ never falls to or below this critical $\chi = 0.026$ value for any temperature[101, 102, 171, 172]. Other measurements suggest a T_{ODT} between ~330-530 °C[100, 170]. While these values neglect film thickness effects[43], the correction is expected to be small (~10 °C) relative to the large difference in reported χ values.

6.2.2 PS-*b*-PMMA Conclusions

Under LSA annealing, BCP phase segregation for a high molecular weight (82 kg/mol) cylinder forming PS-*b*-PMMA was shown to occur on 2-5 ms

timescales at 420 °C. Above 420 °C, the segregation behavior changes markedly suggesting this range for the equilibrium T_{ODT}. This compares with literature estimates of T_{ODT} ranging from at least 330 °C to never occurring. Direct measurement of the T_{ODT} in this system demonstrates the potential of LSA induced segregation to study ultra-high molecular weight PS-*b*-PMMA polymers, establishing a better understanding of the molecular weight dependent effects of driving force and mobility.

6.3 Dissimilar T_g Block Copolymers

An interesting consequence of phase segregation in BCP systems when the blocks exhibit significantly different T_gs is that the material viscosity and diffusivity are dependent upon the segregation. When fully segregated and at an intermediate temperature, the low T_g polymer is mobile but constrained by the vitrified high T_g block. The high T_g segments act then as anchors to impede mass transport. But when disordered, the low T_g segments act as a plasticizer/solvent to the high T_g segments reducing the low frequency viscosity of the system. This is the underlying mechanism that permits the use of rheology to measure order-disorder and order-order transitions[39, 173–175].

This complex dependence of the BCP mobility and viscosity on the degree of ordering further complicates the short time segregation transition behavior. Ordering kinetics from a fully disordered state would likely be enhanced due to the high mobility of the mixed (plasticized) configurations. However, kinetics will slow as order is developed and will be most retarded from the fully ordered state. This may work to suppress the kinetics of the ODT to be similar to the low mobility block by forcing it to interact, or it could allow for faster kinetics, similar to the high mobility block, by allowing the low T_g block to act as a plasticizer.

The author expects that full ordering will not be achieved on any timescale for polymers with T_{ODT} below the highest T_g as the volumes of that block will be vitrified without incorporation of the low T_g block. Similarly, for T_{ODT} above both T_gs, the final ordering or initial disordering rate is likely to be limited by the lowest mobility block with commensurately faster kinetics when not fully ordered.

One additional question is whether this can be directly observed in GISAXS and how this may manifest in ordering/disordering under LSA. X-ray scattering is primarily sensitive to the total electron density contrast and only secondarily to the interface structure (roughness and abruptness) between the two volumes suggesting that the nuances may be small and difficult to observe.

6.3.1 Poly(isoprene)-*block*-poly(styrene) (PI-*b*-PS or IS) Preliminary Data

To elucidate the affect of T_g differences on the short time segregation behavior, many systems can be utilized. PI-*b*-PS is one good choice as it is readily synthesized[176], is well characterized[46], and has a large disparity in T_g with $T_{g,PI}$=~−60 °C and $T_{g,PS}$=~+100 °C. Multiple cylinder forming (f_{PS}=0.67 or f_{PS}=0.33) polymers with molecular weights from 24.8 kg/mol to 213 kg/mol were synthesized by sequential anionic polymerization[176]. Most of these materials were specifically synthesized with high styrene content to enable easier quantification at room temperature when the majority block is vitrified.

All polymers were dissolved in toluene from 1-10 wt%. Segregation studies were performed on samples spun at 500 to 5000 RPM to achieve a target thickness of 500 nm. This thickness was chosen to reduce surface effects to produce

"bulk" like behavior, to provide larger signal for shorter X-ray acquisition times, and to maintain a thermally thin film for all LSA dwell times. Additionally, the most mobile PS rich polymer (24.8 kg/mol) was also studied by GISAXS as a function of the spin rate (40 to 5000 RPM) to understand structure evolution fast and slow solvent quenches and to establish the initial order prior to LSA in this highly mobile system.

Table 6.1: Summary of PI-*b*-PS polymer molecular weights and estimated T_{ODT} from literature with comparable measured T_{ODT} values. *Note: polymer R periodicity is reported for oven annealed, well-ordered, structure and not as-spun films.

Label	Comments	M_N (kg/mol)	f_{PS}	PDI	T_{ODT}^{est} (°C)	q* (nm^{-1})	d (nm)
L (IS–6)	PS Rich	24.8	0.67	1.03	116	0.38	17
R (IS–9)*	PS Rich	47.2	0.67	1.04	232	0.21	30
M (IS–1)	PS Rich	50.7	0.67	1.03	243	0.22	29
N (IS–3)	PS Rich	87.2	0.67	1.03	313	0.14	45
P (IS–2)	PS Rich	120	0.67	1.04	343	0.10	63
Q (IS–7)	PS Rich	213	0.67	1.06	388	0.075	83
S (IS–4)	PI Rich	43.9	0.33	1.03	242	-	-
T (IS–5)	PI Rich	73.5	0.32	1.03	310	-	-
[177]	T_{ODT}^{bulk}=225 °C $T_{ODT}^{980\,nm}$=234 °C	42.4	0.33	1.04	237		~24

Table 6.1 summarizes the PI-*b*-PS polymers under investigation as well as the estimated T_{ODT} and initially measured as-spun periodicity. In contrast to PS-*b*-PMMA, PI-*b*-PS exhibits a significant and readily measured temperature dependence to the Flory-Huggins interaction parameter providing more precise extrapolation at higher temperatures. These reported χ values[178–180] allow estimations that agree well with literature reported values[177] in similar off-stoichiometry systems.

Solvent Quench Effects

All polymers exhibited some GISAXS primary peak scattering in as-spun films indicating that partial segregation does occur during spin coating and the associated solvent quench. Due to the 500 nm target film thickness and dilute polymer solutions used in this work, low spin speeds (<1000 RPM) were required for many polymer solutions potentially allowing for structural organization despite the higher molecular weight and lower mobility. The higher mobility lowest molecular weight system studied below did indeed exhibit significant ordering even at spin speeds of 5000 RPM.

To establish the spin rate dependence, a series of films were tested at various spin speeds for the related mobile PI-*b*-PS polymer system. Spin conditions and resulting film thicknesses are summarized in Table 6.2. The duration of each spin was designed to be sufficiently long for films to dry, to ensure the solvent was mostly removed, all samples were also subjected to a final spin at 2500 RPM for 15 seconds. To avoid any thermally induced post-spin order development, no post-spin bake was performed.

Figure 6.4 shows GISAXS spectra as a function of spin conditions for this low molecular weight PI-*b*-PS system. All exhibit a weak Debye-Scherrer ring which developed into substantial secondary peaks at low spin speeds. While not nearly as organized as after oven annealing, the addition of the low T_g minority block does significantly enhanced the formation of initial phase segregation after spin coating compared to PS-*b*-PMMA. Fully disordered films, ideal for these kinetic studies, could not be achieved for this molecular weight at the highest speeds and accelerations possible with the existing hardware. This observation, and the weak scattering observed for all as-spun films, made it impossilbe to access the fully disordered starting state as used in the previous

Table 6.2: Summary of PI-*b*-PS polymer spin conditions and resultant film thickness. *The first series established the spin speed dependence with the second series at conditions yielding approximately constant thickness for the subsequent studies. As these studies were completed ~2 weeks apart, exact thicknesses vary slightly due to changes in polymer solutions and eivionmental conditions.

Polymer	Sol. Conc. (wt%)	Spin Speed (RPM)	Time (s)	Accel. (RPM/s)	Thickness (nm)
Spin Series					
L (IS–6)*	10	40	600	500	5500±200
	10	100	300	500	3400±100
	10	250	300	5000	1680±20
	10	500	120	5000	1190±10
	10	1000	60	5000	827±3
	10	2000	60	5000	590±2
	10	5000	60	5000	399±2
	10	5000	60	2000	475±5
MW Series					
L (IS–6)*	10	5000	60	2000	525±2
R (IS–9)	5	110	120	2000	540±8
M (IS–1)	5	550	60	2000	503±3
N (IS–3)	5	750	60	2000	560±2
P (IS–2)	5	1050	60	2000	495±5
Q (IS–7)	5	1700	60	2000	500±5
S (IS–4)	5	750	60	2000	483±3
T (IS–5)	5	1200	60	2000	500±3

studies.

LSA Ordering and Disordering of PI-*b*-PS

To probe the thermal disordering kinetics, samples were annealed in a vacuum oven for 12 hours at 150 °C to produce well segregated structures. However, since PI is much more oxygen sensitive than either PS or PMMA, initial anneals failed since the sample were loaded into a hot oven and hence degraded be-

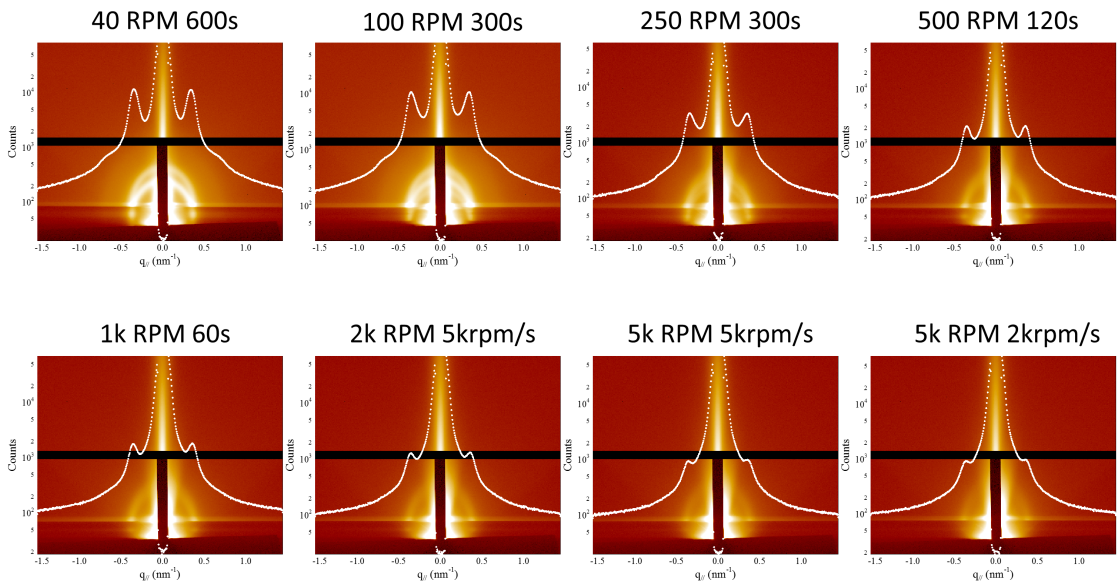

Figure 6.4: Series of spin-coating speeds for rapid solvent quench of 24.8 kg/mol PI-*b*-PS cylinder forming polymer.

fore vacuum was achieved. For subsequent anneals, samples were placed in the oven, pumped to vacuum (<10 mBar) and purged with nitrogen (>0.7 Bar) three times, before evacuating and heating to the target temperature. Quench was performed following a similar protocol where samples were cooled under vacuum to below 100 °C, and then under nitrogen purge to below 40 °C before opening to ambient.

In addition to changes in the oven annealing protocol, samples were also stained with heavy metals to improve scattering contrast and reduce GISAXS acquisition times. Samples of PI-*b*-PS were stained with OsO_4 while PS-*b*-PMMA could have been stained with RuO_4. The initial work on PS-*b*-PMMA specifically chose to avoid staining to avoid any induced swelling or movement of the polymer structure. However, subsequent studies of stained and unstained, well segregated and as-spun samples, showed no significant shift in periodicity or structure in the PS-*b*-PMMA and PI-*b*-PS systems. As staining

was necessary to reduce acquisition times and enable this ambitious study of 8 molecular weights of PI-*b*-PS, all GISAXS acquisitions were obtained on OsO_4 stained samples for consistency after verification that the morphology doesn't change with staining. Some minor concerns regarding staining are noted in Section 6.6.

Due to the process development and limitations of beam availability at CHESS during upgrades over the 2016 annum, only preliminary data are shown below. While most of the initial oven anneals failed, one sample (polymer R, 47.2 kg/mol) exhibited a well ordered structure after oven annealing. This particular sample survived likely due to serendipity as it was at the top of stacked samples in glass petri dishes during the oven anneal. This additional distance from hot surfaces likely delayed heating until the oxygen partial pressure was reduced sufficiently to ensure survival. Additional samples of this polymer annealed on the bottom of this stack did not survive.

Preliminary oven annealed data for this sample are shown in Figure 6.5. The expected cylinder morphology was confirmed (hexagonal spots in Figure 6.5a) with in plane alignment. Integration within the identified band (bars in Figure 6.5a) yields several readily identifiable peaks for tracking the segregation behavior as previously discussed in Chapter 5.

For an lgLSA scan with a maximum temperature of 800 °C, the integrated intensity of the principal peak as a function of position, normalization by the background scattering intensity is shown in Figure 6.6. Similar to work with PS-*b*-PMMA, samples maintain strong scattering up to a critical temperature, which then decreases rapidly to the high temperature, low intensity, plateau.

In contrast with the PS-*b*-PMMA behavior, shorter dwell anneals did not increase this critical transition temperature nor change the plateau scattering

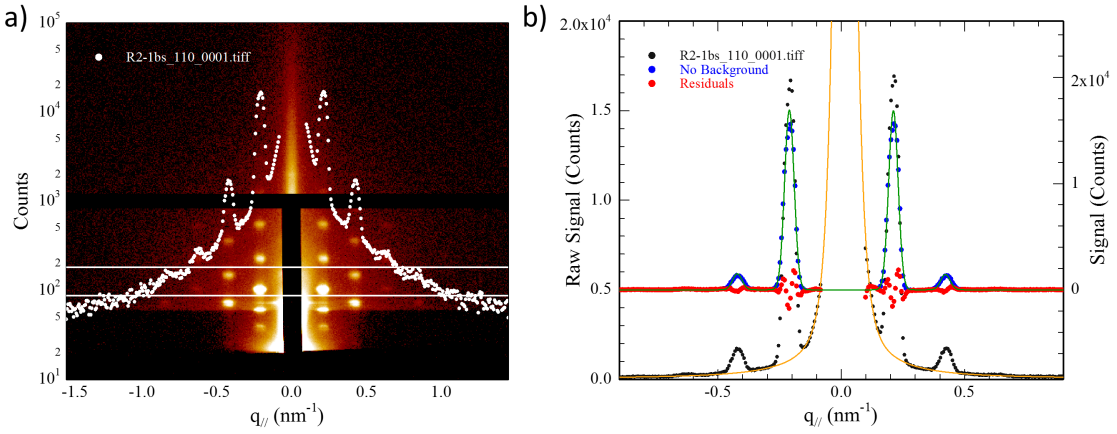

Figure 6.5: (a) Example measured GISAXS pattern for 47.2 kg/mol PI-*b*-PS cylinder forming polymer (b) integrated between the white lines and shown (black) and shown with background subtracted (blue) with residuals (red).

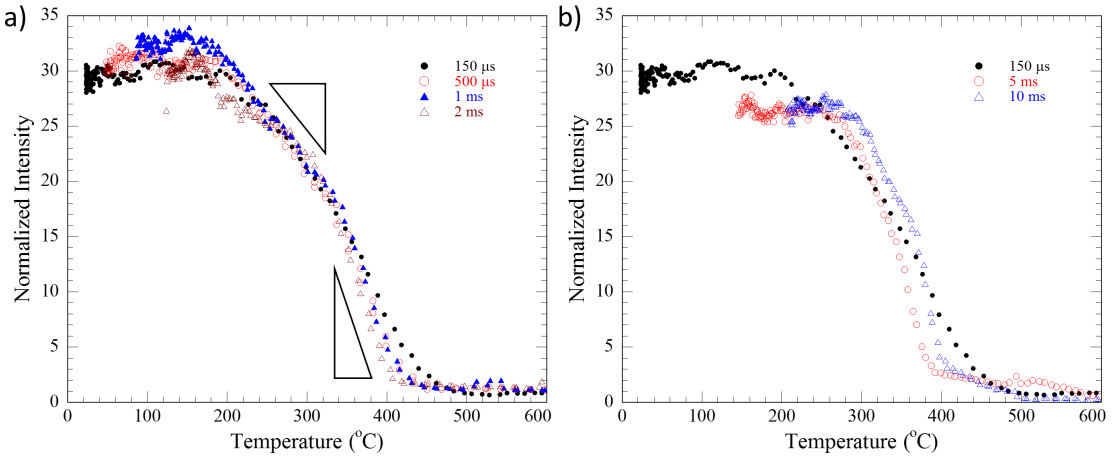

Figure 6.6: Scattering intensity of an initially oven annealed PI-*b*-PS sample for (a) short dwells from 150 μs to 1 ms with essentially identical behavior and temperature slope and (b) long dwells with minor shifts in the onset temperature and no change in the high T plateau level.

intensity. Additionally, this observed critical temperature of ~190 °C is below the calculated T_{ODT} ~230 °C. The remarkable similarity in temperature dependence is also replicated in the intensity rate of change which seems to change slope near 320 °C. For long dwell times (Figure 6.6, the slight shift in the onset temperature is likely within the temperature uncertainty. Also in contrast to the PS-*b*-PMMA behavior, the final high T plateau remains near zero even for the longest dwells studied.

The behavior differences between PI-*b*-PS and the PS-*b*-PMMA samples may be due to the substitution of the low T_g isoprene block, but could also be due to (i) oxidation, damage, or thermal cross linking of the isoprene during LSA, or (ii) partial damage developed during the oven anneal and propagated during the high temperature LSA. Material loss, as measured by optical film thickness loss or GISAXS background intensity, is not observed until much higher temperatures (>600 °C), similar to PS-*b*-PMMA. Consequently, this behavior is likely a structural effect or molecular damage rather than from a macroscale material loss.

As-spun films of this polymer exhibited minimal ordering compared to oven annealed samples. The scattering intensity only slightly increased near the primary peak position indicating an increase in the local correlation rather than complete segregation. After an lgLSA to a maximum temperature of 800 °C, order developed similar to the PS-*b*-PMMA system. Figure 6.7 shows integrated scattering intensity as a function of peak temperature. The high temperature plateau intensity increases with increasing dwell time, with the onset temperature decreasing with longer dwell times (except the potentially error prone 10 ms lgLSA). In contrast to the PS-*b*-PMMA, PI-*b*-PS has a sharp increase in scattering intensity near 400 °C at long dwell times (>2 ms). This feature is not

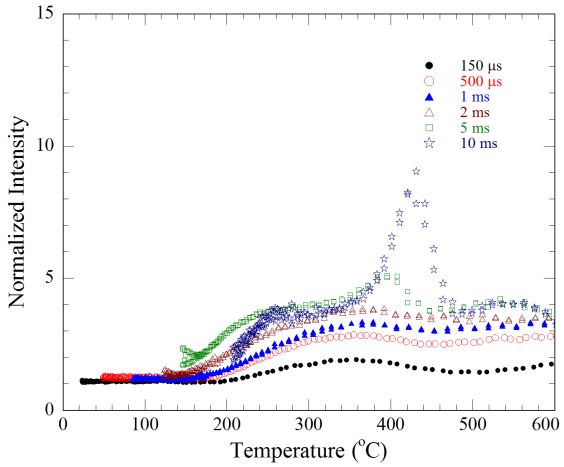

Figure 6.7: Scattering intensity of an initially disordered PI-*b*-PS sample for anneals with dwells from 150 μs to 10 ms. The high T plateau increases with dwell time, with a dramatic peak near 400 °C for the longest dwell.

altogether unexpected as one would expect that anneals very near T_{ODT} would have the maximum time to order with minimal time for disordering. However, the estimated T_{ODT} of 232 °C is far below the observed intensity spike temperature. Notably, the maximum normalized intensity even at this spike under 10 ms lgLSA is only a third of the oven annealed intensity (assuming similar contrast absorption). This suggests significant formation of order in just 10 ms, but that this is insufficient time to fully order.

The inconsistent behavior between the initially ordered and disordered films is perplexing. We believe that the oven annealed sample, and its behavior, is suspect due to the damage that likely occurred during oven annealing. This was the only sample to apparently survive the oven anneal and hence likely developed significant damage but not enough to cause total failure. In particular, the lack of any change in the high temperature plateau residual order (quench determined regime) supports this hypothesis since initially disordered films did exhibit the expected behavior. Annealed samples without damage are

currently awaiting data collection and analysis.Additional experiments to test this hypothesis would include alternatively ordering and disordering the material to test survivability under LSA coupled with other metrology, such as FTIR or NMR, to test for polymer bond modification through damage or crosslinking.

6.4 Exploratory Data on Additional Systems of Interest

Two additional BCP were tested for compatibility with LSA with a focus on establishing whether order was achievable and if that order could be measured and modified under LSA. No detailed temperature scans (lgLSA) have been acquired yet.

6.4.1 Poly(styrene)-*block*-poly(dimethylsiloxane) (PS-*b*-PDMS)

PS-*b*-PDMS is of particular interest for the DSA community due to its combination of high χ and high etch contrast arising from the silicon containing PDMS block. As with most high χ systems, surface chemistry strongly affects the thin film ordering and wetting behavior due to the strong immiscibility and surface energy difference of the two blocks. The polymers tested, summarized in Table 6.3, were acquired from the excess material from past experiments.

PS-*b*-PDMS was dissolved in PGMEA at 2 wt% concentration and spin coated. While previous experiments have shown moderate wetting behavior on bare silicon when spinning from PGMEA, all films dewet at all spin speeds explored. However, spin coating onto oxidized silicon wafers was successful resulting in films with thicknesses from 20 to 140 nm. Thicker films were not attempted as there was insufficient material available. These films were annealed

in a vacuum oven at 150 °C for 12 hours to develop the fully ordered state. However, the films were not stable and dewet during this anneal. Films were also LSA annealed at peak temperatures up to 500 °C and dwell times from 150 μs to 10 ms. Under LSA, the films remained intact on the oxidized silicon substrates.

GISAXS of the as-spun and oven annealed (with islands) samples showed randomly occurring powder diffraction rings with a periodicity of ~4.5 nm. This periodicity did not extend uniformly across the sample. On length scales of 10-100's of μm, the pattern would randomly appear and disappear indicating a complex structure development process. Furthermore, a cylinder morphology of order 15-20 nm was expected and the 4.5 nm periodicity cannot be explained at this time. This morphology was previously observed for material X by Jiang *et al*.[90]. While PS-*b*-PDMS films seemed to survive LSA to temperatures near 500 °C, no conclusions regarding the ordering behavior can be made at this time.

Table 6.3: Summary of tested PS-*b*-PDMS molecular weight, component volume fraction, and PDI.

Label	M_N (kg/mol)	f_{PS}	PDI	Spin Speed (RPM)	Thickness (nm)
U	18.3	0.707	1.02	200	138±20
V	19.5	0.667	1.03	200	78±10
W	20.8	0.663	1.03	200	74±3
X	22.0	0.621	1.03	200	16±4

6.4.2 Poly(isoprene)-*block*-poly(styrene)-*block*-poly(ethylene oxide) (ISO) Preliminary Data

Beyond the DSA community, BCPs are of considerable interest for their ability to form 3d interconnected networks. Three ISO based triblock copolymers

were tested to establish the disordering behavior under LSA. Table 6.4 summarizes the polymer chemistries explored. Polymers with low PEO fractions and a majority polystyrene exhibited well ordered structures after oven annealing at 150 °C for 12 hours under vacuum. Following oven anneals, all films were then annealed by LSA to peak temperatures of 500 °C for dwells from 150 *mu*s to 10 ms.

Table 6.4: Summary of ISO terpolymer molecular weight and component volume fraction.

Label	M_N (kg/mol)	f_{PS}	f_{PI}	f_{PEO}	PDI
Y (ISO#3, 108A)	40.1	0.609	0.279	0.113	1.06
Z (060B)	54.1	0.541	0.265	0.194	1.05
AA (ISO#10, 261A)	26.1	0.261	0.122	0.617	1.07

Figures 6.8 and 6.9 show GISAXS data for three different incidence angles for polymers Y and Z respectively, for both oven annealed (left column) and across LSA annealed (right column) samples. Scans at increasing incidence angle identify scattering from the direct and reflected X-ray beams allowing better structural identification. Since an unfocused GISAXS beam was used to probe the segregation behavior data was collected across all temperatures simultaneously. Loss of order is then observed as development of diffuse scatter rings in addition to signal from phase segregated film areas.

Strong scattering from a periodic structure is evident in the oven annealed samples. In contrast, the LSA samples also shows superimposed diffuse rings, indicating that the polymer has likely disordered after this high temperature anneal. As the GISAXS probes all temperature conditions across the LSA stripe, specific temperatures of disordering cannot be estimated.

The third polymer sample, with a 62 vol% majority ethylene oxide fraction

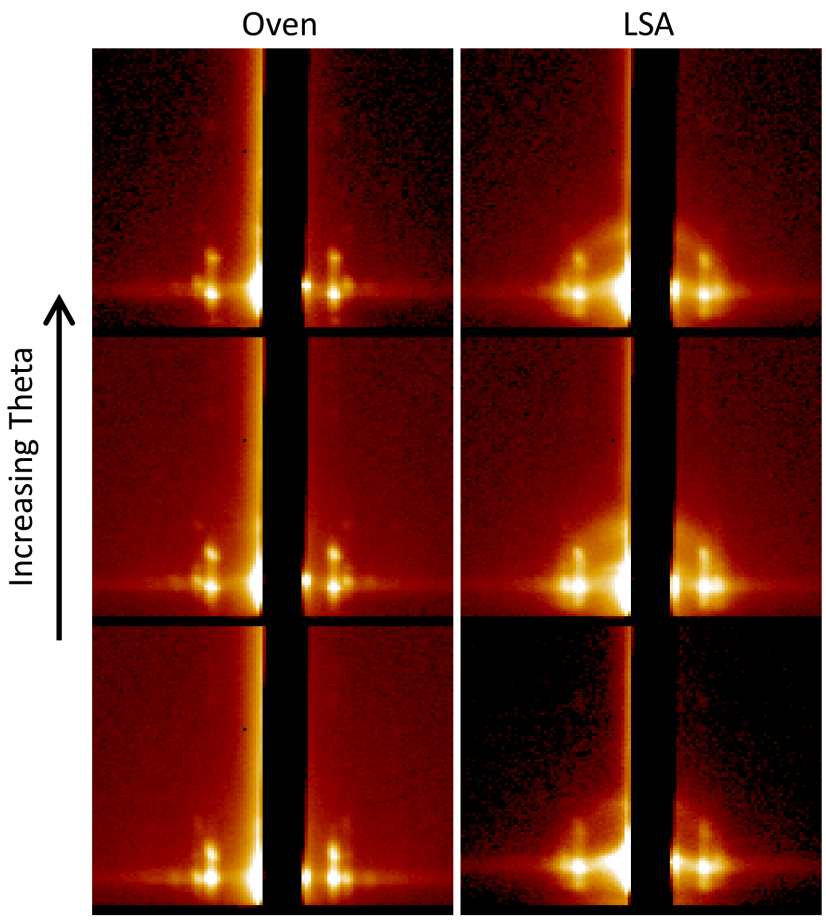

Figure 6.8: Rough scan of GISAXS X-ray incidence angle of polymer Y.

exhibited no significant order formation after neither oven annealing nor under LSA. It was suggested that this behavior might be due to the ethylene oxide crystallizing at temperatures near 50 °C [private communication, Mar. 2016]. The resultant volume change could then distort or otherwise destroy any periodic structures that would form during even transient annealing at high temperatures.

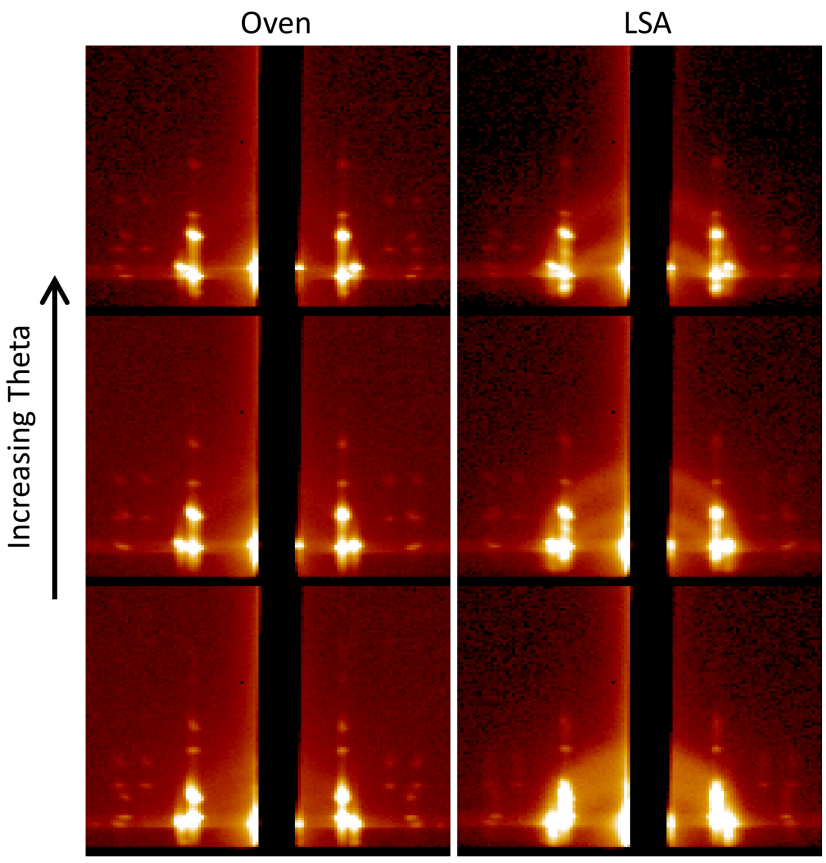

Figure 6.9: Rough scan of GISAXS X-ray incidence angle of polymer Z.

6.5 DSA considerations for LSA

For DSA applications, Chapter 8 showed that defectivity of DSA patterns likely originates from the fast segregation of phases under slow heating conditions (hot plate or oven) in the far from equilibrium conditions. LSA can prove advantageous by "pushing" this initial segregation to occur near T_{ODT} where polymer mobility is increased and the driving force for segregation is decreased allowing better initial alignment to the underlying template. Under this model, LSA primarily benefits DSA processing by (i) increasing the polymer mobility, and (ii) reducing the segregation driving force relative to the directing template alignment driving force. The optimal initial segregation then would occur at

temperatures approaching T_{ODT}.

The segregation driving force decreases rapidly as the temperature approaches T_{ODT}. Access to the ODT by increasing temperature only occurs in systems with a "strong" temperature dependence to χ to reach χN values below the critical segregation value. Some systems, such as PS-*b*-PMMA, exhibit experimentally measured χ values which are temperature insensitive and always remain positive at all temperatures. For such systems, the disordered state is not universally accessible for all molecular weights. A large enough polymer (large N) would, in theory, remain segregated at all temperatures. The rapid change of the PS-*b*-PMMA T_{ODT} with molecular weight is a direct consequence of the temperature insensitivity of χ .

Many high–χ systems exhibit much greater reduction in χ with temperature. Indeed, the asymptotic value at high temperature is often negative reflecting additional entropic contributions. This asymptotic value of χ implies that the mixed state is always theoretically accessible at high temperature. Furthermore, the increased temperature dependence of χ reduce the sensitivity of T_{ODT} to the polymer molecular weight. These two effects suggest that LSA could be widely applicable to high–χ materials providing access to a high mobility state in proximity to the T_{ODT}.

It must be noted that the push toward higher resolution patterning requires shorter chained polymers. With decreasing N, χ must increase to maintain segregation at nominal hot plate annealing temperatures. This requires high–χ materials, which require significant efforts to obtain the standing morphology due to having highly incommensurate blocks with different affinities for each film surface. A leading alternative to thermal processing uses solvents to improve polymer mobility; however, maintaining surface energy balance with yet

another component further complicates processing. This provides yet another reason that a simple thermal process, such as LSA, could prove extremely beneficial.

6.6 Staining for GISAXS Acquisition

Preferentially staining one block with a heavy metal greatly increases scattering contrast and subsequently decreases required acquisition times for GISAXS. This can be done for methyl methacrylate based systems by adding RuO_4, or to isoprene or butadiene systems by adding OsO_4. Toxicity of these compounds merits a warning to the experimenter as special precautions must be taken when staining the films.

RuO_4 can be added via aqueous solution processing while OsO_4 sublimes allowing a vapor based transfer. For PS-*b*-PMMA, samples were submerged in 2 wt% RuO_4 solution for 60 minutes and allowed to dry in a loosely covered petri dish. For PI-*b*-PS, an ampule containing 4 mg of OsO_4 was opened and the crystals were spread through the bottom of a wafer box, with samples suspended in the container and left overnight to stain.

Both of these processes were done by hand and were experimentally uncontrolled, yielding nonuniform stain density on large length scales. This created some additional challenges in analysis. Figure 6.10a shows the principle GISAXS peak scattering intensity for an as-spun PI-*b*-PS sample (R) across all lgLSA conditions. The baseline between lgLSA scans, highlighted with a red dashed line, should remain constant across the sample. However, it is clear that there are significant variations across the sample area. Figure 6.10b shows this data normalized by the background scattering intensity, which should compensate for beam intensity variations and some portion of the stain induced vari-

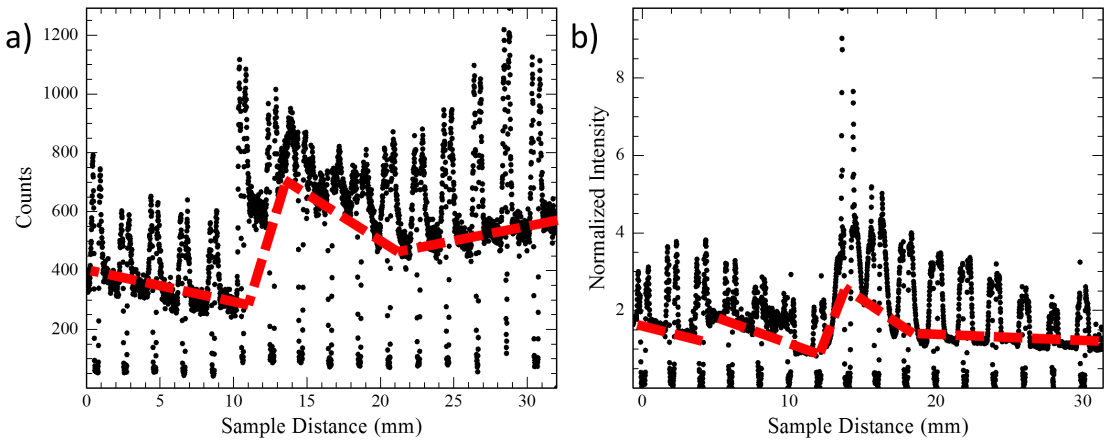

Figure 6.10: Integrated scattering signal intensity of as-spun R polymer across 16 lgLSA scans in (a) raw scattering intensity and (b) intensity normalized by the background fit. Baseline unannealed area scattering signal highlighted by red dashed lines. Oven annealed samples exhibit larger normalized intensities near 30 (AU).

ability. However, even with this normalization, considerable variation remains across the sample.

While normalization yields a better baseline and, in some regions it is close to uniform, there is still variability. This variability is definitely a consequence of the staining process since, before staining, the baseline scattering intensity was level across the sample confirming uniformity of the spin coating process. While this example is extreme and most substrates exhibited relatively monotonic baseline changes, the stain variability must be checked and accounted for.

Data presented in Section 6.3.1 were only from samples where the baseline variations was relatively small. In the future, staining procedure could likely be significantly improved to yield better uniformity. However, no systematic exploration of the staining procedures were undertaken for this initial exploratory work.

6.7 Conclusions

The general applicability of lgLSA for polymer phase behavior identification has been shown for several polymer systems beyond PS-*b*-PMMA. This demonstrates the potential use of LSA to study candidate materials with a range of potential applications beyond DSA. PI-*b*-PS and PI-*b*-PS-*b*-PEO were both shown to exhibit behavior consistent with a well defined and accessible ODT. Preliminary lgLSA studies of stained PI-*b*-PS showed both ordering and disordering under 10 ms laser annealing. Exploratory studies on PS-*b*-PDMS showed stability at LSA temperatures, but dewetting of initial thin films prevented any observation of discernible structures on expected length scales.

6.8 Acknowledgments

Katherine Barteau and Sarah Hesse synthesized the numerous PI-*b*-PS molecular weights and volume fractions, Brandon Wenning synthesized PS-*b*-PDMS polymers, Joerg Werner synthesized PI-*b*-PS-*b*-PEO polymers, and Peter Beaucage and Detlef-M. Smilgies were instrumental in obtaining CHESS time and helping with instrumental setup for these experiments. John Grazul was critical in staining films of interest and obtaining additional sample sets.

CHAPTER 7

FINITE DIFFERENCE MODELING OF SEGREGATION

This chapter will show the efforts to applying the basic Avrami (KMJA) equations, nucleation theory introduced in Chapter 2, and spinodal decomposition toward producing an initial finite element model of the BCP ordering and disordering kinetics. The goal was to replicate the observed scattering intensity behavior as a function of dwell and peak temperature using a finite integration of the LSA temporal profile with ordering rates calculated by Avrami or other model equations. After integration over the full LSA time-temperature profile, a final order parameter is predicted.

7.1 Applying Theories to Modeling

As initially described in Chapter 2, the Kolmogorov, Mehl, Johnson, and Avrami (KMJA) model determines the material transformed volume fraction (Γ) as a function of nucleation and growth rates. This takes the form:

$$\Gamma_{KMJA} = 1 - \exp\left(-\beta t^n\right) \tag{7.1}$$

where Γ is volume transformed, t is time, β is the combined nucleation and growth rate defined below, and n is the "Avrami exponent" which is the sum of the nucleation rate exponent and growth dimensionality (d). This combined nucleation and growth factor β is defined as:

$$\beta = \dot{N}\dot{G}^d \tag{7.2}$$

where $\dot{N}$ is the nucleation rate and $\dot{G}$ is the one dimensional growth rate given by:

$$\dot{N} = \dot{N}_0 \exp\left(-\frac{E_{A1}}{k_b T}\right) \exp\left(-\frac{E_{A2} T_X^2}{k_b T (\Delta T)^2}\right) \tag{7.3}$$

and

$$\dot{G} = Dq \tag{7.4}$$

where $\dot{N}_0$ is the nucleation rate prefactor, E_{A1} is the nucleation thermal attempt activation energy (diffusional), E_{A2} is the activation energy from surface area and volume energetic arguments, T_X is the equilibrium phase boundary temperature, ΔT is the quench depth, D is the species diffusivity, and q is a characteristic diffusion distance.

In order to track the evolution of order, the rate of change of the order parameter is necessary. Taking the first partial derivative in time, $\partial\Gamma/\partial t$:

$$\dot{\Gamma}_{KMJA} = n\beta t^{n-1} \exp\left(-\beta t^n\right) = \beta n t^{n-1} \left(1 - \Gamma\right) \tag{7.5}$$

From rearranging the original Avrami equation for time:

$$t = \left(\frac{-\ln[1-\Gamma]}{\beta}\right)^{1/n} \tag{7.6}$$

yielding the first derivative as:

$$\dot{\Gamma}_{KMJA} = n\beta^{1/n} \left(-ln[1-\Gamma]\right)^{\frac{n-1}{n}} \left(1 - \Gamma\right) \tag{7.7}$$

This is the central equation used to numerically follow ordering in time for these studies. Some modifications and simplifying assumptions are included below.

7.1.1 Polymer and GISAXS Specific Considerations

Ordering vs. Disordering

In order to use the order parameter to model phase segregation in BCPs, the ordering and disordering behavior must be contained within the same function.

In the Avrami equations above, the equations always evolve monotonically toward the Γ=1 state. By defining Γ=1 to be fully ordered, the equations, as written above, are only applicable to polymers in the ordering regime.

To account for the disordering behavior, the direction of $\dot{\Gamma}$ must be reversed as the "end" limiting value switches from 1 for ordering to 0 for disordering and vice versa. To do this, the terms $[1-\Gamma]$ is mapped to $\left[\Gamma_{equilibrium}-\Gamma\right]$ and can be replaced with a heavyside function $[H(T_{\mathrm{ODT}}-T)-\Gamma]$. At temperatures below T_{ODT}, this heavyside yields unity, and at high temperatures it yields zero, encapsulating the polymer ordering/disordering directional behavior of Γ.

In order to reduce oscillations near T_{ODT}, provide a smooth response, and take into account the finite ODT temperature width, a error function with a finite transition width was used instead. In reality, the polymer χN determines the phase segregation equilibrium behavior and the strength of segregation; a more sophisticated model would take this into account. For these calculations, it was believed that the error function approximation was adequate given the uncertainty in χ parameter, diffusion coefficient, and temperature profile. Specifically, the complementary error function was used and replaces $[1-\Gamma]$ by $\left[\frac{1}{2}erfc(\frac{T-T_{\mathrm{ODT}}}{\Delta T})-\Gamma\right]$ where ΔT is the transformation width, numerically set to 1 K.

Within the natural log, the absolute distance between the current state and the end target state (ordered or disordered) is important. This allows an absolute value to be used to avoid logs of negatives which never occur in the original Avrami form. The modified form is then:

$$\dot{\Gamma}_{KMJA} = n\beta^{1/n}\left(-ln\left[|\frac{1}{2}erfc\left(\frac{T-T_{\mathrm{ODT}}}{\Delta T}\right)-\Gamma|\right]\right)^{\frac{n-1}{n}}\left(\frac{1}{2}erfc\left(\frac{T-T_{\mathrm{ODT}}}{\Delta T}\right)-\Gamma\right) \qquad (7.8)$$

where ΔT_{ODT} is the small temperature width (1 °C) over which the polymer ODT occurs.

GISAXS Intensity vs Γ

As stated previously, GISAXS is primarily sensitive to the electron density contrast between two volumes. Given that we have previously defined Γ as the volume of material fully transformed via nucleation and growth, the scattering intensity should scale linearly with Γ. Volume of the film that had transformed will scatter while disordered volumes away from the nucleation and growth interfaces will not.

Spinodal Decomposition

Should the transformation instead occur by spinodal decomposition, or other processes where the polymer continually refines the local density of A and B chains, the scattering intensity would follow $I \propto \Gamma^2$ since X-ray scattering intensity scales as the electron density contrast squared, $\Delta\rho^2_{electron}$. This also changes the meaning of Γ to instead be a density contrast. Models to follow order development within this context would need to account for the local chain dynamics with no explicit nucleation and growth.

Although nucleation and growth is expected for off-symmetric BCP compositions, the rapid heating and quench rates could push the polymer into a spinodal regime. In this case, the rate of change of Γ can be argued to follow the form:

$$\dot{\Gamma}_{spinodal} = KD|T - T_{\mathrm{ODT}}|\left(\Gamma_{equil} - \Gamma\right) \tag{7.9}$$

where K is a temperature independent rate prefactor, D is the polymer diffusivity, $|T - T_{\mathrm{ODT}}|$ is a measure of the driving force for segregation, and $\left(\Gamma_{equil} - \Gamma\right)$ scales the driving force for the distance the system is from the final equilibrium state.

7.1.2 Simplifying Assumptions

To simplify modeling the PS-*b*-PMMA system, diffusivity was taken to be that of the majority block, polystyrene, taken from literature[169, 181, 182]. At temperatures far beyond T_g, polymers have been shown to follow an Arrhenius diffusion relation[105]. If temperatures far above T_{ODT} are to be simulated, the diffusion would need to include a sum of WLF and Arrhenius rates. In other systems or molecular weights, this could become important, especially for extremely high T_{ODT}s.

7.1.3 Practical Considerations

In finite difference implementations, the time step is critical and can produce artifacts in the ordering behavior if chosen to be too large. Empirically, the ordering behavior converged for time steps smaller than $\sim\tau_{dwell}/5000$. For the calculations below, time steps were maintained at $\tau_{dwell}/10^4$.

7.2 Results and Discussion

7.2.1 Spinodal Model Temporal Behavior

Both the Avrami and spinodal segregation models provide a vast parameter space to explore. As expectedly, both models replicate the conceptually expected ordering behavior in these systems. Figure 7.1 shows the calculated order parameter using the spinodal model as a function of time for a series of 10 ms LSA anneals; the LSA time-temperature profile is included for reference and model parameters are summarized in Table 7.1.

For LSA temperatures above T_g but below T_{ODT} (Figure 7.1a), polymer start-

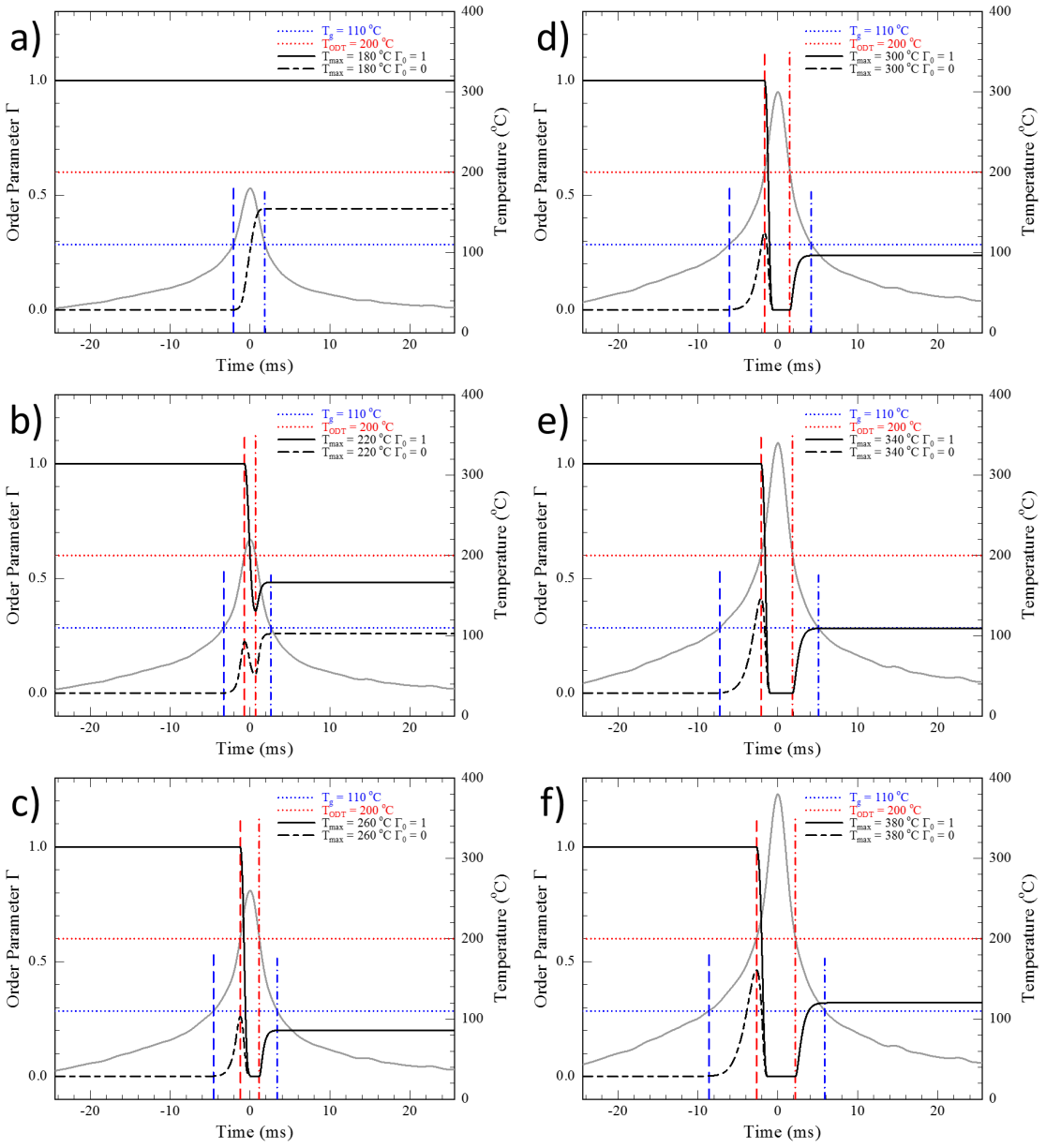

Figure 7.1: Temporal modeling of spinodal ordering behavior of hypothetical polymer with T_g=110 °C and T_{ODT}=200 °C for 10 ms LSA at (a) 180 °C, (a) 220 °C, (a) 260 °C, (a) 300 °C, (a) 340 °C, and (a) 380 °C. Behavior starting from a fully ordered state is represented with solid curves while dashed curves started from the initially disordered state. The LSA time-temperature profile is depicted in grey for the right ordinate.

Table 7.1: Summary of spinodal model parameters used in calculating Figures 7.1-7.3. *C_{1g} = 15 for Figure 7.2c and Figure 7.3.

Label	Value	Units
K (Rate Prefactor)	5*10^5	$\frac{s}{m^2 K}$
D_{T_g} (Diffusivity Prefactor)	5*10^{-19}	$\frac{m^2}{s}$
C_{1g} (WLF Parameter)*	13	unitless
C_{2g} (WLF Parameter)	70	K
T_{ref} = T_g (WLF Reference Temperature)	110	°C
T_{ODT} (ODT Temperature)	200	°C

ing from the fully ordered state (Γ=1) retains that order for all times whereas polymer starting in the disordered state (Γ=0) begin ordering for times when T>T_g.

As the peak LSA temperature is increased to just above T_{ODT} (Figure 7.1b), starting from Γ=1, the film retains order until the temperature reaches T_{ODT} and begins disordering. In this example, the disordering is not complete before the temperature again falls below T_{ODT} and order is redeveloped during quench. Similarly, starting from Γ=0, the material begins to order above T_g and follows a similar path once above T_{ODT}. In this case, there is insufficient time at temperature to fully disorder the film and the final order, after quench, varies depending on the initial state.

Increasing the peak LSA temperature to far above T_{ODT} (Figure 7.1c), the model shows the polymer becoming to fully disordered before developing a history independent final state; this final state is, however, quench dependent. Any further increase in the peak LSA temperature (Figures 7.1d-f) leads to the same completely disordered state at high temperature, and the final state is only modified due to the change in quench rate tail behavior of the LSA thermal profile.

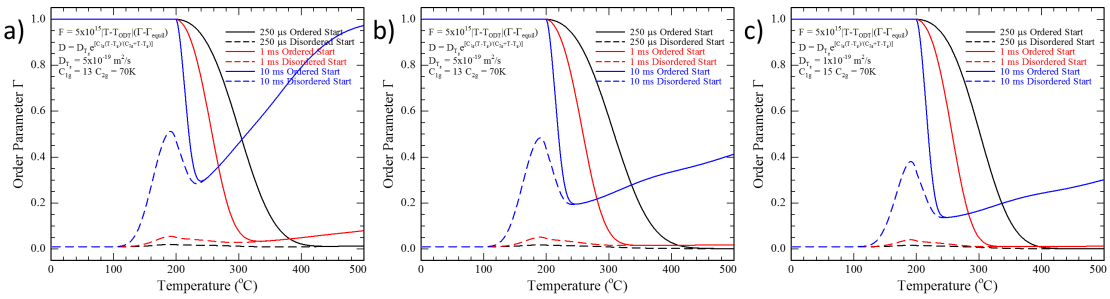

Figure 7.2: Predicted order parameter of spinodal decomposition based ordering for LSA anneals of 250 μs, 1 ms, and 10 ms up to 500 °C starting from the fully ordered and fully disordered states for (a) full LSA temporal profile, (b) LSA temporal profile modified to quench to ambient in $10\tau_{dwell}$, and (c) modified LSA profile with modified polymer diffusivity.

Though Figure 7.1 uses the spinodal model, the general trends are similar for both models. Experimentally, the lgLSA approach only probes the final order as a function of the peak anneal temperature and dwell time. This can be replicated computationally by following the final order parameter after quench for a series of peak LSA temperatures. Each of the subsequent figures in this chapter plots the final order parameter after quench as a function of peak LSA temperature. Figure 7.2a shows the spinodal modeled order parameter starting from the fully disordered and fully ordered states after 250 μs, 1 ms, and 10 ms LSA. The model used literature values for the WLF diffusivity and a rate prefactor value appropriate to obtain significant changes after a 10 ms LSA anneal.

Notably, both models show significant deviation from the observed PS-*b*-PMMA behavior in three ways: (i) the high temperature "plateau" has significant slope, (ii) significant order formation near T_{ODT} when starting from the disordered state, and (iii) strong suppression of the short dwell high temperature order compared to the 10 ms anneal.

7.2.2 High Temperature Slope Behavior

In part, the large slope in the high temperature regime arises from the long high temperature tails during long dwell anneals. These tails, obtained from measured thermistor temperature scans, may be overestimating the effect due to the small chip size and plastic chip holder used in these temperature calibrations. Figure 7.2b uses the same measured LSA scans, but forces the temperature to reach room temperature after 10 dwell times. This duration is in line with Cornell Laser Annealing Simulation Package (CLASP) simulations for the long dwell times, but is dependent on the sample size and back surface thermal resistance. With the faster quench to below T_g, the slope in this regime is significantly reduced.

However, the model still predicts a considerable slope in the high temperature regime. Increasing the WLF diffusion constant C_{1g} (within reason) while keeping overall diffusivities consistent with measured polystyrene values, this high temperature slope can be reduced further but not eliminated, as seen in Figure 7.2c.

7.2.3 T_{ODT} Proximate Behavior

Enhanced order formation for temperatures near T_{ODT}, for initially disordered films, was not observed experimentally in the PS-*b*-PMMA system. However, preliminary data from PI-*b*-PS does exhibit this behavior for the 10 ms dwell (Figure 6.7), with the effect suppressed for successively shorter dwells. The different behavior between these two systems could stem from the highly mobile PI block within PI-*b*-PS BCP; however more investigation is necessary before any firm conclusion can be drawn.

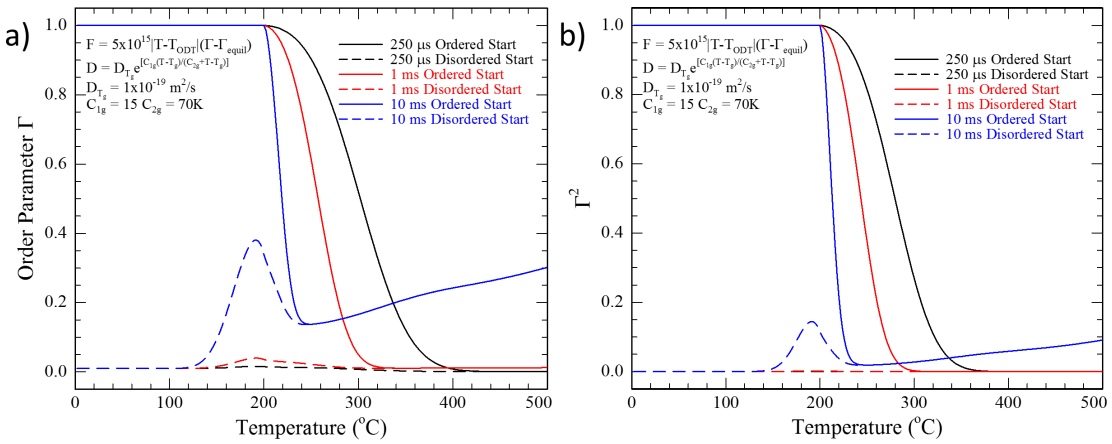

Figure 7.3: Modeled spinodal decomposition (a) order parameter and (b) scattering intensity ($\propto \Gamma^2$) exhibiting suppressed high T scattering intensity.

7.2.4 Dwell Dependent Behavior

Model predictions all show very strong suppression of ordering under short dwell anneals. Experimentally, the collapse of order with decreasing dwell is much weaker. In effect, the model suggests that long dwells would regain much more order than the short dwell times, especially when compared with the observed data for both PS-*b*-PMMA and PI-*b*-PS. No combination of spinodal diffusion parameters, functional forms for diffusivity (WLF or Arrhenius), or rate prefactor was identified that would allow the model predictions to quantitatively match the experimental observations.

These computational models directly predict the order parameter while experiments only infer Γ from the GISAXS scattering intensity, itself stemming from the electron density where $I \propto \Delta\rho^2_{electron} = \Gamma^2$. Figure 7.3a shows the model predicted order parameter as a function of the peak annealed temperature. Figure 7.3b shows Γ^2, which is expected to more closely mimic the normalized GISAXS scattering intensity. While this Γ^2 plot does reduce the slope of

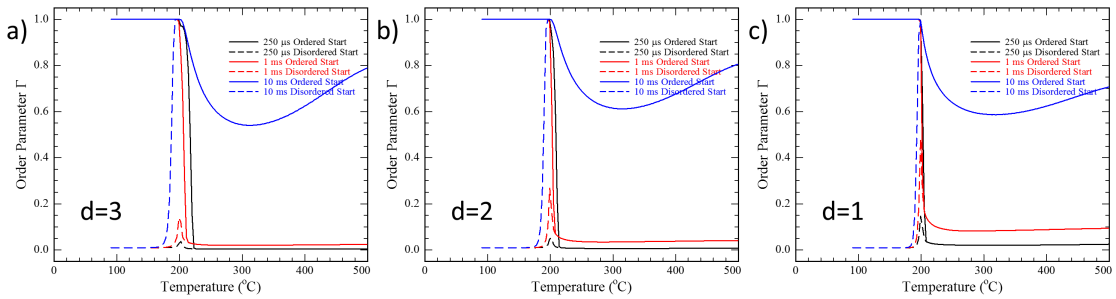

Figure 7.4: Nucleation and growth model output for (a) 3D, (b) 2D, and (c) 1D growth for approximately constant 10 ms LSA order behavior exhibiting increased high temperature ordering for short duration anneals as growth dimensionality is decreased.

the high temperature, it further suppresses the expected scattering intensity of short dwell anneals relative to the 10 ms LSA. Indeed, this exacerbates the discrepancy between the observed and predicted high temperature behavior for all diffusion and rate parameters.

7.2.5 Nucleation and Growth Model

Nucleation and growth modeling by the Avrami equations similarly failed to replicate the high temperature behavior, including both the slope in the high temperature region and the increased scattering intensity near T_{ODT}. Figure 7.4 shows a series of simulations varying the Avrami exponent from 3 to 1 (nominally going from 3-d to 1-d growth) while choosing prefactors to maintain approximately the same 10 ms ordering and disordering behavior. As the growth dimensionality is decreased, the shorter duration anneals show greater high temperature ordering, relative to the 10 ms anneals, but still far less than observed experimentally.

Each of these simulations maintained the same nucleation activation energies E_{A1} and E_{A2}. However, modification of these values were not observed

to yield significant improvement in the high temperature behavior nor agreement across multiple dwell times. A possible alternative to the Avrami equation would be to assume a constant number of nuclei and only model growth. This model, however, approaches the spinodal model described above with a constant driving force as opposed to one dependent on the distance from T_{ODT} and Γ_{equil}. Despite the unphysical nature of this model, it was also tested but showed no significant improvement to the agreement with experiment.

7.2.6 Future Considerations

For future work in this modeling, it will also be important to take into account the finite acquisition area, and thus variation of the μ-GISAXS acquisitions. The finite range of acquisition temperatures will "smear" the profiles by ~10-20 °C. Although this could be included in principle for the current model, the deviation between the model and experiments was too large to warrant the additional complications.

7.3 Conclusions

Modeling of the segregation process as either a spinodal or nucleation and growth type process was successful in replicating the major features observed in LSA ordering and disordering of PS-*b*-PMMA and PI-*b*-PS. However, neither model, as currently implemented, was able to simultaneously replicate multiple dwell times with a single set of parameters. Additionally, several features, such as the high temperature plateau and the constant behavior of the PS-*b*-PMMA ordering near T_{ODT} could not be reproduced. This may stem from the deeply metastable nature of the transient anneals.

Due to the many simplifications within this modeling regime, it is not surprising that the observed data can not be precisely replicated. It is likely that future simulation efforts will need to more precisely model the local segregation dynamics. Atomistic model,s based on molecular dynamics or kinetic Monte Carlo may, indeed be necessary to fully understand the segregation pathways.

CHAPTER 8

APPLICATION OF LSA TO DSA FOR DEFECTIVITY REDUCTION

8.1 Introduction

[1] Directed self-assembly (DSA) of block copolymers has emerged as a likely candidate to enable bottom up lithography for patterning at dimensions below 20 nm. However, defect density currently limits practical implementations. Block copolymers (BCPs), consisting of two or more covalently bonded immiscible polymers, microphase segregate into domains with the geometry determined by the polymer composition. The alignment of phases, such as lamellae and cylinders, can be directed either chemically (chemoepitaxy) or physically (graphoepitaxy) to form intentional patterns[22, 83, 84, 93, 94, 96]. The polystyrene-*block*-poly(methyl methacrylate) (PS-*b*-PMMA) system has been extensively explored and has demonstrated the ability to register patterns via both chemoepitaxy and graphoepitaxy during thermal annealing at temperatures near 250 °C in the minutes time frame. Challenges remain however with regard to defects, registered domain sizes, and line edge roughness (LER)[22, 84, 94, 96]. While annealing for much longer periods improves patterning characteristics, throughput concerns remain. Use of higher temperatures on hot plate timescales to accelerate the alignment is limited by thermal degradation of the polymers.

Early efforts on DSA required thermal anneals for tens of hours at elevated temperatures[86]. Refinements in methods have reduced annealing time to the minutes timescale[96] at temperatures approaching the thermal degradation

[1]The majority of this Chapter was published as: A. G. Jacobs, B. Jung, J. Jiang, C. K. Ober, and M. O. Thompson, "Control of polystyrene-*block*-poly(methyl methacrylate) directed self-assembly by laser-induced millisecond thermal annealing," *Journal of Micro/Nanolithography, MEMS and MOEMS*, **2015**, vol. 14, no. 3, 031205. DOI 10.1117/1.JMM.14.3.031205.

limit. BCP phase segregation has also been demonstrated using rapid thermal annealing on the 10 second time frame at 250 °C[97] and using multiple millisecond pulsed CO_2 laser irradiations[153]; these data suggest DSA could be viable at higher temperatures and correspondingly greater polymer mobility. Others have attempted to circumvent thermal annealing limits by incorporating solvents to swell the BCP film and increase polymer mobility[183, 184], also potentially linked with hot plate[85], or laser induced[82, 95, 155], heating to accelerate segregation and alignment.

Short duration annealing has previously demonstrated the ability to extend polymer processing to higher temperatures[105]. For PS-*b*-PMMA, the processing window, prior to observable material loss, is extended up to ~850 °C at 10 ms compared to ~300 °C in the seconds time frame. This extended process window is utilized to study segregation dependent pattern registration and defectivity of DSA after LSA at high temperature. Indeed, Li *et al.*, suggest that defect annealing at lower χN values[18] is potentially more effective in reducing defectivity due to the lower energy barriers to defect annihilation. The high temperatures available to LSA enables access to this χN regime.

Use of high temperature, short time, thermal annealing can be used independently from, or in conjunction with, conventional thermal anneals. Utilizing LSA alone, the enhanced polymer chain mobility at high temperatures may enable rapid phase segregation and aligned pattern formation. The use of LSA after traditional hot plate processing may anneal out residual defects while maintaining the previously aligned regions. Finally, an initial high temperature anneal may enhance phase segregation and initial interfacial alignment to the directing template allowing for rapid structural development of the fully aligned pattern during a subsequent conventional thermal anneal.

8.2 DSA Sample Preparation and Analysis

DSA alignment studies were performed using lamellae forming PS-*b*-PMMA films obtained from EMD Performance Materials (Merck KGaA). The molecular weight of these films were adjusted to achieve a 15 nm half-pitch. The films were coated on silicon substrates with a directing template consisting of a cross-linked polystryene mat and with a PS-*r*-PMMA random copolymer neutral layer to promote the out of plane orientation. In DSA areas, a 45 nm half-pitch directing chemical template was patterned using 193-*i* lithographically to direct assembly of 15 nm lines/spaces at 3x density multiplication as described by Liu *et al.*[17, 91]. A standard 2 minute hot plate anneal at 250 °C in air was used as the reference annealing condition. LSA samples were annealed using a 980 nm diode laser with a 10 ms dwell at peak temperatures from 300 to 800 °C.

Defect density was quantified as the areal fraction of completely aligned domains using a custom ImageJ[185] macro on large (typically >120 μm^2) areas. For the reference hot plate anneals, multiple areas were imaged to estimate statistical variations in the alignment fraction.

8.3 Results and Discussion

8.3.1 Phase Segregation and DSA under LSA

Having demonstrated that block copolymer segregation occurs on LSA timescales in these cylinder forming films, behavior of the lamellar forming templated BCP samples for DSA was also evaluated. Self-assembly and registration to a directing pattern may require longer duration or multiple LSA anneals due to the small driving force directing pattern formation. From liter-

ature χ values, T_{ODT} for these lamellar forming DSA films was estimated to be between ~200-700 °C[100, 102, 170]. Based on our experimental observations, the effective T_{ODT} in directed regions appears to in the vicinity of 660 °C. This may be higher than the expected bulk T_{ODT} due to preferential interactions with the directing template and thin film dimensions.

Figure 8.1 compares hot plate and LSA annealed DSA structures for the 15 nm half pitch lamellar polymer. Under hot plate annealing for 2 minutes at 250 °C, the pattern density multiplication is well developed, though a significant fraction of the area remains defective (Figure 8.1a). Figure 8.1b shows the morphology developed after a single 10 ms LSA scan at 480 °C. While phase segregation has occurred, little or no alignment is observed by top view SEM. This alignment can be improved using multiple LSA scans below the T_{ODT}, though accumulated damage limits the peak temperature for multiple scans. Figure 8.1c shows the substantial alignment that can be achieved for samples annealed with 100 scans at 450 °C with a 10 ms dwell. Indeed, the alignment is improved relative to the hot plate anneal with ~60% reduced defectivity in larger comparable images. This suggests that alignment and defect reduction is possible on a 1-second time frame at temperatures near 450 °C. However, the large number of LSA scans required makes this process impractical on a manufacturing scale.

8.3.2 Annealing Residual Defects via LSA

From as-spun films, LSA requires multiple scans to develop the full DSA alignment. The high temperature of the LSA, with the dramatically enhanced polymer chain mobility may, however, be sufficient to anneal defects in local areas following the initial alignment achieved during a hot plate anneal. DSA samples were annealed for 2 minutes at 250 °C followed by single or multiple LSA

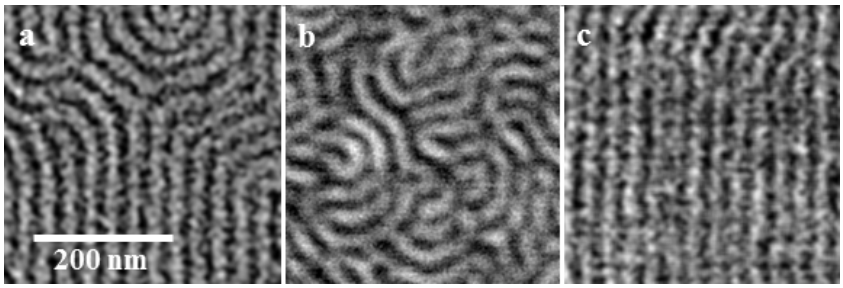

Figure 8.1: DSA alignment of lamellar PS-*b*-PMMA formed during (a) hot plate annealing for 2 minutes at 250 °C in air (b) 10 ms LSA at 480 °C and (c) 10 ms LSA at 450 °C repeated for 100 scans.

scans. To correct for systematic variations in the DSA alignment layer, quantitative measurements of the initial alignment were taken in areas outside the LSA affected zone. Changes in the alignment between these "non-LSA" areas and the LSA affected zones are reported. A representative image from the non-LSA area (Figure 8.2a) shows an alignment of 74%. Based on multiple images in non-LSA areas, the variation in aligned area fraction between different areas on the same substrate was determined to be ±2% while substrate to substrate variability produced baseline alignment from ~60-80%.

Upon annealing once via LSA at up to 700 °C for 10 ms, any improvement is minimal as shown in Figure 8.2c. The alignment after annealing is 70% and is statistically indistinguishable from the control area at 68%. Multiple LSA scans after the standard hot plate anneal (not shown) provide statistically significant reductions in defectivity. After 10 passes at 590 °C, alignment increases to 80% compared to a 62% baseline, representing a 45% relative reduction in defective area. Though effective after multiple LSA scans, the large number of anneals reduces the thermal degradation limit and reduces practicality on the industrial scale.

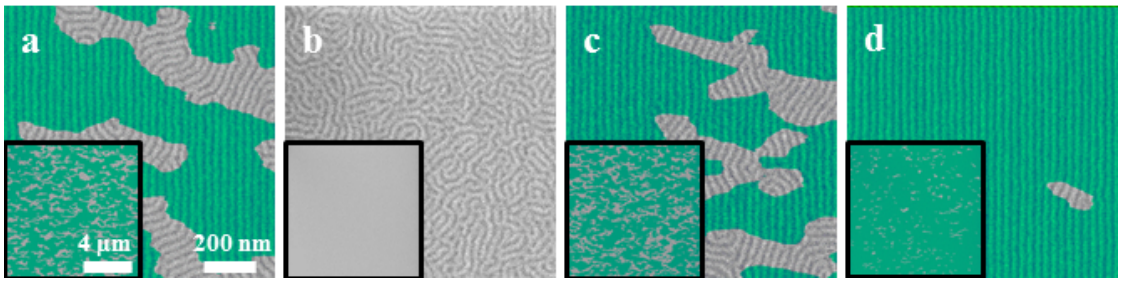

Figure 8.2: SEM images of lamellar PS-*b*-PMMA DSA with superimposed shading of aligned regions. Insets are low magnification images with >120 μm^2 areas used to quantify the aligned area fraction. (a) Standard hot plate anneal for 2 minutes at 250 °C in air, (b) LSA only at 500 °C for 10 ms, (c) standard hot plate anneal with subsequent LSA at 500 °C for 10 ms, and (d) LSA for 10 ms at 510 °C prior to a standard hot plate anneal.

8.3.3 Defectivity Segregation Pathway Dependence

The specific path followed from the deeply metastable initial state to the segregated final state will define the initial ensemble of defects that must be removed by subsequent annealing. This suggests that the initial heating rate may affect the overall defectivity. Since LSA was able to induce segregation but did not induce any visible alignment to the directing template, one might expect an initial LSA anneal prior to hot plate refinement to have little effect. However, samples with LSA defined initial segregation exhibited dramatically improved defectivity. Figure 8.2d shows a film annealed initially to 510 °C for 10 ms by LSA followed by the standard hot plate anneal for 2 minutes at 250 °C in air. The aligned area fraction increased from 74% in control areas (Figure 8.2a) to a maximum of 95.6%, a relative reduction in defective area of >80%. Although LSA alone does not provide sufficient time at temperature to fully align the film, modifications of the initial structure, most likely at the polymer-directing template interface, during the short, high temperature anneal is effective in enabling

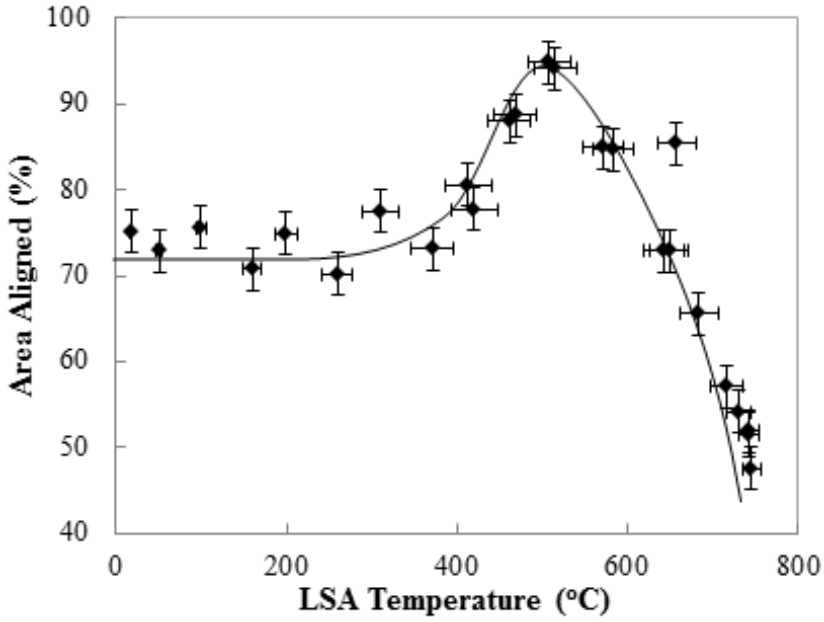

Figure 8.3: Temperature dependence of DSA alignment for 10 ms LSA pre-annealed substrates. Solid line is a guide to the eye only.

higher fidelity pattern formation under a subsequent low temperature anneal.

It is critical to examine the effect of the LSA temperature on this two-step annealing alignment process. To follow the annealing behavior as a function of the peak LSA temperature, SEM images were taken orthogonal to the laser scan direction, *i.e.*, across the Gaussian-like laser intensity profile. This permitted comparison of nominally identically treated samples where only the peak temperature was changed. Figure 8.3 shows the aligned area fraction as a function of this peak LSA temperature. At low LSA temperatures, the final alignment is equivalent to the hot plate alone with a 74% alignment. As the LSA temperature is increased to ~500 °C, the aligned area fraction increases to a peak of 95.6% (Figure 8.2d). At higher LSA temperatures, above ~650 °C, the alignment is reduced and indeed drops below the level for the hot plate only anneal. Notably, this critical temperature is near the estimated T_{ODT} for these films.

The decrease in alignment at the highest temperatures does not appear to be due to film loss or damage. The stability of these BCP films was determined by measuring the film thickness as a function of the peak annealing temperature. For single LSA scans, no measurable thickness loss was observed up to 850 °C for a 10 ms dwell LSA. In addition, films annealed at 800 °C by LSA and subsequently annealed on the hot plate continued to form the expected 15 nm lines/spaces with no visible change in color or texture. While it is possible that the high LSA temperatures may have disturbed the underlying directing pattern, we believe this to be unlikely. First, the BCP itself is stable against thermal degradation up to 850 °C. Second, the cross-linked polystyrene guide stripes were still visible in SEM at temperatures exceeding 1000 °C, though the origin of the image contrast is not known. In addition, modification of defectivity can not be a simple thermal diffusion effect as LSA after the hot plate has only minimal impact on pattern alignment. If the defect reduction process were purely thermal, that is, only dependent upon polymer diffusion, hot plate and LSA treatments would be additive and scale with the effective diffusion distance $\sqrt{Dt}$, with the final result being independent of the annealing order.

Consequently, we believe both the enhanced alignment and loss of alignment at higher temperatures are due to changes in the initial ordering of the BCP film developed during LSA and prior to the hot plate anneal. Ordering behavior of the BCP under spin coating and subsequent thermal processing may explain this behavior. The driving force for phase segregation impacts the film structure starting at the spin coating step. During spin coating, the polymer will develop composition fluctuations while quenching from the swollen solvated state to the kinetically trapped thin film. These composition fluctuations are not fully developed nor completely aligned to the directing template due to

the limited evaporation time. It is likely, however, that some preferential texturing to the directing template does develop which then refines during the hot plate temperature ramp. Phase segregation will be essentially complete during the ramp to the hot plate temperature since only tens of milliseconds are required at 250 °C. Imperfections in this initial alignment then must be annealed out during the remaining anneal time as large scale polymer motion establishes the full DSA alignment.

An apparent ODT was observed in the DSA films above ~660 °C. Approaching the ODT, polymer mobility across the segregated interfaces is greatly enhanced and enables realignment of nucleated phase regions to the directing template, which is ultimately reflected in the lower defectivity after a hot plate anneal. In contrast, heating far above the ODT and then quenching leaves little time for realignment of nuclei to the directing template. This is then exhibited as a greater defect density, larger even than that which develops from the as spun samples. Although potential nascent polymer damage could affect this behavior, it is not believed to be the cause of this decrease in alignment. The most efficient alignment is then expected to occur just below T_{ODT} where the polymer has enhanced mobility but retains defined domains which preferentially align to the directing template.

Recently, Majewski *et al*. published work suggesting that BCP alignment could be induced along thermal gradients via a "cold zone annealing" process[95]. With thermal gradients up to 4 K/μm, alignment was achieved in 49.1 kg/mol cylinder forming PS-*b*-PMMA for laser irradiation to maximum temperatures near ~600 °C (above the measured T_{ODT} of similar molecular weight and volume fraction polymers in Chapter 5). While the present work is similar in many respects, there are also significant differences and we believe

the alignment development is related to the thermal quench rate through an order-disorder transformation rather than as a result of the relatively small spatial thermal gradients. Compared to Majewski's work, the thermal gradients during LSA annealing are actually quite similar and are set primarily by the focus of the line beam, ranging from $\approx 10\,\mathrm{K}/\mu\mathrm{m}$ in the scan direction (X) for irradiation with the CO_2 laser (250 μs to 10 ms dwells) to $\approx 1\,\mathrm{K}/\mu\mathrm{m}$ for the diode laser (10 ms dwell) irradiation. However, gradients along the long axis of the line beam (Y) are reduced by at least an order of magnitude. In contrast, the temporal gradients in this work are orders of magnitude larger reaching nearly $10^6\,\mathrm{K/s}$ for the shortest dwells.

Despite the large asymmetry in the thermal gradients for the line scan beam, both lamellar and cylindrical forming BCP samples, annealed in the absence of any directing template, exhibited no preferential alignment relative to the scan direction. Similarly, no differences were observed for scanning templated DSA samples either parallel or perpendicular to the directing template (Figure 8.2b). This is not overly surprising given that the spatial gradients, on the length scale of the 15 nm phase segregation, are quite small (<0.01 K/nm) and variations in the local driving force are unlikely to be sufficient to induce long range ordering. In contrast, the morphology development observed in Figure 6.3 clearly shows variation for changing thermal quench rates under relatively constant thermal gradient conditions. We thus conclude that the quench rate is the critical parameter controlling the segregation and ordering kinetics of these BCP films.

8.4 Conclusions

While single LSA scans do not provide sufficient time at temperature to achieve full DSA alignment, multiple scans at 450 °C for 10 ms resulted in films with reduced defectivity compared to hot plate annealing alone. When combined with a hot plate anneal, LSA after a hot plate anneal was shown to to be moderately effective in annealing out residual defects. After 10 passes at 590 °C with a 10 ms dwell, defective area was reduced from 36% to 20%.

A greater improvement was achieved by using a single LSA scan prior to the conventional hot plate anneal. Utilizing a single 10 ms LSA at 510 °C followed by a standard hot plate anneal, the overall defectivity was reduced by >80%, with the aligned area fraction increasing from 74% to 95.6%. A maximum in overall defectivity reduction was observed for LSA anneals near 500 °C. The correlation of this observation with an order-disorder transition near 660 °C strongly suggests that initial phase segregation is critical in determining the ultimate DSA alignment fidelity after LSA and hot plate anneals.

8.5 Acknowledgments

Guanyang Lin of EMD Performance Materials (Merck KGaA) is gratefully acknowledged for DSA templated samples as well as Professor Uli Wiesner for useful discussions and use of equipment. Work was performed in part at the Cornell NanoScale Facility (CNF), a member of the National Nanotechnology Infrastructure Network, which is supported by the National Science Foundation (Grant ECCS-0335765) and made use of the Cornell Center for Materials Research (CCMR) shared facilities which are supported through the NSF MRSEC program (DMR-1120296).

CHAPTER 9

CONCLUSIONS AND FUTURE WORK

9.1 Conclusions

Block copolymer (BCP) self-assembly may potentially enable cost-effective next-generation sub-20 nm semiconductor devices and help maintain the pace of Moore's law via directed self-assembly (DSA) lithography. DSA utilizes BCPs starting from deeply metastable states; however, the initial phase segregation kinetics are poorly understood. This initial step is critical to pattern formation, device function, efficacy, and yield, and better kinetic understanding would enable the rational design of processes and devices. In order to develop this understanding, 250 μs to 10 ms duration laser spike anneals (LSA) were performed to probe the kinetics of both BCP segregation and DSA alignment on otherwise inaccessible time and temperature scales.

These short duration anneals were shown to increase the thermal stability of typical organic materials by over 450 °C compared to hot plate limits. This stability was quantified using Arrhenius kinetics with activation enthalpies ranging between 66 and 107 kJ/mol (0.68 and 1.11 eV). Decomposition activation energies scaled inversely with bond polarity and proportional to the primary (backbone) bond formation energy. With increasing polarity, the activation energy for polystyrene decomposition of 91±10 kJ/mol decreased to 75±4 kJ/mol for poly(4-vinylpyridine). The bond formation energy showed even larger changes with decomposition of PS-*b*-PEO (f_{PS}=0.87) exhibiting an E_A=70±1 kJ/mol while PS-*b*-PDMS 4:1 decomposition exhibited an E_A=103±15 kJ/mol.

This extended thermal stability regime was exploited to probe the self-

assembly kinetics of cylinder forming poly(styrene-*block*-methyl methacrylate) (PS-*b*-PMMA, 54 kg/mol, f_{PS}=0.67) by annealing at temperatures up to 550 °C for timescales from 250 μs to 10 ms with heating and cooling rates in excess of 10^6 K/s. Segregation kinetics were quantified by X-ray scattering (μ-GISAXS) and electron microscopy (SEM). An order parameter was defined based on the X-ray scattering intensity to follow segregation and desegregation behavior quantitatively. This allowed the development of kinetic phase maps to describe the phase segregation behavior as a function of the peak temperature and LSA dwell.

Starting from the well ordered, phase segregated state, the polymer starts disordering near T_{ODT} for long dwell anneals. Below 1 ms, the polymer disordering for this molecular weight is kinetically suppressed. For 250 μs LSA, disordering is delayed from the 180 °C T_{ODT} to ≈250 °C. For anneal temperatures in excess of ≈370 °C, the polymer attains the fully disordered state and the resultant morphology is determined by the quench rate through T_{ODT} toward T_g. Both of these onset temperatures asymptotically approach T_{ODT} for long dwell times but diverge got shorter dwells. From an initially disordered state, the behavior follows a similar pattern with phase segregation beginning near T_g, but which is significantly suppressed for the shorter dwells. Additionally, as only order that forms during the initial heating must be removed, the onset of quench determined order occurs at a lower threshold temperature than for the initially segregated material.

This high temperature, history-independent structure, is determined by the quench rate through T_{ODT} toward T_g. The resultant X-ray scattering intensity, $\Gamma_{residual}$, was consistent when starting from either the disordered or the phase segregated states, but does critically depend on the anneal duration. Extrap-

olations from this scattering intensity suggest that this system will retain the initial state to extreme temperatures for quench rates exceeding 10^7 K/s (10 μs dwell), and will develop full phase segregation for quench rates below 10 K/s (10 s dwell).

The kinetic segregation suppression at short dwell times was shown to be consistent with the estimated diffusion rates of the polymer at these temperatures and time scales. This suggests a spinodal-like process governs the initial segregation rather than the preciously expected nucleation and growth mechanism. While nucleation is predicted, and indeed seen in some systems, it is likely that, for deeply metastable states at large undercoolings or superheatings beyond T_{ODT}, the nucleation barrier becomes small leading to diffusion limited segregation behavior.

This behavior was modeled using both Avrami rate equations and using a spinodal decomposition based model. Both models were able to replicate the low- and high- T annealed behavior by choosing appropriate nucleation energy barriers and kinetic prefactors. However, no single set of parameters were able to replicate the behavior over the entire temperature range. Although modeling proved challenging, these calculations showed that reduced Avrami growth dimensionality best replicated the data along with the spinodal model. Both models predicted increased segregation near T_{ODT}. However, no such signal was observed for PS-*b*-PMMA, though preliminary PI-*b*-PS data shows a significant enhancement at long anneal durations. This result warrants further investigation.

These BCP segregation kinetics control the ordering and templating processes required for DSA lithography. High temperature LSA near T_{ODT} was explored as a means to reduce the segregation driving force relative to the align-

ment driving force and increase polymer mobility. This regime should ultimately reduce defectivity during DSA by promoting higher fidelity polymer alignment to the directing template.

DSA alignment of 15 nm lamellae polymer on a 45 nm half-pitch template was examined under hot plate, LSA, and combinations of both, anneals. Defectivity of samples was quantified by the sample area fraction aligned to the directing template via image processing SEM data. Standard hot plate anneals for 2 minutes in air exhibited strong alignment but with ~25-35% defective area with significant sample-to-sample variability. Single LSA scans at dwells up to 10 ms, and at all temperatures, did not provide sufficient time at temperature to achieve any significant DSA alignment. Multiple 10 ms scans at 450 °C did result in films with reduced defectivity compared to hot plate annealing alone, although thermal damage also occurred under these conditions. When combined with a hot plate anneal, LSA after a hot plate anneal was shown to to be moderately effective in annealing out residual defects. After 10 passes at 590°C with a 10 ms dwell, defective area was reduced from 36% to 20%.

A much greater improvement in defectivity was achieved by using a single LSA scan prior to a conventional hot plate anneal. Utilizing a single 10 ms LSA scan at 510°C followed by a standard hot plate anneal, the overall defective area was reduced from 26% to 4.4%, a relative reduction of >80%. The maximum benefit was observed for LSA anneals near ~500 °C, which correlates well with the order-disorder transition near ~660 °C. The significantly faster heating rate under LSA, compared to a traditional hot plate anneal, likely resulted in better initial alignment to the directing template during segregation at high temperature, due to increased polymer mobility. However, no biased alignment after a single LSA anneal could be observed by top-down microscopy. This suggests

significant 3-d structural evolution, or another mechanism, is responsible for this observed reduction in defectivity.

9.2 Future Work

9.2.1 *in-situ* Probing of Sub-millisecond Annealing Behavior of Materials

The most powerful and challenging prospective project would be for *in-situ* measurements of material properties under LSA. This is possible for small probe sizes relative to the laser focus and is not limited merely to BCPs. In the case of this research, *in-situ* measurements with X-ray scattering are especially challenging as a grazing incidence geometry is used to increase the scattering volume and resultant signal. Even for the nominally 20 μm FWHM μGISAXS incident beam, smearing in one direction can be up to 8 mm.

In order to tolerate such a large probe dimension, the LSA incident laser beam must also be enlarged. To maintain the temporal and thermal capabilities, a higher power laser defocused in only one dimension would be ideal. This would require replacing the existing 120 W CO_2 laser with a ~2 kW laser. This power requirements stems from scaling the ~500 μm FWHM focus to a ~8 mm FWHM. In the absence of sufficient laser power, a larger, but sub-optimal, incident angle could be used to minimize the necessary power.

While achievable technically, the tight geometric constraints of GISAXS coupled with requirements for the laser focal plane and sample motion will significantly challenge any experimentalist. To relax some of these constraints, a short wavelength X-ray transmission setup would be beneficial and cause no geo-

metric smearing of the incident X-ray beam. Additionally, to relax constraints of sample motion to define the laser dwell, a rotational geometry would be preferred for stability and increased acquisition time.

Though difficult, these *in-situ* measurements would be especially powerful as it would decouple the metrology and annealing timescales.A long duration LSA, such as 10 ms, could be probed on microsecond time scales. This allows a single acquisition to use a long integration time to probe subtle or large amounts of information at a time resolution only limited by the probe spatial resolution. If the spatial resolution could be relaxed using, for example, a wide beam, many of the experimental challenges would be mitigated. As light based probes are mostly insensitive to material motion and require only flat and uniform films, LSA can be effectively probed by X-ray scattering, diffraction, spectroscopy, flourescence, FTIR, Raman, and similar techniques. The potential to probe structural, chemical, vibrational, and spectroscopic information during LSA would greatly expand the scientific investigations possible.

9.2.2 General Segregation Behavior via Additional Polymers

PS-*b*-PMMA is special as both components have nearly equal T_gs. A low T_g material can act as a plasticizer in polymer blends suggesting that, for BCPs with both a high- and low- T_g block, the disordered structure can have significant mobility. Furthermore, PS-*b*-PMMA is a low χ system with a very weak temperature dependence. Other systems, such as PS-*b*-PDMS, PI-*b*-PS, and PS-*b*-PEO have strong interactions. For moderate polymer molecular weights, disorder may occur before the films thermally decompose. The extended stability of polymers under LSA provides significant opportunities to measure the ODT and examine metastable structures within these polymer systems.

Specifically, measuring T_{ODT} for a series of molecular weights and compositions would, at minimum, allow for precise determination of the temperature dependence of χ and likely bound the absolute value as well. For measurements of multiple compositions, the phase diagram could be measured and asymmetries, such as has been shown for PS-*b*-PI, could be mapped in additional systems. This could allow for verification of predictive theories for skew in the phase behavior.

Regardless of the system, high T_{ODT}s (~300-800 °C) observed under LSA should be verified to be an actual ordering transition rather than damage induced disordering or signal loss in GISAXS (or other metrology). Verification could be as simple as oven annealing to produce phase segregation again but could also involve FTIR or NMR to look for decomposition byproducts.

9.2.3 PS-*b*-PMMA Extension

The short time diffusion limited behavior of PS-*b*-PMMA is in contrast to theoretic predictions of nucleation and growth, as well as nucleation behavior observed in other systems for shallow quenches. This may be symptomatic of the large undercooling/superheating from LSA where the nucleation barrier is greatly reduced. However, additional measurements of other molecular weights of PS-*b*-PMMA would allow confirmation of diffusion scaling relations. As the diffusion can be predicted, this suggests that the kinetic phase map can be used as a critical test of the diffusion limited mechanism.

9.2.4 Directing Template Interactions with LSA

While significant DSA defectivity reduction was shown for LSA anneals prior to traditional processing, the root cause is still not completely known. The effect may be related to interactions with the directing template or to unpinning or avoiding trap states from the initial slow heating on the hot plate. Understanding of the 3-d structure of segregated domains after a LSA and for short (~1-5 seconds) hot plate anneals would be elucidating. Directly measuring the 3-d structure has been shown possible by Nealey *et al*. via TEM tomography providing potential for collaboration or inspiration. Additionally, *in-situ* measurements of even just the 2-d top-down view of hot plate annealed structure would potentially identify trap states hindering subsequent defect annealing.

The presented DSA work utilized anneals in ambient. Preliminary data shows that annealing under a nitrogen rich ambient or a flowing nitrogen environment, modifies the baseline defectivity behavior significantly. Under a nitrogen rich ambient, sample defectivity was as low as ~5% but was inconsistent under the flowing nitrogen gas. The inconsistent behavior under flowing nitrogen may have been from turbulent mixing causing contamination from with nearby air increasing oxygen content, increased particulate impingement on the surface, or induced surface perturbations from the turbulent flow. Future work would benefit from investigations utilizing an inert or dry glove box environment, or otherwise controlled atmosphere for LSA.

APPENDIX A

LSA METROLOGY AND MATERIALS COMPATIBILITY

This appendix enumerates calibration techniques for LSA, and short duration anneals in general using material transformations such as melt and decomposition and direct relative measurements using thin film thermistors. It also discusses inherent biases and non-idealities of these measurements and how to estimate and potentially mitigate their effects. A brief discussion of the extended capabilities of LSA, in terms of substrates, surface films, and anealing ambient is also included. This text is intended to supplement the current LSA manual for future research.

A.1 Absolute Temperature Calibrations

Ideal temperature calibrations are dwell independent, substrate agnostic, internally precisely calibrated, and readily performed. No ideal calibrations exist. To provide precise calibrations, material transformations such as melt, are close to ideal as they occur at externally verifiable and precise temperatures. For simple metals, melt can occur very rapidly yielding dwell independent calibrations. However, many elements interact with the substrate in the molten state making them unsuitable as primary calibrations. Organic or compound material melt can also be used but melt may be kinetically limited yielding dwell dependent issues, or may go through glass transitions rather than a precise melt process. Bell *et al.*[117] summarizes many of the challenges for calibration and details several techniques.

A.1.1 Melt Processes

Substrate Melt

Often the easiest calibration to perform is to observe the substrate melt or damage threshold. In addition to understanding the envelope of conditions available to the substrate, this provides a calibration at the highest temperature available potentially leading to more precise temperature interpolation. For silicon, melt occurs at 1414 °C and is readily identifiable by bright field or dark field optical microscopy of the resolidified grains, as seen in Figure A.1.

While useful in some instances, substrate melting has several drawbacks. In order to observe the melt process, the melting must not only go to the melting point, but also overcome the enthalpy of melt requiring additional energy input. This potentially shifts the melt threshold to higher powers.

Additional substrate specific effects can also shift this temperature calibration. Most materials systems undergo significant perturbations to the thermal conductivity and absorptivity near the melting temperature. For example, molten silicon is metallic and reflects light more strongly than the crystalline phase, potentially leading to surface melt reflecting power while potentially remaining unidentifiable due to single crystal regrowth. Some substrates even undergo catastrophic failure (e.g. glass and sapphire) leading to potential health hazards as well as disqualification of substrate melt measurements. In summary, these effects limit the usefulness of substrate melt relative to other characterization techniques[117].

Thin Film Melt

To circumvent substrate melt limitations, many thin films deposited onto the substrate can be used to calibrate annealing temperatures. This often consists

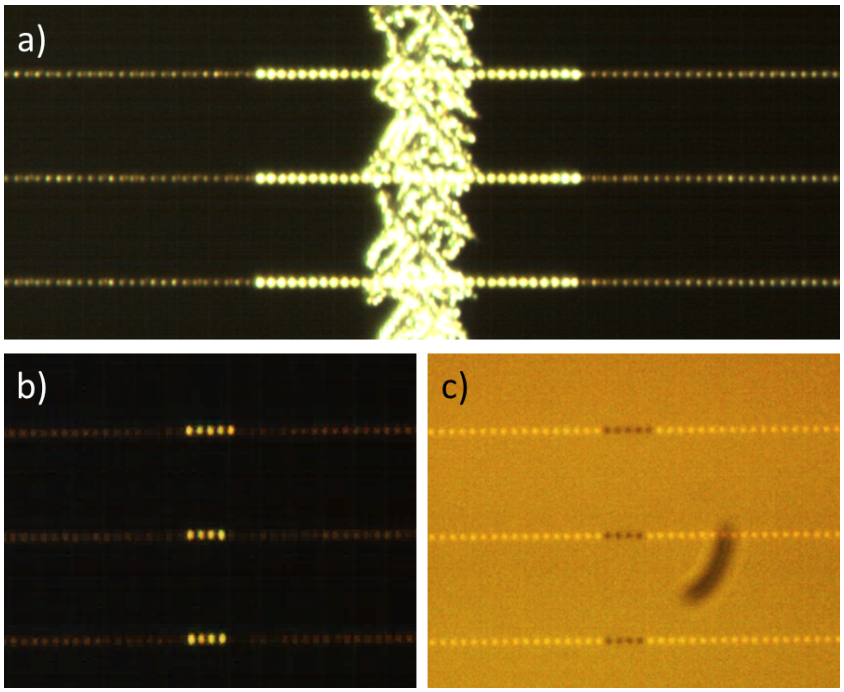

Figure A.1: Calibration by silicon and gold melt. (a) Dark field micrograph of recrystallized silicon melt with wide gold melt region, (b) dark field and (c) bright field image of gold melt onset with narrow melt region. Gold features are patterned at 10 μm intervals providing simultaneous melt width measure.

of deposition of some transparent thin blocking layer, often an oxide or nitride, the calibration material, and patterning to avoid perturbations in the laser absorption. Due to the addition of an interface between materials, compound formation often occurs and must be mitigated for precise transformation temperatures.

Elemental melting points are often more ideal as they occur at discrete temperature, are rapid, and thin films are typically simple to deposit and process. As an example, gold melt is often used as it is unaffected by ambient oxygen and forms spheroidal dots on oxide surfaces after melting providing a clear optical signature in both bright and dark field microscopy, shown in Figure A.1.

While nearly ideal, gold can form a low temperature eutectic with chromium (also silicon, germanium, etc.), a common material used to promote adhesion to the substrate. It also reflects most laser wavelengths leading to perturbations to the temperature profile for dense patterns, as shown in Figure A.2.

The melt of gold at 1064 °C is beyond the stability of some substrates. In this case, a lower temperature calibration material must be used. Most metals have higher melting points. Many low melting point metals prove reactive (e.g. the alkali metals), oxygen sensitive (aluminum, etc.), fab unfriendly (zinc, lead, tin, bismuth, etc.), or toxic/radioactive. Germanium melt may be possible to use but the temperature remains relatively high at 938 °C.

Low temperature calibrations can utilize organic or ionic materials which can undergo melt at much lower temperatures. Due to the relatively sluggish kinetics of melt, there is the potential for dwell dependence in the experimentally observed transition temperatures. Organic films of tetrabutylammonium hexafluorophosphate (TBAHPF) have been successfully utilized by Majewski *et al.*[95, 154] on long anneals (seconds to 100 ms), but no similar films or materials have been explored at Cornell to date.

A.1.2 Thermal Decomposition

The thermal decomposition of thin film organic materials can also be used to calibration temperatures on most substrates. This has proved easier to use on some substrates as the organic material can be spin coated, avoiding high temperature processing. However, thermal decomposition requires its own calibration. Thermal decomposition is significantly dwell dependent and can vary by several hundred degrees by varying dwell from 10 ms to 100 μs (see Chapter 4). The film thickness can also affect the apparent decomposition temperature as thicker

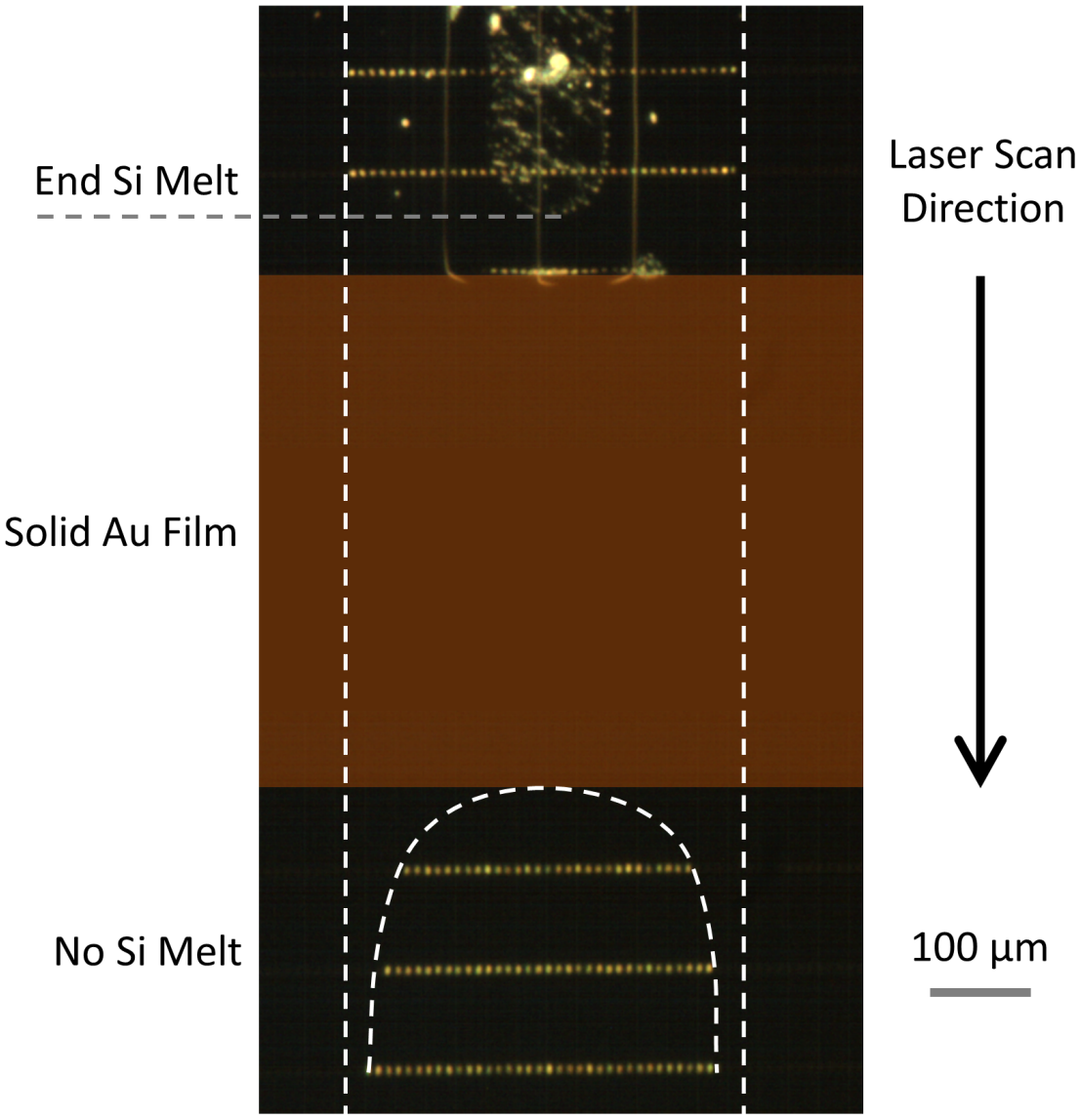

Figure A.2: Gold and silicon melt perturbations near dense gold pattern. White dashed lines show the 1064 °C temperature envelope after scanning from top to bottom. After scanning past the dense pattern, the gold melt width is diminished and varies with distance from the pattern. Silicon melt is not observed again until after a long distance from the dense pattern.

films require more material to volatilize than thinner films. Despite these challenges, this technique has been successfully used for calibrating temperatures on InGaAs/InP substrates[186].

A.1.3 Visual Calibration

When using a new substrate for the first time, rough visual cues can give clues as to the temperatures being achieved. Black body emitters visibly glow at temperatures beyond ~500 °C starting at a faint, deep red and glowing brighter and whiter at higher temperatures.

In my experience calibrating silicon, the substrate only visibly glowed above ~800 °C under the laser. This is probably due to the small area emitting light and short observation time. In a darkened room, 900 °C silicon can be seen with a medium red. At 1064 °C, the melting point of gold, sample areas glow a soft yellow. At the melt of silicon, the material glows white but not blindingly. Higher temperatures, such as during spallation of sapphire, yield blackbody light that can be blindingly white.

Often sparks can be seen while annealing. These arise most often from particulates on the surface, or sample edges, which are heated by the laser to high temperature. To avoid perturbing the anneals, all films should be cleaned handled in cleanroom like conditions and with cleanroom procedures, cleaned for annealing, or at least blown off before annealing.

A.2 Beam Intensity Profiling and Focusing

Beam intensity profiling and thermistor measurements are very similar. Both move a small probe beneath the scanned laser to probe a small section of the

beam. While thermistors directly measure the surface temperature, beam profiling uses a photon detector and a small pinhole to probe the laser intensity profile at the plane of the pinhole. This intensity profile is necessary to determine the actual laser focus, which in turn is then used to determine dwell time.

For the diode laser, a standard photodiode is used. For the CO_2 laser, a mercury-cadmium-telluride (MCT) detector is used. Each detector has separate and distinct amplification circuitry. **The use of the wrong amplifier can damage or destroy the detector or amplifier.** A circular 50 μm diameter pinhole is typically used. Smaller pinholes can be purchased but they require high power to obtain acceptable signal which damages the pinhole. These are actual optics (purchasable Thorlabs or others) and not simply a hole punched through aluminum foil with a pin.

Profiling the beam intensity is used as a final step in focusing the laser. The first step typically uses burn paper to get close to focus with fine adjustments done via profiling with quantification of the beam size. A step by step guide to beam profiling is included at the end of the LSA manual for reference.

A.2.1 CO_2 Laser Focusing Considerations

The CO_2 laser is focused by two crossed cylindrical lenses. One lens defines the short axis of the beam and is in focus (~100 μm), while the other defines the long axis of the beam and is intentionally out of focus (~500 μm currently). In addition to controlling the distance from the lens to the sample plane, the relative rotation of the two lenses, as well as the rotation of both lenses to the sample plane, is important.

Due to the use of two cylindrical lenses, there are several consequences with regard to alignment of the long and short axes. First, if you look at the beam

profile on burn paper at a specific height, the direction the long axis points is very sensitive to the relative rotation of the two lenses. Second, the beam profile changes as a function of optical path length. This can make focusing the CO_2 laser frustrating if not understood. Simultaneously obtaining both the correct focal length and orientation of the CO_2 long axis can be challenging.

To focus the CO_2, I start by mounting the two cylindrical lenses with the correct orientations and viewed the beam with burn paper. I initially focus on the relative rotation of the two lenses to obtain the narrowest beam in one axis possible regardless of beam long axis orientation. Then I focus on the focal length and get it close with burn paper. Once near the correct focal distance, I rotate *both* lenses precisely the amount necessary to align the long axis correctly. This must be done carefully as the relative rotation of the lenses is sensitive to $<0.1^\circ$. Using the verniers gets you close, and you can refocus with the burn paper for relative rotation. Finally, I use the beam profiling to adjust the lens to sample distance precisely to the required beam dimensions.

A.2.2 Diode Laser Focusing Considerations

The diode laser is coupled into a 200 μm core fiber optic out of the laser head. This fiber is coupled to the beam homogenizer which consists of a water cooled quartz homogenizing plate and focusing optics. The homogenizing plate is 2 mm thick, which serves to define the long axis of a top-hat beam profile. The long axis of the homogenizing plate is focused down to the narrow axis of the beam. The tightest focus possible on the narrow axis is set by the fiber optic core diameter as this is imaged onto the sample plane.

In some ways, focusing the diode laser is simpler as there are only two variables: the distance to the sample plane and the homogenizer rotation. The rota-

tion of the homogenizer is more readily discerned compared to the CO_2 optics as multiple images of the top-hat profile overlay when at the correct rotation. The lens to sample distance similarly can be found using burn paper and beam profiling.

Compared to the CO_2, the diode laser is more powerful, but is limited to lower temperatures at short times. This stems from the lower power density from the larger beam focus, currently 2 mm by 300 μm. In addition to requiring greater powers for the same temperature, the lateral temperature profile is significantly dwell dependent. At short dwell times, the peak temperature profile closely follows the intensity profile. At long dwell times, the profile rounds out significantly due to thermal spread, losing the flat top-hat temperature profile. In contrast, thermal spread of the initial CO_2 Gaussian profile only yields a slightly broader Gaussian profile.

A.3 Thermistors: Relative Temperature Calibrations and Temperature Profiling

While absolute calibrations from material melt processes give precise temperatures at a specific power, it does not give the full picture. The temperature to power relation is not linear, arising primarily from the temperature dependent thermal and optical substrate or susceptor properties. Measurements of many material transitions to obtain a dense set of calibrations is typically not practical.

Thermistors provide temperature measurements based on the known temperature dependent resistivity of some material, typically a metal. Custom thin film platinum thermistors and signal amplification circuitry were fabricated to provide measurements at any temperature up to the substrate or thermistor

damage threshold[187]. Platinum was specifically chosen as it provides a near perfectly linear relation between resistivity and temperature from room temperature to above 1000 °C. Though thermistors can, in principle, provide absolute temperature measurements, these measurements are currently used only as a relative measurement.

For measurements, the thermistor is scanned under the laser collecting both current and voltage measurements. To calibrate intermediate powers, the thermistor is aligned to the center of the laser scan and monitored as the power is increased. The power is typically ramped from 0 to a max near ~1200 °C (on silicon), and then back down to zero for several cycles. It is important to ramp iteratively up then down to spot any hysteresis. The maximum temperature is limited to 1200 °C to avoid slip in silicon which would destroy the thermistor.

The primary use of these thermistors is to map out the nonlinear component of the power–temperature relation. Figure A.3 shows the peak thermistor resistance change as a function of CO_2 laser power for dwell times from 150 μs to 5 ms. These data do not follow a linear trend except at low powers. This means that any linear interpolation between zero and a single calibration point, like gold melt, would prove erroneous.

Temperatures from thermistor measurements are then absolutely calibrated by assigning the melting point of gold to the identified power threshold for thin film gold melt. The gold melt calibration, denoted by the dashed-dot line, falls within the thermistor data providing a robust measure of the temperature. As temperatures approach the substrate (silicon) melting point, denoted by the dashed line, the thermistor data shows significant nonlinearity and slope compared to low temperature measurements.

While thermistors allow for precise temperature interpolation, they also pro-

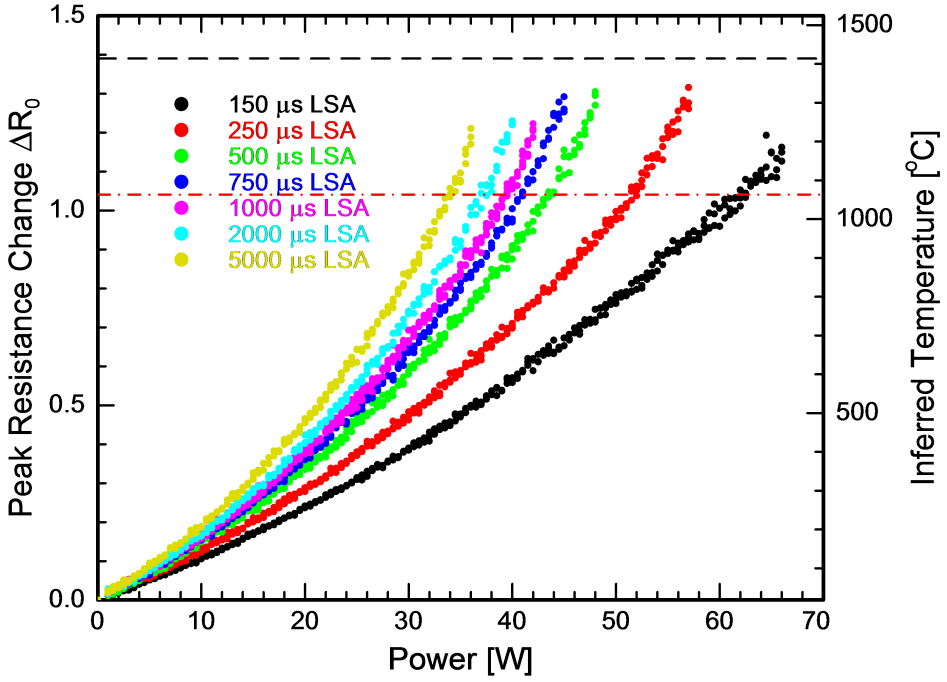

Figure A.3: Peak LSA temperature as a function of laser power for dwell times from 150 μs to 5 ms exhibiting nonlinear behavior. The substrate (silicon) melting point is denoted by the dashed line and calibration temperature (gold melt) is denoted by the dash-dot line.

vide a measure of the spatial and temporal temperature profiles. By recording the resistance as a function of time, and using multiple thermistor measurements from scanning laterally across the laser profile, the full 2D surface temperature profile can be established for each dwell time. Thin film platinum thermistor measurements were obtained for each dwell to yield temperature maps as shown in Figure 5.2a.

These spatial profiles were taken at several peak temperatures; the spatial profile is slightly temperature dependent due to changes in silicon thermal diffusivity with temperature. This yields quantitative data for the peak temperature as a function of lateral position (x- direction) and as a function of the peak temperature. Figure 5.2d shows one measurement of the maximum tempera-

ture experienced as a function of lateral position across a 250 μs LSA. These data were then fit to a sum of Gaussian profiles for conversion from position to peak anneal temperature. These measurements have proven especially important for lgLSA[117] experiments.

Thermistor measurements can be limited in some instances. As currently implemented, these thermistors are integrated into a DIP package for easy replacement if damaged. In these packages, the chip is glued to a plastic body which deviates from the aluminum chuck that samples are placed on during typical LSA. This difference can play a role for "long" LSA anneals when the substrate is no longer thermally thick (typically >1 ms for Si and very pronounced at 10 ms).

The thermistor package will tend to read higher absolute temperatures and take longer to quench toward ambient for long dwells compared to samples annealed on the chuck. This can be accounted for, but is one of many reasons why thermistors are used as a relative temperature measure and absolute temperature calibration on the chuck must also be used. For more detail regarding the design of the thermistor measurements, see the work by Byungki Jung[187]. Also, detailed step by step instructions can be found in the LSA manual.

A.4 Materials Compatibility

A.4.1 Substrates

While silicon has been commonly utilized for LSA, many substrates are suitable for laser based heating. The primary requirements for a suitable substrate material are an ability to absorb the laser light and the tolerance of thermal shock.

The common modes of light absorption for LSA are by interband (direct absorption) and intraband (free carrier) absorption. Semiconductors can readily

absorb light at energies larger than the band gap (E_g). For silicon, this requires photon energies >1.1 eV (λ <~1120 nm) and can be used for any doping concentration. Free carrier absorption, however, requires free electrons or holes in order to absorb light by intraband transitions. For this absorption mechanism, highly doped semiconductors are required. Free carrier absorption scales with λ ($\lambda^{1.5}$ to $\lambda^{3.5}$) and favors very long wavelength sources (such as the CO_2 laser at λ=10.6 μm).

Substrates must also tolerate the large thermal gradients inherent to LSA, which can cause materials to fracture. Figure of merits for the thermal shock resistance, R_{TS}, include:

$$R_{TS,1} = \frac{k_{th} K_{Ic}}{\alpha Y}, [R_{TS,1}] = \frac{W}{m^{1/2}} \tag{A.1}$$

or

$$R_{TS,2} = \frac{k_{th}(1-2\nu)\sigma_t}{\alpha Y}, [R_{TS,2}] = \frac{W}{m} \tag{A.2}$$

where k_{th} is the thermal conductivity, K_{Ic} is the fracture toughness, α is the coefficient of thermal expansion, Y is Young's modulus, ν is Poisson's ratio, and σ_t is the tensile strength[188]. For brittle materials, these forms only differ by a factor of $\sqrt{c_{max}}$, where c_{max} is the maximum defect size.

The most important properties for thermal shock resistance are the thermal conductivity and coefficient of thermal expansion. Materials with a large thermal conductivity also increase the quench rate for a given dwell as heat is more readily quenched into the substrate. However, increasing the thermal conductivity also decreases the anneal duration for which a substrate can be considered thermally thick. For thermally thick substrates, calibrations are more robust, while thermally thin substrates interact significantly with the supporting structure which can cause perturbations to calibrations. Table A.1 lists calculated thermal shock resistance values and select properties for common materials.

Table A.1: Thermal shock resistance and select properties of several semiconductors and relevant materials. *May decompose before melt.

Property	$R_{TS,1}$	k_{th}	K_{IC}	α	Y	T_{melt}	$E_g^{300\,K}$
Units	$W/m^{\frac{1}{2}}$	W/mK	$MPa\,m^{\frac{1}{2}}$	$10^{-6}\,K^{-1}$	GPa	°C	eV
SiC*	1700	360	4.6	3.8	250	2800*	2.36
W	480	173	5	4.5	400	3410	–
Si	270	130	0.83	2.7	150	1414	1.12
GaN*	90-130	130	0.8-1.1	6	181	2200*	3.45
Ge	95	60	1.0	5.9	100	937	0.66
InP	90	70	0.36	4.6	60	1060	1.34
GaAs	45	55	0.41	5.7	85	1240	1.42
Al_2O_3	20-60	17-23	3.3-5	6-7	345	2040	8.8
SiO_2	7-30	1.38	0.6-0.9	0.55	70-200	11-1900	~9

These thermal shock values give a starting point in evaluating potential substrates. Silicon can be annealed nearly to melt with little concern for substrate fracture. Near the melting point (>1300 °C), thermal stress induced slip can leave residual stresses in the substrate causing fracture. In contrast, sapphire (Al_2O_3) substrates, which have 10–20% the thermal shock figure of merit, have only been successfully annealed by LSA to moderate temperatures of ~1000 °C. Attempting higher temperatures, near ~1300-1500 °C, caused surface spallation. Similar results were also observed for GaN, though with less material removal at similar temperatures.

A.4.2 Surface Films

Thin surface films typically yield before fracture, which may circumvent thermal shock limitations. However, films may still mechanically fail and delaminate, buckle, or fracture from thermal expansion mismatch with the substrate. The ideal thin film sample is both transparent to, and noninteracting with, the laser. This would allow the substrate calibration to be used without additional steps or corrections. Ideal films do not exist and the experimentalist must deal with these nonidealities. Even for a fully transparent film, thin film optical interference will modify the reflectivity and must be taken into account. This can either increase or decrease the absorbed power compared to bare substrate. Uniform opaque films shift the absorption to the film and a new peak temperature calibration is necessary. However the relative spatial temperature profiles are likely still accurate since they are largely defined by the substrate thermal transport.

For spatially inhomogeneous or patterned features, both average and local temperature perturbations typically exist. An extreme example of this behavior is shown in Figure A.4, where a highly reflective 100 μm gold grid has severely perturbed polymer decomposition. Even small and isolated features can significantly modify the local temperature profiles.

A.4.3 Substrate and Film Thickness

Both the film and substrate thicknesses play roles in uniformity of annealed areas, both laterally and longitudinally. Ideal substrates are infinitely thick providing bulk material for the thermal quench. Ideal surface films are also thermally thin with minimal temperature gradients through the thickness of the film. The appropriate thickness of each can be calculated from the thermal dif-

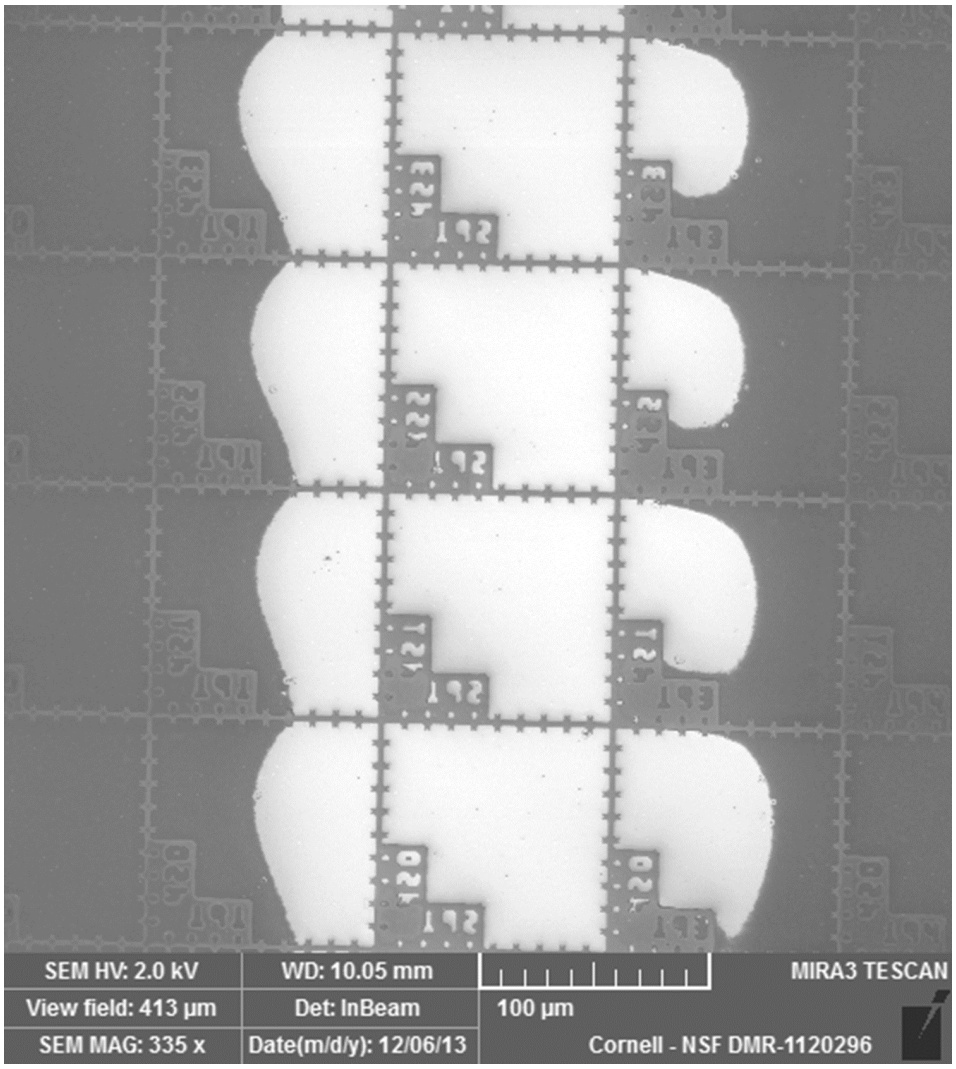

Figure A.4: Local temperature perturbations due to reflections off gold grid modified polymer decomposition yielding a scalloped pattern. Bright area in center is bare silicon, grid lines are 100 nm of gold, polymer is shown in gray. Edge of polymer decomposition is an isotherm which is not uniform along anneal line.

fusion distance. These thicknesses are always flexible and readily modified. Such calculations can help you understand the effects of having too thick of a surface film, or too thin of substrates.

In particular, the substrate is often thermally thick at short dwell times, but thermally thin at long dwell times. For silicon, the substrate is thermally thin for dwells beyond ~1 ms with considerable effects present for 10 ms or longer anneals. Beyond causing excess lateral thermal spread, the substrate "feels" the underlying surface. This can present itself as higher temperatures when annealing over vacuum channels. Variations in the backside thermal resistance are likely the fundamental cause of unexplained variations in temperature along the length of an anneal.

The full thermal spreading behavior must also be properly addressed. Heat spreads both in front of and behind the laser spot. At the start of a laser scan, some distance is required before a steady state temperature profile is established. Conversely, when the scan leaves a sample or approaches the edge, elevated temperatures are transiently experienced by the sample. This can cause failure for anneals near substrate power limits or inconsistent devices near edges. In order to obtain precise GISAXS data, I utilized a long lgLSA scans and cleaved off the first and last ~5 mm of each scan. It is not always possible to remove all edge effects, especially on small sample chips. In these cases, consistency is of paramount importance.

A.5 Annealing Ambient Modifications

In addition to the standard sample holder, several additional devices have been created to modify the annealing ambient. A small high temperature (<700 °C) hot plate can be used to add an elevated temperature baseline to the anneal.

This can, in turn, reduce the thermal shock effects. Heating can also be useful to generate thermal carriers for free carrier absorption, or for improving substrate compatibility.

A windowed chamber for controlling the anneal atmosphere with flowing gas has also been created. This chamber is compatible with solvent laden, or moderately reactive atmospheres, and has previously been used to minimize thermal decomposition of organics using inert atmospheres.

A.6 Comparison Between LSA and Traditional Anneals

As noted in Chapter 4, the LSA anneal duration must be carefully evaluated for proper comparison to isothermal anneals. During LSA, an effective annealing time at the peak temperature (T_{peak}) can be defined assuming an Arrhenius kinetic behavior, as shown in Equation (A.3).

$$t_{\text{eff}} = \int e^{-\frac{E_A}{k_b}\left(\frac{1}{T(t)}-\frac{1}{T_{peak}}\right)}dt \tag{A.3}$$

where E_A is the activation enthalpy and k_b is Boltzmann's constant. For "typical" E_A values of 60-100 kJ/mol (0.6-1 eV), this effective isothermal time varies from 0.7 to 1.3 τ for integrated LSA temporal temperature profiles from –25τ to +25τ. Consequently, the dwell τ, can be used as a reasonable estimate of the equivalent isothermal heating time for a single LSA scan.

When annealing areas of a substrate, the full thermal history must be taken into account. For the current CO_2 setup, the beam is rastered with a small track spacing between adjacent anneals. This track spacing has a significant effect on the effective anneal duration, a small track spacing, to achieve uniformity, anneals the same material at similar temperatures multiple times. For a 1 ms LSA with a track spacing of FWHM/10 (~50 μm), the peak temperature for succes-

sive scans yields only a 0.8%, 7%, and 18% decrease for the next three adjacent scans at the original position. This yields an effective isothermal anneal duration much longer than a single dwell time.

While comparing traditional isothermal anneals to LSA, one can often neglect this point due to the orders of magnitude difference in anneal duration. However, kinetic studies utilizing area anneals should include this effect to avoid biasing results by misinterpreting the LSA dwell time.

APPENDIX B

MACROS

This appendix will contain the general outline of analysis macros and copies the important portions of those macros including the genplot GISAXS analysis and fitting methods, and ImageJ DSA alignment macro.

B.1 Genplot GISAXS Analysis Macros

For the GISAXS analysis, the macros were kept in a centralized folder to maintain a single file version across multiple sample subfolders analyzed. In each subfolder, a macro merely called the analysis macro to do analysis on that particular folder.

B.1.1 Text GISAXS File Analysis

This macro reads in GISAXS text files as images and calculates the principle peak and background characteristics. The text files were generated using ImageJ as Genplot could not read in the tiff file at the time. This macro was used to analyze data used in Chapter 5.

```
genplot reset -silent @echo off
lt 1 pen -1 lw 2

/* ////////////////////////////////////////////////
/* Note: direct beam coords are 519.2958 pixles in x
/* and 194.2157 pixles in y, though flipped so 1024-194
/* meaning 829.7843 in y from tif-> txt transform (or genplot read
   direction)
/*
/* Other center is x,y (524.4572,189.3031), y-> 834.6969 px
/* 46.9x46.9 micron pixel size
/* 1.155 Angstroms Wavelenth
/* Sample Detector distance 1.002 m (double check, I rememer 1.6m)
/* q = 2*PI*sin(theta)/lambda = (SAA) 2*PI/lambda * (ypixel-y0)*
   conversion/S2D_length
/* q approx is true for small angle approximation, actually is q = 4*
   pi*sin(theta/2)/lambda
/* ////////////////////////////////////////////////

alias fit_sides5 \
```

```
        fit nlsfit reset accuracy accu1 equ h1(x) maxiter iter1
           verbose 0 sigma sqrt(y) \
        vary ha1 / -limit 0.01 1E7 vary hb1 / -limit 5 35 vary hx1 /
            -limit -20 20 return \
        retr c1 fit nlsfit fit \
        let p14[%m],q14[%m] = ha1,sigma$[0] \
        let p15[%m],q15[%m] = hb1,sigma$[1] \
        let p16[%m],q16[%m] = hx1,sigma$[2] \
        reset accuracy accu1 equ h1(x)+g3a(x)+g3b(x) maxiter iter1
           verbose 0 sigma sqrt(y) \
        vary ga3a / -limit 0.1 10000 vary ga3b / -limit 0.1 10000
           vary gx3 / -limit (p2low+5) (p2high-5) vary gx3delta / -
           limit -5 5 vary gdx3 / -limit 4 35 return \
        retr c1 fit nlsfit fit \
        let p11[%m],q11[%m] = ga3a+ga3b,sqrt(sigma$[0]^2+sigma$
           [1]^2) \
        let p12[%m],q12[%m] = (2*gx3-gx3delta)/2,(2*sigma$[2]^2+
           sigma$[3]^2)/2 \
        let p13[%m],q13[%m] = gdx3,sigma$[4] \
        return

alias fit_sides50 \
        fit nlsfit reset accuracy accu1 equ h1(x) maxiter iter1
           verbose 0 sigma sqrt(y) \
        vary ha1 / -limit 0.01 1E7 vary hb1 / -limit 5 35 vary hx1 /
            -limit -20 20 return \
        retr c1 fit nlsfit fit \
        let p14[0],q14[0] = ha1,sigma$[0] \
        let p15[0],q15[0] = hb1,sigma$[1] \
        let p16[0],q16[0] = hx1,sigma$[2] \
        reset accuracy accu1 equ h1(x) maxiter iter1 verbose 0 sigma
            sqrt(y) \
        vary ha1 / -limit 0.01 1E7 vary hb1 / -limit 5 35 vary hx1 /
            -limit -20 20 return \
        retr c1 fit nlsfit fit \
        let p14[0],q14[0] = ha1,sigma$[0] \
        let p15[0],q15[0] = hb1,sigma$[1] \
        let p16[0],q16[0] = hx1,sigma$[2] \
        reset accuracy accu1 equ h1(x)+g3a(x)+g3b(x) maxiter iter1
           verbose 0 sigma sqrt(y) \
        vary ga3a / -limit 0.1 10000 vary ga3b / -limit 0.1 10000
           vary gx3 / -limit (p2low+5) (p2high-5) vary gx3delta / -
           limit -5 5 vary gdx3 / -limit 4 35 return \
        retr c1 fit nlsfit fit \
        let p11[0],q11[0] = ga3a+ga3b,sqrt(sigma$[0]^2+sigma$[1]^2)
           \
        let p12[0],q12[0] = (2*gx3-gx3delta)/2,(2*sigma$[2]^2+sigma$
           [3]^2)/2 \
        let p13[0],q13[0] = gdx3,sigma$[4] \
        return

alias fit_sides51 \
        fit nlsfit reset accuracy accu1 equ h1(x) maxiter iter1
           verbose 0 sigma sqrt(y) \
        vary ha1 / -limit 0.01 1E7 vary hb1 / -limit 5 35 vary hx1 /
            -limit -20 20 return \
        retr c1 fit nlsfit fit \
        let p14[0],q14[0] = ha1,sigma$[0] \
        let p15[0],q15[0] = hb1,sigma$[1] \
        let p16[0],q16[0] = hx1,sigma$[2] \
        reset accuracy accu1 equ h1(x)+g3a(x)+g3b(x) maxiter iter1
           verbose 0 sigma sqrt(y) \
        vary ga3a / -limit 0.1 10000 vary ga3b / -limit 0.1 10000
           vary gx3 / -limit (p2low+5) (p2high-5) vary gx3delta / -
```

```
            limit -5 5 vary gdx3 / -limit 4 35 vary ha1 / -limit 0.01
             1E7 vary hb1 / -limit 5 35 vary hx1 / -limit -20 20
            return \
         retr c1 fit nlsfit fit \
         let p11[0],q11[0] = ga3a+ga3b,sqrt(sigma$[0]^2+sigma$[1]^2)
            \
         let p12[0],q12[0] = (2*gx3-gx3delta)/2,(2*sigma$[2]^2+sigma$
            [3]^2)/2 \
         let p13[0],q13[0] = gdx3,sigma$[4] \
         let p14[0],q14[0] = ha1,sigma$[5] \
         let p15[0],q15[0] = hb1,sigma$[6] \
         let p16[0],q16[0] = hx1,sigma$[7] \
         return

alias fit_sides52 \
         fit nlsfit reset accuracy accu1 equ h2(x) maxiter iter1
            verbose 0 sigma sqrt(y) \
         vary ha2 / -limit 0.01 1E7 vary hb2 / -limit 5 35 vary hx2 /
             -limit -20 20 vary hn2 / -limit 2 6 return \
         retr c1 fit nlsfit fit \
         let p14[0],q14[0] = ha2,sigma$[0] \
         let p15[0],q15[0] = hb2,sigma$[1] \
         let p16[0],q16[0] = hx2,sigma$[2] \
         reset accuracy accu1 equ h2(x)+g3a(x)+g3b(x) maxiter iter1
            verbose 0 sigma sqrt(y) \
         vary ga3a / -limit 0.1 10000 vary ga3b / -limit 0.1 10000
            vary gx3 / -limit (p2low+5) (p2high-5) vary gx3delta / -
            limit -5 5 vary gdx3 / -limit 4 20 vary ha2 / -limit 0.01
             1E7 vary hb2 / -limit 5 35 vary hx2 / -limit -20 20 vary
             hn2 / -limit 0.2 6 return \
         retr c1 fit nlsfit fit \
         let p11[0],q11[0] = ga3a+ga3b,sqrt(sigma$[0]^2+sigma$[1]^2)
            \
         let p12[0],q12[0] = (2*gx3-gx3delta)/2,(2*sigma$[2]^2+sigma$
            [3]^2)/2 \
         let p13[0],q13[0] = gdx3,sigma$[4] \
         let p14[0],q14[0] = ha2,sigma$[5] \
         let p15[0],q15[0] = hb2,sigma$[6] \
         let p16[0],q16[0] = hx2,sigma$[7] \
         let p17[0],q17[0] = hn2,sigma$[8] \
         return

alias fit_sides53 \
         fit nlsfit reset accuracy accu1 equ h2(x) maxiter iter1
            verbose 0 sigma sqrt(y) \
         vary ha2 / -limit 0.01 1E7 vary hb2 / -limit 5 35 vary hx2 /
             -limit -20 20 vary hc2 / -limit 0.1 200 vary hdx2 / -
            limit 20 100 return \
         retr c2 fit nlsfit fit \
         let p14[0],q14[0] = ha2,sigma$[0] \
         let p15[0],q15[0] = hb2,sigma$[1] \
         let p16[0],q16[0] = hx2,sigma$[2] \
         reset accuracy accu1 equ h2(x)+g3a(x)+g3b(x) maxiter iter1
            verbose 0 sigma sqrt(y) \
         vary ga3a / -limit 0.1 10000 vary ga3b / -limit 0.1 10000
            vary gx3 / -limit (p2low+5) (p2high-5) vary gx3delta / -
            limit -5 5 vary gdx3 / -limit 4 50 return \
         retr c1 fit nlsfit fit \
         let p11[0],q11[0] = ga3a+ga3b,sqrt(sigma$[0]^2+sigma$[1]^2)
            \
         let p12[0],q12[0] = (2*gx3-gx3delta)/2,(2*sigma$[2]^2+sigma$
            [3]^2)/2 \
         let p13[0],q13[0] = gdx3,sigma$[4] \
         return
```

```
alias fit_sides6 \
         fit nlsfit reset accuracy accu1 equ h1(x) maxiter iter1
            verbose 0 sigma sqrt(y) \
         vary ha1 / -limit 0.01 1E7 vary hb1 / -limit 5 35 vary hx1 /
             -limit -20 20 return \
         retr c1 fit nlsfit fit \
         reset accuracy accu1 equ h1(x)+g3a(x)+g3b(x) maxiter iter1
            verbose 0 sigma sqrt(y) \
         vary ga3a / -limit 0.1 10000 vary ga3b / -limit 0.1 10000
            vary gx3 / -limit (p2low+5) (p2high-5) vary gx3delta / -
            limit -5 5 vary gdx3 / -limit 4 50 return \
         retr c1 fit nlsfit fit \
         return \
         yright on force on label left "Signal (Counts)" label right
            "Signal w/o bkg (Counts)" label bot "Position (Pixels)"
            retr c1 reg left 0 1500 reg bot -250 250 reg right -1.2*
            max(100/1.2,ga3a,ga3b) 1.2*max(100/1.2,ga3a,ga3b) pl -sym
             4 -identify temp ov -fit let y=y-fit(x) ov -sym 4 -pen 2
             -ply right -identify "Residuals" retr c1 let y=y-h1(x)-
            g4(x) ov -sym 4 -pen 4 -ply right ov -f g3a(x)+g3b(x) -
            pen 1 -lt 2 -lw 5 -ply right -identify "Signal Fit"
            yright off force off sleep 0.4

/* Cull and signal peak range limits
setv low_cull,high_cull,midl_cull,midh_cull = 270,770,486,548 /*
   270,770,493(486),545 /* in pixels in raw image
setv p1low,p1high,p2low,p2high = 374,444,594,664
setv gisaxs_x,gisaxs_y = 519.30,834.70
setv gisaxs_q_prop = 2*pi*(46.9/1000)/1002/0.1155 /* inverse nm once
   multiplied by (ypixel-y0)

alloc cs1,cs2,cs3,cs4,cs5,cs6,cs7,cs8,cs11,cs12,cs13,cs21,cs22,cs23
   array 10000
alloc ipt int let ipt = 0

setv fcount = 0
setv loopcount = 0
/* setv rowstart = 660
/* setv rowend = 720
setv rowstart = 680
setv rowend = 770
setv npoints = 0
setv SMAperiod = 5
setv counter = SMAperiod
setv sumvar = 0
setv counter2 = 0
setv counter3 = 0
setv integrand = 0
setv low = 0
setv medium = 0
setv high = 0
setv bkg_area = 1
setv amp,s_amp,pos,s_pos,width,s_width,tot_area,s_tot_area,bkg_area,
   counter = 0,0,0,0,0,0,0,0,0,0
setv normalize_const = 1
setv s_a94,s_a93,s_a92,s_a91,s_a95,x94_delta=0,0,0,0,0,10
alloc c01 curve 1024
alloc c11 curve 1024
alloc afilename string 1
/* alloc afoldername string 1
alloc Tletter string 1
setv count = 0
setv foldercount = 0
alloc folder_list string_array 16
let folder_list[0] = "250us x1"
```

```
let folder_list[1] = "250us x2"
let folder_list[2] = "250us x4"
let folder_list[3] = "250us x8"
let folder_list[4] = "250us x20"
let folder_list[5] = "250us x40"
let folder_list[6] = "500us x1"
let folder_list[7] = "1000us x1"
let folder_list[8] = "1000us x2"
let folder_list[9] = "1000us x5"
let folder_list[10] = "1000us x10"
let folder_list[11] = "2000us x1"
let folder_list[12] = "5000us x1"
let folder_list[13] = "10000us x1"
let folder_list[14] = "10000us x2"
let folder_list[15] = "10000us x10"
cd %afoldername%
declare wherenow cwd()
read "Center.dat" archive folder_centers

let low_cull,high_cull,midl_cull,midh_cull = low_cull-gisaxs_x,
   high_cull-gisaxs_x,midl_cull-gisaxs_x,midh_cull-gisaxs_x
let p1low,p1high,p2low,p2high = p1low-gisaxs_x,p1high-gisaxs_x,p2low-
   gisaxs_x,p2high-gisaxs_x

define f1(x) = 10^3*fa1/[(x-fx1)^4+0.1]+fb1 /* remove 10^3 if go to q
   ^-2 again
define f2(x) = 10^3*fa2/[(x-fx2)^4+0.1]+fb2
define f3(x) = 10^6*fa1/[(x)^4+0.1]+fb1
define f4(x) = 10^6*fa2/[(x)^4+0.1]+fb2
define g1(x) = ga1*gaussn(x,gx1,gdx1)
define g2(x) = ga2*gaussn(x,gx2,gdx2)
define g91(x) = a91*a94*gaussn(x,(x94-x93-x92-x91),dx91)
define g92(x) = a92*a94*gaussn(x,(x94-x93-x92),dx92)
define g93(x) = a93*a94*gaussn(x,(x94-x93),dx93)
define g94(x) = a94*gaussn(x,(x94),dx94)
define g95(x) = a95*a94*gaussn(x,(x94+x95),dx95)

define h1(x) = 10^6*ha1/[(x-hx1)^4+0.1]+hb1
define h2(x) = 10^6*ha2/[abs(x-hx2)^hn2+0.1]+hb2+hc2*gaussn(x,hx2,
   hdx2)

define g3a(x) = ga3a*gaussn(x,(gx3),gdx3) /* right side
define g3b(x) = ga3b*gaussn(x,(gx3delta-gx3),gdx3) /* left side
/* define g3a(x) = ga3a*lorentzian(x,(gx3),gdx3)/lorentzian(0,gx3,
   gdx3) /* right side
/* define g3b(x) = ga3b*lorentzian(x,(gx3delta-gx3),gdx3)/lorentzian
   (0,(gx3delta-gx3),gdx3) /* left side

define g4(x) = ga4*gaussn(x,-hx1,gdx4)

setv ha1,hx1,hb1=1e3,-4,26
setv ha2,hx2,hn2,hb2,hc2,hdx2=1e3,-4,6,26,100,50
setv ga3a,ga3b,gx3,gx3delta,gdx3 = 50,50,90,0,10
setv ga4,gdx4 = 10,50

setv a91,a92,a93,a94,a95=0.1,0.2,0.38,1200,0.18
setv x91,x92,x93,x94,x95=7.7,6.7,5.7,15,3.3
setv dx91,dx92,dx93,dx94,dx95=2,2,1.2,1.2,2
setv accu1,accu2,iter1,iter2 = 1E-7,5E-7,3000,3000

setv npeaks = 1
setv npeaksmax = 0
if (npeaksmax) let npeaks = 0
setv visualize1 = 0 /* Show fitting of individual rows of image
setv visualize2 = 0 /* Show fitting of qz peaks out of fits from qxy
```

```
setv visualize3 = 1 /* Write to genplot terminal when completed every
    x images and time
setv visualize3_period = 20
setv visualize4 = 0 /* write to genplot terminal time of files being
   written
setv overwrite = 1

if (visualize4) asctime(time())


/* Main loop for all folders, modify first number to change where to
   start
loop %x=0,15,1 {

   setv count = strlen(wherenow)
   let count = count-4

/*   declare afoldername = delstr(wherenow,0,count)+" "+folder_list[%
   x]+" Linear Amplitude Fitting "+int2base(npeaks,10)+" qz peaks"
   declare afoldername = delstr(fname[0],4,strlen(fname[0])-1)+" "+
      folder_list[%x]+" Linear Int Qz"

   if (overwrite==0) if (isfile("%afoldername%.dat")) goto nextfolder

   if (isdir(folder_list[%x])==0) goto nextfolder

   declare afoldername = wherenow+"/"+folder_list[%x]+"/"
   cmdlin cd %afoldername%

   let fcount = 0
   foreach (*.txt) fcount = fcount+1
   if (fcount==0) cd .. goto nextfolder

   alloc area curve fcount
   alloc findex curve fcount
   alloc fname string_array fcount

   foreach (*.txt) let fname[%i] = %f
   sort -strings fname -strict

   alloc ds1,ds2,ds3,ds4,ds5,ds6,ds11,ds12,ds13,ds14,w91,w92,w93,w94,
      w95,ds1n,ds4n,ds11n,ds14n array fcount

/* /* Loop for reading and analyzing all files within the folder
   loop fcount {
      let afilename = fname[%i]
      if (filesize(afilename)/1024/1024<3) goto nextfile

      read -3d tempSurf %afilename% -silent
      let findex:y[%i] = atof(delstr(delstr(fname[%i],0,12),4))
      setv findexcount = %i
      alloc p11,p12,p13,p14,p15,p16,p17,q11,q12,q13,q14,q15,q16,q17
         array 2 /* (rowend-rowstart+1)

      setv ha1,hx1,hb1=1e6,-4,26
      setv ga3a,ga3b,gx3,gx3delta,gdx3,ga4,gdx4 = 50,50,90,0,10,10,50

         matrix row_get tempSurf rowstart,rowend
         let x=x-gisaxs_x
         cull keep xrange low_cull high_cull
         cull delete xrange midl_cull midh_cull cull keep xrange 0
            600 archive rightfull

         matrix row_get tempSurf (rowstart+1),(rowend+1) /* this
            shifts the read of the left side to +1 from the right
            side to make in parallel moreso
         let x=x-gisaxs_x
         cull keep xrange low_cull high_cull
```

```
         cull delete xrange midl_cull midh_cull cull keep xrange -600
              0 archive leftfull
         retr leftfull retr rightfull -append cull delete for y>min(
            @max(leftfull),@max(rightfull)) archive c1

         /* ensure no errors when fitting each amplitude
         let ha1,hb1,hx1,ga3a,ga3b,gx3,gx3delta,gdx3 = min(max(ha1,2)
            ,9e6),min(max(hb1,6),34),min(max(hx1,-19),19),min(max(
            ga3a,0.2),9999),min(max(ga3b,0.2),9999),min(max(gx3,p2low
            +6),p2high-4),min(max(gx3delta,-4),4),min(max(gdx3,5),34)

         retr c1 cull delete xrange p1low,p1high cull delete xrange
            p2low,p2high archive c2
         fit_sides53 /* p11 peak amplitude, p12 peak position, p13
            peak width, p14 bkg amp, p15 bkg yoffset, p16 xoffset,
            qxx is sigma of repsective p
         retr c1 let y=fit(x) archive left_fit \
         retr c1 let y=y-fit(x) archive left_subtracted
/* eval hn2

         alloc temp string 1
         let temp = "Data from\nFile "+int2base(Findex:y[findexcount
            ],10)
         if (visualize1) yright on force on label left "Signal (
            Counts)" label right "Signal w/o bkg (Counts)" label bot
            "Position (Pixels)" retr c1 reg left 0 1500 reg bot -250
            250 reg right -1.2*max(100/1.2,ga3a,ga3b) 1.2*max
            (100/1.2,ga3a,ga3b) pl -sym 4 -identify temp ov -fit ov -
            f h2(x) let y=y-fit(x) ov -sym 4 -pen 2 -ply right -
            identify "Residuals" retr c1 let y=y-h1(x)-g4(x) ov -sym
            4 -pen 4 -ply right ov -f g3a(x)+g3b(x) -pen 1 -lt 2 -lw
            5 -ply right -identify "Signal Fit" yright off force off
            /* sleep 0.4

      let amp,s_amp,pos,s_pos,width,s_width,tot_area,s_tot_area,
         bkg_area,counter,integrand = 0,0,0,0,0,0,0,0,0,0,0
      let pos,s_pos,width,s_width,normalize_const=p12[0],q12[0],p13
          [0],q13[0],(ha2)*1 /* gisaxs_q_prop

      let ds1[%i],ds11[%i]=p11[0],q11[0]
      let ds2[%i] = pos                                /* Average
         position in pixels
      let ds12[%i] = s_pos                             /* standard
         deviation of the average peak position in pixels
      let ds3[%i] = width                              /* Average
         width in pixels
      let ds13[%i] = s_width                           /* standard
         deviation of the average peak width in pixels
      let ds1n[%i],ds11n[%i] = ds1[%i]/normalize_const,ds11[%i]/
         normalize_const

      if (visualize3) if (mod(%i,visualize3_period)==0) printf "File
         = %g Date & Time = %s" %i upcase(asctime(time()))
      let area:x[%i] = findex:y[%i]
      /* eval ha1
      :nextfile
   }

   let area:x = (area:x-@ave(area:x))*10-folder_centers:y[%x]
   let area:y=ds1
   cmdlin cd ..
/*   setv count = strlen(wherenow)

/* /* Convert position to Temperature
      /* Note, in old lab, CO2 beam approximated by Gaussian of 226.7
         um sigma for 1ms dwell
```

```
/* Note in new lab, 1ms can be approximated (width of region)
    as edgeworth(x,0,520,0.17,-0.3)/edgeworth(0,0,0.17,-0.3) but
     divide width by two (skew can be as low as ~0.12 to give
    ~2% error at T>0.4)
/* Note in new lab, 250us can be approximated (width of region)
     as edgeworth(x,0,430,0.1,-0.3)/edgeworth(0,0,0.1,-0.3) but
    divide width by two
/* Note in new lab, 10ms can be approximated (width of region)
    as edgeworth(x,0,650,0,1.3)/edgeworth(0,0,650,0,1.3)
    *(1-0.28)+0.28 but divide width by two
/* difference in sigma from 520/2 vs 430/2 -> 82.7% narrower at
     250 us vs 1ms at ~600 C
/* difference in sigma from 520/2 vs 650/2 -> 125% of width at
    10ms vs 1ms at ~600C plus base offset, for full wafer
    samples I am estimating that the offset is much smaller thus
     dividing offset in half since heat goes to full silicon
    wafer and also to metal chuck rather than plastic base in
    thermistor
/* Fit for 1ms old lab of edgeworth gives 14.876*edgeworth(x,x0
    ,0.234 mm, 0.61 skew, 0.506 kurtosis)
       /* New update as of 11/1/15
          ////////////////////////////////////
       /* Fit instead of double gaussian where high intensity
          central gaussian plus lower larger gaussian to account
           for thermal diffusion tails - fits data much better
          without skew or kurtosis
       /* Fit to (width of region) yields the following values
          for new lab T(width)=gaussn(x,0,s1)*(1-x1)+gaussn(x,0,
          s2)*x1
             /* 250 us s1,s2,x1=292.5,544.7,0.37 (note 0.37 was
                fit max for x1, allowing greater made s2 narrow
                and messed up fit)
             /* 500 us s1,s2,x1=304.1,650.1,0.37
             /* 1 ms s1,s2,x1=362.7,1136.7,0.238147
             /* 2 ms s1,s2,x1=384.5,1354.3,0.257950
             /* 5 ms s1,s2,x1=362.1,1370.0,0.285776
             /* 10 ms s1,s2,x1=491.5,2328.6,0.342579
       /* all these fit values taken for high power (~1100 C)
          scan which is slightly narrowed over low temperature
          scans
       /* For ~500 C Max T (adding high and med T profiles to
          estimate)
             /* 250 us s1,s2,x1=395.9,786.2,0.195266
             /* 500 us s1,s2,x1=401.6,978.8,0.269583
             /* 1 ms s1,s2,x1=422.4,1264.4,0.281278
             /* 2 ms s1,s2,x1=461.4,1870.7,0.229394
             /* 5 ms s1,s2,x1=467.6,1870.3,0.279116
             /* 10 ms s1,s2,x1=492.6,2333.5,0.342857
       /* Fitting actual position temperature profile for 1ms
          yielded s1,s2,x1=189.1,728.5,0.168436
       /* Old lab data fits to 1ms skewed profile yields x0,s1,
          sk1,ku1,a1=0.1176,0.3204,1.4353,3.5381,0.9527 in mm
          where appropriate (no baseline slope removal)
       /* If only fitting a gaussian function, yeilds s1=0.2267
          or 226.7 micron sigma for profile but with significant
           skew (with no baseline slope removal)
       /* If only allowing skew (no kurtosis), yields s1=0.2233
          or 223.3 micron sigma and sk1=0.5147 skew. (note it
          fits very well with small kurtosis once baseline slope
           removed)
       /* For ease of translation, I take this skewed profile
          width similarity to the gaussian as validation that
          the width is likely the same as stated for gaussian,
          ~226.7 microns
```

```
      /* Note: The old lab data for the profile was taken
           at 40W (~800 C) so I use the high T spatial
          profiles in the new lab to determine the scaling
           factor
/* Translating new lab data to old lab means that for the
    1ms sigma_old=226.7 microns, sigma_new=362.7/2=181.35
    or ~0.799955*sigma_old
/* Since I expect the thermal diffusion to remain the
   same, s2 should remain the same between the labs, any
   changes due to the absorption size should be much
   smaller
      /* Note: Since all my data was taken in the 400-700
           C range, I take the widths estimated at 500 C
          and scale it to the new lab by this 25% scale
          factor
/* For each time (250us -> 10ms) multiply s1*1.25 and
   divide by 2 (width -> spatial causing the factor of 2)
    and keep all other values (s2,x1) the same thus:
      /* 250 us let s1,s2,x1
         =395.9*1.25/2,786.2/2,0.195266
      /* 500 us let s1,s2,x1
         =401.6*1.25/2,978.8/2,0.269583
      /* 1 ms let s1,s2,x1=422.4*1.25/2,1264.4/2,0.281278
      /* 2 ms let s1,s2,x1=461.4*1.25/2,1870.7/2,0.229394
      /* 5 ms let s1,s2,x1=467.6*1.25/2,1870.3/2,0.279116
      /* 10 ms let s1,s2,x1
         =492.6*1.25/2,2333.5/2,0.342857
/* This is also validated by the intensity profiles which
    show the new lab to have xwidth = 508.2 microns vs
   old lab xwidth = 588.2 which is ~16% larger and
   roughly in agreement with 25% calculated from profiles
/* disagreement between 16% and 25% may be in part
   explained by the difference in LSA profile direction:
   in old lab, lsa profiles were taken // to long axis (
   step in short axis) whereas in new lab taken // to
   short axis and stepped in long axis
/* New note as of 11/2/15 - larger hump in profiles are
   from residual heat during LSA of thermistors to
   utilize fit of LSA thermal width in temperature and
   scale to old lab
/* this means that the widths of LSA will need to be
   scaled by ~16% larger due to spatial difference, the
   earlier noted 25% included the 1ms residual
   temperature hump
/* Performing the same analysis on the old lab data for
   900us 40W (1ms suggests ~800 C), sigma ~ 186.8 microns
    compared to 211.0 microns in the new lab.
/* This is ~13% larger than the old lab despite the old
   lab supposedly being 16% wider beam on the long axis
   ??? Note, If I instead take ~1100C as the peak T,
   sigma ~ 193 microns, if 1300 C, sigma ~181 microns
/* I am not sure what this means, but for first guess, I
   will take the new lab fit parameters and multiply the
   width by 588.2/508.2 = 1.1574
      /* 250 us setv slope1,intercept1
         =-0.0762859*588.2/508.2,253.415
      /* 500 us setv slope1,intercept1
         =-0.0657785*588.2/508.2,256.717
      /* 1 ms setv slope1,intercept1
         =-0.0585507*588.2/508.2,257.813
      /* 2 ms setv slope1,intercept1
         =-0.0610199*588.2/508.2,261.133
      /* 5 ms setv slope1,intercept1
         =-0.0677013*588.2/508.2,272.380
```

```
                  /* 10 ms setv slope1,intercept1
                     =-0.0666809*588.2/508.2,275.695

   /* Obtain temperature of sample, 400, 550, 700 C
   setv count = strlen(fname[0])
/*   setv count11 = count-1
   declare Tletter = delstr(delstr(fname[0],4,strlen(fname[0])-1)
      ,0,3)

   let low = strspn(Tletter,"a") let medium = strspn(Tletter,"b") let
       high = strspn(Tletter,"c")
   if (low) setv maxT = 400
   if (medium) setv maxT = 550
   if (high) setv maxT = 700

/* kept for posterity, used on 8/22/15 for calculations, made
   obsolete on 11/1/15
   if (%x<7) setv LSAwidth = 188.2 /* microns = 0.827*227.6
   if (%x==7) setv LSAwidth = 207 /* microns = ~0.91*227.6
   if (%x>7) {
      if (%x<11) setv LSAwidth = 227.6 /* microns = 1ms width
      if (%x<13) setv LSAwidth = 227.6 /* can set for 2/5ms width
      if (%x>12) setv LSAwidth = 284.5
   }
   retr area
   if (%x<13) retr area let x = (maxT-23)*gaussn(x,0,LSAwidth)+23
   if (%x>12) retr area let x = (maxT-23)*edgeworth(x,0,LSAwidth
      ,0,1.3)/edgeworth(0,0,LSAwidth,0,1.3)*0.86+23+(maxT-23)*0.14
   archive area_T

goto skipped9

/* New temperature calibration as of 11/1/15
   if (%x<6) setv LSAwidth1,LSAwidth2,LSAx1=395.9*1.157/2,786.2/2,0
      /* 0.195266  /* 250us widths
   if (%x==6) setv LSAwidth1,LSAwidth2,LSAx1=401.6*1.157/2,978.8/2,0
      /* 0.269583   /* 500us widths
   if (%x>6) {
      if (%x<11) setv LSAwidth1,LSAwidth2,LSAx1
         =422.4*1.157/2,1264.4/2,0 /* 0.281278   /* 1ms widths
      if (%x==11) setv LSAwidth1,LSAwidth2,LSAx1
         =461.4*1.157/2,1870.7/2,0 /* 0.229394  /* 2ms widths
      if (%x==12) setv LSAwidth1,LSAwidth2,LSAx1
         =467.6*1.157/2,1870.3/2,0 /* 0.279116  /* 5ms widths
      if (%x>12) setv LSAwidth1,LSAwidth2,LSAx1
         =492.6*1.157/2,2333.5/2,0 /* 0.342857   /* 10 ms widths
   }
   retr area let x=(maxT-23)*(gaussn(x,0,LSAwidth1)*(1-LSAx1)+gaussn(
      x,0,LSAwidth2)*LSAx1)+23 archive area_T
:skipped9

goto skipped10
/* New temperature calibration as of 11/2/15
   if (%x<6) setv slope1,intercept1=-0.0762859*588.2/508.2,253.415
       /* 250us widths
   if (%x==6) setv slope1,intercept1=-0.0657785*588.2/508.2,256.717
       /* 500us widths
   if (%x>6) {
      if (%x<11) setv slope1,intercept1
         =-0.0585507*588.2/508.2,257.813   /* 1ms widths
      if (%x==11) setv slope1,intercept1
         =-0.0610199*588.2/508.2,261.133   /* 2ms widths
      if (%x==12) setv slope1,intercept1
         =-0.0677013*588.2/508.2,272.380   /* 5ms widths
```

```
      if (%x>12) setv slope1,intercept1
         =-0.0666809*588.2/508.2,275.695   /* 10 ms widths
   }
   setv LSAwidth1=intercept1+slope1*maxT
   retr area let x=(maxT-23)*gaussn(x,0,LSAwidth1)+23 archive area_T
:skipped10

   /* Output Data

   let ds5 = area:x           /* x coordinate of all points in
      microns
   let ds6 = area_T:x         /* Temperature of all points
   let ds2 = ds2*gisaxs_q_prop  /* peak position in q space now
   let ds3 = ds3*gisaxs_q_prop  /* peak width in q space now
   let ds12 = ds12*gisaxs_q_prop  /* standard deviation of peak
      position in q space now
   let ds13 = ds13*gisaxs_q_prop  /* standard deviation of peak width
       in q space now
   let ds4 = ds4*gisaxs_q_prop  /* peak area in counts * q space now
   let ds14 = ds14*gisaxs_q_prop  /* standard deviation of peak area
      in counts * q space now

   let ds4 = ds1*ds3*sqrt(6.283185)             /* Total integrated
      area in pixels and counts
   let ds14 = (6.283185)*sqrt(ds11^2*ds3^2+ds1^2*ds13^2)  /* Standard
       deviation of the integrated peak area in pixels and counts
   let ds4n = ds4/normalize_const
   let ds14n = ds14/normalize_const

   setv count = strlen(wherenow)
   let count = count-4
   declare afoldername = delstr(fname[0],4,strlen(fname[0])-1)+" "+
      folder_list[%x]+" Linear Int Qz"

   /* columns are (1) x position, (2) Temperature, (3) Int Area, (4)
      Amplitude, (5) Position in q space, (6) width in q space, (7)
      std dev in peak area, (8) std dev in peak amplitude, (9) std
      dev in peak position, (10) std dev in peak width, (11) peak
      area normalized, (12) peak intensity normalized, (13) peak area
       normalized sigma, (14) peak intensity normalized sigma
   write %afoldername%.dat -list ds5 ds6 ds4 ds1 ds2 ds3 ds14 ds11
      ds12 ds13 ds4n ds1n ds14n ds11n /* -silent
   afoldername
   if (visualize4) asctime(time())
   cmdlin cd %wherenow%

   let area_T:y=ds1n
   label bot "Temperature (\deg C)" label left "Normalized Amplitude
      (Counts/bkg)" yright on reg bot auto reg left 0 1.1*@max(area_T
      :y) reg right 0 1.1*@max(ds3) retr area_T pl -sym 4 -erry ds11n
       -identify %afoldername% retr area_T let y=ds3 ov -sym 4 -pen 2
       -erry ds13 -identify "Peak Width" -ply right yright off

   :nextfolder
}

dev -g
xeq -return
```

B.1.2 Tiff GISAXS File Analysis

This Genplot macro reads in GISAXS images in tiff format and fits the first order peaks and background for plotting as a function of position and temperature. LSA anneal centers are read in from manual centering done before running the macro. This macro was used for preliminary analysis of data for Section 6.3.1.

```
genplot reset -silent @echo off
lt 1 pen -1 lw 2

/* ////////////////////////////////////////////////
/* For CHESS Run 3-2016 Analysis
/* Pilatus Detector (407 rows x 487 columns) with 30 rows dark at
   center
/*    for distance between subdetectors
/* Pixel size = 172 microns = 0.172 mm
/* SDD = 1533 mm
/* lambda = 0.1162 nm
/* x0 = ~249
/* y0 = ~30.6
/*
/* Direct beam measured approx x,y = 238.2 pm 2.9, 30.6 pm 2.1 pixels
/*     but x is mirrored in tiff read
/* LaB6 calibration x,y,SDD= 238.217,30.630,1533.102
/*
/* q = 2*PI*sin(theta)/lambda = (SAA) 2*PI/lambda * (ypixel-y0)*
   conversion/S2D_length
/* q approx is true for small angle approximation, actually is q = 4*
   pi*sin(theta/2)/lambda
/* ////////////////////////////////////////////////

/* ////////////////////////////////////////////
/* Aliased Fuctions (for Fitting) */

alias fit_sides82 \
      fit nlsfit reset accuracy accu2 equ l1(x)+g41(x)+g42(x) maxiter
          iter1 verbose 0 sigma sqrt(y+4) range -0.9 0.9 \
      vary lg1 / -limit 10^0 3*10^6 vary lx1 / -limit -0.01 0.03 vary
          lgdx1 / -limit 0.005 0.3 \
      vary ga41 / -limit 0.1 10^5 vary ga41a / -limit 0.02 50 vary
         gx4 / -limit p2low p2high vary gx4delta / -limit -p2delta
         p2delta vary gdx4 / -limit 0.005 0.07 \
      vary ga42 / -limit 0.1 10^4 vary ga42a / -limit 0.02 50 vary
         lb1 / -limit -60 40 \
      vary la1 / -limit 1 10E4 vary ldx1 / -limit 0.005 1.2 return \
      retr cfitme let ldx1,lb1,ga41,ga42,ga41a,ga42a,gx4,gdx4,
         gx4delta=max(ldx1,0.015),25,max(ga41,300),max(ga42,100),1,1,
         max(min(gx4,p2high-3*(p2high-p2low)/4),p2low+(p2high-p2low)
         /10),min(max(gdx4,0.01),0.03),0 fit nlsfit fit \
      let p11[0],q11[0] = ga41+ga41a*ga41,sqrt(sigma$[3]^2*(1+ga41a
         ^2)+ga41^2*sigma$[4]^2) \
      let p12[0],q12[0] = ga42+ga42a*ga42,sqrt(sigma$[8]^2*(1+ga42a
         ^2)+ga42^2*sigma$[9]^2) \
      let p13[0],q13[0] = 0,0 \
      let p14[0],q14[0] = 0,0 \
      let p15[0],q15[0] = (2*gx4-gx4delta)/2,(2*sigma$[5]^2+sigma$
         [6]^2)/2 \
      let p16[0],q16[0] = gdx4,sigma$[7] \
      let p21[0],q21[0] = la1,sigma$[0] \
```

```
      let p22[0],q22[0] = lx1,sigma$[1] \
      let p23[0],q23[0] = ldx1,sigma$[2] \
      let p24[0],q24[0] = lb1,sigma$[10] \
      let p25[0],p26[0] = chisqr$,integrate(l1(x),-0.5,xlcull-0.01)+
         integrate(l1(x),xhcull+0.01,0.5) \
      return

alias fit_center \
      fit nlsfit reset accuracy accu2 equ c1(x)+c2(x)+c3(x)+c4(x)
         maxister iter1 verbose 0 \
      vary ca1 / vary ca2 / vary ca3 / vary ca4 / vary cx0 / vary
         cdx1 / vary cdx2 / vary cdx3 / vary cdx4 / return \
      retr c_center fit nlsfit fit return

alias centerme \
      loop fcount let position:x[%i],position:y[%i]=abs(((%i)-
         burn_center)*dist_mult-floor((((%i)-burn_center)*dist_mult
         +1000)/2000)*2000),v1[%i]

alias plotme \
      retr position cull keep irange testnum*200 (testnum+1)*200 reg
         auto pl -lt 1

/* ////////////////////////////////////////////
/* Define Variables */

/* Filepaths and strings
alloc tfname,atemp string 1
let tfname=afoldername_sub
let tfname=delstr(tfname,0,strlen(tfname)-5)
let tfname=delstr(tfname,0,strcspn(tfname,"/"))
alloc foldernames string_array 4
let foldernames[0]=afoldername_sub+tfname+"-1a/"
let foldernames[1]=afoldername_sub+tfname+"-1b/"
let foldernames[2]=afoldername_sub+tfname+"-2a/"
let foldernames[3]=afoldername_sub+tfname+"-2b/"
alloc anneal_list string_array 16

/* Conter variables
setv fcount=0
setv testsumcounter=0
setv foldercounter=0
setv whichpeak=0

/* Folders and file lists
alloc afilename,afilename2 string 1

/* Do not change global variables
setv pxsize,sdd,lambda,x0,y0 = 0.172,1533.1,0.1162,248.35,30.6
setv introwstart0,introwstart,intrownum,introwend=96,96,32,
   introwstart+intrownum  /* 1st peak and second peak above yoneida
   vinyard, wide integration
setv introwstart0,introwstart,intrownum,introwend=96,96,16,
   introwstart+intrownum  /* 1st peak above yoneida vinyard only
/* setv introwstart0,introwstart,intrownum,introwend=96+16,96,16,
   introwstart+intrownum  /* 2nd peak above yoneida vinyard only
/* setv introwstart0,introwstart,intrownum,introwend=96-16,96,12,
   introwstart+intrownum   /* yoneida vinyard band only
setv intcolstart,intcolend=235,240
setv xlcull,xhcull=-0.079,0.094     /* In qx nm^-1

setv peak_temperature=0             /* individual peak temperature
   value for thermal profiles
setv dist_mult = 10  /* 10.0255           /* microns per image /*
   Correct to +-0.001 best 10.021 to 10.019
```

```
setv burn_center = 91.0             /* position of initial burn
   center in microns, shoudl be near image 100 (1000um) /* could be
   90.7 to 91.3 (whether matching start of burn upturn or end)
alloc c_center curve 200            /* curve for position,
   temperature

alloc realtemp16 array 16           /* redefined for each folder
alloc realtemp32 array 32           /* contains all temperatures
foreach (0,6,15) let realtemp32[%f],realtemp32[%f+16]=1200,1200  /*
   250us burn
foreach (1,2,3,4,5,13) let realtemp32[%f],realtemp32[%f+16]=500,800
   /* 250us anneals
let realtemp32[14],realtemp32[14+16]=500,800          /* 150us
   anneals
let realtemp32[12],realtemp32[12+16]=500,800          /* 500us
   anneals
let realtemp32[11],realtemp32[11+16]=500,800          /* 750us
   anneals
let realtemp32[10],realtemp32[10+16]=500,800          /* 1ms anneals
let realtemp32[9],realtemp32[9+16]=500,800            /* 2ms anneals
let realtemp32[8],realtemp32[8+16]=500,800            /* 5ms anneals
let realtemp32[7],realtemp32[7+16]=500,800            /* 10ms anneals

/* ////////////////////////////////////
/* Define Functions */
define g41(x) = ga41*gaussn(x,(gx4)+gx4delta,gdx4)+ga41a*ga41*gaussn(
   x,-gx4+gx4delta,gdx4)    /* peak1
define g42(x) = ga42*gaussn(x,2*(gx4)+gx4delta,gdx4)+ga42a*ga42*
   gaussn(x,-2*gx4+gx4delta,gdx4)    /* peak1
/* define g43(x) = ga43*gaussn(x,3*(gx4)+gx4delta,gdx4)+ga43a*ga43*
   gaussn(x,-3*gx4+gx4delta,gdx4)    /* peak1
/* define g44(x) = ga44*gaussn(x,4*(gx4)+gx4delta,gdx4)+ga44a*ga44*
   gaussn(x,-4*gx4+gx4delta,gdx4)    /* peak1
setv ga41,ga42,ga43,ga44,ga41a,ga42a,ga43a,ga44a =
   10^4,10^3,10^1,10^1,1,1,1,1
setv gx4,gx4delta=0.21,0
setv gdx4=0.02

define l1(x) = la1*lorentzian(x,(lx1),ldx1)/lorentzian(0,lx1,ldx1)+
   lb1+lg1*exp(-(abs(x-lx1)/lgdx1)^ln1)   /* lorentzian background
setv la1,lx1,ldx1,lb1,lg1,lgdx1,ln1=10^3,0,0.25,2,10^6,0.06,1

define c1(x) = ca1*gaussn(x,cx0,cdx1)
define c2(x) = ca2*gaussn(x,cx0,cdx2)
define c3(x) = ca3*gaussn(x,cx0,cdx3)
define c4(x) = ca4*gaussn(x,cx0,cdx4)
setv ca1,ca2,ca3,ca4,cx0,cdx1,cdx2,cdx3,cdx4=1,1,1,1,0,1,1,1,1

setv accu1,accu2,iter1,iter2 = 1E-5,1E-5,1000,1000
setv p2low,p2high,p2delta = 0.19,0.39,0.005
alloc p11,p12,p13,p14,p15,p16,q11,q12,q13,q14,q15,q16 array 2 /* (
   rowend-rowstart+1)
alloc p21,p22,p23,p24,p25,p26,q21,q22,q23,q24,q25,q26 array 2 /* (
   rowend-rowstart+1)

/* ////////////////////////////////////////
/* Define Output Plots or Debugging */
setv fixedintrowstart=1
setv skiptome=0
setv skippoints=1 /* one of every x points calculated
setv skiptofolder=0
setv skipanalysis1=0
setv skipanalysis2=0
setv waitme=0
setv fit0=0
```

```
setv fit82=1
setv visualize1=0  /* bitmaps with overlaid integrations of c12 and
   c22
setv visualize2=0  /* fit and data of qz integrated areas shown
setv visualize3=1  /* print folder, time, and iteration numer
setv visualize3time=20  /* how many files to skip between readouts
setv fast_test=0

/* ////////////////////////////////////////
/* Folder Loop for Within Each Sample Polymer */
loop 4 {

      if (%i<skiptofolder) goto nextfolder
      let foldercounter=%i
      let anneal_list[0] = "10250us_x01"  /* burn 1200 C
      let anneal_list[1] = "00250us_x40"
      let anneal_list[2] = "00250us_x20"
      let anneal_list[3] = "00250us_x08"
      let anneal_list[4] = "00250us_x04"
      let anneal_list[5] = "00250us_x02"
      let anneal_list[6] = "20250us_x01"  /* burn 1200 C
      let anneal_list[7] = "10000us_x01"
      let anneal_list[8] = "05000us_x01"
      let anneal_list[9] = "02000us_x01"
      let anneal_list[10] = "01000us_x01"
      let anneal_list[11] = "00750us_x01"
      let anneal_list[12] = "00500us_x01"
      let anneal_list[13] = "00250us_x01"
      let anneal_list[14] = "00150us_x01"
      let anneal_list[15] = "30250us_x01" /* burn 1200 C

            foreach (0,6,15) let anneal_list[%f]=anneal_list[%f]+"
               _1200C"
            if (mod(foldercounter,2)) let atemp="_0800C"
            if (mod(foldercounter,2)==0) let atemp="_0500C"
            foreach (1,2,3,4,5,7,8,9,10,11,12,13,14) let anneal_list
               [%f]=anneal_list[%f]+atemp
            loop 16 let realtemp16[%i]=realtemp32[%i+16*mod(
               foldercounter,2)]

            if (visualize3) eval foldernames[foldercounter]
            cd foldernames[foldercounter]
            let fcount,testsumcounter=0,1
            foreach (*.tiff) fcount = fcount+1
            if (fcount==0) goto nextfolder

            alloc fname string_array fcount

            foreach (*.tiff) let fname[%i] = %f
            sort -strings fname -strict

            alloc temperatures curve 16
            read temperatures.dat -col 2 3 -silent archive
               temperatures /* x values are temperature, y values are
                position in images

            alloc m11,m12,m21,m22 surface fcount 487
            alloc v1,v2,v3,v4,v5,v6,v7,v8,v9,v10,v11,v12,s1,s2,s3,s4,
               s5,s6,s7,s8,s9,s10,s11,s12 array fcount
            alloc vv1,vv2,vv3,vv4,vv5,vv6,vv7,vv8,vv9,vv10,vv11,vv12,
               ss1,ss2,ss3,ss4,ss5,ss6,ss7,ss8,ss9,ss10,ss11,ss12
               array fcount
            alloc vposition,vtemperature array fcount
            alloc position curve fcount

            /* ////////////////////////////////////
```

```
/* File Loop for Each File - Data Read and Distillation
   */
loop fcount {
      if (%i<skiptome) goto nextfile
      if (mod(%i,skippoints)) goto nextfile
      if (fast_test) goto nextfile
      if (visualize3) if (mod(%i,visualize3time)==0)
         printf asctime(time())+" File: %i"
      /* ////////////////////////
      /* Read Data and Create Curves for Analysis */
      let afilename = fname[%i]
            read -tiff test %afilename% -silent
      let test:z=abs(test:z)+1 matrix dup test test2
      if (%i==skiptome) matrix dup test testsum let
         testsum:z=0
      if (%i==0) matrix dup test testsum let testsum:z=0
      let test2:z=log(test2:z)

      let introwstart,intrownum,introwend=introwstart0
         ,16,introwstart+intrownum  /* 1st peak above
         yoneida vinyard only
      matrix test row_get introwstart,introwend
      let x=4*pi*sin(atan((x*487/@max(x)-x0)*pxsize/sdd)
         /2)/lambda let y=(y-1)*(introwend-introwstart)+1
          archive c11 /* let y=log(y) archive c12
      retr c11 matrix row_put m11 %i
      retr c11 cull delete xrange xlcull,xhcull archive
         c11 let y=log(y) archive c12

      if (visualize1) {
            label left "Counts" label bot "q_{//} (nm
               ^{-1})"
            force on log left on reg bot auto reg left 1
               5 pl log left off
            ov test2 -bitmap -palette afm -zrange @min(
               test2:z)+0.5 @max(test2:z)-2.0 -xrange
               @min(test2:x) @max(test2:x) -yrange @min(
               test2:y) @max(test2:y)
            retr c12 ov -sym 4 -pen 0 -symsize 0.1 -
               identify %afilename%
            create y=introwstart/407*4+1 -range -2 2 -
               points 10 ov -lt 1 -lw 4 -pen 0
            create y=introwend/407*4+1 -range -2 2 -
               points 10 ov -lt 1 -lw 4 -pen 0
            if (waitme) wait
            sleep 0.5
            }
      /* at this point c11 and c21 are actual summed
         counts (with 1 count pedestal) for narrow and
         wide regions respectively
      /* and then c12 and c22 are the log of their
         counterparts c11 and c21 respectively

      /* ////////////////////////
      /* Fitting Data and Saving Parameters */
      /* Parameters saved in vectors where v is value, s
         is sigma, 0-fcount is full integration from band
          to sub detector end, fcount-(2*fcount-1) is
         narrow integration for first peak
      /* v1-2 are amplitudes of first 2 peaks, v3-v4 are
         normalized by v12, v5=qx position,v6=dqx,v7=la1,
         v8=lx1,v9=ldx1,v10=lb1,v11=reduced chi squared,
         v12=integrated background (normalize by this), s
          are variances if applicable
```

```
if (%i==skiptome) let ga41,ga42,ga43,ga44
   =10^4,10^2,1,1
if (%i>skiptome) let ga41,ga42,gx4,gdx4,la1,lx1,
   ldx1,lb1=max(v1[%i-1]/2,200),max(v2[%i-1]/2,200)
   ,v5[%i-1],v6[%i-1],v7[%i-1],v8[%i-1],v9[%i-1],
   v10[%i-1]
retr c11 archive cfitme if (skipanalysis1==0)
   fit_sides82
if (skipanalysis1==0) if (visualize2) if (fit0==0)
   label bot "q_{||} (nm^{-1})" label left "Raw
   Signal (Counts)" label right "Signal (Counts)"
   force on yright on reg left 0 2E4 reg bot -0.9
   0.9 reg right -1*max(500,ga41/3*1.5) max(1500,
   ga41*1.5) pl -sym 4 -pen rgb(20,20,20) -symsize
   0.1 -identify %afilename% -ply left ov -f l1(x)
   -points 10^4 -pen rgb(255,165,12) -lw 3 -lt 1 -
   ply left let y=y-l1(x) ov -sym 4 -pen 4 -ply
   right -identify "No Background" let y=y-g41(x)-
   g42(x) ov -sym 4 -pen 2 -ply right -identify "
   Residuals" ov -f g41(x)+g42(x) -points 10^4 -pen
    rgb(0,150,0) -lt 1 -lw 3 -ply right yright off
   force off
if (skipanalysis1==0) let v1[%i],v2[%i],v3[%i],v4[%
   i],v5[%i],v6[%i],v7[%i],v8[%i],v9[%i],v10[%i],
   v11[%i],v12[%i]=p11[0],p12[0],p13[0],p14[0],p15
   [0],p16[0],p21[0],p22[0],p23[0],p24[0],p25[0],
   p26[0]
if (skipanalysis1==0) let s1[%i],s2[%i],s3[%i],s4[%
   i],s5[%i],s6[%i],s7[%i],s8[%i],s9[%i],s10[%i],
   s11[%i],s12[%i]=q11[0],q12[0],q13[0],q14[0],q15
   [0],q16[0],q21[0],q22[0],q23[0],q24[0],q25[0],
   q26[0]
if (skipanalysis1==0) let v3[%i],v4[%i],s3[%i],s4[%
   i]=v1[%i]/v12[%i],v2[%i]/v12[%i],s1[%i]/v12[%i],
   s2[%i]/v12[%i]

let introwstart,intrownum,introwend=introwstart0
   +16,16,introwstart+intrownum  /* 2nd peak above
   yoneida vinyard only
matrix test row_get introwstart,introwend
let x=4*pi*sin(atan((x*487/@max(x)-x0)*pxsize/sdd)
   /2)/lambda let y=(y-1)*(introwend-introwstart)+1
    archive c11 /* let y=log(y) archive c12
retr c11 cull delete xrange xlcull,xhcull archive
   c11 let y=log(y) archive c12

if (visualize1==2) {
      label left "Counts" label bot "q_{//} (nm
         ^{-1})"
      force on log left on reg bot auto reg left 1
         5 pl log left off
      ov test2 -bitmap -palette afm -zrange @min(
         test2:z)+0.5 @max(test2:z)-2.0 -xrange
         @min(test2:x) @max(test2:x) -yrange @min(
         test2:y) @max(test2:y)
      retr c12 ov -sym 4 -pen 0 -symsize 0.1 -
         identify %afilename%
      create y=introwstart/407*4+1 -range -2 2 -
         points 10 ov -lt 1 -lw 4 -pen 0
      create y=introwend/407*4+1 -range -2 2 -
         points 10 ov -lt 1 -lw 4 -pen 0
      if (waitme) wait
      sleep 0.5
      }
```

```
      /* at this point c11 and c21 are actual summed
         counts (with 1 count pedestal) for narrow and
         wide regions respectively
      /* and then c12 and c22 are the log of their
         counterparts c11 and c21 respectively

      /* //////////////////////////
      /* Fitting Data and Saving Parameters */
      /* Parameters saved in vectors where v is value, s
         is sigma, 0-fcount is full integration from band
          to sub detector end, fcount-(2*fcount-1) is
         narrow integration for first peak
      /* v1-2 are amplitudes of first 2 peaks, v3-v4 are
         normalized by v12, v5=qx position,v6=dqx,v7=la1,
         v8=lx1,v9=ldx1,v10=lb1,v11=reduced chi squared,
         v12=integrated background (normalize by this), s
          are variances if applicable

      if (%i==skiptome) let ga41,ga42,ga43,ga44
         =10^4,10^2,1,1
      if (%i>skiptome) let ga41,ga42,gx4,gdx4,la1,lx1,
         ldx1,lb1=max(vv1[%i-1]/2,200),max(vv2[%i
         -1]/2,200),vv5[%i-1],vv6[%i-1],vv7[%i-1],vv8[%i
         -1],vv9[%i-1],vv10[%i-1]
      retr c11 archive cfitme if (skipanalysis2==0)
         fit_sides82
      if (skipanalysis2==0) if (visualize2) if (fit0==0)
         label bot "q_{||} (nm^{-1})" label left "Raw
         Signal (Counts)" label right "Signal (Counts)"
         force on yright on reg left 0 2E4 reg bot -0.9
         0.9 reg right -1*max(500,ga41/3*1.5) max(1500,
         ga41*1.5) pl -sym 4 -pen rgb(20,20,20) -symsize
         0.1 -identify %afilename% -ply left ov -f l1(x)
         -points 10^4 -pen rgb(255,165,12) -lw 3 -lt 1 -
         ply left let y=y-l1(x) ov -sym 4 -pen 4 -ply
         right -identify "No Background" let y=y-g41(x)-
         g42(x) ov -sym 4 -pen 2 -ply right -identify "
         Residuals" ov -f g41(x)+g42(x) -points 10^4 -pen
          rgb(0,150,0) -lt 1 -lw 3 -ply right yright off
         force off
      if (skipanalysis2==0) let vv1[%i],vv2[%i],vv3[%i],
         vv4[%i],vv5[%i],vv6[%i],vv7[%i],vv8[%i],vv9[%i],
         vv10[%i],vv11[%i],vv12[%i]=p11[0],p12[0],p13[0],
         p14[0],p15[0],p16[0],p21[0],p22[0],p23[0],p24
         [0],p25[0],p26[0]
      if (skipanalysis2==0) let ss1[%i],ss2[%i],ss3[%i],
         ss4[%i],ss5[%i],ss6[%i],ss7[%i],ss8[%i],ss9[%i],
         ss10[%i],ss11[%i],ss12[%i]=q11[0],q12[0],q13[0],
         q14[0],q15[0],q16[0],q21[0],q22[0],q23[0],q24
         [0],q25[0],q26[0]
      if (skipanalysis2==0) let vv3[%i],vv4[%i],ss3[%i],
         ss4[%i]=vv1[%i]/vv12[%i],vv2[%i]/vv12[%i],ss1[%i
         ]/vv12[%i],ss2[%i]/vv12[%i]

      if (mod(%i+70,200)<100) let testsum:z,
         testsumcounter=testsum:z+test:z,testsumcounter+1

      :nextfile
      } /* end file loop
if (fast_test) let v1,v2,v3,v4,v5,v6,v7,v8,v9,v10,v11,v12
   ,s1,s2,s3,s4,s5,s6,s7,s8,s9,s10,s11,s12,vv1,vv2,vv3,
   vv4,vv5,vv6,vv7,vv8,vv9,vv10,vv11,vv12,ss1,ss2,ss3,ss4
   ,ss5,ss6,ss7,ss8,ss9,ss10,ss11,ss12
   =0,0,0,
```

```
/* //////////////////////////
/* Set Directory and Output Matricies */
cd ..
if (foldercounter==0) let afilename="-1a"
if (foldercounter==1) let afilename="-1b"
if (foldercounter==2) let afilename="-2a"
if (foldercounter==3) let afilename="-2b"
let afilename=delstr(tfname,0,1)+afilename+"_int_rows_"+
   int2base(nint(introwstart),10)+"-"+int2base(nint(
   introwend),10)+".dat"
if (fast_test==0) write %afilename% -surface m11 -notext
   -ascii -silent
if (foldercounter==0) let afilename="-1a"
if (foldercounter==1) let afilename="-1b"
if (foldercounter==2) let afilename="-2a"
if (foldercounter==3) let afilename="-2b"
let afilename = delstr(tfname,0,1)+afilename+"_composite_
   "+int2base(testsumcounter,10)+"_seconds.dat"
if (fast_test==0) write %afilename% -surface testsum -
   notext -ascii -silent

/* //////////////////////////
/* Output important values for each temperature
loop 16 {
      let burn_center,peak_temperature=temperatures:y[%i
         ],temperatures:x[%i]
      let position:x=dist_mult*(i-burn_center)

      /* New update as of 11/1/15 ///////////////
      /* Fit instead of double gaussian where high
         intensity central gaussian plus lower larger
         gaussian to account for thermal diffusion tails
         - fits data much better without skew or kurtosis
      /* Fit to (width of region) yields the following
         values for new lab T(width)=gaussn(x,0,s1)*(1-x1
         )+gaussn(x,0,s2)*x1
            /* 250 us s1,s2,x1=292.5,544.7,0.37 (note
               0.37 was fit max for x1, allowing greater
               made s2 narrow and messed up fit)
            /* 500 us s1,s2,x1=304.1,650.1,0.37
            /* 1 ms s1,s2,x1=362.7,1136.7,0.238147
            /* 2 ms s1,s2,x1=384.5,1354.3,0.257950
            /* 5 ms s1,s2,x1=362.1,1370.0,0.285776
            /* 10 ms s1,s2,x1=491.5,2328.6,0.342579
      /* all these fit values taken for high power (~1100
          C) scan which is slightly narrowed over low
         temperature scans
      /* For ~500 C Max T (adding high and med T profiles
          to estimate)
            /* 250 us s1,s2,x1=395.9,786.2,0.195266
            /* 500 us s1,s2,x1=401.6,978.8,0.269583
            /* 1 ms s1,s2,x1=422.4,1264.4,0.281278
            /* 2 ms s1,s2,x1=461.4,1870.7,0.229394
            /* 5 ms s1,s2,x1=467.6,1870.3,0.279116
            /* 10 ms s1,s2,x1=492.6,2333.5,0.342857

      setv anneal_time = nint(mod(atof(delstr(anneal_list
         [%i],5)),10000))  /* anneal_list[0] = "10250
         us_x01"
      /* New temperature calibration as of 11/1/15
      if (anneal_time==150) setv LSAwidth1,LSAwidth2,
         LSAx1=390.0/2,586.2/2,0.195266  /* 150us
         placeholder 5/20/16
```

```
                    if (anneal_time==250) setv LSAwidth1,LSAwidth2,
                       LSAx1=395.9/2,786.2/2,0.195266  /* 250us widths
                    if (anneal_time==500) setv LSAwidth1,LSAwidth2,
                       LSAx1=401.6/2,978.8/2,0.269583   /* 500us widths
                    if (anneal_time==750) setv LSAwidth1,LSAwidth2,
                       LSAx1=410.0/2,1120.0/2,0.275000  /* 750us
                       placeholder 5/20/16
                    if (anneal_time==1000) setv LSAwidth1,LSAwidth2,
                       LSAx1=422.4/2,1264.4/2,0.281278  /* 1ms widths
                    if (anneal_time==2000) setv LSAwidth1,LSAwidth2,
                       LSAx1=461.4/2,1870.7/2,0.229394  /* 2ms widths
                    if (anneal_time==5000) setv LSAwidth1,LSAwidth2,
                       LSAx1=467.6/2,1870.3/2,0.279116  /* 5ms widths
                    if (anneal_time==0) setv LSAwidth1,LSAwidth2,LSAx1
                       =492.6/2,2333.5/2,0.342857   /* 10 ms widths
                    retr position let y=(peak_temperature-23)*(gaussn(x
                       ,0,LSAwidth1)*(1-LSAx1)+gaussn(x,0,LSAwidth2)*
                       LSAx1)+23 archive position

/*                  retr position cull keep xrange max(-1000,-1*
   burn_center*dist_mult+1) min(1000,burn_center*dist_mult-1)
                    retr position cull keep xrange -1000 1000
                    alloc vposition,vtemperature,t1,t2,t3,t4,t5,t6,t11,
                       t12,tt1,tt2,tt3,tt4,tt5,tt6,tt11,tt12,u1,u2,u3,
                       u4,u5,u6,u11,u12,uu1,uu2,uu3,uu4,uu5,uu6,uu11,
                       uu12 array @count(x)

                    retr position let y=v1 cull keep xrange -1000 1000
                       let t1=round(y,6)
                    retr position let y=v2 cull keep xrange -1000 1000
                       let t2=round(y,6)
                    retr position let y=v3 cull keep xrange -1000 1000
                       let t3=round(y,6)
                    retr position let y=v4 cull keep xrange -1000 1000
                       let t4=round(y,6)
                    retr position let y=v5 cull keep xrange -1000 1000
                       let t5=round(y,8)
                    retr position let y=v6 cull keep xrange -1000 1000
                       let t6=round(y,8)
                    retr position let y=v11 cull keep xrange -1000 1000
                        let t11=round(y,6)
                    retr position let y=v12 cull keep xrange -1000 1000
                        let t12=round(y,6)
                    let position:x=dist_mult*(i-burn_center)
                    retr position let y=vv1 cull keep xrange -1000 1000
                        let tt1=round(y,6)
                    retr position let y=vv2 cull keep xrange -1000 1000
                        let tt2=round(y,6)
                    retr position let y=vv3 cull keep xrange -1000 1000
                        let tt3=round(y,6)
                    retr position let y=vv4 cull keep xrange -1000 1000
                        let tt4=round(y,6)
                    retr position let y=vv5 cull keep xrange -1000 1000
                        let tt5=round(y,8)
                    retr position let y=vv6 cull keep xrange -1000 1000
                        let tt6=round(y,8)
                    retr position let y=vv11 cull keep xrange -1000
                       1000 let tt11=round(y,6)
                    retr position let y=vv12 cull keep xrange -1000
                       1000 let tt12=round(y,6)
                    let position:x=dist_mult*(i-burn_center)
                    retr position let y=s1 cull keep xrange -1000 1000
                       let u1=round(y,6)
                    retr position let y=s2 cull keep xrange -1000 1000
                       let u2=round(y,6)
```

```
            retr position let y=s3 cull keep xrange -1000 1000
               let u3=round(y,6)
            retr position let y=s4 cull keep xrange -1000 1000
               let u4=round(y,6)
            retr position let y=s5 cull keep xrange -1000 1000
               let u5=round(y,8)
            retr position let y=s6 cull keep xrange -1000 1000
               let u6=round(y,8)
            let position:x=dist_mult*(i-burn_center)
            retr position let y=ss1 cull keep xrange -1000 1000
                let uu1=round(y,6)
            retr position let y=ss2 cull keep xrange -1000 1000
                let uu2=round(y,6)
            retr position let y=ss3 cull keep xrange -1000 1000
                let uu3=round(y,6)
            retr position let y=ss4 cull keep xrange -1000 1000
                let uu4=round(y,6)
            retr position let y=ss5 cull keep xrange -1000 1000
                let uu5=round(y,8)
            retr position let y=ss6 cull keep xrange -1000 1000
                let uu6=round(y,8)
            let u11,u12,uu11,uu12=0,0,0,0
            retr position cull keep xrange -1000 1000 let
               vposition = position:x let vtemperature =
               position:y

            if (foldercounter==0) let afilename = anneal_list[%
               i]+"_Oven_results"
            if (foldercounter==1) let afilename = anneal_list[%
               i]+"_Oven_results"
            if (foldercounter==2) let afilename = anneal_list[%
               i]+"_Spun_results"
            if (foldercounter==3) let afilename = anneal_list[%
               i]+"_Spun_results"

            retr position cull keep xrange -1000 1000 let
               vposition=x let vtemperature=y
            /* columns are (odd is value, even is sigma) (1)
               position (2) temperature (3 v1) amp peak 1, (4
               v2) amp peak 2, (5 v3) amp peak 1 norm, (7 v4)
               amp peak 2 norm, (9 v5) qx position, (11 v6) dqx
               , (13 v11) reduced chi squared, [fit 2s] (14 vv1
               ) peak 1, (16 vv2) peak 2, (18 vv3) peak 1 norm,
                (20 vv4) peak 2 norm, (22 vv5) qx position, (24
                vv11) reduced chi squared
            write %afilename%.dat -list vposition vtemperature
               t1 t2 t3 u3 t4 u4 t5 u5 t6 u6 t11 tt1 uu1 tt2
               uu2 tt4 uu4 tt5 uu5 tt11 / -silent
            eval afilename
            }

      wait

/* ////////////////////
/* Split Files to Individual LSA Regions */
/* First find center of first LSA region by fitting a series of
    even functions
loop 200 let c_center:x[%i],c_center:y[%i]=10*%i,v1[%i]

/* ////////////////////
/* Determine LSA Center and Determine Temperature as F(Position
   ) */

/* ////////////////////
/* Output Data (1 massive file or 1 for each dwell/repeat?) */
```

```
      :nextfolder
      } /* end folder loop

dev -g
xeq -return
```

B.1.3 Genplot Macro to find the LSA Scan Center

This macro does a quick analysis to fit the peak and background characteristics then manually go through to modify the center value to determine the actual center value.

```
genplot reset -silent @echo off
lt 1 pen -1 lw 2

/* ////////////////////////////////////////////////
/* Note: direct beam coords are 519.2958 pixles in x
/* and 194.2157 pixles in y, though flipped so 1024-194
/* meaning 829.7843 in y from tif-> txt transform (or genplot read
   direction)
/*
/* Other center is x,y (524.4572,189.3031), y-> 834.6969 px
/* 46.9x46.9 micron pixel size
/* 1.155 Angstroms Wavelenth
/* Sample Detector distance 1.002 m (double check, I rememer 1.6m)
/* q = 2*PI*sin(theta)/lambda = (SAA) 2*PI/lambda * (ypixel-y0)*
   conversion/S2D_length
/* ////////////////////////////////////////////////

/* Cull and signal peak range limits
setv low_cull,high_cull,midl_cull,midh_cull = 270,770,493,545 /* in
   pixels in raw image
setv p1low,p1high,p2low,p2high = 374,444,594,664
setv gisaxs_x,gisaxs_y = 519.30,834.70
setv gisaxs_q_prop = 2*pi*(46.9/1000)/1002/0.1155 /* inverse nm once
   multiplied by (ypixel-y0)

alloc cs1,cs2,cs3,cs4,cs5,cs6,cs7,cs8,cs11,cs12,cs13,cs21,cs22,cs23
   array 10000
alloc ipt int let ipt = 0

setv fcount = 0
setv loopcount = 0
setv rowstart = 680
setv rowend = 740
setv npoints = 0
setv SMAperiod = 5
setv counter = SMAperiod
setv sumvar = 0
setv counter2 = 0
setv counter3 = 0
setv low = 0
setv medium = 0
setv high = 0
setv bkg_area = 1
setv userTemp=0
alloc c01 curve 1024
```

```
alloc c11 curve 1024
alloc afilename string 1
/* alloc afoldername string 1
cd %afoldername%
alloc Tletter string 1
count = 0
declare wherenow cwd()
setv foldercount = 0
alloc folder_list string_array 16
let folder_list[0] = "250us x1"
let folder_list[1] = "250us x2"
let folder_list[2] = "250us x4"
let folder_list[3] = "250us x8"
let folder_list[4] = "250us x20"
let folder_list[5] = "250us x40"
let folder_list[6] = "500us x1"
let folder_list[7] = "1000us x1"
let folder_list[8] = "1000us x2"
let folder_list[9] = "1000us x5"
let folder_list[10] = "1000us x10"
let folder_list[11] = "2000us x1"
let folder_list[12] = "5000us x1"
let folder_list[13] = "10000us x1"
let folder_list[14] = "10000us x2"
let folder_list[15] = "10000us x10"
setv npeaks = 1

let low_cull,high_cull,midl_cull,midh_cull = low_cull-gisaxs_x,
   high_cull-gisaxs_x,midl_cull-gisaxs_x,midh_cull-gisaxs_x
let p1low,p1high,p2low,p2high = p1low-gisaxs_x,p1high-gisaxs_x,p2low-
   gisaxs_x,p2high-gisaxs_x

alloc temp string 1

:start

setv count = strlen(wherenow)
let count = count-4

setv -integer userTemp = &getarg -prompt "Folder number: " -default
   800

if (userTemp>15) goto end
declare afoldername = delstr(wherenow,0,count)+" "+folder_list[
   userTemp]+" Linear Amplitude Fitting "+int2base(npeaks,10)+" qz
   peaks"

if (isfile("%afoldername%.dat")==0) goto end

let temp=afoldername+".dat"
read %temp% -col 1 4 archive area

:middle
   read "Center.dat" -silent archive folder_centers
   let area:x = (area:x-@ave(area:x))-folder_centers:y[userTemp]

   setv count = strlen(wherenow)

   /* Convert X to Temperature
   /* Note, in old lab, CO2 beam approximated by Gaussian of 226.7um
      sigma for 1ms dwell
   /* Note in new lab, 1ms can be approximated (width of region) as
      edgeworth(x,0,520,0.17,-0.3)/edgeworth(0,0,0.17,-0.3) but
      divide width by two (skew can be as low as ~0.12 to give ~2%
      error at T>0.4)
```

```
   /* Note in new lab, 250us can be approximated (width of region) as
        edgeworth(x,0,430,0.1,-0.3)/edgeworth(0,0,0.1,-0.3) but divide
        width by two
   /* Note in new lab, 10ms can be approximated (width of region) as
      edgeworth(x,0,650,0,1.3)/edgeworth(0,0,650,0,1.3)*(1-0.28)+0.28
        but divide width by two
   /* difference in sigma from 520/2 vs 430/2 -> 82.7% narrower at
      250 us vs 1ms at ~600 C
   /* difference in sigma from 520/2 vs 650/2 -> 125% of width at 10
      ms vs 1ms at ~600C plus base offset, for full wafer samples I
      am estimating that the offset is much smaller thus dividing
      offset in half since heat goes to full silicon wafer and also
      to metal chuck rather than plastic base in thermistor
   /* Fit for 1ms old lab of edgeworth gives 14.876*edgeworth(x,x0
      ,0.234 mm, 0.61 skew, 0.506 kurtosis)

   /* Obtain temperature of sample, 400, 550, 700 C
   setv count11 = count-1
   declare Tletter = delstr(wherenow,0,count11)

   let low = strspn(Tletter,"a") let medium = strspn(Tletter,"b") let
        high = strspn(Tletter,"c")
   if (low) setv maxT = 400
   if (medium) setv maxT = 550
   if (high) setv maxT = 700
   if (foldercount<7) setv LSAwidth = 188.2 /* microns = 0.827*227.6
   if (foldercount==7) setv LSAwidth = 207 /* microns = ~0.91*227.6
   if (foldercount>7) {
      if (foldercount<11) setv LSAwidth = 227.6 /* microns = 1ms
         width
      if (foldercount<13) setv LSAwidth = 227.6 /* can set for 2/5ms
         width
      if (foldercount>12) setv LSAwidth = 284.5
   }
   retr area
   if (foldercount<13) let x = (maxT-23)*gaussn(x,0,LSAwidth)+23
   if (foldercount>12) let x = (maxT-23)*edgeworth(x,0,LSAwidth
      ,0,1.3)/edgeworth(0,0,LSAwidth,0,1.3)*0.86+23+(maxT-23)*0.14
   archive area_T

   /* Display Data

   let count = count-4

userTemp
declare afoldername = delstr(wherenow,0,count)+" "+temp+" Spatial"
afoldername /* maxT LSAwidth low medium high

/* retr area reg auto pl -l&s -sym 4 wait
retr area_T reg auto pl -l&s -sym 4 /* wait

setv -integer userTemp2 = &getarg -prompt "Redo Temperature: " -
   default 0

if (userTemp2) goto middle

:end

if (userTemp<16) goto start

dev -g
xeq -return
```

B.1.4 Genplot Macros for Making Movies

Some datasets were converted to movies to help explain the lgLSA process as it pertained to the GISAXS analysis. This required creating saving many images in Genplot which were then loaded into Gimp (a freeware version of Adobe Illustrator) to create movies.

Plotting Individual Datapoints in Sequence

```
genplot reset -silent @echo off
lt 1 pen -1 lw 2
cd gohere

setv a,b,c,width,delta=50,50,250,20,25
define f1(x)=a+b*erf((x-c)/width)
define f2(x)=a+b*erfc((x-c)/width)
setv rgbvalue = 102 /* 102, 153, 204

alias fitme1 \
      setv a,b,c,width=50,50,250,20 \
      fit nlsfit reset equ f1(x) verbose 0 maxiter 1000 \
      vary a / -limit 0.01 100 vary b / -limit 0.01 100 vary c / -
         limit 100 500 vary width / -limit 1 100 \
      return \
      retr c1 fit nlsfit fit \
      return \
      ov -fit -pen 2 -lt 3 -lw 4 -ply right

alias fitme2 \
      setv a,b,c,width=50,50,250,20 \
      fit nlsfit reset equ f2(x) verbose 0 maxiter 1000 \
      vary a / -limit 0.01 100 vary b / -limit 0.01 100 vary c / -
         limit 100 500 vary width / -limit 1 100 \
      return \
      retr c1 fit nlsfit fit \
      return \
      ov -fit -pen 1 -lt 2 -lw 4 -ply left

alloc folder_list string_array 16
let folder_list[0] = "250us x1"
let folder_list[1] = "250us x2"
let folder_list[2] = "250us x4"
let folder_list[3] = "250us x8"
let folder_list[4] = "250us x20"
let folder_list[5] = "250us x40"
let folder_list[6] = "500us x1"
let folder_list[7] = "1000us x1"
let folder_list[8] = "1000us x2"
let folder_list[9] = "1000us x5"
let folder_list[10] = "1000us x10"
let folder_list[11] = "2000us x1"
let folder_list[12] = "5000us x1"
let folder_list[13] = "10000us x1"
let folder_list[14] = "10000us x2"
let folder_list[15] = "10000us x10"
alloc name string
```

```
yright on
force yes
label left "Normalized Intensity (AU)"
/* label right "Peak Position q_{xy} (nm^{-1})"
label right "Peak Width in q_{||} (nm^{-1})"
label bot "LSA Temperature (\deg C)"
reg bot 0 600
reg left -0.2 1.4
reg right 0.0 0.05
axis

loop %d=0,15,1 {

   let name = delstr(cwd(),0,(strlen(cwd())-4))+" "+folder_list[%d]+"
       Linear Int Qz.dat"
   foreach ("%name%") {

      read %name% -col 2 11 -silent let y=y*10^6 archive int_%d
      read %name% -col 2 12 -silent let y=y*10^6 archive a_%d
      read %name% -col 2 5 -silent archive x0_%d
      read %name% -col 2 6 -silent let y=y*2.355 archive dx0_%d
      read %name% -col 2 14 -silent let y=y*10^6 archive as_%d
      read %name% -col 2 10 -silent let y=y*2.355 archive dx0s_%d

      read %name% -col 1 11 -silent let y=y*10^6 archive int_p_%d
      read %name% -col 1 12 -silent let y=y*10^6 archive a_p_%d
      read %name% -col 1 5 -silent archive x0_p_%d
      read %name% -col 1 6 -silent let y=y*2.355 archive dx0_p_%d
      read %name% -col 1 14 -silent let y=y*10^6 archive as_p_%d
      read %name% -col 1 10 -silent let y=y*2.355 archive dx0s_p_%d

         /* eval name
         cd folder_list[%d]
         if (isdir("images")==0) mkdir("images")
         cd images
         if (isdir("plot position")==0) mkdir("plot position")
         if (isdir("plot temperature")==0) mkdir("plot temperature")

      retr int_%d let y=1 let x=1 archive c1 setv points=@sum(c1)-1

      loop %e=0,points,1 {

         label left "Normalized Intensity (AU)"
         label right "Peak FWHM in q_{||} (nm^{-1})"
         label bot "LSA Temperature (\deg C)"
/*         retr as_%d cull delete irange (%e+1) points
         retr a_%d cull delete irange (%e+1) points reg bot 0 600 reg
             left 0 100 reg right 0 0.15 pl -sym 4 -pen rgb(rgbvalue,
            rgbvalue,rgbvalue) -ply left -erry as_%d:y ov -sym 4 -pen
             1 -ply left
/*         retr a_%d cull delete irange (%e+1) points ov -sym 4 -pen
   1 -ply left

         retr dx0_%d cull delete irange (%e+1) points ov -sym 5 -pen
            rgb(255,rgbvalue,rgbvalue) -ply right -erry dx0s_%d:y ov
            -sym 5 -pen 2 -ply right

         cd "plot temperature\"
         if (%e==(a_%d:npt-1)) retr a_%d cull delete for y<0.15*@max(
            y) archive c1 fitme2 retr dx0_%d cull delete for y>0.14
            archive c1 fitme1 eval %e sleep 1

         declare afilename = cwd()+"/"+delstr(name,13)+"_"+int2base(%
            e,10)+" plot temperature.eps"
         hcopy dev eps
         %afilename%
```

```
         /* if (%e==89) if (%d==1) dev -g xeq return

         label left "Normalized Intensity (AU)"
         label right "Peak FWHM in q_{||} (nm^{-1})"
         label bot "Position (\mu m)"
         retr a_p_%d cull delete irange (%e+1) points reg bot -600
            600 reg left 0 100 reg right 0 0.15 pl -sym 4 -pen rgb(
            rgbvalue,rgbvalue,rgbvalue) -ply left -erry as_p_%d:y ov
            -sym 4 -pen 1 -ply left
         retr dx0_p_%d cull delete irange (%e+1) points ov -sym 5 -
            pen rgb(255,rgbvalue,rgbvalue) -ply right -erry dx0s_%d:y
             ov -sym 5 -pen 2 -ply right
         cd .. cd "plot position\"
         declare afilename = cwd()+"/"+delstr(name,13)+"_"+int2base(%
            e,10)+" plot position.eps"
         hcopy dev eps
         %afilename%
         cd ..
      }
         cd .. cd ..
   }
}

dev -g
xeq -return
```

Creating GISAXS Images with Overlaid Data and Fits

```
genplot reset -silent @echo off
lt 1 pen -1 lw 2
cd gohere
/* size 9 7.45 margins 0.85 1 0.85 0.85 offset 0.35 0
shrink 1.1

/* ////////////////////////////////////////////////
/* Note: direct beam coords are 519.2958 pixles in x
/* and 194.2157 pixles in y, though flipped so 1024-194
/* meaning 829.7843 in y from tif-> txt transform (or genplot read
   direction)
/*
/* Other center is x,y (524.4572,189.3031), y-> 834.6969 px
/* 46.9x46.9 micron pixel size
/* 1.155 Angstroms Wavelenth
/* Sample Detector distance 1.002 m (double check, I rememer 1.6m)
/* q = 2*PI*sin(theta)/lambda = (SAA) 2*PI/lambda * (ypixel-y0)*
   conversion/S2D_length
/* ////////////////////////////////////////////////

alias fit_sides53 \
         fit nlsfit reset accuracy accu1 equ h2(x) maxiter iter1
            verbose 0 sigma sqrt(y) \
         vary ha2 / -limit 0.01 1E7 vary hb2 / -limit 5 35 vary hx2 /
             -limit -20 20 vary hc2 / -limit 0.1 200 vary hdx2 / -
            limit 20 100 return \
         retr c2 fit nlsfit fit \
         let p14[0],q14[0] = ha2,sigma$[0] \
         let p15[0],q15[0] = hb2,sigma$[1] \
         let p16[0],q16[0] = hx2,sigma$[2] \
         reset accuracy accu1 equ h2(x)+g3a(x)+g3b(x) maxiter iter1
            verbose 0 sigma sqrt(y) \
         vary ga3a / -limit 0.1 10000 vary ga3b / -limit 0.1 10000
            vary gx3 / -limit (p2low+5) (p2high-5) vary gx3delta / -
            limit -5 5 vary gdx3 / -limit 4 20 return \
         retr c1 fit nlsfit fit \
```

```
        let p11[0],q11[0] = ga3a+ga3b,sqrt(sigma$[0]^2+sigma$[1]^2)
            \
        let p12[0],q12[0] = (2*gx3-gx3delta)/2,(2*sigma$[2]^2+sigma$
            [3]^2)/2 \
        let p13[0],q13[0] = gdx3,sigma$[4] \
        return

/* Cull and signal peak range limits
setv low_cull,high_cull,midl_cull,midh_cull = 270,770,486,548 /*
   270,770,493(486),545 /* in pixels in raw image
setv p1low,p1high,p2low,p2high = 374,444,594,664
setv gisaxs_x,gisaxs_y = 519.30,834.70
setv gisaxs_q_prop = 2*pi*(46.9/1000)/1002/0.1155 /* inverse nm once
   multiplied by (ypixel-y0)

alloc cs1,cs2,cs3,cs4,cs5,cs6,cs7,cs8,cs11,cs12,cs13,cs21,cs22,cs23
   array 10000
alloc ipt int let ipt = 0

setv temperature = 0
setv stemperature = 0
setv position = 0
setv sposition = 10
setv stmax = 0.02 /* fraction
setv fcount = 0
setv loopcount = 0
/* setv rowstart = 660
/* setv rowend = 720
setv rowstart = 680
setv rowend = 770
setv npoints = 0
setv SMAperiod = 5
setv counter = SMAperiod
setv sumvar = 0
setv counter2 = 0
setv counter3 = 0
setv integrand = 0
setv low = 0
setv medium = 0
setv high = 0
setv bkg_area = 1
setv amp,s_amp,pos,s_pos,width,s_width,tot_area,s_tot_area,bkg_area,
   counter = 0,0,0,0,0,0,0,0,0,0
setv normalize_const = 1
setv s_a94,s_a93,s_a92,s_a91,s_a95,x94_delta=0,0,0,0,0,10
alloc c01 curve 1024
alloc c11 curve 1024
alloc afilename string 1
/* alloc afoldername string 1
alloc Tletter string 1
setv count = 0
setv foldercount = 0
alloc folder_list string_array 16
let folder_list[0] = "250us x1"
let folder_list[1] = "250us x2"
let folder_list[2] = "250us x4"
let folder_list[3] = "250us x8"
let folder_list[4] = "250us x20"
let folder_list[5] = "250us x40"
let folder_list[6] = "500us x1"
let folder_list[7] = "1000us x1"
let folder_list[8] = "1000us x2"
let folder_list[9] = "1000us x5"
let folder_list[10] = "1000us x10"
let folder_list[11] = "2000us x1"
```

```
let folder_list[12] = "5000us x1"
let folder_list[13] = "10000us x1"
let folder_list[14] = "10000us x2"
let folder_list[15] = "10000us x10"
/* cd %afoldername%
declare wherenow cwd()
read "Center.dat" archive folder_centers

let low_cull,high_cull,midl_cull,midh_cull = low_cull-gisaxs_x,
   high_cull-gisaxs_x,midl_cull-gisaxs_x,midh_cull-gisaxs_x
let p1low,p1high,p2low,p2high = p1low-gisaxs_x,p1high-gisaxs_x,p2low-
   gisaxs_x,p2high-gisaxs_x

define f1(x) = 10^3*fa1/[(x-fx1)^4+0.1]+fb1 /* remove 10^3 if go to q
   ^-2 again
define f2(x) = 10^3*fa2/[(x-fx2)^4+0.1]+fb2
define f3(x) = 10^6*fa1/[(x)^4+0.1]+fb1
define f4(x) = 10^6*fa2/[(x)^4+0.1]+fb2
define g1(x) = ga1*gaussn(x,gx1,gdx1)
define g2(x) = ga2*gaussn(x,gx2,gdx2)
define g91(x) = a91*a94*gaussn(x,(x94-x93-x92-x91),dx91)
define g92(x) = a92*a94*gaussn(x,(x94-x93-x92),dx92)
define g93(x) = a93*a94*gaussn(x,(x94-x93),dx93)
define g94(x) = a94*gaussn(x,(x94),dx94)
define g95(x) = a95*a94*gaussn(x,(x94+x95),dx95)

define h1(x) = 10^6*ha1/[(x-hx1)^4+0.1]+hb1
define h2(x) = 10^6*ha2/[abs(x-hx2)^hn2+0.1]+hb2+hc2*gaussn(x,hx2,
   hdx2)
define g3a(x) = ga3a*gaussn(x,(gx3),gdx3) /* right side
define g3b(x) = ga3b*gaussn(x,(gx3delta-gx3),gdx3) /* left side
define g4(x) = ga4*gaussn(x,-hx1,gdx4)

setv ha1,hx1,hb1=1e3,-4,26
setv ha2,hx2,hn2,hb2,hc2,hdx2=1e3,-4,6,26,100,50
setv ga3a,ga3b,gx3,gx3delta,gdx3 = 50,50,90,0,10
setv ga4,gdx4 = 10,50

setv a91,a92,a93,a94,a95=0.1,0.2,0.38,1200,0.18
setv x91,x92,x93,x94,x95=7.7,6.7,5.7,15,3.3
setv dx91,dx92,dx93,dx94,dx95=2,2,1.2,1.2,2
setv accu1,accu2,iter1,iter2 = 1E-7,5E-7,3000,3000

setv npeaks = 1
setv npeaksmax = 0
if (npeaksmax) let npeaks = 0
setv visualize1 = 1 /* Show fitting of individual rows of image
setv visualize2 = 1 /* Show fitting of qz peaks out of fits from qxy
setv visualize3 = 1 /* Write to genplot terminal when completed every
    x images and time
setv visualize3_period = 20
setv visualize4 = 1 /* write to genplot terminal time of files being
   written
setv overwrite = 1

if (visualize4) asctime(time())

/* Main loop for all folders, modify first number to change where to
   start
loop %x=0,15,1 {

   setv count = strlen(wherenow)
   let count = count-4

/*   declare afoldername = delstr(fname[0],4,strlen(fname[0])-1)+" "+
   folder_list[%x]+" Linear Int Qz"
```

```
   if (isdir(folder_list[%x])==0) goto nextfolder

   declare afoldername = wherenow+"/"+folder_list[%x]+"/"
   cmdlin cd %afoldername%

   let fcount = 0
   foreach (*.txt) fcount = fcount+1
   if (fcount==0) cd .. goto nextfolder

   alloc area curve fcount
   alloc findex curve fcount
   alloc fname string_array fcount

   foreach (*.txt) let fname[%i] = %f
   sort -strings fname -strict

/*   alloc ds1,ds2,ds3,ds4,ds5,ds6,ds11,ds12,ds13,ds14,w91,w92,w93,
    w94,w95,ds1n,ds4n,ds11n,ds14n array fcount

/* /* Loop for reading and analyzing all files within the folder
   loop fcount {
      let afilename = fname[%i]
      if (filesize(afilename)/1024/1024<3) goto nextfile

      read -3d tempSurf %afilename% -silent

      let findex:y[%i] = atof(delstr(delstr(fname[%i],0,12),4))
      setv findexcount = %i
      alloc p11,p12,p13,p14,p15,p16,p17,q11,q12,q13,q14,q15,q16,q17
         array 2 /* (rowend-rowstart+1)
      setv ha1,hx1,hb1=1e6,-4,26
      setv ga3a,ga3b,gx3,gx3delta,gdx3,ga4,gdx4 = 50,50,90,0,10,10,50
         matrix row_get tempSurf rowstart,rowend
         let x=x-gisaxs_x
         cull keep xrange low_cull high_cull
         cull delete xrange midl_cull midh_cull cull keep xrange 0
            600 archive rightfull

         matrix row_get tempSurf (rowstart+1),(rowend+1) /* this
            shifts the read of the left side to +1 from the right
            side to make in parallel moreso
         let x=x-gisaxs_x
         cull keep xrange low_cull high_cull
         cull delete xrange midl_cull midh_cull cull keep xrange -600
             0 archive leftfull
         retr leftfull retr rightfull -append cull delete for y>min(
            @max(leftfull),@max(rightfull)) archive c1

         /* ensure no errors when fitting each amplitude
         let ha1,hb1,hx1,ga3a,ga3b,gx3,gx3delta,gdx3 = min(max(ha1,2)
            ,9e6),min(max(hb1,6),34),min(max(hx1,-19),19),min(max(
            ga3a,0.2),9999),min(max(ga3b,0.2),9999),min(max(gx3,p2low
            +6),p2high-4),min(max(gx3delta,-4),4),min(max(gdx3,5),34)

         retr c1 cull delete xrange p1low,p1high cull delete xrange
            p2low,p2high archive c2
         fit_sides53 /* p11 peak amplitude, p12 peak position, p13
            peak width, p14 bkg amp, p15 bkg yoffset, p16 xoffset,
            qxx is sigma of repsective p
         retr c1 let y=fit(x) archive left_fit \
         retr c1 let y=y-fit(x) archive left_subtracted

      let tempSurf:x=(tempSurf:x-gisaxs_x)*gisaxs_q_prop
      let tempSurf:y=-(tempSurf:y-gisaxs_y)*gisaxs_q_prop
      let tempSurf:z=log(tempSurf:z)
```

```
      let findex:y[%i] = atof(delstr(delstr(fname[%i],0,12),4))
      setv findexcount = %i

/* /* Convert position to Temperature
      /* Note, in old lab, CO2 beam approximated by Gaussian of 226.7
         um sigma for 1ms dwell
      /* Note in new lab, 1ms can be approximated (width of region)
         as edgeworth(x,0,520,0.17,-0.3)/edgeworth(0,0,0.17,-0.3) but
          divide width by two (skew can be as low as ~0.12 to give
         ~2% error at T>0.4)
      /* Note in new lab, 250us can be approximated (width of region)
          as edgeworth(x,0,430,0.1,-0.3)/edgeworth(0,0,0.1,-0.3) but
         divide width by two
      /* Note in new lab, 10ms can be approximated (width of region)
         as edgeworth(x,0,650,0,1.3)/edgeworth(0,0,650,0,1.3)
         *(1-0.28)+0.28 but divide width by two
      /* difference in sigma from 520/2 vs 430/2 -> 82.7% narrower at
          250 us vs 1ms at ~600 C
      /* difference in sigma from 520/2 vs 650/2 -> 125% of width at
         10ms vs 1ms at ~600C plus base offset, for full wafer
         samples I am estimating that the offset is much smaller thus
          dividing offset in half since heat goes to full silicon
         wafer and also to metal chuck rather than plastic base in
         thermistor
      /* Fit for 1ms old lab of edgeworth gives 14.876*edgeworth(x,x0
         ,0.234 mm, 0.61 skew, 0.506 kurtosis)

      /* Obtain temperature of sample, 400, 550, 700 C
      setv count = strlen(fname[0])
      declare Tletter = delstr(delstr(fname[0],4,strlen(fname[0])-1)
         ,0,3)
      let low = strspn(Tletter,"a") let medium = strspn(Tletter,"b")
         let high = strspn(Tletter,"c")
      if (low) setv maxT = 400
      if (medium) setv maxT = 550
      if (high) setv maxT = 700
      if (%x<7) setv LSAwidth = 188.2 /* microns = 0.827*227.6
      if (%x==7) setv LSAwidth = 207 /* microns = ~0.91*227.6
      if (%x>7) {
         if (%x<11) setv LSAwidth = 227.6 /* microns = 1ms width
         if (%x<13) setv LSAwidth = 227.6 /* can set for 2/5ms width
         if (%x>12) setv LSAwidth = 284.5
      }
      let position = atof(delstr(delstr(fname[%i],0,12),4))-atof(
         delstr(delstr(fname[0],0,12),4))
      let position = (10*position-10*fcount/2)-folder_centers:y[%x]
      if (%x<13) let temperature = (maxT-23)*gaussn(position,0,
         LSAwidth)+23
      if (%x>12) let temperature = (maxT-23)*edgeworth(position,0,
         LSAwidth,0,1.3)/edgeworth(0,0,LSAwidth,0,1.3)*0.86+23+(maxT
         -23)*0.14
      let sposition = 10
      let stemperature = 0
      if (%x<13) let stemperature = abs((maxT-23)*gaussn((position+
         sposition),0,LSAwidth)-(maxT-23)*gaussn((position-sposition)
         ,0,LSAwidth))/2
      if (%x>12) let stemperature = abs(((maxT-23)*edgeworth((
         position+sposition),0,LSAwidth,0,1.3)/edgeworth(0,0,LSAwidth
         ,0,1.3)*0.86+23+(maxT-23)*0.14)-((maxT-23)*edgeworth((
         position-sposition),0,LSAwidth,0,1.3)/edgeworth(0,0,LSAwidth
         ,0,1.3)*0.86+23+(maxT-23)*0.14))/2
      let stemperature = sqrt(stemperature^2+(stmax*(temperature-23))
         ^2+9)

            if (isdir("images")==0) mkdir("images")
```

```
            cd images
            if (isdir("fits")==0) mkdir("fits")
            cd fits
            alloc temp string 1 let temp = int2base(round(temperature
               ,0),10)+" \pm "+int2base(round(stemperature,0),10)+" \
               deg C\n"+folder_list[%x]+" LSA"
            retr c1 let x=x*gisaxs_q_prop archive c1 retr c1
            yright on force on label left "Signal (AU)" label right "
               Signal w/o bkg (AU)" label bot "q_{||} (nm^{-1})" reg
               left 0 1500 reg bot -0.5 0.5 reg right -0.7*max
               (70/0.7,ga3a,ga3b) 1.3*max(130/1.3,ga3a,ga3b) axis pl
               -sym 4 /* -identify temp /* -250*gisaxs_q_prop 250*
               gisaxs_q_prop
               ov -f fit(x/gisaxs_q_prop) ov -f h2(x/gisaxs_q_prop) -
                  pen 4 /* -identify "Backgound Fit"
               let y=y-h2(x/gisaxs_q_prop) ov -sym 4 -pen 2 -ply
                  right /* let y=y-fit(x/gisaxs_q_prop) ov -sym 4 -
                  pen 2 -ply right /* -identify "Residuals"
               retr c1 let y=y-h1(x/gisaxs_q_prop)-g4(x/gisaxs_q_prop
                  )
               ov -sym 4 -pen 4 -ply right
               ov -f g3a(x/gisaxs_q_prop)+g3b(x/gisaxs_q_prop) -pen 1
                    -lt 2 -lw 5 -ply right /* -identify "Signal Fit"
               force off yright off
            let afilename=delstr(afilename,strlen(afilename)-4)+"
               fits.eps"
            /* let afilename=afoldername+afilename
            hcopy dev eps
            %afilename%
            /* wait
            cd .. /* now in images folder cd ..

/* palette rainbow -? /* gives all palettes why didn't I know about
   this???
      label bot "q_{||} (nm^{-1})" label left "q_{\perp} (nm^{-1})"
         label right " "
      alloc temp string 1
      let temp = int2base(round(temperature,0),10)+" \pm "+int2base(
         round(stemperature,0),10)+" \deg C\n"+folder_list[%x]+" LSA"
      yright on force on reg left 0 1 reg right 0 1 reg bot -0.5 0.5
         pl tempSurf -bitmap -palette hot -zrange log(20) log(2000) -
         identify temp -pen 0 force off yright off

/*       declare afoldername = wherenow+"/"+folder_list[%x]+"/images/"
/*       cd %afoldername%
            if (isdir("raw")==0) mkdir("raw")
            cd raw
      let afilename = fname[%i]
      let afilename=delstr(afilename,strlen(afilename)-4)+" raw.eps"

      /* let afilename=afoldername+afilename
      hcopy dev eps
      %afilename%
/* wait
      cd .. cd .. /* now in subfolder with each text image file
      :nextfile
   }
   cmdlin cd ..

   /* Output Data
   setv count = strlen(wherenow)
   let count = count-4
   declare afoldername = delstr(fname[0],4,strlen(fname[0])-1)+" "+
      folder_list[%x]+" Linear Int Qz"
```

```
   /* columns are (1) x position, (2) Temperature, (3) Int Area, (4)
      Amplitude, (5) Position in q space, (6) width in q space, (7)
      std dev in peak area, (8) std dev in peak amplitude, (9) std
      dev in peak position, (10) std dev in peak width, (11) peak
      area normalized, (12) peak intensity normalized, (13) peak area
       normalized sigma, (14) peak intensity normalized sigma
/*   write %afoldername%.dat -list ds5 ds6 ds4 ds1 ds2 ds3 ds14 ds11
   ds12 ds13 ds4n ds1n ds14n ds11n /* -silent
/*   afoldername
/*   cmdlin cd %wherenow%

/*   let area_T:y=ds1n
/*   label bot "Temperature (\deg C)" label left "Normalized
   Amplitude (Counts/bkg)" retr area_T reg bot auto reg left 0 1.1*
   @max(area_T:y) pl -sym 4 -erry ds11n -identify %afoldername%

   :nextfolder
}

dev -g
xeq -return
```

B.2 Modeling Macros

This is the compilation of Genplot and C programs used for simulations shown in Chapter 7.

B.2.1 Genplot Control Macro for Modeling

```
genplot reset -silent @echo off
lt 1 pen -1 lw 2
label left "Order Parameter \Gamma"
label bot "Temperature (\deg C)"
reg left -0.05 1.05 reg bot 0 500
force on
log bot off

/*
   ////////////////////////////////////////////////////////////////////////////

/* BCP simulation: Parameters and Function linkes (use listv -h)
/* Functions
/*  bcp()      Print this message
/*  diff(T)    Diffusivity function (m^2/s)
/*  force(T,g) Driving force function
/*  tnorm(time) Normalized temperature versus time
/* Variables
/*  T_g        Glass transition temperature (default 110 oC)
/*  T_odt      ODT transition temperature (default 200 oC)
/*  D0         Diffusion prefactor in WLF (default 6*10^-19 m^2/s)
/*  c1g        WLF parameter (default 13 unitless)
/*  c2g        WLF parameter (default 70 K)
/*  D02        Diffusion prefactor of Arrhenius (default 2*10^-8 m^2/
   s)
/*  E_a        Activation enthalpy (default 60 kJ/mol)
```

```
/*  T_width    Width of ODT conversion from order to disorder (
   default 25 K)
/*  K0         Prefactor in rate (default 5*10^17)
/*  dwell      Dwell time (default 2*10^-3 s)
/*  t_start    Start time of simulation (default -0.1 units of dwell)
/*  t_end      End time of simulation (default 3 units of dwell)
/*  T_RT       Room temperature (default 25 oC)
/*  T_max      Maximum temperature (default 500 oC)
/*  T_model    Temperature profile model (0=T_profile curve 1=square,
    2=triangle [default])
/*  gamma_0    Starting value (default 1 unitless [range 0-1])
/*
   ////////////////////////////////////////////////////////////////////////////


user -load bcp2
/* user -load bcpavrami

/* need to modify dwell (to suit every type of T profile), T_width,
   T_model at start
/* curves passed as T_model must be in x units of dwells

/*
   ////////////////////////////////////////////////////////////////////////////

/* Modeling and plotting script for BCP order parameter for
   hypothetical
/* models of diffusion, driving force, and degree of segregation
/* Order Parameter = Gamma(time, Temperature)
/* Diffusivity = D(Temperature,Gamma) [D(gamma) is equivalent in this
    case to D(chi)]
/* degree of segregation depends on above or below TODT
/*
/* Solve dGamma/dt = D*F*(piecewise gamma) as function of t,
/* integrate over LSA like triangle functions in temperature
/*
/*
   ////////////////////////////////////////////////////////////////////////////


/* aliased functions to produce normalized T_profile for the bcp user
    module

alias LSA_profile \
  let filename = temporal_list[temporal_test] \
  read %filename% -silent let y=y-@min(y) let y=y/@max(y) let x=x
     /1000/(base2int(time_us,10)*10^-6) \
  cull delete for y<((80-T_RT)/(max_maxT-T_RT)) let x=x-@min(x) let
     t_end=@max(x)-0.1 archive T_profile

alias LSA_profile_mod \
  let filename = temporal_list[temporal_test] \
  read %filename% -silent let x=x/1000/(base2int(time_us,10)*10^-6)
     archive resistance let x1=@max(x) \
  fit spline -silent \
  let tau = (base2int(time_us,10)*10^-3) \
  solve fit(x)-zero_crit 0.2*x1 0.8*x1 -iter 10000 -res x0 -silent \
  let avg_low=min(2500*(x0+(ntau*tau+tau-dntau*tau/2))/x1,2450) let
     avg_high=min(2500*(x0+(ntau*tau+tau+dntau*tau/2))/x1,2500) \
  let y1=@avg(y,avg_low,avg_high) \
  retr resistance setv yold=@max(y) let y=max(y*(-1*min(floor((x-x0)/
     x0),0))+(y-y1)/(yold-y1)*max(ceil(0.5*(x-x0)/(x1-x0)),0),0) let
     y=y-@min(y) let y=y/@max(y) let x=x-@min(x) \
  let x=x-@min(x) let t_end=@max(x)-0.1 archive T_profile

/*  cull delete for y<((80-T_RT)/(max_maxT-T_RT)) \
```

```
alias predefined_profile \
  retr temporal_profile let y=y-@min(y) let y=y/@max(y) let x = x/
     @max(x) t_end=@max(x) archive T_profile

alias do_label \
  label left "Order Parameter \Gamma" label bot "Temperature (\deg C)
     " reg left -0.05 1.05 reg bot 0 500 \
  axis \
  let name="F = "+int2base(k0*10^(-1*floor(log(k0))),10)+"x10^{"+
     int2base(floor(log(k0)),10)+"}|T-T_{ODT}|(\Gamma-\Gamma_{equil})
     " \
  identify name -place 0.4 6.2 -nomark \
  let name="D = D_{T_{g}}e^{[C_{1g}(T-T_{g})/(C_{2g}+T-T_{g})]}" \
  identify name -place 0.4 5.85 -nomark \
  let name="D_{T_{g}} = "+int2base(d0*10^(ceil(-log(d0))),10)+"x10
     ^{-"+int2base(ceil(-log(d0)),10)+"} m^{2}/s" \
  identify name -place 0.4 5.55 -nomark \
  let name="C_{1g} = "+int2base(c1g,10)+" C_{2g} = "+int2base(c2g,10)
     +"K" \
  identify name -place 0.4 5.3 -nomark \
  let name=" "+name2+"WLF Diffusion \n " \
  let name=name+name3 \
  identify name -place 5.3 6.2 -nomark

alias do_label2 \
  label left "Order Parameter \Gamma" label bot "Temperature (\deg C)
     " reg left -0.05 1.05 reg bot 0 500 \
  axis \
  let name="F = "+int2base(k0*10^(-1*floor(log(k0))),10)+"x10^{"+
     int2base(floor(log(k0)),10)+"}|T-T_{ODT}|(\Gamma-\Gamma_{equil})
     " \
  identify name -place 0.4 6.2 -nomark \
  let name="D = D_{T_{g}}e^{[C_{1g}(T-T_{g})/(C_{2g}+T-T_{g})]}" \
  identify name -place 0.4 5.85 -nomark \
  let name="D_{T_{g}} = "+int2base(d0*10^(ceil(-log(d0))),10)+"x10
     ^{-"+int2base(ceil(-log(d0)),10)+"} m^{2}/s" \
  identify name -place 0.4 5.55 -nomark \
  let name="C_{1g} = "+int2base(c1g,10)+" C_{2g} = "+int2base(c2g,10)
     +"K" \
  identify name -place 0.4 5.3 -nomark \
/*   let name=" "+name2+"WLF Diffusion \n " \
/*   let name=name+name3 \
/*   identify name -place 5.3 6.2 -nomark

/*   let name="    + D_{0}e^{[-E_{A}/k_{b}T]}" \
/*   identify name -place 0.4 5.55 -nomark \
/*   let name="D_{0} = "+int2base(d02*10^(ceil(-log(d02))),10)+"x10
    ^{-"+int2base(ceil(-log(d02)),10)+"} m^{2}/s" \
/*   identify name -place 0.4 4.6 -nomark \
/*   let name="E_{A} = "+int2base(E_a,10)+" kJ/mol" \
/*   identify name -place 0.4 4.35 -nomark \
/*   let name=name+" \n D_{BCP} = D_{PS} / "+int2base(d_factor,10) \

/* User defined simulation conditions
   ////////////////////////////////////////////////////////////////////////

setv min_maxT,max_maxT,delta_maxT = 0,500,2
setv n = 1                          /* number of values to test in
   terms of gammastart (i.e. 0, 0.5 1 for n=2)
setv fstart,fend = 0,2              /* Files to start and end at (up
   to value of 6)
setv do_LSA = 1                     /* Unmodified quench
setv do_LSA_mod = 0                 /* modified to quench to RT
```

```
setv do_triangle = 0                /* Triangle wave temporal thermal
    profile, within
setv do_trap = 0                    /* Trapezoidal wave temporal
   thermal profile
setv do_inf_quench = 0              /* Square wave
setv do_const_quench = 0            /* Not implemented
setv T_width = 0.1                  /* /* Width of ODT conversion
   from order to disorder (default 25 K)
setv T_arr_dom = 550                /* deg C
setv save_me = 0                    /* Save plots if =1
setv d_factor = 30                  /* Factor of diffusivity of PS vs
    BCP at 230 C
/* setv show_values = 1             /* supposed to show temporal
   evolution...

if (do_LSA+do_LSA_mod+do_triangle+do_trap+do_const_quench>1) printf "
   Choose one thermal profile idiot" dev -g xeq -return

/* Defining Materials Constants etc
   ////////////////////////////////////////////////////////////////////////

setv T_g = 110                 /* Glass transition temperature (
   default 110 oC)
setv T_odt = 200               /* ODT transition temperature (default
   200 oC)
setv D0 = 6*10^-19             /* Diffusion prefactor in WLF (default
   6*10^-19 m^2/s)
setv c1g = 13                  /* WLF parameter (default 13 unitless)
setv c2g = 70                  /* WLF parameter (default 70 K)
setv D02 = 2*10^-8             /* Diffusion prefactor of Arrhenius (
   default 2*10^-8 m^2/s)
setv E_a = 150                 /* Activation enthalpy (default 60 kJ/
   mol)
setv K0 = 5*10^15              /* Prefactor in rate (default 5*10^17)
setv mw,mw0,alpha = 53.8,53.8,-2  /* Assumes relative to H polymer
   (53.8 kg/mol), C=67.1, B=82, alpha=-2 is entangled chains (
   reptation)
setv kb = 1.3806488*10^-23     /* J/mol-K /* 8.617*10^-5 eV/K
setv na = 6.022141*10^23       /* avagadro's constant #/mol
setv d230 = 5*10^-14           /* diffusivity of PS at 230 oC given in
    paper

/* D=Do(T)*M^(alpha) where alpha = -2 for pure reptation, M = MW,
   alpha = -1 for non-entangled polymers
/* low MW BCPs follow rouse scaling (alpha=-1) and typical WLF
   diffusion
/* Likely, my BCPs follow reptation scaling (alpha=-2) or worse since
    entangled BCPs do not quite scale
/* to reptation from phase segregated regions and typical WLF
   diffusion
/* WLF: D=Dtg*exp{C1g(T-Tg)/[C2g+(T-Tg)]}

/* Defining annealing conditions, often changed in loops
   ////////////////////////////////////////////////////////////////////////

setv dwell = 1*10^-3  /* Dwell time (default 2*10^-3 s)
setv t_start = -0.1  /* Start time of simulation (default -0.1 units
   of dwell)
setv t_end = 3    /* End time of simulation (default 3 units of dwell
   )
setv T_RT = 20    /* Room temperature (default 25 oC)
setv T_max = 500  /* Maximum temperature (default 500 oC)
let T_model = 0   /* Temperature profile model (0=T_profile curve 1=
   square, 2=triangle [default])
setv gamma_0 = 1  /* Starting value (default 1 unitless [range 0-1])
```

```
setv ntau = 10    /* distance from peak T which is defined as room T
   in modified LSA
setv dntau = 0.5  /* region over which to average in time in modified
    LSA
setv npoints = 10^4

/* Initializing other variables, Units in deg C and Seconds
   ////////////////////////////////////////////////////////////////////////

setv culltemp = 0
setv tau = 0
setv temp = 0
setv count=0
setv fraction=0
setv x1 = 1
setv y0 = 1
setv x0 = 0
setv y1 = 1
setv zero_crit = 0.995
setv avg_low,avg_high = 2450,2500
setv gamma = 0
setv Tmax = 300 /* C
setv gammastart = 0.2 /* Start disordered = 0, start ordered = 1
setv temporal_test = fstart /* which file to test for the temporal
   profile
setv count=0
alloc time_us string 1
alloc name string 1
alloc name2 string 1
alloc name3 string 1
alloc filename string 1
alloc temporal_list string_array 7
let temporal_list[0] = "250us 300C temporal.dat"
let temporal_list[1] = "1000us 300C temporal.dat"
let temporal_list[2] = "10000us 300C temporal.dat"
let temporal_list[3] = "150us 300C temporal.dat"
let temporal_list[4] = "500us 300C temporal.dat"
let temporal_list[5] = "2000us 300C temporal.dat"
let temporal_list[6] = "5000us 300C temporal.dat"
alloc gammas curve 1000
setv temperature_plots=0

/* Define Functions for reference if I want to calculate at a
   specific point
define dArrhenius(T) = d02*exp(-1*(E_a*1000)/(kb*na)/(T+273.15))
define dwlf(T) = d0*exp(c1g*(T-T_g)/(c2g+T-T_g))
define F(T,gamma) = k0*abs(T-T_odt)*(erfc((T-T_odt)/T_width)/2-gamma)
define d(T) = dwlf(T)+dArrhenius(T)
define dgammadt(T,gamma) = d(T)*(mw/mw0)^(alpha)*F(T,gamma)

loop %c=15,15,2 {
let c1g=%c
let c2g=70


/* Having chosen C1g, C2g and the Arrhenius dominance temperature,
/* And given a total diffusivity at one temperature, find d0 and d02
let d0=d230*d0/dwlf(230)/d_factor
let d02=dwlf(t_arr_dom)*d02/darrhenius(T_arr_dom)

/* solve darrhenius(x)-dwlf(x) (T_g+50) (T_g+500) -res T_arr_dom -
   silent -noerrors
/* let T_arr_dom = nint(T_arr_dom)

/* Loop through all possible temporal profiles
/* printf asctime(time())
```

```
loop %b=1,1,1 {

/* index: 0=LSA, 1=LSA mod, 2=triangle, 3=trapezoid, 4=inf quench sq
   wave
/* eval %b
if (%b==0) let do_lsa,do_lsa_mod,do_triangle,do_trap,do_inf_quench
   =1,0,0,0,0
if (%b==1) let do_lsa,do_lsa_mod,do_triangle,do_trap,do_inf_quench
   =0,1,0,0,0
if (%b==2) let do_lsa,do_lsa_mod,do_triangle,do_trap,do_inf_quench
   =0,0,1,0,0
if (%b==3) let do_lsa,do_lsa_mod,do_triangle,do_trap,do_inf_quench
   =0,0,0,1,0
if (%b==4) let do_lsa,do_lsa_mod,do_triangle,do_trap,do_inf_quench
   =0,0,0,0,1

/* let do_lsa,do_lsa_mod,do_triangle,do_trap,do_inf_quench=0,1,0,0,0


let T_model = 0

/* Loop through all LSA Dwell times and if LSA chosen, LSA temporal
   thermal profiles
loop %a=fstart,fend,1 {
  let temporal_test = %a
  printf temporal_list[temporal_test]+" "+asctime(time())
  let time_us=delstr(temporal_list[temporal_test],(strlen(
     temporal_list[temporal_test])-20))
  let dwell=base2int(time_us,10)*10^-6

  if (do_inf_quench) let T_model=1 let name2=time_us+"\mu s at Peak T
      \n " let name3=int2base(100,10)+"\% at Peak T"+"\n infinite
     quench"
  if (do_triangle) let T_model = 2 let name2=time_us+"\mu s Triangle
     \n Thermal Profile \n " let name3=" "
  if (do_LSA) let name2=time_us+" \mu s LSA \n Thermal Profile \n "
     let name3= "Unmodified Quench" LSA_profile
  if (do_LSA_mod) let name2=time_us+"\mu s LSA \n Thermal Profile \n
     " let name3= "Room T at t_{0}+"+int2base(ntau,10)+"\tau"
     LSA_profile_mod
  if (do_trap) {
    let name2=time_us+"\mu s Trapezoidal \n Thermal Profile \n " let
       name3=int2base(int((t2-t1)*100),10)+"\% at Peak T"
    setv t1,t2=0.45,0.55
    create y=x/t1 -range 0 t1 -points npoints*t1 archive one
    create y=1 -range t1 t2 -points npoints*(t2-t1) archive two
    create y=1-(x-t2)/(1-t2) -range t2 1 -points npoints*(1-t2)
       archive three
    retr one retr two -append retr three -append sort -strict -silent
        /* archive temporal_profile
    /* predefined_profile
    let y=y-@min(y) let y=y/@max(y) let x = x/@max(x) let t_end=@max(
       x) archive T_profile
  }
  if (do_const_quench==9.5) {
    let name2=time_us+"\mu s Const Quench \n Thermal Profile \n " let
        name3=" "
    setv t1,t2,fwidth=0.5,1,10^-3
    create y=1 -range 0 t1 -points npoints*(t1) archive one
    create y=1-(x-t1)/(1-t1) -range t1 1 -points npoints*(1-t1)
       archive two
    retr one retr two -append archive temporal_profile
    predefined_profile
  }

  do_label
```

```
  /* Loop through starting order conditions (gamma_0)
  loop %z=0,n,1 {
    let gamma_0 = max((1-%z/n),10^-2)
    let count=0
    /* Loop through peak temperatures of each profile (abcissa of
       plots)
    loop %y=min_maxT,max_maxT,delta_maxT {
      let T_max=%y
      if (temperature_plots) let gamma_0=1
      user /* reg auto pl sleep 2 /* running user defined c program
      archive c1
      let gammas:x[count]=T_max
      let gammas:y[count]=c1:y[@index(c1:x,@max(x))-10]
      let count=count+1
      if (temperature_plots) {
        retr T_profile let y=y*(T_max-T_RT)+T_RT archive T_profile2
        retr T_profile2 cull delete yrange 0 @max(y)*0.99 setv xbar=
           @average(x) retr T_profile2 let x=x-xbar archive
           T_profile2 /* let xbar=-@min(x)
        yright on force on label right "Temperature (\deg C)" label
           bot "Time (ms)" identify -place 5 6.4 reg bot 0.5*@min(
           T_profile2:x) 0.5*@max(T_profile2:x) reg left -0.1 1.3
           reg right 0 400 retr T_profile2 pl -lw 4 -lt 1 -pen 18 -
           ply right /* -3*base2int(time_us,10)/10^3 5*base2int(
           time_us,10)/10^3
        alloc tempname string 1 let tempname="T_{g} = "+int2base(T_g
           ,10)+" \deg C" create y=T_g -range @min(T_profile2:x)
           @max(T_profile2:x) ov -lw 5 -lt 4 -pen 4 -ply right -
           identify %tempname% /* "T_{g} = %int2base(T_g,10)% \deg C
           "
        let tempname="T_{ODT} = "+int2base(T_odt,10)+" \deg C"
           create y=T_odt -range @min(T_profile2:x) @max(T_profile2:
           x) ov -lw 5 -lt 4 -pen 2 -ply right -identify %tempname%
           /* "T_{ODT} = %int2base(T_odt,10)% \deg C"
        retr T_profile2 cull delete yrange 0 110 setv x11,x12=@min(x
           ),@max(x) alloc temp curve 2 let temp:x=x11 let temp:y
           [0]=0 let temp:y[1]=T_g+70 retr temp ov -lw 4 -lt 2 -pen
           4 -ply right let temp:x=x12 retr temp ov -lw 4 -lt 3 -pen
            4 -ply right
        if (T_max > T_odt) retr T_profile2 cull delete yrange 0 200
           setv x11,x12=@min(x),@max(x) alloc temp curve 2 let temp:
           x=x11 let temp:y[0]=0 let temp:y[1]=T_odt+150 retr temp
           ov -lw 4 -lt 2 -pen 2 -ply right let temp:x=x12 retr temp
            ov -lw 4 -lt 3 -pen 2 -ply right
        let tempname="T_{max} = "+int2base(T_max,10)+" \deg C \
           Gamma_{0} = 1" retr c1 let x=x/base2int(time_us,10)*10^6-
           xbar ov -lw 4 -lt 1 -pen 1 -identify %tempname%
        let gamma_0=0
        user
        archive c1
        alloc tempname string 1 let tempname="T_{max} = "+int2base(
           T_max,10)+" \deg C \Gamma_{0} = 0" retr c1 let x=x/
           base2int(time_us,10)*10^6-xbar ov -lw 4 -lt 7 -pen 1 -
           identify %tempname% /* sleep 0.5 wait
        }
      }
    retr gammas cull delete for x==0
    archive gammas_%a_%z
/*     retr gammas_%a_%z ov -sym 4 -l&s -pen %z+1 -symsize 0.1 /* -
   identify name
  }
  create y=x -range -0.1 0.51 -points 10 let x=T_g ov -lt 2 -pen 1
  create y=x -range -0.1 1.1 -points 10 let x=T_odt ov -lt 6 -pen 2
```

```
  if (save_me) dev pm
}
} /* Big Loop
} /* c2g loop

  printf asctime(time())


yright off
  label left "Order Parameter \Gamma" label bot "Temperature (\deg C)
     " reg left -0.05 1.05 reg bot 0 500 \
  axis \
  let name="F = "+int2base(k0*10^(-1*floor(log(k0))),10)+"x10^{"+
     int2base(floor(log(k0)),10)+"}|T-T_{ODT}|(\Gamma-\Gamma_{equil})
     " \
  identify name -place 0.4 6.2 -nomark \
  let name="D = D_{T_{g}}e^{[C_{1g}(T-T_{g})/(C_{2g}+T-T_{g})]}" \
  identify name -place 0.4 5.85 -nomark \
  let name="D_{T_{g}} = "+int2base(d0*10^(ceil(-log(d0))),10)+"x10
     ^{-"+int2base(ceil(-log(d0)),10)+"} m^{2}/s" \
  identify name -place 0.4 5.55 -nomark \
  let name="C_{1g} = "+int2base(c1g,10)+" C_{2g} = "+int2base(c2g,10)
     +"K" \
  identify name -place 0.4 5.3 -nomark \
identify -place 5.0 6.2 -nomark

setv const=1
retr gammas_000_000 let y=y^const ov -lt 1 -pen 1 -lw 3 -identify
    "250 \mu s Ordered Start"
retr gammas_000_001 let y=y^const ov -lt 2 -pen 1 -lw 3 -identify
    "250 \mu s Disordered Start"
retr gammas_001_000 let y=y^const ov -lt 1 -pen 2 -lw 3 -identify "1
    ms Ordered Start"
retr gammas_001_001 let y=y^const ov -lt 2 -pen 2 -lw 3 -identify "1
    ms Disordered Start"
retr gammas_002_000 let y=y^const ov -lt 1 -pen 4 -lw 3 -identify "10
     ms Ordered Start"
retr gammas_002_001 let y=y^const ov -lt 2 -pen 4 -lw 3 -identify "10
     ms Disordered Start"

dev -g
xeq -return
```

B.2.2 Genplot User Module bcpavrami.c

User module for modeling Avrami nucleation and growth like segregation behavior. This must be compiled and placed in the genplot local folder equivalent to that below.

```
Program Files (x86)\cgs\Genplot\NT\Local

/** bcpavrami.c
 ** Routine to simulate the ordering of BCPs with a complex
    temperature
 ** profile. Allows arbitrary models for the forcing function and the
 ** diffusivity, as well as arbitrary temperature profiles.
 **/

/** ================================================================
  user -load bcpavrami
```

```
  label bot "Time [s]" reg bot t_start*dwell t_end*dwell
  label left "Order [AU]" reg left 0 1

  echo Triangle temperature profile
  let t_model = 2
  axis foreach (300 250 240 230 220 210 200 190 180) let t_max = %f
     user ov
  sleep 2

  echo Square temperature profile
  let t_model = 1
  axis foreach (300 250 240 230 220 210 200 190 180) let t_max = %f
     user ov
  sleep 2

  echo Curve based profile using sin-like profile
  let t_model = 0
  create -curve T_Profile y = sin(pi*x) -range 0 1 -points 200
  axis foreach (300 250 240 230 220 210 200 190 180) let t_max = %f
     user ov
  sleep 2

  echo Curve based profile using Gaussian profile
  let t_model = 0
  create -curve T_Profile y = 2^{-((x-1)/0.5)^2} -range -1 3 -points
     200
  axis foreach (300 250 240 230 220 210 200 190 180) let t_max = %f
     user ov
  sleep 2

  echo Can also extract the temperature profile as used (to check)
  3d user let y = z 2d
  label left "Temperature [\deg C]"
  region auto plot
==============================================================================
     **/

#define MODULENAME "bcpavrami"

/* ------------------------------ */
/* Feature test macros    */
/* ------------------------------ */
#define _POSIX_SOURCE                              /* Always require
   POSIX standard */
#include "preload.h"

/* ------------------------------ */
/* Standard include files */
/* ------------------------------ */
#include <stdio.h>
#include <stdlib.h>
#include <float.h>
#include <math.h>

/* ------------------------------ */
/* Local include files    */
/* ------------------------------ */
#define NO_PATH_EXTENSIONS                 /* Avoid GENPLOT errors
   with GCC */
#include "mytypes.h"
#include "extends.h"
#include "lexp.h"
#include "user.h"

/* ------------------------------ */
/* My local typedef's and defines */
/* ------------------------------ */
```

```
#define R   (8.3144E-3)       /* Gas constant kJ/mol-K */

/* ------------------------------ */
/* My external function prototypes */
/* ------------------------------ */

/* ------------------------------ */
/* My internal function prototypes */
/* ------------------------------ */
static int my_help(int type, TMPREAL *result, TMPREAL *args);
static int my_diff(int type, TMPREAL *result, TMPREAL *args);
static int my_force(int type, TMPREAL *result, TMPREAL *args);
static int my_tnorm(int type, TMPREAL *result, TMPREAL *args);
static int my_beta(int type, TMPREAL *result, TMPREAL *args);

double ERF_S(int key, double x);
#define erfc(x) (ERF_S(2,x))

/* ------------------------------ */
/* My usage of other external fncs */
/* ------------------------------ */

/* ------------------------------ */
/* My share of global externals */
/* ------------------------------ */

/* ------------------------------ */
/* Locally defined global vars */
/* ------------------------------ */

double T_g = 110;                   /* glass transition temperature (
   oC) */
double T_odt = 200;           /* ODT transition temperature (oC)  */
double D0 = 6E-19;            /* Diffusion prefactor in WLF */
double c1g = 13;                    /* WLF parameter */
double c2g =70;               /* WLF parameter */
double D02 = 2E-8;            /* Diffusion prefactor of Arrhenius */
double E_a = 60;                    /* Activation enthalpy (kJ/mol)
     */
double T_width = 25;          /* Width of ODT conversion from order
   to disorder */
double K0 = 5E17;                   /* Prefactor in rate */
double avrami_n = 3;          /* Avrami exponent for time and
   diffusivity (n-1) */
double N0 = 1E-8;             /* Nucleation rate prefactor fit value
   */
double E_a_N = 60;            /* Nucleation activation energy (kJ/mol
   ) */
double E_a_N_0 = 60;          /* Nucleation attempt frequency
   activation energy (kJ/mol */

double dwell = 2E-3;          /* Dwell time */
double t_start = -0.1;  /* Starting time of simulation (units of
   dwell) */
double t_end = 3;                   /* Ending time of simulation (
   units of dwell) */
double T_RT = 25;                   /* Room temperature */
double T_max = 500;           /* Maximum temperature */
int  T_model = 2;             /* Model for the temperature profile */

double gamma_0 = 1.0;   /* Starting value for gamma */

/*
   ============================================================================

-- Return "mobility" or "diffusivity" of chains
--
```

```
-- Usage: double = Diffusivity(double T)
--
-- Input: T - temperature in oC
--
-- Output: none
--
-- Return: value proportional to the diffusivity
================================================================================
    */
double Diffusivity(double T) {
      if (T_g-T > c2g) T = T_g-c2g+2;           /* Avoid exploding
         exponential in WLF */
      return D0*exp(c1g*(T-T_g)/(c2g+T-T_g))+D02*exp(-E_a/R/(T+273));
}

/*
   ================================================================================

-- Return driving force factor for chain alignment (order parameter)
--
-- Usage: double = Force(double T, double gamma)
--
-- Input: T - temperature in oC
--     gamma - order parameter
--
-- Output: none
--
-- Return: value proportional to the driving force for alignment
================================================================================
    */
double Force(double T, double gamma) {
      double gamma_eq, drive;
      gamma_eq = 0.5 * erfc((T-T_odt)/T_width);                    /*
         Equilibrium gamma of T */
      drive = gamma_eq - gamma;                                    /*
         Driving force               */
      /* drive *= fabs(T-T_odt); removed for avrami calculation */
         /* Optional scaling of driving force */
      return drive;
}

/*
   ================================================================================

-- Return Avrami beta factor (no force function and no prefactor)
--
-- Usage:   double = Beta(double T, double gamma)
--
-- Input:   T - temperature in oC
--          gamma - order parameter
--
-- Output:  none
--
-- Return:  value proportional to the slope of gamma(t)
================================================================================
    */
double Beta(double T) {
/*    double beta, gamma_eq; */
/*    double dgdt_a , drive; */
/*    gamma_eq = 0.5 * erfc((T-T_odt)/T_width); */                 /*
   Equilibrium gamma of T */
/*    drive = gamma - gamma_eq; */                                 /*
   Driving force                */
/*    beta = N0 * exp(-E_a_N/(R*(T+273.0)*pow(fabs(T-T_odt+0.1),2.0))
   ); */ /* *Diffusivity(T); */ /* Determining factor of
   nucleation_rate*growth_rate^n, now distance scaling factor q is a
   part of N0 */
```

```
/*    dgdt_a = avrami_n * pow(beta,(1.0/avrami_n)) * pow((-log
    (1.0001-(gamma-gamma_eq))),((avrami_n-1.0)/avrami_n)); */  /*
    Calculation of slope from beta and calculated tOptional scaling of
     driving force */
       return N0 * exp(-E_a_N/(R*(T+273)*pow((fabs(T-T_odt)+0.01),2.0)
          )); /* avrami_n * pow(beta,(1.0/avrami_n)) * pow((-log
          (1.0001-(gamma-gamma_eq))),((avrami_n-1.0)/avrami_n)); */
}

/*
    ============================================================================

-- Return normalized temperature corresponding to a given simulation
    time
--
-- Usage: double = tnorm(double t_prime);
--
-- Input: t_prime - normalized time (seconds / dwell)
--
-- Output: none
--
-- Return: [0-1] value corresponding to RT to Tmax
============================================================================
     */
/* Structure for dealing with "curve" based temperature profiles.
    Must
 * be setup before calling tnorm for the first time. To make sure
 * things are safe, ipt should always be set to 0 initially. Code
 * assumes constant extension of temperature profile before and after
 * given data.
 *
 * Curve must be normalized [0,1] on Y and in units of dwell time in X
     .
 * This allows scaling of the profile for different dwells and
 * temperatures. If you want to use absolute temperatures, just set
 * T_RT to 0.0 and T_max to 1.0
 * */
struct {
      REAL *x, *y;                          /* X and Y pointers */
      int npt;                                    /* Number of
         points in curve */
      int ipt;                                    /* Current
         index that corresponds to tprime */
} Tcurve = {NULL, NULL, 0, 0};

double tnorm(double tprime) {
      double tnow=0;

      /* Use a curve profile */
      if (T_model == 0) {
            while (Tcurve.ipt > 0    && Tcurve.x[Tcurve.ipt] > tprime)
                Tcurve.ipt--;  /* Get between two valid points */
            while (Tcurve.ipt < Tcurve.npt-1 && Tcurve.x[Tcurve.ipt
               +1] < tprime) Tcurve.ipt++;  /* Next point */
            if (tprime < Tcurve.x[Tcurve.ipt]) {
                  tnow = Tcurve.y[Tcurve.ipt];
            } else if (tprime > Tcurve.x[Tcurve.ipt+1]) {
                  tnow = Tcurve.y[Tcurve.ipt+1];
            } else {
                  tnow = Tcurve.y[Tcurve.ipt] + (Tcurve.y[Tcurve.ipt
                     +1]-Tcurve.y[Tcurve.ipt])/(Tcurve.x[Tcurve.ipt
                     +1]-Tcurve.x[Tcurve.ipt])*(tprime-Tcurve.x[
                     Tcurve.ipt]);
            }

      /* Simple square wave */
      } else if (T_model == 1) {
```

```
            tnow = (tprime > 0 && tprime < 1) ? 1.0 : 0.0 ;

      /* Simple triangle wave */
      } else if (T_model == 2) {
                                    /* Simple triangle wave */
            if (tprime < 0 || tprime > 1) {
                  tnow = 0;
            } else if (tprime < 0.5) {
                  tnow = 2*tprime;
            } else if (tprime < 1.0) {
                  tnow = 2*(1-tprime);
            }
      }
      return tnow;
}

/*
   ============================================================================

-- Main program
--
-- Usage: int main()
--
-- Input:
--
-- Output:
--
-- Return:
--
-- Notes: Self-contained test routine. Will run with values set above
   .
==============================================================================
    */
int Simulate_BCP(int show_values, REAL *time, REAL *temperature, REAL
    *order, int maxpts) {

      double gamma, gamma_last, dgdt;
      double Tnow;
                                          /* Temperature */
      double t, dt, max_dt, t_report, dt_report;
/*    double t_avrami, beta_avrami, dgdt_avrami; */   /* Added for
   avrami calculation */
      double beta2, templog, force_sign, force_amp, diff_const;
      int npt;

      max_dt  = 1E-4*dwell;
                           /* maximum time step */
      dt_report = dwell/100;
                           /* 100 points per dwell unit reported */

      gamma_last = gamma = gamma_0;
                     /* Starting value */

      npt = 0;
                                                    /* No points so
         far */
      t_report = t = t_start*dwell;
                     /* Starting time */
      while (t < t_end*dwell) {
            Tnow = T_RT + (T_max-T_RT)*tnorm(t/dwell);      /*
               Current temperature */
            /* dgdt = K0 * Diffusivity(Tnow) * Force(Tnow,gamma); */
               /* Rate of change of order */
            diff_const = Diffusivity(Tnow); if (diff_const < 1E-30)
               diff_const = 1E-30;
            beta2 = N0 * exp(-E_a_N_0/(R*(Tnow+273))) * exp(-E_a_N/(R
               *(Tnow+273)*(Tnow-T_odt+0.001)*(Tnow-T_odt+0.001)))*
```

```
               diff_const*diff_const; /* *pow(diff_const,avrami_n-1);
                */ /* Modified: Rate of change of order */
/*          if (fabs(beta2) < 1E-30) beta2 = 0; */                /*
   Don't let it be exactly zero */
            force_amp = Force(Tnow,gamma);

/*          if (force_amp<0) {
               force_sign = -1;
            }
            else {
               force_sign = 1;
            } */
/*          force_amp = fabs(force_amp); */

            templog = fabs(-log(fabs(force_amp)+1E-9));
/*          if (fabs(templog) < 1E-30) templog = 0; */           /*
   Don't let it be exactly zero */

/*          TTYprintf("Before"); TTYprintf(" Beta, Force, Log: %E %E
   %E \n", beta2, force_amp, templog); TTYflush(); */
            dgdt = force_amp * K0 * avrami_n * pow(beta2,(1.0/
               avrami_n)) * pow(templog,((avrami_n-1.0)/avrami_n));
/*          TTYprintf(" After\n"); TTYflush(); */

            if (fabs(dgdt) < 1E-30) dgdt = 1E-30;                /*
               Don't let it be exactly zero */
            dt = 1E-3 / fabs(dgdt);
                                 /* Allow to change by 0.1% */
            if (dt > max_dt) dt = max_dt;
                           /* Require at least 10^4 steps over dwell
               window */
            gamma += dgdt*dt;
            if (gamma > 1.0) gamma = 1.0;
            if (gamma < 0.0) gamma = 0.0;
            t += dt;

            /* Store/print values on periodic basis ... either in
               time or given change */
            if (t > t_report || fabs(gamma-gamma_last) > 0.01) {
               if (show_values) { printf("%f %f %f %g\n", 1E3*t,
                  Tnow, gamma, dgdt); fflush(stdout); }
               if (npt < maxpts) {
                     if (time != NULL)  time[npt]    = (REAL) t;
                     if (temperature != NULL) temperature[npt] = (
                        REAL) Tnow;
                     if (order   != NULL) order[npt] = (REAL)
                        gamma;
                     npt++;
               }
               t_report = t+dt_report;
               gamma_last = gamma;
            }
      }

      return npt;
}


/*
   ============================================================================

-- Main program
--
-- Usage: int main()
--
-- Input:
--
```

```
-- Output:
--
-- Return:
--
-- Notes: Self-contained test routine. Will run with values set above
    .
================================================================================
     */
int main(void) {
      Simulate_BCP(TRUE, NULL, NULL, NULL, 0);
      return 0;
}


/*
    ================================================================================

-- These routines provide extensions to GENPLOT through user written
    code.
-- Interface is provided at four levels
--   USER            - Run user operation (such as read oscilloscope)
--   READ <file> -USER - Read data file using user algorithm
--   USER -READ <file>
--   WRITE <file> -USER - Write data file in user format
--   USER -WRITE <file>
--   <cmds>          - Installed command interpreter
--
-- These routines are linked into a dynamic link library that is
    loaded at
-- run time using the USER -LOAD function. Only the functions desired
     need
-- be defined - others will default. Following functions may be
    defined:
--
-- int UserInit(void)
-- int UserExit(void)
-- int UserCmd(int key, char *cmd, char *Curve)
-- int UserFnc(char *Curve)
-- int UserRead (char *file, char *Curve)
-- int UserWrite(char *file, char *Curve)
--
-- The "Curve" variable is the character name of the active Curve in
    GENPLOT.
-- This string is passed so the structure can be expanded if
    necessary. The
-- routines GVGetInfo is used to obtain a pointer to the true CURVE
    structure.
--
--                int itype;
--                CURVE **aptr, *curve;
--                if (! GVGetInfo(Curve, &itype, (void **) &aptr))
    return(-1);
--                if (itype != GV_2DCURVE && itype != GV_3DCURVE)
    return(-1);
--     curve = *aptr;
--
-- Once linked by GVGetInfo, the curve structure include at least the
     elements
--
--                curve->x, curve->y, curve->z - pointers to REAL
    arrays (z may be NULL)
--                curve->npt  - number of points in arrays currently
    valid
--                curve->nptmax - number of points allocated for x,y,
    z arrays
--     curve->ids  - 80 character identifier string
--
```

```
-- The size of a CURVE structure may be increased using a GVResize()
   call.
--
--                int GVResize(char *Curve, int newsize);
--
-- GVResize returns TRUE if successful in increasing size, or FALSE
   for any
-- errors. The address of the curve structure will not change,
   however
-- pointers within the structure may be redefined. If using curve->x[
   i]
-- indexing, there is no problem. However, if using *x type
   addressing,
-- pointers may have to be reset after a GVResize.
================================================================================
    */

/*================================================================================

-- User function initialization procedure. If defined, this routine
   is
-- called just after the module is loaded. Run time per-instance
-- initialization should be performed by this routine. At minimum,
   the
-- routine should print a message indicating successful load and
   version.
--
-- Usage: Initialize the dynamic link module (local control)
--
-- Syntax: int UserInit(void);
--
-- Inputs: none
--
-- Output: local control only
--
-- Returns: 0 ==> all is okay
--       !0 ==> error, abort and free this module
--
-- Notes: UserInit() will be called before any other procedures in
   the module
================================================================================
    */
int UserInit(void) {

      TTYprintf("Dynamic user module for %s loaded successfully\n",
         MODULENAME);

      GVLinkFnc("bcp", 0, 0, &my_help);         /* Help function */
      GVLinkFnc("tnorm", 0, 1, &my_tnorm);  /* Temperature versus
         time */
      GVLinkFnc("diff", 0, 1, &my_diff);        /* diffusivity */
      GVLinkFnc("force", 0, 2, &my_force);  /* driving force function
          */
      GVLinkFnc("beta", 0, 2, &my_beta);  /* avrami slope function */


      GVLinkDouble("T_g", 0, &T_g);                  /* glass
         transition temperature (oC) */
      GVLinkDouble("T_odt", 0, &T_odt);         /* ODT transition
         temperature (oC)  */
      GVLinkDouble("D0", 0, &D0);                    /* Diffusion
         prefactor in WLF */
      GVLinkDouble("c1g", 0, &c1g);                  /* WLF
         parameter */
      GVLinkDouble("c2g", 0, &c2g);                  /* WLF
         parameter */
```

```
      GVLinkDouble("D02", 0, &D02);                    /* Diffusion
         prefactor of Arrhenius */
      GVLinkDouble("E_a", 0, &E_a);                    /* Activation
         enthalpy (kJ/mol)     */
      GVLinkDouble("T_width", 0, &T_width);  /* Width of ODT
         conversion from order to disorder */
      GVLinkDouble("K0", 0, &K0);                      /* Segregation
         Rate prefactor */
      GVLinkDouble("N0", 0, &N0);                      /* Nucleation
         Rate prefactor */
      GVLinkDouble("avrami_n", 0, &avrami_n);              /* Avrami
          exponenet */
      GVLinkDouble("E_a_N", 0, &E_a_N);                    /*
         Nucleation Rate Activation Energy */
      GVLinkDouble("E_a_N_0", 0, &E_a_N_0);                /*
         Nucleation Rate Attempt Frequency Activation Energy */

      GVLinkDouble("dwell", 0, &dwell);          /* Dwell time */
      GVLinkDouble("t_start", 0, &t_start);  /* Starting time of
         simulation (units of dwell) */
      GVLinkDouble("t_end", 0, &t_end);          /* Ending time of
         simulation (units of dwell) */
      GVLinkDouble("T_RT", 0, &T_RT);            /* Room temperature
         */
      GVLinkDouble("T_max", 0, &T_max);          /* Maximum
         temperature */
      GVLinkInt("T_model", 0, &T_model);

      GVLinkDouble("gamma_0", 0, &gamma_0);  /* Starting value */

      /* Print the help */
      my_help(0, NULL, NULL);

      return 0;
}

/*=========================================================================

-- User function termination procedure. If defined, this routine is
-- called just before the module is released from memory. Run time
-- per-instance termination should be performed by this routine. If
   no
-- termination is required, this routine need not be defined.
--
-- Usage: De-initialize the dynamic link module (local control)
--
-- Syntax: int UserExit(void);
--
-- Inputs: none
--
-- Output: local control only
--
-- Returns: 0 ==> all is okay
--       !0 ==> error (doesn't matter, but tell me if it makes you
   happy)
=========================================================================
    */
int UserExit(void) {

      int i;
      static char *names[] = {"T_g", "T_odt", "E_a", "c1g", "c2g", "
         D0", "D02",
                                                        "dwell", "
                                                           t_start", "
                                                           t_end", "
                                                           gamma_0", "
                                                           K0", "
```

```
                                                        T_width",
                                                  "T_RT", "T_max
                                                      ", "T_Model
                                                      ", NULL};

      TTYprintf("Releasing the %s user module\n", MODULENAME);
      for (i=0; names[i] != NULL; i++) GVDeallocate(names[i]);

      return(0);
}

/*============================================================================

-- User function to process data, or otherwise, based on a single
   command.
-- This is a single procedure that is linked to the existing command
   structure
-- of GENPLOT through the USER command. For multiple commands, use
   the
-- UserCmd() procedure.
--
-- Usage: Single entry point for procedure executation via USER
   command.
--
-- Syntax: int UserFnc(char *Curve);
--
-- Inputs: Curve - "name of curve" from Genplot
--
-- Output: Whatever you desire
--
-- Returns: 0 ==> all is okay
--       !0 ==> return error
============================================================================
    */
int UserFnc(char *Curve) {

      int itype;
      CURVE **aptr, *curve;

/* If using T_model = 0, load the T_profile curve */
      if (0 == T_model) {
            if (! GVGetInfo("T_Profile", &itype, (void **) &aptr) ||
                (itype != GV_2DCURVE && itype != GV_3DCURVE)) {
                  ERRprintf("T_Profile curve does not exist, but you
                      asked for the curve temperature model\n");
                  return(-1);
            }
            curve = *aptr;
            Tcurve.x = curve->x;
            Tcurve.y = curve->y;
            Tcurve.npt = curve->npt;
            Tcurve.ipt = 0;
      } else {
            Tcurve.x = Tcurve.y = NULL;
            Tcurve.npt = Tcurve.ipt = 0;
      }

/* Get pointer to main curve x and y arrays */
      if (! GVGetInfo(Curve, &itype, (void **) &aptr)) return(-1);
      if (itype != GV_2DCURVE && itype != GV_3DCURVE) return(-1);
      curve = *aptr;

/* And go simulate */
      curve->npt = Simulate_BCP(FALSE, curve->x, curve->z, curve->y,
         curve->nptmax);
      return 0;
}
```

```
/*
   ============================================================================

-- External function to be linked into the function evaluator
--
-- Usage: int <fnc>(int itype, TMPREAL *result, TMPREAL *args);
--      int <fnc>(int itype, TMPREAL *result, TMPREAL args[], char *
   sargs[]);
--      int <fnc>(int itype, char **result, TMPREAL args[], char *
   sargs[]);
--
-- Inputs: itype - 0 ==> Real call, result & args are TMPREAL *
--             1 ==> Complex call, result & args really TMPCOMPLEX *
--       result - pointer to where result should be stored
--       args  - pointer to array of arguments from call
--
-- Returns: 0 ==> everything is okay
--       !0 ==> function is not implemented (only valid for type=1)
--
-- Notes: The same call is used for both REAL format and COMPLEX
   function
--      evaluations. The pointers result and args are typecast to
   TMPREAL *
--      but are really TMPCOMPLEX * if itype = 1.
--
--      If function does not want to deal with complex arguments,
   return
--      -1 and function will be recalled with the real part of each
   arg
--      only, and will set the real part of a complex as the result.
--
-- Call Sequence: GVLinkFnc("name", int flags, int nargs, &fnc));
--            GVLinkFnc("square", 0, 1, &square);
==============================================================================
    */
static int my_diff(int type, TMPREAL *result, TMPREAL *args) {
      if (type != 0) return -1;
      *result = Diffusivity((double) args[0]);
      return 0;
}

static int my_force(int type, TMPREAL *result, TMPREAL *args) {
      if (type != 0) return -1;
      *result = Force((double) args[0], (double) args[1]);
      return 0;
}

static int my_tnorm(int type, TMPREAL *result, TMPREAL *args) {
      if (type != 0) return -1;
      *result = tnorm((double) args[0]);
      return 0;
}

static int my_beta(int type, TMPREAL *result, TMPREAL *args) {
      if (type != 0) return -1;
      *result = Beta((double) args[0]);
      return 0;
}

static int my_help(int type, TMPREAL *result, TMPREAL *args) {

      TTYprintf("\nBCP simulation: Parameters and Function linkes (
         use listv -h)\n"
                        " Functions\n"
                        "  bcp()      Print this message\n"
                        "  diff(T)    Diffusivity function\n"
                        "  force(T,g) Driving force function\n"
```

```
                            "  tnorm(time) Normalized temperature versus
                               time\n"
                            "  beta(T) Slope of avrami function\n"
                            " Variables\n"
                            "  T_g        Glass transition temperature (
                               oC)\n"
                            "  T_odt      ODT transition temperature (oC)
                               \n"
                            "  D0         Diffusion prefactor in WLF\n"
                            "  c1g        WLF parameter\n"
                            "  c2g        WLF parameter\n"
                            "  D02        Diffusion prefactor of
                               Arrhenius\n"
                            "  E_a        Activation enthalpy (kJ/mol)\n"
                            "  T_width    Width of ODT conversion from
                               order to disorder\n"
                            "  K0         Prefactor in rate\n"
                            "  dwell      Dwell time\n"
                            "  t_start    Start time of simulation (units
                                of dwell)\n"
                            "  t_end      End time of simulation (units
                               of dwell)\n"
                            "  T_RT       Room temperature\n"
                            "  T_max      Maximum temperature\n"
                            "  T_model    Temperature profile model (0=
                               T_profile curve 1=square, 2=triangle)\n"
                            "  gamma_0    Starting value\n"
                            "  avrami_n   Avrami exponent\n"
                            "  N0         Nucleation and growth rate
                               prefactor\n"
                            "  E_a_N      Nucleation rate activation
                               energy\n"
                            "  E_a_N_0    Nucleation rate attempt
                               frequency activation energy\n"
                           );
      return 0;
}

/*
   ================================================================================

-- Usage: REAL = POLY_E(X,ARRAY,I1) - Polynomial evaluation
--     REAL = RPOLY_E(X,NUMER,I1,DENOM,I2) - Rational polynomial
   evaluation
--
-- Input: X      - argument
--      ARRAY(0:I1) - coefficients of polynomial
--      NUMER(0:I1) - coefficients for numerator
--      DENOM(0:I2) - coefficients for denominator
--      I1,I2     - maximum coefficient
--
-- Output: POLY_E = A(0) + A(1)*X + A(2)*X*X + A(3)*X*X*X + ...
--
--              N(0) + N(1)*X + N(2)*X*X + N(3)*X*X*X + ...
--      RPOLY_E = ----------------------------------------
--              D(0) + D(1)*X + D(2)*X*X + D(3)*X*X*X + ...
================================================================================
    */
static double poly_e(double x, double *numer, int iorder) {

            double tmp;
            numer += iorder;
                     /* Go to end of the array */
            tmp = *numer;
            while (iorder--) tmp = tmp*x + *(--numer);
            return(tmp);
```

```
      }
static double rpoly_e(double x, double *numer, int i1, double *denom,
    int i2) {

            double top, bot;

            numer += i1;
            denom += i2;
            top = *numer;
            bot = *denom;
            while (i1--) top = top*x + *(--numer);
            while (i2--) bot = bot*x + *(--denom);
            return(top/bot);
}

/*
   ============================================================================

--  Function to evaluate the error function
--
--  Usage: real = ERF_S(key,X)
--
--  Inputs: X - Input argument of the error function.
--                       KEY - which to return 1 => ERF
--
         2 => ERFC
--
         3 => NDTR (normal distribution value)
--
                       = erfc[-x/sqrt(2)]/2.0
--
--  Output: ERF_S - Output value of the error or complementary
   function.
--
-- Comments on NDTR:
--
-- Computes Y = P(X) = probability that the random variable U,
   distributed
-- normally on (0,1), is less than or equal to X.
--
-- NOTE: NDTR(X) = {1+erf[X/sqrt(2)]} / 2.0
--
   ============================================================================
    */
#define ERF_XMIN        1.0E-5
        /* Low X range starts */
#define ERF_XLARGE 4.1875                                           /*
   Large X range starts */
#define SQRPI           0.56418958354775628690        /* 1/sqrt(pi)
   */
#define SQRT2I          0.70710678118654752445        /* 1/sqrt(2) */

#define ERFC_MAX        27.226

double ERF_S(int key, double x) {

      double xerf=0, xerfc=0, xsq, xi;    /* Initialize to avoid GCC
         warning */
      int flags=0;
#define B_NEG           0x01                                    /*
   Argument was negative */
#define B_ERFC    0x02                                  /* xerfc is
   valid, not xerf */
#define B_UNNORM        0x04                                    /* Needs
   the e^{x^2}/2 mult */

/* Coefficients for 0.0 <= Y < .477 */
```

```
      static double p[] = {1.128379167615, 0.0908744014861,
         0.01670667572898};
      static double q[] = {1.0,   0.413868661356, 0.05276291052144};
/* Coefficients for .477 <= Y <= 4.0 */
      static double p1[] = {0.99999011363, 0.93099282488,
         0.41114638022, 0.076369325737, 5.841349927e-06};
      static double q1[] = {1.0,  2.0592722535, 1.7352416832,
         0.7260948247, 0.13560588011};
/* Coefficients for correction above 4.0-8.0 */
      static double r0[] = {-4.147022992e-008, 6.577948625e-006,
         -0.0004594082129, 0.01821908914, -0.4827995598,
         -9.578360558, 16.48487473};
      static double r1[] = {-1.701077849e-006, 8.30114368e-005,
         -0.001881676726, 0.0252633635, -0.2128335088, 1.102018595,
         -3.16755867, 3.729088545};

/* ... If NDTR, must cheat a little */
      if (key == 3) x = -x*SQRT2I;        /* If NDTR, argument = -x/
         sqrt(2) */

      if (x < 0.0) {                                          /* Work
         only with positive quantities */
            flags |= B_NEG;
            x = -x;
      }
      xsq = x*x;

/* ... Very small, just use simplest approximation */
      if (x < ERF_XMIN) {
            xerf = x*p[0];                                    /* Next
               term is x^3, so ignore */

/* ... ABS(Y) <= .477, evaluate approximation for erf */
      } else if (x < 0.477) {
            xerf = x * rpoly_e(xsq, p,2, q,2) ;

/* ... .477 <= ABS(Y) <= 4.0 --- Accuracy worst - 7E-10 maximum
   deviation */
      } else if (x < 4.0) {
            flags |= B_ERFC;
            xerfc = exp(-xsq) * rpoly_e(x,p1,4,q1,4); /* Big
               polynomial fit */

/* ... 4.0 < y < infty, asymptotic series expansion for ERFC */
/* ... Accurate to 1E-10 in the unnormalized value */
      } else {
            flags |= B_ERFC | B_UNNORM;
            xi  = 1.0/xsq;
                     /* X inverse */
            xerfc = SQRPI * (1.0+xi*(-0.5+xi*(0.75+xi*(-1.875+6.625*
               xi))));
            if (x < 8) {
                  xerfc += poly_e(xi, r0, 6);
            } else {
                  xerfc += poly_e(1/x, r1, 7);
            }
/*          if (xi > 0.0184258) xerfc -= 0.1407615*pow(xi
   -0.0184258,3); */ /* Empirical correction */
      }

/* Handle ln(erfc) separately */
      if (key == 4) {
            if (! (flags & B_ERFC)) {
                        /* Two possibilities */
```

```
                  if (flags & B_NEG) xerf = -xerf;
                           /* Get xerf                    */
                  if (x < 1E-3) {
                                    /* Do ln(1-erf) self */
                        xerfc = -xerf*(1+xerf*(1/2.0+xerf*(1/3.0+xerf
                           *(1/4.0+xerf/5.0))));
                  } else {
                        xerfc = log(1.0-xerf);
                  }
            } else if (! (flags & B_UNNORM)) {                    /*
               Simple erfc */
                  if (flags & B_NEG) xerfc = 2.0-xerfc;
                  xerfc = log(xerfc);
            } else if (flags & B_NEG) {
                     /* Large negative args */
                  xerfc = (x > 7) ? 0 : xerfc*exp(-xsq)/x;
                  xerfc = log(2.0-xerfc);
            } else {
                                                 /* Use expansion
               */
                  xerfc = log(xerfc) - xsq - log(x);
            }
            return xerfc;
      }

/* Correct for normalization, deal with erf/erfc correct */
      if (x > ERFC_MAX) {
               /* Out of range */
            xerfc = 0.0;
            xerf = 1.0;
      } else if (flags & B_UNNORM) {                  /* Have erfc w/
         out e^x^2/x */
            xerfc *= exp(-xsq)/x;
            xerf = 1.0-xerfc;
      } else if (flags & B_ERFC) {                          /* Have
         only xerfc */
            xerf = 1.0-xerfc;
      } else {
            xerfc = 1.0-xerf;
      }
      if (flags & B_NEG) {xerf = -xerf; xerfc = 2.0-xerfc;}

      if (key == 3) return(xerfc/2);            /* NDTR(x)   */
      if (key == 2) return(xerfc);                    /* ERFC(x)   */
      return(xerf);
               /* ERF(x)    */
}
```

B.2.3 Genplot User Module bcp2.c

User module for modeling spinodal decomposition like segregation behavior. This must be compiled and placed in the genplot local folder equivalent to that below.

```
Program Files (x86)\cgs\Genplot\NT\Local
```

```
/** bcp.c
 ** Routine to simulate the ordering of BCPs with a complex
    temperature
 ** profile. Allows arbitrary models for the forcing function and the
 ** diffusivity, as well as arbitrary temperature profiles.
 **/

/** ================================================================
 user -load bcp
 label bot "Time [s]" reg bot t_start*dwell t_end*dwell
 label left "Order [AU]" reg left 0 1

 echo Triangle temperature profile
 let t_model = 2
 axis foreach (300 250 240 230 220 210 200 190 180) let t_max = %f
    user ov
 sleep 2

 echo Square temperature profile
 let t_model = 1
 axis foreach (300 250 240 230 220 210 200 190 180) let t_max = %f
    user ov
 sleep 2

 echo Curve based profile using sin-like profile
 let t_model = 0
 create -curve T_Profile y = sin(pi*x) -range 0 1 -points 200
 axis foreach (300 250 240 230 220 210 200 190 180) let t_max = %f
    user ov
 sleep 2

 echo Curve based profile using Gaussian profile
 let t_model = 0
 create -curve T_Profile y = 2^{-((x-1)/0.5)^2} -range -1 3 -points
    200
 axis foreach (300 250 240 230 220 210 200 190 180) let t_max = %f
    user ov
 sleep 2

 echo Can also extract the temperature profile as used (to check)
 3d user let y = z 2d
 label left "Temperature [\deg C]"
 region auto plot
================================================================================
    **/

#define MODULENAME "bcp"

/* ------------------------------ */
/* Feature test macros    */
/* ------------------------------ */
#define _POSIX_SOURCE                          /* Always require
   POSIX standard */
#include "preload.h"

/* ------------------------------ */
/* Standard include files */
/* ------------------------------ */
#include <stdio.h>
#include <stdlib.h>
#include <float.h>
#include <math.h>

/* ------------------------------ */
/* Local include files    */
/* ------------------------------ */
```

```
#define NO_PATH_EXTENSIONS                /* Avoid GENPLOT errors
   with GCC */
#include "mytypes.h"
#include "extends.h"
#include "lexp.h"
#include "user.h"

/* ------------------------------ */
/* My local typedef's and defines */
/* ------------------------------ */
#define R   (8.3144E-3)       /* Gas constant kJ/mol-K */

/* ------------------------------ */
/* My external function prototypes */
/* ------------------------------ */

/* ------------------------------ */
/* My internal function prototypes */
/* ------------------------------ */
static int my_help(int type, TMPREAL *result, TMPREAL *args);
static int my_diff(int type, TMPREAL *result, TMPREAL *args);
static int my_force(int type, TMPREAL *result, TMPREAL *args);
static int my_tnorm(int type, TMPREAL *result, TMPREAL *args);

double ERF_S(int key, double x);
#define erfc(x) (ERF_S(2,x))

/* ------------------------------ */
/* My usage of other external fncs */
/* ------------------------------ */

/* ------------------------------ */
/* My share of global externals */
/* ------------------------------ */

/* ------------------------------ */
/* Locally defined global vars */
/* ------------------------------ */

double T_g = 110;                   /* glass transition temperature (
   oC) */
double T_odt = 200;           /* ODT transition temperature (oC)  */
double D0 = 6E-19;            /* Diffusion prefactor in WLF */
double c1g = 13;                    /* WLF parameter */
double c2g =70;               /* WLF parameter */
double D02 = 2E-8;            /* Diffusion prefactor of Arrhenius */
double E_a = 60;                    /* Activation enthalpy (kJ/mol)
      */
double T_width = 25;          /* Width of ODT conversion from order
   to disorder */
double K0 = 5E17;                   /* Prefactor in rate */

double dwell = 2E-3;          /* Dwell time */
double t_start = -0.1;  /* Starting time of simulation (units of
   dwell) */
double t_end = 3;                   /* Ending time of simulation (
   units of dwell) */
double T_RT = 25;                   /* Room temperature */
double T_max = 500;           /* Maximum temperature */
int  T_model = 2;             /* Model for the temperature profile */
int  show_values = 0;
double gamma_0 = 1.0;   /* Starting value for gamma */

/*
   ============================================================================
```

```
-- Return "mobility" or "diffusivity" of chains
--
-- Usage: double = Diffusivity(double T)
--
-- Input: T - temperature in oC
--
-- Output: none
--
-- Return: value proportional to the diffusivity
================================================================================
    */
double Diffusivity(double T) {
      if (T_g-T > c2g) T = T_g-c2g+2;           /* Avoid exploding
         exponential in WLF */
      return D0*exp(c1g*(T-T_g)/(c2g+T-T_g))+D02*exp(-E_a/R/(T+273));
}

/*
   ============================================================================

-- Return driving force factor for chain alignment (order parameter)
--
-- Usage: double = Force(double T, double gamma)
--
-- Input: T - temperature in oC
--      gamma - order parameter
--
-- Output: none
--
-- Return: value proportional to the driving force for alignment
================================================================================
    */
double Force(double T, double gamma) {
      double gamma_eq, drive;
      gamma_eq = 0.5 * erfc((T-T_odt)/T_width);       /* Equilibrium
         gamma of T */
      drive = gamma_eq - gamma;
               /* Driving force                */
      drive *= fabs(T-T_odt);
               /* Optional scaling of driving force */
      return drive;
}

/*
   ============================================================================

-- Return normalized temperature corresponding to a given simulation
   time
--
-- Usage: double = tnorm(double t_prime);
--
-- Input: t_prime - normalized time (seconds / dwell)
--
-- Output: none
--
-- Return: [0-1] value corresponding to RT to Tmax
================================================================================
    */
/* Structure for dealing with "curve" based temperature profiles.
   Must
 * be setup before calling tnorm for the first time. To make sure
 * things are safe, ipt should always be set to 0 initially. Code
 * assumes constant extension of temperature profile before and after
 * given data.
 *
 * Curve must be normalized [0,1] on Y and in units of dwell time in X
   .
 * This allows scaling of the profile for different dwells and
 * temperatures. If you want to use absolute temperatures, just set
```

```
 * T_RT to 0.0 and T_max to 1.0
 * */
struct {
      REAL *x, *y;                          /* X and Y pointers */
      int npt;                                    /* Number of
         points in curve */
      int ipt;                                    /* Current
         index that corresponds to tprime */
} Tcurve = {NULL, NULL, 0, 0};

double tnorm(double tprime) {
      double tnow=0;

      /* Use a curve profile */
      if (T_model == 0) {
            while (Tcurve.ipt > 0    && Tcurve.x[Tcurve.ipt] > tprime)
                Tcurve.ipt--;  /* Get between two valid points */
            while (Tcurve.ipt < Tcurve.npt-1 && Tcurve.x[Tcurve.ipt
               +1] < tprime) Tcurve.ipt++;  /* Next point */
            if (tprime < Tcurve.x[Tcurve.ipt]) {
                  tnow = Tcurve.y[Tcurve.ipt];
            } else if (tprime > Tcurve.x[Tcurve.ipt+1]) {
                  tnow = Tcurve.y[Tcurve.ipt+1];
            } else {
                  tnow = Tcurve.y[Tcurve.ipt] + (Tcurve.y[Tcurve.ipt
                     +1]-Tcurve.y[Tcurve.ipt])/(Tcurve.x[Tcurve.ipt
                     +1]-Tcurve.x[Tcurve.ipt])*(tprime-Tcurve.x[
                     Tcurve.ipt]);
            }

      /* Simple square wave */
      } else if (T_model == 1) {
            tnow = (tprime > 0 && tprime < 1) ? 1.0 : 0.0 ;

      /* Simple triangle wave */
      } else if (T_model == 2) {
                                    /* Simple triangle wave */
            if (tprime < 0 || tprime > 1) {
                  tnow = 0;
            } else if (tprime < 0.5) {
                  tnow = 2*tprime;
            } else if (tprime < 1.0) {
                  tnow = 2*(1-tprime);
            }
      }
      return tnow;
}

/*
    ========================================================================

-- Main program
--
-- Usage: int main()
--
-- Input:
--
-- Output:
--
-- Return:
--
-- Notes: Self-contained test routine. Will run with values set above
    .
=========================================================================
     */
int Simulate_BCP(int show_values, REAL *time, REAL *temperature, REAL
     *order, int maxpts) {
```

```
      double gamma, gamma_last, dgdt;
      double Tnow;
                                        /* Temperature */
      double t, dt, max_dt, t_report, dt_report;
      int npt;

      max_dt  = 1E-4*dwell;
                           /* maximum time step */
      dt_report = dwell/100;
                           /* 100 points per dwell unit reported */

      gamma_last = gamma = gamma_0;
                    /* Starting value */

      npt = 0;
                                                    /* No points so
          far */
      t_report = t = t_start*dwell;
                    /* Starting time */
      while (t < t_end*dwell) {
            Tnow = T_RT + (T_max-T_RT)*tnorm(t/dwell);      /*
               Current temperature */
            dgdt = K0 * Diffusivity(Tnow) * Force(Tnow,gamma); /*
               Rate of change of order */
            if (fabs(dgdt) < 1E-30) dgdt = 1E-30;                /*
               Don't let it be exactly zero */
            dt = 1E-3 / fabs(dgdt);
                              /* Allow to change by 0.1% */
            if (dt > max_dt) dt = max_dt;
                           /* Require at least 10^4 steps over dwell
               window */
            gamma += dgdt*dt;
            if (gamma > 1.0) gamma = 1.0;
            if (gamma < 0.0) gamma = 0.0;
            t += dt;

            /* Store/print values on periodic basis ... either in
               time or given change */
            if (t > t_report || fabs(gamma-gamma_last) > 0.01) {
                  if (show_values) { printf("%f %f %f %g\n", 1E3*t,
                     Tnow, gamma, dgdt); fflush(stdout); }
                  if (npt < maxpts) {
                        if (time != NULL)  time[npt]    = (REAL) t;
                        if (temperature != NULL) temperature[npt] = (
                           REAL) Tnow;
                        if (order   != NULL) order[npt] = (REAL)
                           gamma;
                        npt++;
                  }
                  t_report = t+dt_report;
                  gamma_last = gamma;
            }
      }

      return npt;
}

/*
   ============================================================================

-- Main program
--
-- Usage: int main()
--
-- Input:
```

```
--
-- Output:
--
-- Return:
--
-- Notes: Self-contained test routine. Will run with values set above
   .
=============================================================================
    */
int main(void) {
      Simulate_BCP(TRUE, NULL, NULL, NULL, 0);
      return 0;
}


/*
   ============================================================================

-- These routines provide extensions to GENPLOT through user written
   code.
-- Interface is provided at four levels
--   USER            - Run user operation (such as read oscilloscope)
--   READ <file> -USER - Read data file using user algorithm
--   USER -READ <file>
--   WRITE <file> -USER - Write data file in user format
--   USER -WRITE <file>
--   <cmds>          - Installed command interpreter
--
-- These routines are linked into a dynamic link library that is
   loaded at
-- run time using the USER -LOAD function. Only the functions desired
    need
-- be defined - others will default. Following functions may be
   defined:
--
-- int UserInit(void)
-- int UserExit(void)
-- int UserCmd(int key, char *cmd, char *Curve)
-- int UserFnc(char *Curve)
-- int UserRead (char *file, char *Curve)
-- int UserWrite(char *file, char *Curve)
--
-- The "Curve" variable is the character name of the active Curve in
   GENPLOT.
-- This string is passed so the structure can be expanded if
   necessary. The
-- routines GVGetInfo is used to obtain a pointer to the true CURVE
   structure.
--
--                int itype;
--                CURVE **aptr, *curve;
--                if (! GVGetInfo(Curve, &itype, (void **) &aptr))
   return(-1);
--                if (itype != GV_2DCURVE && itype != GV_3DCURVE)
   return(-1);
--     curve = *aptr;
--
-- Once linked by GVGetInfo, the curve structure include at least the
    elements
--
--                curve->x, curve->y, curve->z - pointers to REAL
   arrays (z may be NULL)
--                curve->npt  - number of points in arrays currently
   valid
--                curve->nptmax - number of points allocated for x,y,
   z arrays
--     curve->ids - 80 character identifier string
--
```

```
-- The size of a CURVE structure may be increased using a GVResize()
   call.
--
--                int GVResize(char *Curve, int newsize);
--
-- GVResize returns TRUE if successful in increasing size, or FALSE
   for any
-- errors. The address of the curve structure will not change,
   however
-- pointers within the structure may be redefined. If using curve->x[
   i]
-- indexing, there is no problem. However, if using *x type
   addressing,
-- pointers may have to be reset after a GVResize.
================================================================================
    */

/*================================================================================

-- User function initialization procedure. If defined, this routine
   is
-- called just after the module is loaded. Run time per-instance
-- initialization should be performed by this routine. At minimum,
   the
-- routine should print a message indicating successful load and
   version.
--
-- Usage: Initialize the dynamic link module (local control)
--
-- Syntax: int UserInit(void);
--
-- Inputs: none
--
-- Output: local control only
--
-- Returns: 0 ==> all is okay
--       !0 ==> error, abort and free this module
--
-- Notes: UserInit() will be called before any other procedures in
   the module
================================================================================
    */
int UserInit(void) {

      TTYprintf("Dynamic user module for %s loaded successfully\n",
         MODULENAME);

      GVLinkFnc("bcp", 0, 0, &my_help);         /* Help function */
      GVLinkFnc("tnorm", 0, 1, &my_tnorm);  /* Temperature versus
         time */
      GVLinkFnc("diff", 0, 1, &my_diff);        /* diffusivity */
      GVLinkFnc("force", 0, 2, &my_force);  /* driving force function
          */

      GVLinkDouble("T_g", 0, &T_g);                  /* glass
         transition temperature (oC) */
      GVLinkDouble("T_odt", 0, &T_odt);         /* ODT transition
         temperature (oC)  */
      GVLinkDouble("D0", 0, &D0);                    /* Diffusion
         prefactor in WLF */
      GVLinkDouble("c1g", 0, &c1g);                  /* WLF
         parameter */
      GVLinkDouble("c2g", 0, &c2g);                  /* WLF
         parameter */
      GVLinkDouble("D02", 0, &D02);                  /* Diffusion
         prefactor of Arrhenius */
```

```
      GVLinkDouble("E_a", 0, &E_a);                    /* Activation
         enthalpy (kJ/mol)     */
      GVLinkDouble("T_width", 0, &T_width);  /* Width of ODT
         conversion from order to disorder */
      GVLinkDouble("K0", 0, &K0);                      /* Rate
         prefactor */

      GVLinkDouble("dwell", 0, &dwell);          /* Dwell time */
      GVLinkDouble("t_start", 0, &t_start);  /* Starting time of
         simulation (units of dwell) */
      GVLinkDouble("t_end", 0, &t_end);          /* Ending time of
         simulation (units of dwell) */
      GVLinkDouble("T_RT", 0, &T_RT);            /* Room temperature
         */
      GVLinkDouble("T_max", 0, &T_max);          /* Maximum
         temperature */
      GVLinkInt("T_model", 0, &T_model);
      GVLinkInt("show_values", 0, &show_values);  /* determine
         whether to show temporal evolution */

      GVLinkDouble("gamma_0", 0, &gamma_0);  /* Starting value */

      /* Print the help */
      my_help(0, NULL, NULL);

      return 0;
}

/*============================================================================

-- User function termination procedure. If defined, this routine is
-- called just before the module is released from memory. Run time
-- per-instance termination should be performed by this routine. If
   no
-- termination is required, this routine need not be defined.
--
-- Usage: De-initialize the dynamic link module (local control)
--
-- Syntax: int UserExit(void);
--
-- Inputs: none
--
-- Output: local control only
--
-- Returns: 0 ==> all is okay
--        !0 ==> error (doesn't matter, but tell me if it makes you
   happy)
============================================================================
    */
int UserExit(void) {

      int i;
      static char *names[] = {"T_g", "T_odt", "E_a", "c1g", "c2g", "
         D0", "D02",
                                                      "dwell", "
                                                         t_start", "
                                                         t_end", "
                                                         gamma_0", "
                                                         K0", "
                                                         T_width",
                                                      "T_RT", "T_max
                                                         ", "T_Model
                                                         ", "
                                                         show_values
                                                         ", NULL};

      TTYprintf("Releasing the %s user module\n", MODULENAME);
      for (i=0; names[i] != NULL; i++) GVDeallocate(names[i]);
```

```
      return(0);
}

/*============================================================================

-- User function to process data, or otherwise, based on a single
   command.
-- This is a single procedure that is linked to the existing command
   structure
-- of GENPLOT through the USER command. For multiple commands, use
   the
-- UserCmd() procedure.
--
-- Usage: Single entry point for procedure executation via USER
   command.
--
-- Syntax: int UserFnc(char *Curve);
--
-- Inputs: Curve - "name of curve" from Genplot
--
-- Output: Whatever you desire
--
-- Returns: 0 ==> all is okay
--       !0 ==> return error
============================================================================
    */
int UserFnc(char *Curve) {

      int itype;
      CURVE **aptr, *curve;

/* If using T_model = 0, load the T_profile curve */
      if (0 == T_model) {
            if (! GVGetInfo("T_Profile", &itype, (void **) &aptr) ||
                (itype != GV_2DCURVE && itype != GV_3DCURVE)) {
                   ERRprintf("T_Profile curve does not exist, but you
                       asked for the curve temperature model\n");
                   return(-1);
            }
            curve = *aptr;
            Tcurve.x = curve->x;
            Tcurve.y = curve->y;
            Tcurve.npt = curve->npt;
            Tcurve.ipt = 0;
      } else {
            Tcurve.x = Tcurve.y = NULL;
            Tcurve.npt = Tcurve.ipt = 0;
      }

/* Get pointer to main curve x and y arrays */
      if (! GVGetInfo(Curve, &itype, (void **) &aptr)) return(-1);
      if (itype != GV_2DCURVE && itype != GV_3DCURVE) return(-1);
      curve = *aptr;

/* And go simulate */
      curve->npt = Simulate_BCP(FALSE, curve->x, curve->z, curve->y,
         curve->nptmax);
      return 0;
}

/*
   ============================================================================

-- External function to be linked into the function evaluator
--
-- Usage: int <fnc>(int itype, TMPREAL *result, TMPREAL *args);
```

```
--      int <fnc>(int itype, TMPREAL *result, TMPREAL args[], char *
    sargs[]);
--      int <fnc>(int itype, char **result, TMPREAL args[], char *
    sargs[]);
--
-- Inputs: itype - 0 ==> Real call, result & args are TMPREAL *
--             1 ==> Complex call, result & args really TMPCOMPLEX *
--       result - pointer to where result should be stored
--       args  - pointer to array of arguments from call
--
-- Returns: 0 ==> everything is okay
--       !0 ==> function is not implemented (only valid for type=1)
--
-- Notes: The same call is used for both REAL format and COMPLEX
    function
--      evaluations. The pointers result and args are typecast to
    TMPREAL *
--      but are really TMPCOMPLEX * if itype = 1.
--
--      If function does not want to deal with complex arguments,
    return
--      -1 and function will be recalled with the real part of each
    arg
--      only, and will set the real part of a complex as the result.
--
-- Call Sequence: GVLinkFnc("name", int flags, int nargs, &fnc));
--            GVLinkFnc("square", 0, 1, &square);
================================================================================
     */
static int my_diff(int type, TMPREAL *result, TMPREAL *args) {
      if (type != 0) return -1;
      *result = Diffusivity((double) args[0]);
      return 0;
}

static int my_force(int type, TMPREAL *result, TMPREAL *args) {
      if (type != 0) return -1;
      *result = Force((double) args[0], (double) args[1]);
      return 0;
}

static int my_tnorm(int type, TMPREAL *result, TMPREAL *args) {
      if (type != 0) return -1;
      *result = tnorm((double) args[0]);
      return 0;
}

static int my_help(int type, TMPREAL *result, TMPREAL *args) {

      TTYprintf("\nBCP simulation: Parameters and Function linkes (
         use listv -h)\n"
                        " Functions\n"
                        "  bcp()      Print this message\n"
                        "  diff(T)    Diffusivity function\n"
                        "  force(T,g) Driving force function\n"
                        "  tnorm(time) Normalized temperature versus
                           time\n"
                        " Variables\n"
                        "  T_g        Glass transition temperature (
                           oC)\n"
                        "  T_odt      ODT transition temperature (oC)
                           \n"
                        "  D0         Diffusion prefactor in WLF\n"
                        "  c1g        WLF parameter\n"
                        "  c2g        WLF parameter\n"
                        "  D02        Diffusion prefactor of
                           Arrhenius\n"
```

```
                            "  E_a        Activation enthalpy (kJ/mol)\n"
                            "  T_width    Width of ODT conversion from
                                order to disorder\n"
                            "  K0         Prefactor in rate\n"
                            "  dwell      Dwell time\n"
                            "  t_start    Start time of simulation (units
                                 of dwell)\n"
                            "  t_end      End time of simulation (units
                                of dwell)\n"
                            "  T_RT       Room temperature\n"
                            "  T_max      Maximum temperature\n"
                            "  T_model    Temperature profile model (0=
                                T_profile curve 1=square, 2=triangle)\n"
                            "  gamma_0    Starting value\n"
                            "  show_values Show temporal profile (1=yes)"
                           );
      return 0;
}

/*
   ========================================================================

-- Usage: REAL = POLY_E(X,ARRAY,I1) - Polynomial evaluation
--     REAL = RPOLY_E(X,NUMER,I1,DENOM,I2) - Rational polynomial
   evaluation
--
-- Input: X      - argument
--      ARRAY(0:I1) - coefficients of polynomial
--      NUMER(0:I1) - coefficients for numerator
--      DENOM(0:I2) - coefficients for denominator
--      I1,I2     - maximum coefficient
--
-- Output: POLY_E = A(0) + A(1)*X + A(2)*X*X + A(3)*X*X*X + ...
--
--              N(0) + N(1)*X + N(2)*X*X + N(3)*X*X*X + ...
--      RPOLY_E = ------------------------------------------
--              D(0) + D(1)*X + D(2)*X*X + D(3)*X*X*X + ...
========================================================================
    */
static double poly_e(double x, double *numer, int iorder) {

            double tmp;
            numer += iorder;
                     /* Go to end of the array */
            tmp = *numer;
            while (iorder--) tmp = tmp*x + *(--numer);
            return(tmp);
      }

static double rpoly_e(double x, double *numer, int i1, double *denom,
    int i2) {

            double top, bot;

            numer += i1;
            denom += i2;
            top = *numer;
            bot = *denom;
            while (i1--) top = top*x + *(--numer);
            while (i2--) bot = bot*x + *(--denom);
            return(top/bot);
}

/*
   ========================================================================

--  Function to evaluate the error function
--
```

```
--  Usage: real = ERF_S(key,X)
--
--  Inputs: X - Input argument of the error function.
--                       KEY - which to return 1 => ERF
--
         2 => ERFC
--
         3 => NDTR (normal distribution value)
--
                       = erfc[-x/sqrt(2)]/2.0
--
--  Output: ERF_S - Output value of the error or complementary
    function.
--
-- Comments on NDTR:
--
-- Computes Y = P(X) = probability that the random variable U,
    distributed
-- normally on (0,1), is less than or equal to X.
--
-- NOTE: NDTR(X) = {1+erf[X/sqrt(2)]} / 2.0
--
    ============================================================================
     */
#define ERF_XMIN        1.0E-5
         /* Low X range starts */
#define ERF_XLARGE 4.1875                                              /*
    Large X range starts */
#define SQRPI           0.56418958354775628690        /* 1/sqrt(pi)
    */
#define SQRT2I          0.70710678118654752445        /* 1/sqrt(2) */

#define ERFC_MAX        27.226

double ERF_S(int key, double x) {

      double xerf=0, xerfc=0, xsq, xi;    /* Initialize to avoid GCC
         warning */
      int flags=0;
#define B_NEG           0x01                                    /*
    Argument was negative */
#define B_ERFC    0x02                                  /* xerfc is
    valid, not xerf */
#define B_UNNORM        0x04                                    /* Needs
    the e^{x^2}/2 mult */

/* Coefficients for 0.0 <= Y < .477 */
      static double p[] = {1.128379167615, 0.0908744014861,
         0.01670667572898};
      static double q[] = {1.0,   0.413868661356, 0.05276291052144};
/* Coefficients for .477 <= Y <= 4.0 */
      static double p1[] = {0.99999011363, 0.93099282488,
         0.41114638022, 0.076369325737, 5.841349927e-06};
      static double q1[] = {1.0,  2.0592722535, 1.7352416832,
         0.7260948247, 0.13560588011};
/* Coefficients for correction above 4.0-8.0 */
      static double r0[] = {-4.147022992e-008, 6.577948625e-006,
         -0.0004594082129, 0.01821908914, -0.4827995598,
         -9.578360558, 16.48487473};
      static double r1[] = {-1.701077849e-006, 8.30114368e-005,
         -0.001881676726, 0.0252633635, -0.2128335088, 1.102018595,
         -3.16755867, 3.729088545};

/* ... If NDTR, must cheat a little */
      if (key == 3) x = -x*SQRT2I;        /* If NDTR, argument = -x/
         sqrt(2) */
```

```
      if (x < 0.0) {                                          /* Work
         only with positive quantities */
            flags |= B_NEG;
            x = -x;
      }
      xsq = x*x;

/* ... Very small, just use simplest approximation */
      if (x < ERF_XMIN) {
            xerf = x*p[0];                                    /* Next
               term is x^3, so ignore */

/* ... ABS(Y) <= .477, evaluate approximation for erf */
      } else if (x < 0.477) {
            xerf = x * rpoly_e(xsq, p,2, q,2) ;

/* ... .477 <= ABS(Y) <= 4.0 --- Accuracy worst - 7E-10 maximum
   deviation */
      } else if (x < 4.0) {
            flags |= B_ERFC;
            xerfc = exp(-xsq) * rpoly_e(x,p1,4,q1,4); /* Big
               polynomial fit */

/* ... 4.0 < y < infty, asymptotic series expansion for ERFC */
/* ... Accurate to 1E-10 in the unnormalized value */
      } else {
            flags |= B_ERFC | B_UNNORM;
            xi  = 1.0/xsq;
                     /* X inverse */
            xerfc = SQRPI * (1.0+xi*(-0.5+xi*(0.75+xi*(-1.875+6.625*
               xi))));
            if (x < 8) {
                  xerfc += poly_e(xi, r0, 6);
            } else {
                  xerfc += poly_e(1/x, r1, 7);
            }
/*          if (xi > 0.0184258) xerfc -= 0.1407615*pow(xi
   -0.0184258,3); */ /* Empirical correction */
      }

/* Handle ln(erfc) separately */
      if (key == 4) {
            if (! (flags & B_ERFC)) {
                        /* Two possibilities */
                  if (flags & B_NEG) xerf = -xerf;
                        /* Get xerf                    */
                  if (x < 1E-3) {
                                    /* Do ln(1-erf) self */
                        xerfc = -xerf*(1+xerf*(1/2.0+xerf*(1/3.0+xerf
                           *(1/4.0+xerf/5.0))));
                  } else {
                        xerfc = log(1.0-xerf);
                  }
            } else if (! (flags & B_UNNORM)) {                    /*
               Simple erfc */
                  if (flags & B_NEG) xerfc = 2.0-xerfc;
                  xerfc = log(xerfc);
            } else if (flags & B_NEG) {
                     /* Large negative args */
                  xerfc = (x > 7) ? 0 : xerfc*exp(-xsq)/x;
                  xerfc = log(2.0-xerfc);
            } else {
                                                /* Use expansion
               */
                  xerfc = log(xerfc) - xsq - log(x);
```

```
            }
            return xerfc;
      }

/* Correct for normalization, deal with erf/erfc correct */
      if (x > ERFC_MAX) {
               /* Out of range */
            xerfc = 0.0;
            xerf = 1.0;
      } else if (flags & B_UNNORM) {                  /* Have erfc w/
         out e^x^2/x */
            xerfc *= exp(-xsq)/x;
            xerf = 1.0-xerfc;
      } else if (flags & B_ERFC) {                          /* Have
         only xerfc */
            xerf = 1.0-xerfc;
      } else {
            xerfc = 1.0-xerf;
      }
      if (flags & B_NEG) {xerf = -xerf; xerfc = 2.0-xerfc;}

      if (key == 3) return(xerfc/2);            /* NDTR(x)   */
      if (key == 2) return(xerfc);                    /* ERFC(x)   */
      return(xerf);
               /* ERF(x)    */
}
```

B.3 DSA Alignment Calculation ImageJ Macro

The ImageJ alignment macro requires vertical DSA lines on a 2^n pixel square image. It works on the principle of performing an asymmetric blur to make defects become gray relative to the white/black lines and spaces. It then performs some binary operations to select all area that is aligned vertically and all area that is gray. These then define the aligned and defective areas and calculates the defective area relative to the total image area, neglecting edge effects. Options to provide skeleton or other output files are commented out with "//" symbols. This macro was used for calculation of aligned area fraction and highlighted said area in Chapter 8.

```
//////////////////
// Program written by Alan G. Jacobs of Cornell University to
// measure the defective are of L/S BCP DSA for general BCP
// and SEM dimensions with arbitrary mags. For best results,
// the SEMs should be high enough mag to have lines and
// spaces take up at least 4-5 pixels (2.7 nm/px works for 15nm L/S)
//
```

```
// Any results published should acknowledge or add as secondary
   author the macro author.
//
// Known issues include:
// --edges may show defects when none occur due to threshold issues.
// ---Corrected for with edge exlusion in percent
//
// Contact
// -- agj27@cornell.edu
//
//////////////////
//Requires 4s for 1024 square image
//Suggests ~25s for 4096 square image

dir = getDirectory("Choose a Directory ");
count = 1;

// nPixles = getNumber("Image width in Pixels", 4096);
nmWidth = getNumber("Width of ALL images (nm)", 11100);
bcpWidth = getNumber("Approx period of BCP Lamellae (Lo, nm)", 28);
threshRad = getNumber("Local Threshold radius (in BCP Lo)", 2.2);
overlayYes = getNumber("Make overlaid images? (1=yes, otherwise no)",
    1);
edgeExclusion = getNumber("Edge exclusion % for defectivity analys
   ",2);
outputName = getString("Enter name of output file (date is appended):
    ", "SEM file areal defectivity fraction");
timeStamp = getNumber("Timestamp at top of output file? (1=yes) ", 1)
   ;

getDateAndTime(year, month, dayOfWeek, dayOfMonth, hour, minute,
   second, msec)
month = month +1;

dateString = " " + year;
if (month<10) {dateString = dateString+"0";}
dateString = dateString + month;
if (dayOfMonth<10) {dateString = dateString+"0";}
dateString = dateString+dayOfMonth;

timeString = " ";
if (hour<10) {timeString = timeString+"0";}
timeString = timeString+hour+":";
if (minute<10) {timeString = timeString+"0";}
timeString = timeString+minute+":";
if (second<10) {timeString = timeString+"0";}
timeString = timeString+second;

// Note, Files overwrite so date in name to differentiate
logFile = dir + outputName + dateString + ".txt";
logFileCmd = File.open(logFile);
if (timeStamp == 1) { print(logFileCmd, "\n" + "Data Analysis Started
   :"+ dateString + timeString); }

list = getFileList(dir);
 for (i=0; i<list.length; i++) {
   if (endsWith(list[i], "/"))
     listFiles(""+dir+list[i]);
   else
     print((count++) + ": " + dir + list[i]);
 }

n = lengthOf(list);
for (j=0; j<n; j++){

if(endsWith(list[j],".tif"))
```

```
{
open(dir + list[j]);
name = File.nameWithoutExtension;

w = getWidth();
wLarge = 4*w;

run("Set Scale...", "distance=w known=nmWidth pixel=1 unit=nm");
pxlsPnm = w/nmWidth;

run("Canvas Size...", "width=w height=w position=Top-Left");
run("8-bit");
getStatistics(area, mean, min, max, std, histogram);
BrightMult = 165/mean;
run("Multiply...", "value=BrightMult");

//run("Size...", "width=wLarge height=wLarge constrain average
    interpolation=Bilinear");

print("Analyzing " + name);
run("Smooth");
//run("Gaussian Blur...", "sigma=3");
print("Thresholding...");

//auto local threshold at about 2.2 Lo (default) and choosing number
    of pixels
threshRadPx = threshRad*bcpWidth*pxlsPnm;
var threshArg = "method=Niblack radius="+threshRadPx+" parameter_1=0
    parameter_2=0 white";
//24 pixels for 100kx image

run("Auto Local Threshold", threshArg);
run("Smooth");
print("Making Binary...");
run("Make Binary");
//saveAsPath = getDirectory("image") + File.nameWithoutExtension + "
    Binary.tif";
//saveAs("Tiff", saveAsPath);

//print("Skeletonizing...");
//run("Skeletonize");
//saveAsPath = getDirectory("image") + File.nameWithoutExtension + "
    Skeleton.tif";
//saveAs("Tiff", saveAsPath);

//print("Shrinking Skeleton...");
//run("Invert LUT");
//run("Size...", "width=w height=w constrain average interpolation=
    Bilinear");
//run("Enhance Contrast...", "saturated=0.4 normalize equalize");
//saveAsPath = getDirectory("image") + File.nameWithoutExtension + "
    SkeletonSmall.tif";
//saveAs("Tiff", saveAsPath);

//print("Making Voronoi plot... ");
//run("Undo");
//run("Voronoi");
//saveAsPath = getDirectory("image") + File.nameWithoutExtension + "
    Voronoi.tif";
//saveAs("Tiff", saveAsPath);

//close();
//run("Close All");

//////////////////////
///for calculation of defectivity area
```

```
//open(getDirectory("image") + File.nameWithoutExtension + " Binary.
   tif");

//3D blurr args, typ x=1, y=12, z=1, for 2.77nm/px (100kx), yblur is
   ~1Lo
print("Blurring...");
gaussBlurRad = bcpWidth*pxlsPnm;
gaussBlurArg = "x=1 y="+gaussBlurRad+" z=1";
run("Gaussian Blur 3D...", gaussBlurArg);

//getRawStatistics(area, mean);
print("Thresholding (Again)...");
//run("Auto Threshold", "method=Triangle white");
run("Auto Threshold", "method=Minimum white");
//run("Invert LUT");

//3D blurr args, typ x=12, y=1, z=1, for 2.77nm/px (100kx), xblur is
   ~1Lo
print("Isolating Aligned Regions");
gaussBlurArg = "x="+gaussBlurRad+" y=1 z=1";
run("Gaussian Blur 3D...", gaussBlurArg);
run("Auto Threshold", "method=Default white");

wSmall = w*(1-edgeExclusion/200);
run("Canvas Size...", "width=wSmall height=wSmall position=Center");

getRawStatistics(area, mean);

if( mean <= 127){
      mean = 256-mean;
      run("Invert");
}

getHistogram(values, counts, 2);
run("Canvas Size...", "width=w height=w position=Center");

run("Size...", "width=w height=w constrain average interpolation=
   Bilinear");
//saveAsPath = dir + name + " Defective Area.tif";
//saveAs("Tiff", saveAsPath);

if( overlayYes == 1){

print("Plotting Overlaid Image");
run("RGB Color");
//run("Invert");
//run("Multiply...", "value=0.200");
run("Split Channels");
close();
close();
run("Multiply...", "value=0.25");
run("Invert");
//run("Subtract...", "value=60");

redimage = getTitle();
//print(redimage);

run("Subtract...", "value=254");

open(dir + name + ".tif");
//run("Size...", "width=w height=w constrain average interpolation=
   Bilinear");
//run("Canvas Size...", "width=w height=w position=Top-Left");

run("RGB Color");

name1 = name + ".tif (red)";
```

```
//run("Multiply...", "value=1.0");

name2 = name + ".tif";
//run("Multiply...", "value=1.0");

imageCalculator("Multiply", name1, name2);

open(dir + list[j]);

run("Canvas Size...", "width=w height=w position=Top-Left");
run("RGB Color");
run("Split Channels");

close();
close();
//BrightMult2 = 1/BrightMult;
//run("Multiply...", "value=BrightMult");

grayimage = getTitle();

//open(getDirectory("image") + File.nameWithoutExtension + "
   Defective Area.tif");

run("RGB Merge...", "red=["+redimage+"] green=["+grayimage+"] blue
   =["+redimage+"]");
run("8-bit Color", "number=256");
run("Flatten");

run("Multiply...", "value=BrightMult");

run("RGB Color");
name2 = getTitle();
run("Split Channels");
//selectWindow(greenimage2);
//run("Multiply...", "value=0.5");
run("Subtract...", "value=96");
run("Add...", "value=96");
//old green value 128//////////////////

redimage2 = name2 + " (red)";
greenimage2 = name2 + " (green)";
blueimage2 = name2 + " (blue)";

run("RGB Merge...", "red=["+redimage2+"] green=["+greenimage2+"] blue
   =["+blueimage2+"]");

//setColor("green");
//fontsize = w/32;

//setFont("Serif", fontsize);
//drawString((mean/255) + " Aligned", fontsize, 2*fontsize);

//run("Set Scale...", "distance=1024 known=2770 pixel=1 unit=nm");
//run("Scale Bar...", "width=500 height=10 font=fontsize color=Green
   background=None location=[Lower Left] serif");

run("8-bit Color", "number=256");
run("Flatten");

run("8-bit Color", "number=256");

saveAsPath = dir + name + " Green Overlay No Label.tif";
saveAs("Tiff", saveAsPath);

//File.delete(dir + name + " Binary.tif");
//File.delete(dir + name + " Binary Defective Area.tif");

//close();
```

```
} //closing if for Overlaying Images

run("Close All");

// Writing the actual fraction aligned in tab delimited format,
// first column is file name, second is fraction aligned. "\t" is tab
    ,
// "\n" is new line, "\s" is new space
print(logFileCmd,"\n" + name + "\t" + mean/255);
}
}
print("Fin!");
```

BIBLIOGRAPHY

[1] T. P. Lodge, "Block copolymers: past successes and future challenges", *Macromolecular Chemistry and Physics*, vol. 204, no. 2, pp. 265–273, 2003. DOI: 10.1002/macp.200290073.

[2] E. W. Cochran, C. J. Garcia-Cervera, and G. H. Fredrickson, "Stability of the gyroid phase in diblock copolymers at strong segregation", *Macromolecules*, vol. 39, no. 7, pp. 2449–2451, 2006. DOI: 10.1021/ma0527707.

[3] M. P. Stoykovich, M. Müller, S. O. Kim, H. H. Solak, E. W. Edwards, J. J. de Pablo, and P. F. Nealey, "Directed assembly of block copolymer blends into nonregular device-oriented structures.", *Science (New York, N.Y.)*, vol. 308, no. 5727, pp. 1442–1446, 2005. DOI: 10.1126/science.1111041.

[4] J.-B. Chang, H. K. Choi, A. F. Hannon, A. Alexander-Katz, C. A. Ross, and K. K. Berggren, "Design rules for self-assembled block copolymer patterns using tiled templates", *Nature Communications*, vol. 5, pp. 1–9, 2014. DOI: 10.1038/ncomms4305.

[5] G. E. Moore, "Cramming more components onto integrated circuits", *Electronics*, vol. 38, no. 8, p. 4, 1965. DOI: 10.1109/N-SSC.2006.4785860.

[6] G. E. Moore, "Microprocessors and integrated electronic technology", *Proceedings of the IEEE*, vol. 64, no. 6, pp. 837–841, 1976. DOI: 10.1109/PROC.1976.10233.

[7] I. Ferain, C. A. Colinge, and J.-P. Colinge, "Multigate transistors as the future of classical metalâăşoxideâăşsemiconductor field-effect transis-

tors", *Nature*, vol. 479, no. 7373, pp. 310–316, 2011. DOI: 10.1038/nature10676.

[8] T. Azuma, T. Chijimatsu, M. Endo, T. Fedynyshyn, H. Feldmann, E. Gallagher, R. Garreis, C. Garza, T. Gau, F. Goodwin, R. Gronheid, N. Hayashi, F. Kalk, K. Kasama, I. Kim, P. Kearney, S. Kobayashi, T. Konishi, Y. Ku, K. Kurihara, D. Kyser, S.-J. Lin, D. Millward, M. Malloy, P. Mangat, V. Nagaswami, H. Nakashima, P. Naulleau, M. Neisser, Y. Okubo, K. Ohmori, M. Okumura, M. Preil, D. Resnick, K. Takahashi, H. Takeda, W. Trybula, F. Uesawa, M. Vasconi, G. Vandenberghe, P. Ware, J. Wiesner, J. Wiley, G. Willson, O. Wood, S. Wurm, T. Yamaguchi, J. Yamamoto, and J. Zimmerman, *Lithography*, 2015.

[9] ASML, *Asml twinscan nxt:1980di*, 2016.

[10] Y. Wei, "Extendability of 193nm immersion lithography", *SPIE Newsroom*, pp. 2–5, 2008. DOI: 10.1117/2.1200802.0974.

[11] B. W. Smith, A. Bourov, Y. Fan, L. Zavyalova, N. Lafferty, and F. Cropanese, "Approaching the numerical aperture of water-immersion lithography at 193-nm", *Proceedings of SPIE Advanced Lithography*, vol. 5377, pp. 273–284, 2004. DOI: 10.1117/12.537262.

[12] J. Yu, W. Xiao, W. Kang, and Y. Chen, "Understanding the critical challenges of self-aligned octuple patterning", *Optical Microlithography XXVII*, vol. 9052, 90521P, 2014. DOI: 10.1117/12.2046094.

[13] B. Wu and A. Kumar, "Extreme ultraviolet lithography: a review", *Journal of Vacuum Science & Technology B: Microelectronics and Nanometer Structures*, vol. 25, no. 6, p. 1743, 2007. DOI: 10.1116/1.2794048.

[14] S. Kang, W.-L. Wu, K. W. Choi, A. De Silva, C. K. Ober, and V. M. Prabhu, "Characterization of the photoacid diffusion length and reaction kinetics in euv photoresists with ir spectroscopy", *Macromolecules*, vol. 43, no. 9, pp. 4275–4286, 2010. DOI: 10.1021/ma902548a.

[15] ASML, *Asml twinscan nxe:3300b*, 2016.

[16] R. Peeters, S. Lok, E. van Alphen, N. Harned, P. Kuerz, M. Lowisch, H. Meijer, D. Ockwell, E. van Setten, G. Schiffelers, J.-W. van der Horst, J. Stoeldraijer, R. Kazinczi, R. Droste, H. Meiling, and R. Kool, "Asml's nxe platform performance and volume introduction", *Proceedings of SPIE Advanced Lithography*, vol. 8679, 86791F, 2013. DOI: 10.1117/12.2010932.

[17] C.-C. Liu, P. F. Nealey, A. K. Raub, P. J. Hakeem, S. R. J. Brueck, E. Han, and P. Gopalan, "Integration of block copolymer directed assembly with 193 immersion lithography", *Journal of Vacuum Science & Technology B: Microelectronics and Nanometer Structures*, vol. 28, no. 6, C6B30, 2010. DOI: 10.1116/1.3501348.

[18] W. Li, P. F. Nealey, J. J. de Pablo, and M. Müller, "Defect removal in the course of directed self-assembly is facilitated in the vicinity of the order-disorder transition", *Physical Review Letters*, vol. 113, no. 16, pp. 1–5, 2014. DOI: 10.1103/PhysRevLett.113.168301.

[19] F. S. Bates, "Block copolymer thermodynamics: theory and experiment", *Annual Review of Physical Chemistry*, vol. 41, pp. 525–557, 1990. DOI: 10.1146/annurev.pc.41.100190.002521.

[20] F. S. Bates, "Polymer-polymer phase behavior", *Science*, vol. 251, pp. 898–905, 1991.

[21] M. Muthukumar, C. K. Ober, and E. L. Thomas, "Competing interactions and levels of ordering in self-organizing polymeric materials", *Science*, vol. 277, no. August, pp. 1225–1232, 1997. DOI: 10.1126/science.277.5330.1225.

[22] C. M. Bates, M. J. Maher, D. W. Janes, C. J. Ellison, and C. G. Willson, "Block copolymer lithography", *Macromolecules*, vol. 47, no. 1, pp. 2–12, 2014. DOI: 10.1021/ma401762n.

[23] O. Hellwig, J. K. Bosworth, E. Dobisz, D. Kercher, T. Hauet, G. Zeltzer, J. D. Risner-Jamtgaard, D. Yaney, and R. Ruiz, "Bit patterned media based on block copolymer directed assembly with narrow magnetic switching field distribution", *Applied Physics Letters*, vol. 96, p. 052 511, 2010. DOI: 10.1063/1.3293301.

[24] R. M. Dorin, W. A. Phillip, H. Sai, J. Werner, M. Elimelech, and U. B. Wiesner, "Designing block copolymer architectures for targeted membrane performance", *Polymer*, vol. 55, no. 1, pp. 347–353, 2014. DOI: 10.1016/j.polymer.2013.09.038.

[25] X. L. Chen and S. A. Jenekhe, "Block conjugated copolymers : toward quantum-well nanostructures for exploring spatial confinement effects on electronic, optoelectronic, and optical phenomena", *Macromolecules*, vol. 9297, no. 96, pp. 6189–6192, 1996. DOI: 10.1021/ma9605715.

[26] K. F. Freed and A. I. Pesci, "Theory of the molecular origins of the entropic portion of the flory chi parameter for polymer blends", *The Journal of Chemical Physics*, vol. 87, no. 12, pp. 7342–7344, 1987. DOI: 10.1063/1.453329.

[27] M. G. Bawendi and K. F. Freed, "Systematic corrections to flory-huggins theory: polymer-solvent-void systems and binary blend-void systems", *J.Chem.Phys*, vol. 88, no. 1988, pp. 2741–2756, 1988. DOI: 10.1063/1.454005.

[28] K. F. Freed and M. G. Bawendi, "Lattice theories of polymeric fluids", *The Journal of Physical Chemistry*, vol. 93, no. 6, pp. 2194–2203, 1989. DOI: 10.1021/j100343a006.

[29] S. J. Mumby and P. Sher, "Determination of chi from liquid-liquid phase data and the computation of phase diagrams for quasi-binary polymer solutions and blends", *Macromolecules*, vol. 27, no. 3, pp. 689–694, 1994. DOI: 10.1021/ma00081a011.

[30] L. Leibler, "Theory of microphase separation in block copolymers", *Macromolecules*, vol. 13, no. 10, pp. 1602–1617, 1980. DOI: 10.1021/ma60078a047.

[31] G. H. Fredrickson and E. Helfand, "Fluctuation effects in the theory of microphase separation in block copolymers", *The Journal of Chemical Physics*, vol. 87, no. 1, p. 697, 1987. DOI: 10.1063/1.453566.

[32] J.-L. Barrat and G. H. Fredrickson, "Collective and single-chain correlations near the block copolymer order-disorder transition", *Journal of Chemical Physics*, vol. 95, no. 2, pp. 1281–1289, 1991. DOI: 10.1063/1.461109.

[33] J. D. Vavasour and M. D. Whitmore, "Self-consistent mean field theory of the microphases of diblock copolymers", *Macromolecules*, vol. 25, no. 20, pp. 5477–5486, 1992. DOI: 10.1021/ma00046a055.

[34] M. W. Matsen and M. Schick, "Microphases of a diblock copolymer with conformational asymmetry", *Macromolecules*, vol. 27, pp. 4014–4015, 1994. DOI: 10.1002/bit.260190912.

[35] J. D. Vavasour and M. D. Whitmore, "Self consistent theory of block copolymers with conformation assymetry", *Macromolecules*, vol. 29, p. 5244, 1996.

[36] M. W. Matsen and F. S. Bates, "Unifying weak- and strong-segregation block copolymer theories", *Macromolecules*, vol. 29, no. 4, pp. 1091–1098, 1996. DOI: 10.1021/ma951138i.

[37] T. Hashimoto, "Time-dependent ginzburg-landau approach for microphase-separation kinetics of block polymers", *Macromolecules*, vol. 20, no. 2, pp. 465–468, 1987. DOI: 10.1021/ma00168a053.

[38] C. D. Han, J. Kim, and J. K. Kim, "Determination of the order-disorder transition temperature", *Macromolecules*, vol. 22, pp. 383–394, 1989. DOI: 10.1021/ma00191a071.

[39] J. H. Rosedale and F. S. Bates, "Rheology of ordered and disordered symmetric poly(ethylenepropylene)-poly(ethylethylene) diblock copolymers", *Macromolecules*, vol. 23, no. 8, pp. 2329–2338, 1990. DOI: 10.1021/ma00210a032.

[40] K. Amundson, E. Helfand, S. S. Patel, X. Quan, and S. D. Smith, "Optical characterization of ordering and disordering of block copolymer microstructure", *Macromolecules*, vol. 25, pp. 1935–1940, 1992. DOI: Doi10.1021/Ma00033a016.

[41] F. S. Bates, J. H. Rosedale, and G. H. Fredrickson, "Fluctuation effects in a symmetric diblock copolymer near the order-disorder transition",

Journal of Chemical Physics, vol. 92, pp. 6255–6270, 1990. DOI: 10.1063/1.458350.

[42] C. K. Shelton and T. H. Epps III, "Mapping substrate surface field propagation in block polymer thin films", *Macromolecules*, vol. 49, pp. 574–580, 2016. DOI: 10.1021/acs.macromol.5b00833.

[43] A. Menelle, T. P. Russell, S. H. Anastasiadis, S. K. Satija, and C. F. Majkrzak, "Ordering of thin diblock copolymer films", *Physical Review Letters*, vol. 68, no. 1, pp. 67–70, 1992. DOI: 10.1103/PhysRevLett.68.67.

[44] I. Saito, T. Miyazaki, and K. Yamamoto, "Depth-resolved structure analysis of cylindrical microdomain in block copolymer thin film by grazing-incidence small-angle x-ray scattering utilizing low-energy x-rays", *Macromolecules*, vol. 48, no. 22, pp. 8190–8196, 2015. DOI: 10.1021/acs.macromol.5b01883.

[45] T.-y. Lo, A. Dehghan, P. Georgopanos, A. Avgeropoulos, A.-C. Shi, and R.-M. Ho, "Orienting block copolymer thin films via entropy", *Macromolecules*, vol. 49, pp. 624–633, 2016. DOI: 10.1021/acs.macromol.5b02685.

[46] A. K. Khandpur, S. Forster, F. S. Bates, I. W. Hamley, A. J. Ryan, W. Bras, K. Almdal, and K. Mortensen, "Polyisoprene-polystyrene diblock copolymer phase diagram near the order-disorder transition", *Macromolecules*, vol. 28, pp. 8796–8806, 1995. DOI: 10.1021/ma00130a012.

[47] J.-H. Ahn and W.-C. Zin, "Mechanism of morphological transition from lamellar/perforated layer to gyroid phases", *Macromolecular Research*, vol. 11, no. 3, pp. 152–156, 2003. DOI: 10.1007/BF03218345.

[48] G. H. Fredrickson and K. Binder, "Kinetics of metastable states in block copolymer melts", *The Journal of Chemical Physics*, vol. 91, no. 11, p. 7265, 1989. DOI: 10.1063/1.457294.

[49] F Liu and N Goldenfeld, "Dynamics of phase separation in block copolymer melts", *Physical Review A*, vol. 39, no. 9, pp. 4805–4810, 1989.

[50] A. Chakrabarti, R. Toral, and J. D. Gunton, "Microphase separation in block copolymers", *Physical Review Letters*, vol. 63, no. 24, pp. 2661–2664, 1989.

[51] G. C. Paquette, "Front propagation in a diblock copolymer melt", *Physical Review A*, vol. 44, no. 10, pp. 6577–6599, 1991. DOI: 10.1103/PhysRevA.44.6577.

[52] K. Binder, "Nucleation phenomena in polymeric systems", *Physica A: Statistical Mechanics and its Applications*, vol. 213, no. 1-2, pp. 118–129, 1995. DOI: 10.1016/0378-4371(94)00153-K.

[53] A. Hoffmann, J.-U. Sommer, and A. Blumen, "Statics and dynamics of dense copolymer melts: a monte carlo simulation study", *The Journal of Chemical Physics*, vol. 106, no. 16, p. 6709, 1997. DOI: 10.1063/1.473668.

[54] M. Murat, G. S. Grest, and K. Kremer, "Statics and dynamics of symmetric diblock copolymers: a molecular dynamics study", *Macromolecules*, vol. 32, pp. 595–609, 1999. DOI: 10.1021/ma981512p.

[55] Q. Wang, P. F. Nealey, and J. J. De Pablo, "Monte carlo simulations of asymmetric diblock copolymer thin films confined between two homogeneous surfaces", *Macromolecules*, vol. 34, pp. 3458–3470, 2001. DOI: 10.1021/ma0018751.

[56] S. R. Ren and I. W. Hamley, "Cell dynamics simulations of microphase separation in block copolymers", *Macromolecules*, vol. 34, pp. 116–126, 2001. DOI: 10.1021/ma000678z.

[57] K. Yamada, M. Nonomura, and T. Ohta, "Kinetics of morphological transitions in microphase-separated diblock copolymers", *Macromolecules*, vol. 37, pp. 5762–5777, 2004. DOI: 10.1021/ma049687o.

[58] H. H. Solak, E. W. Edwards, M. P. Stoykovich, M. Muller, J. J. De Pablo, and P. F. Nealey, "Mechanism and kinetics of ordering in diblock copolymer thin films on chemically nanopatterned substrates", *Journal of Polymer Science Part B*, vol. 43, pp. 3444–3459, 2005. DOI: 10.1002/polb.20643.

[59] A. A. Gavrilov, Y. V. Kudryavtsev, P. G. Khalatur, and A. V. Chertovich, "Simulation of phase separation in melts of regular and random multiblock copolymers", *Polymer Science, Ser. A*, vol. 53, no. 9, pp. 827–836, 2011. DOI: 10.1134/S0965545X11090033.

[60] N. Ji, P. Tang, and F. Qiu, "Kinetic pathways of lamellae to gyroid transition in weakly segregated diblock copolymers", *Macromolecules*, vol. 48, pp. 8681–8693, 2015. DOI: 10.1021/acs.macromol.5b02023.

[61] C. R. Harkless, M. A. Singh, S. E. Nagler, G. B. Stephenson, and J. L. Jordan-Sweet, "Small-angle x-ray-scattering study of ordering kinetics in a block copolymer", *Physical Review Letters*, vol. 64, no. 19, pp. 2304–2308, 1990. DOI: 10.1103/PhysRevLett.64.2285.

[62] M. A. Singh, C. R. Harkless, S. E. Nagler, R. F. Shannon, and S. S. Ghosh, "Time-resolved small-angle x-ray-scattering study of ordering kinetics

in diblock styrene-butadiene", *Physical Review B*, vol. 47, no. 14, pp. 8425–8435, 1993. DOI: 10.1103/PhysRevB.47.8425.

[63] G. Floudas, D. Vlassopoulos, M. Pitsikalis, N. Hadjichristidis, and M. Stamm, "Order-disorder transition and ordering kinetics in binary diblock copolymer mixtures of styrene and isoprene", *The Journal of Chemical Physics*, vol. 104, no. 5, p. 2083, 1996. DOI: 10.1063/1.470965.

[64] M. J. Heinzer, S. Han, J. A. Pople, D. G. Baird, and S. M. Martin, "In situ measurement of block copolymer ordering kinetics during the drying of solution-cast films using small-angle x-ray scattering", *Macromolecules*, vol. 45, no. 8, pp. 3471–3479, 2012. DOI: 10.1021/ma2026429.

[65] H. Nie, R. Bansil, K. Ludwig, M. Steinhart, C. Konak, and J. Bang, "Time-resolved small-angle x-ray scattering study of the kinetics of disorder-order transition in a triblock copolymer in a selective solvent for the middle block", *Macromolecules*, vol. 36, pp. 8097–8106, 2003. DOI: 10.1021/ma034357+.

[66] T. Q. Chastek and T. P. Lodge, "Grain shapes and growth kinetics of the cylinder phase in a block copolymer solution", *Macromolecules*, vol. 37, pp. 4891–4899, 2004. DOI: 10.1021/ma049502d.

[67] Z. Liu, M. T. Shaw, and B. S. Hsiao, "Ordering kinetics of the bcc morphology in diblock copolymer solutions over a wide temperature range", *Macromolecules*, vol. 37, pp. 9880–9888, 2004. DOI: 10.1021/ma0484330.

[68] Z. Liu, M. T. Shaw, and B. S. Hsiao, "Ordering kinetics of body-centered-cubic morphology in diblock copolymer solutions at low temperatures",

Journal of Rheology, vol. 48, pp. 1389–1405, 2004. DOI: 10.1122/1.1807842.

[69] Y. Liu, H. Nie, R. Bansil, M. Steinhart, J. Bang, and T. P. Lodge, "Kinetics of disorder-to-fcc phase transition via an intermediate bcc state", *Physical Review E*, vol. 73, no. 6, p. 061 803, 2006. DOI: 10.1103/PhysRevE.73.061803.

[70] C.-Y. Wang and T. P. Lodge, "Unexpected intermediate state for the cylinder-to-gyroid transition in a block copolymer solution", *Macromolecular Rapid Communications*, vol. 32, pp. 49–54, 2002. DOI: 10.1002/1521-3927(20020101)23:1<49::AID-MARC49>3.0.CO;2-X.

[71] T. Q. Chastek and T. P. Lodge, "Measurement of gyroid single grain growth rates in block copolymer solutions", *Macromolecules*, vol. 36, pp. 7672–7680, 2003. DOI: 10.1021/ma034833w.

[72] M. J. Park, J. Bang, T. Harada, K. Char, and T. P. Lodge, "Epitaxial transitions among fcc, hcp, bcc, and cylinder phases in a block copolymer solution", *Macromolecules*, vol. 37, pp. 9064–9075, 2004. DOI: 10.1021/ma049285g.

[73] Y. Liu, M. Li, R. Bansil, and M. Steinhart, "Kinetics of phase transition from lamellar to hexagonally packed cylinders for a triblock copolymer in a selective solvent", *Macromolecules*, vol. 40, pp. 9482–9490, 2007. DOI: 10.1021/ma071192m.

[74] J. S. Trent, "Electron microscopy of ps/pmma and rubber modified polymer blends: use of ruthenium tetroxide as a new staining agent", *Journal of Polymer Science. Polymer Letters Edition*, vol. 19, no. 6, pp. 315–319, 1981. DOI: 10.1002/pol.1981.130190607.

[75] E. Kim, S. Choi, R. Guo, D. Y. Ryu, C. J. Hawker, and T. P. Russell, "Transition behavior of ps-b-pmma films on the balanced interfacial interactions", *Polymer*, vol. 51, no. 26, pp. 6313–6318, 2010. DOI: 10.1016/j.polymer.2010.10.055.

[76] N. Sakamoto and T. Hashimoto, "Order-disorder transition of low molecular weight polystyrene-block-polyisoprene. 1. saxs analysis of two characteristic temperatures", *Macromolecules*, vol. 28, pp. 6825–6834, 1995. DOI: 10.1021/ma00124a018.

[77] J. Als-Nielsen and D. McMorrow, *Elements of Modern X-ray Physics*, 2nd ed. Wiley, 2010, pp. 134–145.

[78] Y. S. Jung and C. A. Ross, "Solvent-vapor-induced tunability of self-assembled block copolymer patterns", *Advanced Materials*, vol. 21, no. 24, pp. 2540–2545, 2009. DOI: 10.1002/adma.200802855.

[79] K. Fukunaga, H. Elbs, R. Magerle, and G. Krausch, "Large-scale alignment of abc block copolymer microdomains via solvent vapor treatment", *Macromolecules*, vol. 33, no. 3, pp. 947–953, 2000. DOI: 10.1021/ma9910639.

[80] S. H. Kim, M. J. Misner, T. Xu, M. Kimura, and T. P. Russell, "Highly oriented and ordered arrays from block copolymers via solvent evaporation", *Advanced Materials*, vol. 16, no. 3, pp. 226–231, 2004. DOI: 10.1002/adma.200304906.

[81] A. F. Hannon, W. Bai, A. Alexander-Katz, and C. A. Ross, "Simulation methods for solvent vapor annealing of block copolymer thin films", *Soft matter*, vol. 11, no. 19, pp. 3794–805, 2015. DOI: 10.1039/c5sm00324e.

[82] J. P. Singer, K. W. Gotrik, J. H. Lee, S. E. Kooi, C. A. Ross, and E. L. Thomas, "Alignment and reordering of a block copolymer by solvent-enhanced thermal laser direct write", *Polymer*, vol. 55, no. 7, pp. 1875–1882, 2014. DOI: 10.1016/j.polymer.2014.02.028.

[83] J. Y. Cheng, C. A. Ross, H. I. Smith, and E. L. Thomas, "Templated self-assembly of block copolymers: top-down helps bottom-up", *Advanced Materials*, vol. 18, no. 19, pp. 2505–2521, 2006. DOI: 10.1002/adma.200502651.

[84] P. A. Rincon Delgadillo, R. Gronheid, C. J. Thode, H. Wu, Y. Cao, M. Neisser, M. Somervell, K. Nafus, and P. F. Nealey, "Implementation of a chemo-epitaxy flow for directed self-assembly on 300-mm wafer processing equipment", *Journal of Micro/Nanolithography, MEMS, and MOEMS*, vol. 11, no. 3, p. 031 302, 2012. DOI: 10.1117/1.JMM.11.3.031302.

[85] K. W. Gotrik and C. A. Ross, "Solvothermal annealing of block copolymer thin films", *Nano Letters*, vol. 13, no. 11, pp. 5117–5122, 2013. DOI: 10.1021/nl4021683.

[86] S. Xiao, X. Yang, E. W. Edwards, Y.-H. La, and P. F. Nealey, "Graphoepitaxy of cylinder-forming block copolymers for use as templates to pattern magnetic metal dot arrays.", *Nanotechnology*, vol. 16, no. 7, S324–S329, 2005. DOI: 10.1088/0957-4484/16/7/003.

[87] A. Singh, W. Knaepen, S. Sayan, Z. el Otell, B. T. Chan, J. W. Maes, and R. Gronheid, "Impact of sequential infiltration synthesis on pattern fidelity of dsa lines", *Proceedings of SPIE Advanced Lithography*, vol. 9425, 94250N–7, 2015. DOI: 10.1117/12.2086091.

[88] J. Zhang, J. Wu, M. Li, V. V. Ginzburg, J. D. Weinhold, M. B. Clark, P. Trefonas III, and P. D. Hustad, "New materials for directed self-assembly for advanced patterning", *Proc. of SPIE*, vol. 9051, p. 905 111, 2014. DOI: 10.1117/12.2046328.

[89] C. Reboul, G. Fleury, K. Aissou, C. Brochon, E. Cloutet, C. Nicolet, X. Chevalier, C. Navarro, R. Trion, G. Cunge, and G. Hadziioannou, "Self-assembly of si-containing block copolymers with high-segregation strength: toward sub-10nm features in directed self-assembly", *Proceedings of SPIE Advanced Lithography*, vol. 9049, pp. 904925 –904 933, 2014. DOI: 10.1117/12.2046099.

[90] J. Jiang, A. G. Jacobs, M. O. Thompson, and C. K. Ober, "Laser spike annealing of dsa photoresists", *Journal of Photopolymer Science and Technology*, vol. 28, no. 5, pp. 631–634, 2015. DOI: 10.2494/photopolymer.28.631.

[91] C.-C. Liu, C. J. Thode, P. A. Rincon Delgadillo, G. S. W. Craig, P. F. Nealey, and R. Gronheid, "Towards an all-track 300 mm process for directed self-assembly", *Journal of Vacuum Science & Technology B: Microelectronics and Nanometer Structures*, vol. 29, no. 6, 06F203, 2011. DOI: 10.1116/1.3644341.

[92] P. W. Majewski and K. G. Yager, "Latent alignment in pathway-dependent ordering of block copolymer thin films", *Nano Letters*, vol. 15, no. 8, pp. 5221–5228, 2015. DOI: 10.1021/acs.nanolett.5b01463.

[93] M. P. Stoykovich and P. F. Nealey, "Block copolymers and conventional lithography", *Materials Today*, vol. 9, no. 9, pp. 20–29, 2006. DOI: 10.1016/S1369-7021(06)71619-4.

[94] S. Ji, C.-C. Liu, W. Liao, A. L. Fenske, G. S. W. Craig, and P. F. Nealey, "Domain orientation and grain coarsening in cylinder-forming poly(styrene-b-methyl methacrylate) films", *Macromolecules*, vol. 44, no. 11, pp. 4291–4300, 2011. DOI: 10.1021/ma2005734.

[95] P. W. Majewski and K. G. Yager, "Millisecond ordering of block copolymer films via photothermal gradients", *ACS Nano*, vol. 9, no. 4, pp. 3896–3906, 2015. DOI: 10.1021/nn5071827.

[96] A. M. Welander, H. Kang, K. O. Stuen, H. H. Solak, M. Müller, J. J. de Pablo, and P. F. Nealey, "Rapid directed assembly of block copolymer films at elevated temperatures", *Macromolecules*, vol. 41, no. 8, pp. 2759–2761, 2008. DOI: 10.1021/ma800056s.

[97] F. Ferrarese Lupi, T. J. Giammaria, M. Ceresoli, G. Seguini, K. Sparnacci, D. Antonioli, V. Gianotti, M. Laus, and M. Perego, "Rapid thermal processing of self-assembling block copolymer thin films.", *Nanotechnology*, vol. 24, no. 31, p. 315 601, 2013. DOI: 10.1088/0957-4484/24/31/315601.

[98] A. Singh, R. Krishnan, and S. Puri, "Kinetics of microphase separation in block copolymers: a molecular-dynamics study", *EPL (Europhysics Letters)*, vol. 109, no. 2, p. 26 006, 2015. DOI: 10.1209/0295-5075/109/26006.

[99] H. M. Jin, S. H. Lee, J. Y. Kim, S.-W. Son, B. H. Kim, H. K. Lee, J. H. Mun, S. K. Cha, J. S. Y. Kim, P. F. Nealey, K. J. Lee, and S. O. Kim, "Laser writing block copolymer self-assembly on graphene light-absorbing layer", *ACS Nano*, vol. 10, no. 3, pp. 3435–3442, 2016. DOI: 10.1021/acsnano.5b07511.

[100] J. G. Kennemur, M. A. Hillmyer, and F. S. Bates, "Synthesis, thermodynamics, and dynamics of poly(4-tert-butylstyrene-b-methyl methacrylate)", *Macromolecules*, vol. 45, no. 17, pp. 7228–7236, 2012. DOI: 10.1021/ma301047y.

[101] T. P. Russell, R. P. Hjelm Jr, and P. A. Seeger, "Temperature dependence of the interaction parameter of polystyrene and poly(methyl methacrylate)", *Macromolecules*, vol. 23, pp. 890–893, 1990. DOI: 10.1021/ma00205a033.

[102] Z. Yue, E. Sivaniah, and T. Hashimoto, "Saxs analysis of the order-disorder transition and the interaction parameter of polystyrene-block-poly(methyl methacrylate)", *Macromolecules*, vol. 41, no. 24, pp. 9948–9951, 2008. DOI: 10.1021/ma8013004.

[103] J. Y. Wang, W. Chen, and T. P. Russell, "Ion-complexation-induced changes in the interaction parameter and the chain conformation of ps-b-pmma copolymers", *Macromolecules*, vol. 41, no. 13, pp. 4904–4907, 2008. DOI: 10.1021/ma800718z.

[104] V. Mishra, G. H. Fredrickson, and E. J. Kramer, "Effect of film thickness and domain spacing on defect densities in directed self-assembly of cylindrical morphology block copolymers", *ACS Nano*, vol. 6, no. 3, pp. 2629–2641, 2012. DOI: 10.1021/nn205120j.

[105] B. Jung, J. Sha, F. Paredes, M. Chandhok, T. R. Younkin, U. B. Wiesner, C. K. Ober, and M. O. Thompson, "Kinetic rates of thermal transformations and diffusion in polymer systems measured during submillisecond laser-induced heating", *ACS Nano*, vol. 6, no. 7, pp. 5830–5836, 2012. DOI: 10.1021/nn300008a.

[106] W. A. Johnson and R. F. Mehl, "Reaction kinetics in processes of nucleation and growth", *American Institute of Mining and Metallurgical Engineers – Transactions*, vol. 135, pp. 416–441, 1939.

[107] M. Avrami, "Kinetics of phase change. i general theory", *The Journal of Chemical Physics*, vol. 7, no. 12, p. 1103, 1939. DOI: 10.1063/1.1750380.

[108] M. Avrami, "Kinetics of phase change. ii - transformation-time relations for random distribution of nuclei", *Journal of Chemical Physics*, vol. 8, no. 1940, pp. 212–224, 1940. DOI: 10.1063/1.1750631.

[109] M. Avrami, "Granulation, phase change, and microstructure kinetics of phase change. iii", *The Journal of Chemical Physics*, vol. 9, no. 2, p. 177, 1941. DOI: 10.1063/1.1750872.

[110] J. N. Hay, "Application of the modified avrami equations to polymer crystallisation kinetics", *British Polymer Journal*, vol. 3, no. 2, pp. 74–82, 1971. DOI: 10.1002/pi.4980030205.

[111] J. N. Hay and Z. J. Przekop, "Extensions of the avrami equation to various polymer crystallization models", *Journal of Polymer Science: Polymer Physics Edition*, vol. 17, no. 6, pp. 951–959, 1979. DOI: 10.1002/pol.1979.180170605.

[112] J. Vazquez, P. L. Lopez-Alemany, P. Villares, and R. Jimenez-Garay, "Generalization of the avrami equation for the analysis of non-isothermal transformation kinetics. application to the crystallization of the cu0.20as0.30se0.50 alloy", *Journal of Physics and Chemistry of Solids*, vol. 61, no. 4, pp. 493–500, 2000. DOI: 10.1016/S0022-3697(99)00260-7.

[113] J. Wang, H. C. Kou, X. F. Gu, J. S. Li, L. Q. Xing, R. Hu, and L. Zhou, "On discussion of the applicability of local avrami exponent: errors and solutions", *Materials Letters*, vol. 63, no. 13-14, pp. 1153–1155, 2009. DOI: 10.1016/j.matlet.2009.01.027.

[114] D. Martin, "Application of kolmogorov-johnson-mehl-avrami equations to non-isothermal conditions", *Computational Materials Science*, vol. 47, no. 3, pp. 796–800, 2010. DOI: 10.1016/j.commatsci.2009.11.005.

[115] S. K. H. Fung, H. T. Huang, S. M. Cheng, K. L. Cheng, S. W. Wang, Y. P. Wang, Y. Y. Yao, C. M. Chu, S. J. Yang, W. J. Liang, Y. K. Leung, C. C. Wu, C. Y. Lin, S. J. Chang, S. Y. Wu, C. F. Nieh, C. C. Chen, T. L. Lee, Y. Jin, S. C. Chen, L. T. Lin, Y. H. Chiu, H. J. Tao, C. Y. Fu, S. M. Jang, K. F. Yu, C. H. Wang, T. C. Ong, Y. C. See, C. H. Diaz, M. S. Liang, and Y. C. Sun, "65nm cmos high speed, general purpose and low power transistor technology for high volume foundry application", *Symposium on VLSl Technology Digest of Technical Papers*, pp. 92–93, 2004. DOI: 10.1109/VLSIT.2004.1345411.

[116] T. Yamamoto, T. Kubo, T. Sukegawa, E. Takii, Y. Shimamune, N. Tamura, T. Sakoda, M. Nakamura, H. Ohta, T. Miyashita, H. Kurata, S. Satoh, M. Kase, and T. Sugii, "Junction profile engineering with a novel multiple laser spike annealing scheme for 45-nm node high performance and low leakage cmos technology", *Technical Digest - International Electron Devices Meeting, IEDM*, no. 001, pp. 143–146, 2007. DOI: 10.1109/IEDM.2007.4418885.

[117] R. T. Bell, A. G. Jacobs, V. C. Sorg, B. Jung, M. O. Hill, B. E. Treml, and M. O. Thompson, "Lateral temperature-gradient method for high-throughput characterization of material processing by millisecond laser

annealing", *ACS Combinatorial Science*, vol. 18, no. 9, pp. 548–558, 2016. DOI: 10.1021/acscombsci.6b00043.

[118] K. Iyengar, B. Jung, M. Willemann, P. Clancy, and M. O. Thompson, "Experimental determination of thermal profiles during laser spike annealing with quantitative comparison to 3-dimensional simulations", *Applied Physics Letters*, vol. 100, no. 21, p. 211 915, 2012. DOI: 10.1063/1.4717745.

[119] R. Li, S. Cornaby, M. Kamperman, and D.-M. Smilgies, "Nanocomposite characterization on multiple length scales using usaxs", *Journal of Synchrotron Radiation*, vol. 18, no. 5, pp. 697–701, 2011. DOI: 10.1107/S0909049511024873.

[120] R. Huang, T. Szebenyi, M. Pfeifer, A. Woll, D.-M. Smilgies, K. Finkelstein, D. Dale, Y. Wang, J. Vila-Comamala, R. Gillilan, M. Cook, and D. H. Bilderback, "Application of chess single-bounce capillaries at synchrotron beamlines", *Journal of Physics: Conference Series*, vol. 493, p. 012 034, 2014. DOI: 10.1088/1742-6596/493/1/012034.

[121] M. Vayer, T. H. Nguyen, and C. Sinturel, "Ruthenium staining for morphological assessment and patterns formation in block copolymer films", *Polymer*, vol. 55, no. 4, pp. 1048–1054, 2014. DOI: 10.1016/j.polymer.2014.01.013.

[122] S. I. Stupp and P. V. Braun, "Molecular manipulation of microstructures: biomaterials, ceramics, and semiconductors", *Science*, vol. 277, no. 5330, pp. 1242–1248, 1997. DOI: 10.1126/science.277.5330.1242.

[123] W. D. Callister Jr., *Materials Science and Engineering an Introduction*, 7th. Wiley, 2007. DOI: 978-0-471-73696-7.

[124] E. S. Freeman and B. Carroll, "The application of thermoanalytical techniques to reaction kinetics: the thermogravimetric evaluation of the kinetics of the decomposition of calcium oxalate monohydrate", *The Journal of Physical Chemistry*, vol. 62, no. 4, pp. 394–397, 1958. DOI: 10.1021/j150562a003.

[125] A. W. Coats and J. P. Redfern, "Kinetic parameters from thermogravimetric data", *Nature*, vol. 201, pp. 68–69, 1964. DOI: 10.1038/201068a0.

[126] H. L. Friedman, "Kinetics of thermal degradation of char-forming plastics from thermogravimetry. application to a phenolic plastic", *Journal of Polymer Science Part C: Polymer Symposia*, vol. 6, no. 1, pp. 183–195, 1964. DOI: 10.1002/polc.5070060121.

[127] K. Pielichowski and J. Njuguna, *Thermal Degradation of Polymeric Materials*. Shawbury, UK: Rapra Technology Limited, 2005.

[128] M. J. O'Neill, "Measurement of specific heat functions by differential scanning calorimetry", *Analytical Chemistry*, vol. 38, no. 10, pp. 1331–1336, 1966. DOI: 10.1021/ac60242a011.

[129] W. Xie, Z. Gao, W.-P. Pan, D. Hunter, A. Singh, and R. Vaia, "Thermal degradation chemistry of alkyl quaternary ammonium montmorillonite", *Chemistry of Materials*, vol. 13, no. 9, pp. 2979–2990, 2001. DOI: 10.1021/cm010305s.

[130] I. B. Johns, E. A. McElhill, and J. O. Smith, "Thermal stability of some organic compounds", *Journal of Chemical & Engineering Data*, vol. 7, no. 2, pp. 277–281, 1962. DOI: 10.1021/je60013a036.

[131] S. Duquesne, M. Le Bras, S. Bourbigot, R. Delobel, G. Camino, B. Eling, C. Lindsay, and T. Roels, "Thermal degradation of polyurethane and

polyurethane/expandable graphite coatings", *Polymer Degradation and Stability*, vol. 74, no. 3, pp. 493–499, 2001. DOI: 10.1613/jair.301. arXiv: 9605103 [cs].

[132] E. P. Giannelis, "Polymer layered silicate nanocomposites", *Advanced materials*, vol. 8, no. 1, pp. 29–35, 1996. DOI: 10.1002/adma.19960080104.

[133] M. Alexandre and P. Dubois, "Polymer layered-silicate nanocomposites: preparation, properties and uses of a new class of materials", *Materials Science and Engineering*, vol. 28, no. March, pp. 1–63, 2000. DOI: 10.1016/S0927-796X(00)00012-7.

[134] H. M. El-Kaderi, J. R. Hunt, J. L. Mendoza-Cortes, A. P. Cote, R. E. Taylor, M. O'Keeffe, and O. M. Yaghi, "Designed synthesis of 3d covalent organic frameworks", *Science*, vol. 316, no. April, pp. 268–273, 2007. DOI: 10.1126/science.1139915.

[135] S. S.-Y. Chui, S. M.-F. Lo, J. P. H. Charmant, A. G. Orpen, and I. D. Williams, "A chemically functionalizable nanoporous material [cu3(tma)2(h2o)3]n", *Science*, vol. 283, no. February, pp. 1148–1150, 1999. DOI: 10.1126/science.283.5405.1148.

[136] U. Mueller, M. Schubert, F. Teich, H. Puetter, K. Schierle-Arndt, and J. Pastré, "Metalâăşorganic frameworksâăť prospective industrial applications", *J. Mater. Chem.*, vol. 16, no. 7, pp. 626–636, 2006. DOI: 10.1039/B511962F.

[137] A. A. Minakov, D. A. Mordvintsev, and C. Schick, "Melting and reorganization of poly(ethylene terephthalate) on fast heating (1000 k/s)", *Poly-*

mer, vol. 45, no. 11, pp. 3755–3763, 2004. DOI: 10.1016/j.polymer.2004.03.072.

[138] B. Jung, P. Satish, D. N. Bunck, W. R. Dichtel, C. K. Ober, and M. O. Thompson, "Laser-induced sub-millisecond heating reveals distinct tertiary ester cleavage reaction pathways in a photolithographic resist polymer", *ACS Nano*, vol. 8, no. 6, pp. 5746–5756, 2014. DOI: 10.1021/nn500549w.

[139] A. G. Jacobs, B. Jung, J. Jiang, C. K. Ober, and M. O. Thompson, "Control of polystyrene-block-poly(methyl methacrylate) directed self-assembly by laser-induced millisecond thermal annealing", *Journal of Micro/Nanolithography, MEMS, and MOEMS*, vol. 14, no. 3, p. 031 205, 2015. DOI: 10.1117/1.JMM.14.3.031205.

[140] A. G. Jacobs, C. Liedel, H. Peng, L. Wang, D.-M. Smilgies, C. K. Ober, and M. O. Thompson, "Kinetics of block copolymer phase segregation during sub-millisecond transient thermal annealing", *Macromolecules*, vol. 49, no. 17, pp. 6462–6470, 2016. DOI: 10.1021/acs.macromol.6b00698.

[141] D. P. Brunco, M. O. Thompson, C. E. Otis, and P. M. Goodwin, "Temperature measurements of polyimide during krf excimer laser ablation", *Journal of Applied Physics*, vol. 72, no. 9, p. 4344, 1992. DOI: 10.1063/1.352198.

[142] W. Chung, M. O. Thompson, P. Wickboldt, D. Toet, and P. G. Carey, "Room temperature indium tin oxide by xecl excimer laser annealing for flexible display", *Thin Solid Films*, vol. 460, no. 1, pp. 291–294, 2004. DOI: 10.1016/j.tsf.2004.01.050.

[143] R. M. Silverstein, F. X. Webster, and D. J. Kiemle, *Spectrometric Identification of Organic Compounds*, Seventh. Wiley, 2005, pp. 1–550. DOI: 10.1016/0022-2860(76)87024-X.

[144] C. D. Doyle, "Estimating thermal stability of experimental polymers by empirical thermogravimetric analysis", *Analytical Chemistry*, vol. 33, no. 1, pp. 77–79, 1961. DOI: 10.1021/ac60169a022.

[145] A. A. Apostolov, S. Fakirov, E. Vassileva, R. D. Patil, and J. E. Mark, "Dsc and tga studies of the behavior of water in native and crosslinked gelatin", *Journal of Applied Polymer Science*, vol. 71, no. 3, pp. 465–470, 1999. DOI: 10.1002/(SICI)1097-4628(19990118)71:3<465::AID-APP13>3.0.CO;2-1.

[146] M. Kamruddin, P. K. Ajikumar, R. Nithya, G. Mangamma, A. K. Tyagi, and B. Raj, "Effect of water of crystallization on synthesis of nanocrystalline ceria by non-hydrolytic method", *Powder Technology*, vol. 161, no. 2, pp. 145–149, 2006. DOI: 10.1016/j.powtec.2005.10.003.

[147] N. Grassie, *Developments in Polymer Degradation - 7*. Elsevier Applied Science Publishers, 1987.

[148] N. Grassie and G. Scott, *Polymer Degradation and Stabilization*. Cambridge University Press, 1988.

[149] H. Ito, "Chemical amplification resists for microlithography", in *Advances in Polymer Science*, vol. 172, 2005, pp. 37–245. DOI: 10.1007/b97574.

[150] C. Tang, E. M. Lennon, G. H. Fredrickson, E. J. Kramer, and C. J. Hawker, "Evolution of block copolymer square arrays", *Science*, vol. 322, pp. 429–432, 2008. DOI: 10.1126/science.1162950.

[151] M. P. de Jong, L. J. van IJzendoorn, and M. J. A. de Voigt, "Stability of the interface between indium-tin-oxide and poly(3,4-ethylenedioxythiophene)/poly(styrenesulfonate) in polymer light-emitting diodes", *Applied Physics Letters*, vol. 77, pp. 2255–2257, 2000. DOI: 10.1063/1.1315344.

[152] S. A. McDonald, G. Konstantatos, S. Zhang, P. W. Cyr, E. J. D. Klem, L. Levina, and E. H. Sargent, "Solution-processed pbs quantum dot infrared photodetectors and photovoltaics", *Nature materials*, vol. 4, no. 2, pp. 138–142, 2005. DOI: 10.1038/nmat1299.

[153] J.-L. Tang and M.-A. Tsai, "Rapid formation of block copolymer thin film based on infrared laser irradiation", *2007 Conference on Lasers and Electro-Optics - Pacific Rim*, pp. 17–18, 2007. DOI: 10.1109/CLEOPR.2007.4391384.

[154] P. W. Majewski and K. G. Yager, "Block copolymer response to photothermal stress fields", *Macromolecules*, vol. 48, no. July, pp. 4591–4598, 2015. DOI: 10.1021/acs.macromol.5b00955.

[155] A. G. Jacobs, B. Jung, C. K. Ober, and M. O. Thompson, "Control of ps-b-pmma directed self-assembly registration by laser induced millisecond thermal annealing", *Proc. of SPIE*, vol. 9049, 90492B, 2014. DOI: 10.1117/12.2046513.

[156] A. G. Jacobs, C. Liedel, C. K. Ober, and M. O. Thompson, "Understanding of ps-b-pmma phase segregation under laser-induced millisecond thermal annealing", *Proc. of SPIE*, vol. 9423, pp. 942 309–1, 2015. DOI: 10.1117/12.2086057.

[157] G. Singh, K. G. Yager, B. Berry, H. C. Kim, and A. Karim, "Dynamic thermal field-induced gradient soft-shear for highly oriented block copolymer thin films", *ACS Nano*, vol. 6, no. 11, pp. 10 335–10 342, 2012. DOI: 10.1021/nn304266f.

[158] B. C. Berry, A. W. Bosse, J. F. Douglas, R. L. Jones, and A. Karim, "Orientational order in block copolymer films zone annealed below the order-disorder transition temperature", *Nano Letters*, vol. 7, no. 9, pp. 2789–2794, 2007. DOI: 10.1021/nl071354s.

[159] K. G. Yager, N. J. Fredin, X. Zhang, B. C. Berry, A. Karim, and R. L. Jones, "Evolution of block-copolymer order through a moving thermal zone", *Soft Matter*, vol. 6, pp. 92–99, 2010. DOI: 10.1039/b916200c.

[160] G. Singh, K. G. Yager, D. M. Smilgies, M. M. Kulkarni, D. G. Bucknall, and A. Karim, "Tuning molecular relaxation for vertical orientation in cylindrical block copolymer films via sharp dynamic zone annealing", *Macromolecules*, vol. 45, no. 17, pp. 7107–7117, 2012. DOI: 10.1021/ma301004j.

[161] J. Sha, B. Jung, M. O. Thompson, C. K. Ober, M. Chandhok, and T. R. Younkin, "Submillisecond post-exposure bake of chemically amplified resists by co2 laser spike annealing", *Journal of Vacuum Science & Technology B: Microelectronics and Nanometer Structures*, vol. 27, pp. 3020–3024, 2009. DOI: 10.1116/1.3263173.

[162] J. W. Cahn, "Transformation kinetics during continuous cooling", *Acta Metallurgica*, vol. 4, no. 6, pp. 572–575, 1956. DOI: 10.1016/0001-6160(56)90158-4.

[163] J. W. Cahn, "Phase separation by spinodal decomposition in isotropic system", *The Journal of Chemical Physics*, vol. 42, no. 1965, pp. 93–99, 1965. DOI: 10.1063/1.1695731.

[164] I. H. Leubner, "Particle nucleation and growth models", *Current Opinion in Colloid & Interface Science*, vol. 5, no. 1-2, pp. 151–159, 2000. DOI: 10.1016/S1359-0294(00)00048-0.

[165] Y. Yoneda, "Anomalous surface reflection of x rays", *Physical Review B*, vol. 131, no. 5, pp. 2010–2013, 1963. DOI: 10.1103/physrev.131.2010.

[166] G. H. Vineyard, "Grazing-incidence diffraction and the distorted-wave approximation for the study of surfaces", *Physical Review B*, vol. 26, no. 8, pp. 4146–4159, 1982. DOI: 10.1103/physrevb.26.4146.

[167] O. Kratky and G. Porod, "Diffuse small-angle scattering of x-rays in colloid systems.", *Journal of Colloid Science*, vol. 4, pp. 35–70, 1949. DOI: 10.1016/0095-8522(49)90032-X.

[168] J. Crank, *The Mathematics of Diffusion*, 2nd ed. Oxford University Press, 1975.

[169] M. Antonietti, J. Coutandin, and H. Sillescu, "Chainlength and temperature dependence of self-diffusion coefficients in polystyrene", *Makromol. Chem., Rapid Commun.*, vol. 5, no. 9, pp. 525–528, 1984. DOI: 10.1002/marc.1984.030050907.

[170] T. A. Callaghan and D. R. Paul, "Interaction energies for blends of poly(methyl methacrylate), polystyrene, and poly(a-methylstyrene) by the critical molecular weight method", *Macromolecules*, vol. 26, pp. 2439–2450, 1993. DOI: 10.1021/ma00062a008.

[171] B. Stuhn, "Relation between the microphase separation transition and the glass transition in diblock copolymers", *Journal of Polymer Science, Part B: Polymer Physics*, vol. 30, no. 9, pp. 1013–1019, 1992. DOI: 10.1002/polb.1992.090300909.

[172] H. Ahn, D. Y. Ryu, Y. Kim, K. W. Kwon, J. Lee, and J. Cho, "Phase behavior of polystyrene- b -poly(methyl methacrylate) diblock copolymer", *Macromolecules*, vol. 42, no. 20, pp. 7897–7902, 2009. DOI: 10.1021/ma901313a.

[173] G. Floudas, B. Vazaiou, F. Schipper, R. Ulrich, U. B. Wiesner, H. Iatrou, and N. Hadjichristidis, "Poly(ethylene oxide-b-isoprene) diblock copolymer phase diagram", *Macromolecules*, vol. 34, no. 9, pp. 2947–2957, 2001. DOI: 10.1021/ma001957p.

[174] D. M. A. Buzza, A. H. Fzea, J. B. Allgaier, R. N. Young, R. J. Hawkins, I. W. Hamley, T. C. B. McLeish, and T. P. Lodge, "Linear melt rheology and small-angle x-ray scattering of ab diblocks vs a2b2 four arm star block copolymers", *Macromolecules*, vol. 33, no. 22, pp. 8399–8414, 2000.

[175] G. Floudas, R. Ulrich, U. B. Wiesner, and B. Chu, "Nucleation and growth in order-to-order transitions of a block copolymer", *Europhysics Letters (EPL)*, vol. 50, no. 2, pp. 182–188, 2007. DOI: 10.1209/epl/i2000-00252-0.

[176] T. S. Bailey, H. D. Pham, and F. S. Bates, "Morphological behavior bridging the symmetric ab and abc states in the poly(styrene-b-isoprene-b-ethylene oxide) triblock copolymer system", *Macromolecules*, vol. 34, no. 20, pp. 6994–7008, 2001. DOI: 10.1021/ma0103371.

[177] C. Shin, D. Y. Ryu, J. Huh, J. H. Kim, and K.-W. Kim, "Order-to-order transitions of block copolymer in film geometry", *Macromolecules*, vol. 42, pp. 2157–2160, 2009. DOI: 10.1021/ma802737s.

[178] N. Owens, I. S. Gancarz, and T. P. Russell, "Investigation of the microphase separation transition in low molecular weight diblock copolymers", *Macromolecules*, vol. 22, no. 24, pp. 3380–3387, 1989. DOI: 10.1021/ma00198a032.

[179] L. J. Fetters, D. J. Lohse, T. D. Richter, T. A. Witten, and A. Zirkelt, "Connection between polymer molecular weight, density, chain dimensions, and melt viscoelastic properties", *Macromolecules*, vol. 27, no. 17, pp. 4639–4647, 1994. DOI: 10.1021/ma00095a001.

[180] C. Lai, W. B. Russel, R. A. Register, G. R. Marchand, and D. H. Adamson, "Phase behavior of styrene-isoprene diblock derivatives with varying conformational asymmetry", *Macromolecules*, vol. 33, no. 9, pp. 3461–3466, 2000. DOI: 10.1021/ma991156q.

[181] R. Bachus and R. Kimmich, "Molecular weight and temperature dependence of self-diffusion coefficients in polyethylene and polystyrene melts investigated using a modified n.m.r. field-gradient technique", *Polymer*, vol. 24, no. 8, pp. 964–970, 1983. DOI: 10.1016/0032-3861(83)90146-5.

[182] G. Fleischer, "Temperature dependence of self diffusion of polystyrene and polyethylene in the melt an interpretation in terms of the free volume theory", *Polymer Bulletin*, vol. 11, no. 1, pp. 75–80, 1984. DOI: 10.1007/BF00401718.

[183] J. K. Bosworth, C. T. Black, and C. K. Ober, "Selective area control of self-assembled pattern architecture using a lithographically patternable block copolymer", *ACS Nano*, vol. 3, no. 7, pp. 1761–1766, 2009. DOI: 10.1021/nn900343u.

[184] M. Y. Paik, J. K. Bosworth, D.-M. Smilgies, E. L. Schwartz, X. Andre, and C. K. Ober, "Reversible morphology control in block copolymer films via solvent vapor processing: an in situ gisaxs study", *Macromolecules*, vol. 43, no. 9, pp. 4253–4260, 2010. DOI: 10.1021/ma902646t.

[185] C. A. Schneider, W. S. Rasband, and K. W. Eliceiri, "Nih image to imagej: 25 years of image analysis", *Nature Methods*, vol. 9, no. 7, pp. 671–675, 2012. DOI: 10.1038/nmeth.2089.

[186] V. C. Sorg, S. N. Zhang, P. Clancy, and M. O. Thompson, "Dopant activation and deactivation in ingaas during sub-millisecond thermal annealing", *ECS Transactions*, vol. 66, no. 4, pp. 117–124, 2015. DOI: 10.1149/06604.0117ecst.

[187] B. Jung, "Laser-induced millisecond heating of polymers and small molecules for pattern development", PhD thesis, Cornell University, 2014.

[188] M. W. Barsoum, *Fundamentals of Ceramics*, 2nd, B. Cantor and M. J. Goringe, Eds. Taylor & Francis, 2003.